MATERIALS FOR ENERGY: COMPLEX OXIDES AND NITRIDES FOR NEW POLYMER ELECTROLYTE MEMBRANE FUEL CELL CATALYSTS AND SUPPORTS

A Dissertation
Presented to the Faculty of the Graduate School
of Cornell University
In Partial Fulfillment of the Requirements for the Degree of
Doctor of Philosophy

By
Raymond Gabriel Burns III
August 2013

MATERIALS FOR ENERGY: COMPLEX OXIDES AND NITRIDES FOR NEW POLYMER ELECTROLYTE MEMBRANE FUEL CELL CATALYSTS AND SUPPORTS

Raymond Gabriel Burns III, Ph. D.
Cornell University 2013

The currently used carbon-based catalyst supports in polymer electrolyte membrane fuel cells (PEMFC) are not sufficiently stable. New, non-carbon catalyst supports are required for large-scale commercialization of PEMFCS, and must be stable in low pH (1-2) and up to +1.5 V (vs. SHE). The material also needs to be porous and conducting (at least 0.1 S cm^{-1}). Furthermore, the catalyst support should also be capable of strongly binding Pt or Pt-based catalysts.

Previous research in the DiSalvo group has focused on doped, conducting metal oxides, yet materials with suitable conductivities have been difficult to prepare. In this work, binary and ternary transition metal nitrides are explored as potential replacements for carbon-based catalyst supports. Many nitrides have the required conductivity and chemical stability need for applications in PEMFCs, while their preparation as mesoporous solids is not well reported. In this work, Ti-based mixed metal catalyst supports were prepared as nanoparticles and thin films, and their utility for PEMFC applications investigated using a variety of material characterization techniques. Nitride compounds with Ti, Nb, Cr are conducting as both nanoparticles and thin films, and shown improved oxidation resistance when prepared as co-precipitated nanoparticles.

In addition to catalyst supports, $LaMO_3$ (M=Mn, Ni, Fe, Co) perovskites were prepared and studied as oxygen reduction catalysts for alkaline fuel cells. This work shows that these compounds favor the 2-electron reduction of O_2 to H_2O_2 rather than full reduction to H_2O. Additionally, the chemical stability of the material is discussed, and found to be unsatisfactory for applications in alkaline fuel cells.

BIOGRAPHICAL SKETCH

Raymond G. Burns III was born in Louisville, KY, in 1985. He is the oldest of 4 children. He attended Most Blessed Sacrament grade school where his favorite subjects were social studies and history. Despite his initial disinterest in science, Raymond had an innate curiosity about the world around him and enjoyed learning how things were put together. This "tinkerer" mentality evolved through his formative years and through high school where he further developed his interest in science and math. While attending DeSales High School, his fascination with the living and physical world expanded as he studied Biology, Chemistry, and Physics, with a particular interest in Chemistry. Raymond found the chemical world the perfect bridge between the worlds of physics and biology, and believed that the true applications of science were born out of chemistry. Raymond used this passion for chemistry to earn a position with the Colgate-Palmolive Company as a Quality Assurance Laboratory Technician upon graduation.

Raymond then attended Bellarmine University in Louisville, KY, where he chose to major in Chemistry with minors in Physics and Mathematics. Bellarmine University could not have been a better choice for Raymond. Because of its belief in the liberal arts, Bellarmine exposed Raymond to a world beyond the laboratory. He had the opportunity to study Art, Photography, Theology, Social Justice, and to travel to Ireland and Guatemala -- all things that aided in developing him into a whole person. In addition to the stunning academic program, Bellarmine offered Raymond the opportunity to meet some of his greatest friends and allies who continue to support him and enrich his life today.

Upon graduating from Bellarmine in 2007, Raymond chose to take a sabbatical and spend a year as a volunteer teacher with the service organization WorldTeach in Micronesia. While this experience ultimately ended prematurely and unsuccessfully, Raymond learned several valuable lessons about how others in the world live and how each person plays a role in shaping the world around them. Raymond spent the remainder of the year working for Süd-Chemie, Inc.

in Louisville where he worked on developing new catalysts for several industrial processes. This experience helped Raymond develop an interest in materials science and materials for energy applications.

Raymond started in the Ph.D. program in the Department of Chemistry and Chemical Biology at Cornell University in the Fall of 2008. He had developed an interest in fuel cells and was drawn to Cornell by the work being done in the Cornell Fuel Cell Institute lead by Prof. Héctor Abruña and Prof. Frank DiSalvo. Raymond joined the DiSalvo group where he began the long process of learning about materials science and solid-state chemistry – two subjects he had never studied before.

Raymond spent the next several years on a roller coaster, at times being productive in research, and at times exploring other opportunities or subjects of interest. Raymond feels extremely grateful for the flexibility his advisor showed in allowing him to explore various paths including becoming a Firefighter/EMT, interning for Environmental Health & Safety, and even supporting his choice to study at Oxford University in the UK for three months. In light of these experiences, both the ups and the downs, Raymond is extremely happy with his life at present, and is looking forward to the future.

After graduation, Raymond will be taking a position with ExxonMobil Research and Engineering Company in Paulsboro, NJ, where he will serve as a Product Research Technologist in their Lubricant Products Division.

Dedicated to my friends and family

ACKNOWLEDGMENTS

First and foremost, I would like to thank my advisor, Prof. Frank DiSalvo. I entered Cornell with a desire to work on fuel cells, but didn't have a clear picture of what that really meant. I spoke to several faculty members who each told me about the interesting research they were doing in their group, but Frank was the only professor to start by asking what my interests were. This initial interaction set the stage for our professional relationship, and is a testament to Frank's approach to letting students set their own path. I really appreciated Frank's patience and guidance as I worked (and at times struggled) to figure out what it was that I really wanted to do. At times I was productive at research, and at other times Frank gave me the freedom to explore other topics that interested me, including studying abroad at Oxford for a semester, and interning with Environmental Health & Safety. I sincerely appreciate Frank's willingness to let me find my own path and his sage advice along the way.

Thank you also to Prof. Hector Abruña and Prof. Bruce van Dover for agreeing to serve on my committee. Each of you played a large role in making me the researcher I am today, and I sincerely appreciate all the time and energy you have put into providing opportunities for young scientists like me to glean from your wisdom and learn about interesting topics. Thank you for your tireless efforts in making the Energy Materials Center at Cornell (EMC2) a great team to work with.

In addition to my committee members, I also must thank the countless support staff of the user facilities around campus that helped make my research possible. Thanks to Jon Shu, Mick Thomas, John Grazul, John Hunt, and Steve Kriske for keeping all of CCMRs equipment running and helping me troubleshoot when things went wrong.

Thanks to Nate Ellis for teaching me how to be a machinist and how to be a better person. I don't think I would have made it through this thing without our daily chats (or rants and raves) about life, liberty, and the pursuit of happiness. Thanks for taking the time to teach me about things, and to let me make my own mistakes. You have become one of my best friends.

Thank you to all the other students and post-docs who collaborated and suffered with me. Thanks to Dr. Steven Burkhardt, Dr. Michael Lowe, Dr. Eric Rus, and Dr. David Finkelstein for helping me understand the finer points of Electrochemistry. Thanks to Dr. Brian Leonard for teaching me how to do science, to make beer, and for letting me move in with him. Thanks to Dr. Mark Dreibelbis and Heather Edvenson for introducing me to the DiSalvo group, and sharing an office with me. Thanks to Dr. Chin Subban for all the help in lab and being your cheerful, wonderful self. Thanks to Dr. Minghui Yang for teaching me about Reitveld refinements. Thanks to Dr. Qin Zhou, Dr. Deli Wang, and Dr. Zhiming Cui for helping me do electrochemical measurements. Thanks to Dr. James O'Dea for helping me get the thin film project started, you really put a lot of time and effort into helping me learn and understand AFM. Thanks to Julia Mundy and Houlin Xin for help with TEM imaging, and Megan Holtz for STEM and EELS measurements. Thanks to Anna Legard and Dr. John Gregoire for teaching me about Tubby and letting me sputter some films. Thanks to Ritu, Spencer, Juho, Joerg, Mihn, Hao, and Doug for being part of the DiSalvo group. Finally, thanks to all the other researchers in EMC2 for collaborating and sharing your collective knowledge.

I couldn't have done this research without the help of my undergraduates. Thanks to Joseph Singh and Mayra Hernández-Rivera. Although our time together was short we accomplished a lot and I thank you both for the time you dedicated to our project. Thank you to Michael De Sienna. What can I say about you? You are great and took the little bit of information we had, and ran with it. I said from the start that the Perovskite project was yours, and you never disappointed me. Thank you for your dedication and for sticking with me for two years, your future is bright my friend.

Thanks to all my classmates, although we grew apart over the years I treasure the time we spent together as first years. Thanks to Will and Martha for spending hours on Quantum homework with me. Thanks to Angie, Megan, and Erica for hosting parties and for my birthday cake. Thanks also to Dave, Nikhil, Ryan, Pasqual, Henry, Kevin, and the others for your willingness to get some beers and talk science.

Thanks to Prof. Simon Clarke and his research group for welcoming me into your lab for a few months. I learned a great deal from you all and had a wonderful time exploring Oxford. Thanks to Alex and the Trinity College crew for "Risk Vine Rouge" and all the nights on the lash.

Thank you to Dr. Pat Holt, Dr. Graham Ellis, and Bob Bernauer for teaching me about chemistry in the first place. Thank you for inspiring me to continue studying, and inspiring me to learn all I can. Thanks to all the faculty at Bellarmine University for encouraging me to be the best version of myself both in and out of the lab.

Thank you to my friends and family in Louisville. Thanks to my parents for their constant encouragement and love, the best parts of me come from the both of you. Thanks to Jimmy, Billy, and Kathleen for being amazing siblings and for letting me be your big brother. Thanks to Anna for all the late night chats and keeping me sane. Thanks to Hannah for encouraging me to always look on the bright side of life. Thanks to Jess for letting me officiate your wedding.

Thank you to the Cornell Center for Materials Research and to the Energy Materials Center at Cornell for providing financial support throughout the course of my graduate career. Thanks to BJ, Terry, and Darren and all the other staff at Goldie's for all the free soda and sandwiches. Thanks to Pat Hine, Suzanne Koehl, Vonnie Ellis, Sharon de Roos, Robin Nichols, Kelly Case and all the other administrative staff that made the "Big Red Tape" cut a little easier.

Finally, thank you to Danica for loving me and for inspiring me everyday to be the best man that I can be. Thank you for being the amazing, strong, vibrant, sexy woman I love more than anything else. Thanks for all that you do to help me make it through each day, thanks for teaching me how to skate, and for helping me see the man I want to become. I can't wait to start the next chapter of our journey together.

TABLE OF CONTENTS

LIST OF FIGURES

LIST OF TABLES

CHAPTER 1

FUEL CELLS: EFFICIENCY AND CHALLENGES

1.1 Fuel Cells and Efficiency

It is difficult in 2013 to deny that the production, consumption, and storage of energy are among the top technological challenges facing our world. As the demand for fossil fuels increases, the call for alternative, more efficient and clean sources of energy becomes loud and clear. While many new technologies are under development to address this need, deficiencies in materials properties and other problems have hindered the successful replacement of fossil fuel burning energy sources. Currently deployed technologies often rely on heat-driven engines. These engines are inherently limited in efficiency by the 2nd law of thermodynamics via the Carnot limit, which states that the maximum efficiency achievable by a heat-driven engine is a function of the operating temperature of the engine, as well as the temperature of the environment in which it operates, Figure 1.1.

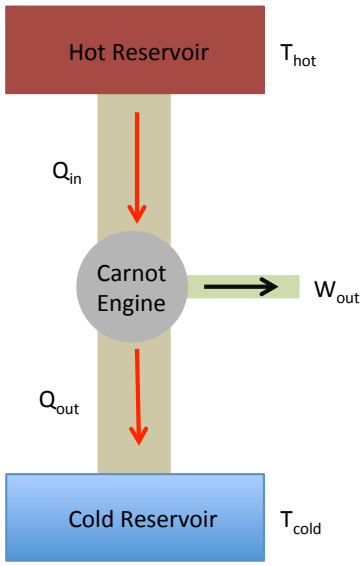

$$\eta = \frac{T_{hot} - T_{cold}}{T_{hot}} = \frac{Q_{in} - Q_{out}}{Q_{in}}$$

Figure 1.1 A schematic of the Carnot Cycle. T_{hot} and T_{cold} represent the temperatures of the hot and cold reservoirs respectively (or engine and enivronment, respectively). Q_{in} represents the heat input to the engine, while Q_{out} represents the heat rejected to the cold reservoir. W_{out} is the maximum effective work produced by the engine and is governed by the efficiency (η) calculated using the equation on the right.

A classic example of these limitations is the internal combustion engine (ICE) which powers most automobiles on the roads today. The ICE operates via the carnot cycle and is only capable of achieving approximately 30% efficiency in the highest performing engines. Many are much less at only 20-25% efficient, rejecting the remaining energy and power as heat (Q_{out}, via exhaust gases and the radiator) to the atmosphere (T_{cold}).[1] An additional example are the steam turbines that operate the US power grid. These generators are slightly higher in efficiency but only approximately 35-40%. One reason behind this diminished effiency is the lack of long-term durability of materials in the high temperature operating environment within the device (T_{hot}). Even with new and advanced materials, many scientists predict that heat cycle engienes will never achieve more than 50-60% maximum effiency.[2] It is clear that a new path forward is needed to make significant gains in how we consume, produce, and store energy.

Fuel Cells (FC), first invented in 1839 by Sir William Grove[3], may be poised to revolutionize the way we use energy, but many challenges must first be overcome for this technology to be fully realized. Fuel cells operate by directly coverting a chemical fuel to electricy via Oxidation-Reduction (redox) chemistry. Because this is not a thermally driven cycle, FCs are not subject to the Carnot limit. In theory, all of the free energy (ΔG) of fuel oxidation could be converted to electrical energy. However, one must be careful in defining efficency when comparing fuel cell efficencies to thermally driven systems. For example, in ICEs the efficency is determined by the fraction of the enthalpy (ΔH) which converted to energy. It is known from thermodynamics that:

$$\Delta G = \Delta H - T\Delta S \tag{1.1}$$

Where TΔS is due to the entropy change of the system undergoing reaction. This expression demonstrates that while fuel cells do not use a thermal cycle to generate electricity from chemical fuels, the maximum energy available for work (ΔG) is a function of temperature. This temperature dependence arises from the TΔS term, which directly contains T. ΔS for gaseous reactants and products is only weakly T dependant above room temperature, and depends on both the identity and stoichiometric ratios of reactants and products. Generally, ΔS can be either negative or positive. Based on this logic, practical efficiencies in room temperature (RT) fuel cells could *potentially* reach approximately 90% (depending on the fuel) assuming no other sources of inefficiency within the device. This also demonstrates that the realizable efficiency for a fuel cell only drops as the operating temperature increases.

In addition to these thermodynamic considerations, several additional issues continue to hinder the full deployment of fuel cell technologies. As the power extracted from a fuel cell increases, for example, irreversible losses occur since the system is driven out of equilibrium. Also, deficiencies in materials, overcoming the slow reaction kinetics of the oxygen reduction reaction (ORR) at the FC cathode, and poor impurity tolerance in the fuel stream at the FC anode continue to challenge researchers. Further, system durability and cost are currently limiting factors. Each of these issues ultimately can be traced to the limits imposed by the current materials available for fuel cell construction. Despite these challenges, the promise of high efficiency and, with a proper fuel supply chain, potentially low greenhouse gas emissions have made fuel cells an attractive research and development objective. [4,5]

A simple fuel cell consists of two electrodes (anode and cathode) separated by an ionic conductor (which may be liquid, solid, or polymeric). There are many different types of fuel cell technologies that are generally described by their operating temperature, type of fuel that is used,

and the ionic species that is transported within the device. Table 1.1, below, describes several of these types of fuel cells.

Table 1.1 Types of fuel cell technologies by fuel type, operating temperature, and transported species.

Fuel Cell Type	Fuel Type	Electrolyte	Transported Species	Operating Temperature (°C)
Polymer Electrolyte Membrane (PEM)	High Purity H_2	Perfluorinated Sulfonic Acid Ionomer (Nafion™)	H_3O^+(aq)	0-80
Alakline	High Purity H_2	KOH in PVC felt	OH^-(aq)	90
Phosporic Acid	H_2	H_3PO_4 in pourous SiC bonded w/ Teflon™ or other polymeric materials	H^+	200
Molten Carbonate	H_2	Li_2CO_3/K_2CO_3 liquid	CO_3^{2-}(l)	650
Solid Oxide	H_2, CH_4	$Zr_{0.92}Y_{0.08}O_{1.96}$ceramic	O^{2-}	700-1000
Direct Methanol PEM	CH_3OH	Perfluorinated Sulfonic Acid Ionomer (Nafion™)	H_3O^+(aq)	60-120

Among these different fuel cell technologies, the Polymer Electrolyte Membrane, or Proton Exchange Membrane, Fuel Cell (PEMFC) is of the most interest due to its low temperature of operation (0-80 ºC) and its reasonable start-stop capability.[6] Additionally the higher power density and lower relative cost when compared with other fuel cell technologies make PEMFCs particularly suited for a variety of portable power applications, possibly including replacing the ICE in automobiles.

1.2 Proton Exchange Membrane Fuel Cells

Proton Exchange Membrane Fuel Cells (PEMFCs) operate by conducting hydrated hydrogen ions across a polymeric membrane between the positive and negative terminals of a fuel cell. Specifically, a fuel, such as H_2, is introduced at the anode (negative terminal) where it undergoes catalytic oxidation to 2 hydrogen ions and 2 electrons. The electrons are sent through an external circuit to do electrical work while the hydrated hydrogen ions are selectively transported across the polymeric membrane to the cathode (positive terminal). At the cathode oxygen (usually as air) is introduced and recombines with the hydrogen ions and electrons via catalytic reduction to water (i.e. the Oxygen Reduction Reaction or ORR). Figure 1.2, below, shows the general process for a standard PEMFC.

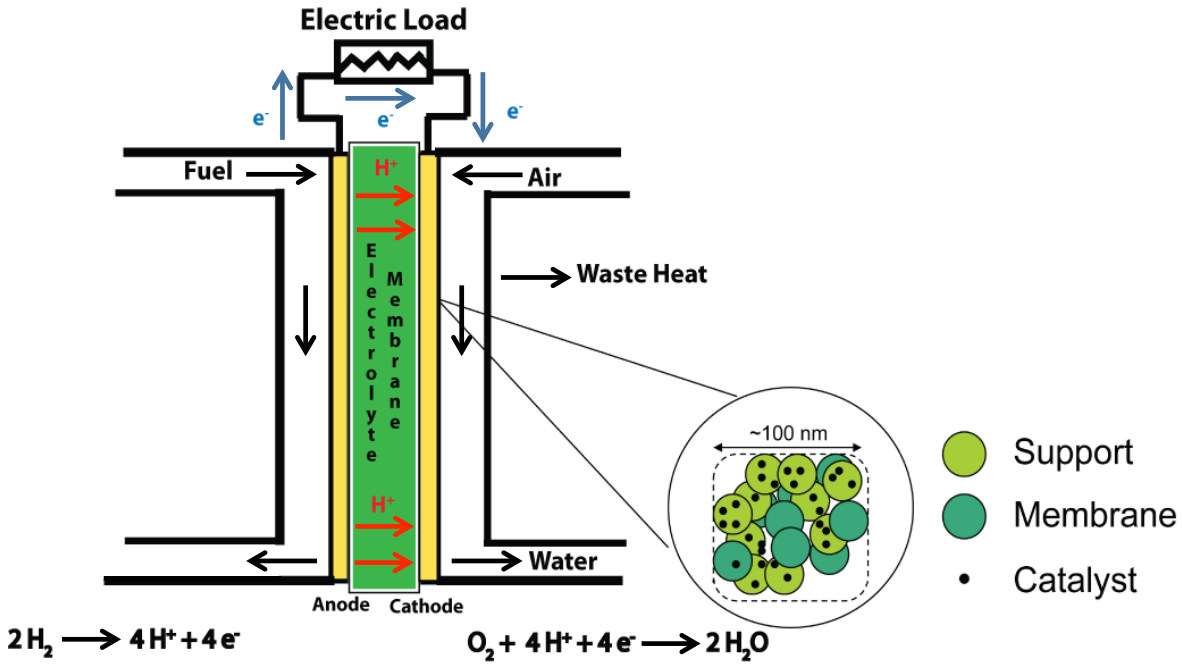

Figure 1.2 Schematic of a PEMFC

The heart of the PEMFC is the Membrane Electrode Assembly, or MEA (colored portion in Figure 1.2), which consists of the anode layer, the polymer electrolyte membrane, and the

cathode layer.[6] Typically the anode and cathode layers, both of which consist of catalyst nanoparticles deposited on the support material dispersed with ionomer nanoparticles of the membrane material (blown-up region in Figure 1.2), are prepared as an "ink" in a suitable solvent and painted onto the polymeric membrane. The ionomer in the catalyst layer provides the necessary ionic conductivity to facilitate mass transport from the nanoscopic interfaces to the larger pores of the MEA and eventually to the polymer membrane itself. Additionally, the MEA must be in electrical contact with an external circuit. This is facilitated by first incorporating a Gas-Diffusion Layer (GDL), which not only facilitates electron transport, but also disperses gaseous reactants and products for maximum utilization of the catalyst surface area. Then a "bipolar plate" is used as both a current collector, and to connect several MEAs together in series in order to obtain higher operating voltages. The connected MEAs form what is called a "stack". The interface that allows for the transport of gaseous species, electrons, and ions is referred to as the "Triple-Phase Boundary."

1.3 Materials Property Requirements and Challenges

The benefits of using fuel cells for portable power applications are apparent, but fuel cell vehicles and generators are hardly rolling off assembly lines. The disconnect comes in realizing that cartoons such as Figure 1.2 paint a highly idealized picture of the elegant chemistry which must take place at both the anode and cathode, and fails to address the current limitations of the materials which comprise the device. While researchers have made admirable improvements over the last decade, material durability, cost, and life cycle performance continue to thwart full integration of fuel cell technology into modern infrastructure. Current PEMFCs require complex control schemes and associated hardware to achieve adequate durability, but at the cost of

performance and efficiency.[7] Even still, the catalyst support, electrode layers, and membrane all undergo chemical degradation after only hundreds or perhaps thousands of start/stop cycles. Also, the currently used catalyst materials are based on Pt or other precious metals and their alloys, which make fuel cells rather expensive for commercial applications. Finally there are also a number of issues surrounding the "clean" production of *pure* hydrogen gas as a fuel and the lack of any infrastructure to dispense it as easily and as wide spread as gasoline. [5,8] It is clear that there are many roadblocks ahead for the full deployment of PEMFCs for commercial markets.

1.3.1 Proton Exchange Membrane

The first PEMFCs were in development as early as 1955 by researchers at General Electric, and went through several early generations of technology, including using phenolic membranes and membranes based on poly(styrene sulfonic acid). By the mid-1960's these GE PEMFCs were in use in NASA's GEMINI series of spacecraft and, when placed in a stack, were capable of power generation of up to 1-kW. Despite great technological advances, these early membranes suffered from deficiencies in their mechanical properties and required extremely pure fuel and oxidant to operate at suitable efficiencies. Of course on space missions, pure H_2 and O_2 are available from storage on board as liquid propellant for the rockets. Additionally, the hydrogen ion conductivity through these membranes was insufficient to even reach a power density of 100 mW/cm^2.[9]

In the late-1960's a major breakthrough in polymer membranes was made by Walther Grot of DuPont when he synthesized a sulfonated tetrafluoroethylene copolymer known today as Nafion®. Nafion became the first in a class of membrane materials known as ionomers due to

their ionic properties. [10,11] Additionally, the Nafion family of membranes possessed superior thermal, chemical, and mechanical stability compared to any other membrane on the market at the time. Demonstrated membrane lifetimes in the best materials were only around 3,000 hours at 50°C while Nafion showed and extended lifetime of nearly 50,000 hours in equivalent conditions.[9] Nafion became the clear industry leader of the time, and has, until recently, been the gold standard for fuel cell membranes.

Nafion is a perfluorosulfonic acid (PFSA) membrane, which makes it extremely stable under both oxidizing and reducing conditions. The backbone is made from tetrafluoroethylene (PTFE: DuPont's TEFLON™), which is then copolymerized with sulfonated perfluorovinyl ether. This unique structure is highly acidic, a favorable property of fuel cell membranes, and is capable of achieving proton conductivities on the order of approximately 10^{-2} S cm^{-1}.[12] In a fuel cell, Nafion membranes must be hydrated in order to achieve their proton conducting abilities, which makes water balance an extremely important operational parameter for PEMFCs. Operation at higher temperatures, especially above 100ºC, requires pressurization to keep sufficient water in the membrane; however, mechanical performance is reduced, and membrane degradation rates are increased at such temperatures. Therefore, Nafion membranes are typically operated near 80ºC.

In a Direct Methanol Fuel Cell (DMFC), Nafion suffers from methanol crossover; the fuel leaks from the anode side of the fuel cell to the cathode side of the fuel cell, resulting in an overall loss of power and efficiency. Nafion also has a high electro-osmotic drag coefficient (flux of water molecules/flux of hydrogen ions), which makes water management difficult at high current densities. These properties, coupled with the potentially environmentally toxic

nature of the fluorinated polymer have created an enormous drive to find cheaper, more stable, and more environmentally benign PEMFC membranes.

While Nafion has proven not to be a viable candidate for a mass-marketable DMFC, it has helped researchers clarify the necessary properties for a good electrolyte membrane candidate. Among the necessary properties are; high thermal, chemical, and mechanical stability in fuel cell operating conditions; high proton conductivity with zero electronic conductivity and low resistance; good water uptake at high temperature operation (>100 °C); low permeability to fuels and oxidants; flexibility to work with a wide range of fuels; and low production cost ($5-15 ft^{-2}). With these necessary properties in mind, researchers have pursued, generally, three avenues in the search for new PEMFC membranes: 1. modified perfluorinated ionomer membranes; 2. functionalization of aromatic hydrocarbon polymers/membranes; and 3. acid-base doping of a thermo-stable polymers.[9]

Modifying Nafion membranes involves incorporating inorganic materials such as zirconium or boron phosphates, or other heteropolyacids (such as phosphotungstic acid and phosphomolybdic acid) into a Nafion matrix at high temperature. Membranes prepared in this manner have been shown to out perform Nafion up to temperatures of 150°C in DMFCs. Composite membranes of Nafion with silicon oxide for use in fuel cells operating between 80-150°C have also been reported to have superior performance than to Nafion. [13-15] In each of the studies reviewed, incorporation of inorganic or other polymeric materials into a Nafion matrix has reduced methanol crossover and improved proton conductivities by almost 3-fold.

In the approach of functionalizing aromatic hydrocarbon polymers/membranes, the most studied material has been sulfonated polyether ether ketone (SPEEK). SPEEK has unique advantages over other aromatic hydrocarbon polymers in that it has relatively low methanol

permeation, reasonable conductivity, and very good mechanical properties including good flexibility and strength in thin films. The ability to make the polymer thin also leads to an overall reduction of resistance to protonic flow.[9] Despite these advantages, improvements in proton conductivity are needed in order to make SPEEK a viable replacement candidate for Nafion. To achieve this, researchers have begun studying SPEEK membranes incorporated with inorganic materials. These approaches have had mixed success, while the best results involved incorporating SPEEK with various heteropolyacids (HPAs) which were capable of achieving proton conductivities of 10^{-1} S cm^{-1} at 100°C and were shown to be thermally stable up to 250°C.[16] Despite the improved conductivities, the HPAs slowly leach out of these membranes. To correct this problem, researchers used zeolite and mesoporous molecular sieves to bind the HPAs and then incorporated the dry molecular sieve powders into a SPEEK matrix. These membranes showed comparable proton conductivities at approximately 150°C and were found to be thermally and mechanically stable. [17,18]

Aside from SPEEK based membranes, researchers have also investigated polymers such as sulfonated poly(arylene ether sulfone) incorporated with HPAs, poly(vinyl alcohol) (PVA) with HPAs[19], and PVA blended with poly(styrene sulfonic acid).[20] Each of these studies showed mixed results with the overriding theme of reducing methanol crossover and maintaining or improving proton conductivities when compared to Nafion at fuel cell operating temperatures (80-150°C). Polymer composites, prepared via sol-gel processing, consisting of poly(ethylene oxide), poly(propylene oxide), or polyvinylidene fluoride with silicon dioxide also showed significant improvement in reducing methanol permeation and increasing proton conductivity.[21]

Lastly the approach of acid-base doping of thermo-stable polymers has also yielded promising findings. Poly(benzimidazole) (PBI) is highly thermo-stable (T_m > 600°C), and when

doped with phosphoric acid has been used to prepare composite membranes with inorganic materials such as zirconium phosphate and HPAs. The conductivity of these membranes was found to be dependant on the doping level, relative humidity, and temperature but in general was found to be excellent when compared to Nafion and also showed decreased methanol permeation and low electro-osmotic drag. [22,23] Preparations with other acids (such as HCl, HNO_3, and $HClO_4$) also showed similar results.[24]

Among all these studies, work by Rikukawa and Sanui[25] identified 60 potential alternatives to PFSA membranes. A further study by Mehta and Cooper[26] narrowed the list of 60 potential membrane materials to 16 that satisfied what they considered to be the necessary criteria for an environmentally friendly, viable alternative to PFSA membranes. While many of these potential alternatives have been studied and have shown promise, much more needs to be done to improve stability under fuel cell operating conditions, increase lifetime, and to reduce materials costs.

1.3.2 Electrocatalyst Layers

An electrocatalyst layer forms both the anode and cathode of the fuel cell. In PEMFCs, the cathode performs the Oxygen Reduction Reaction (ORR) over a Pt or Pt-based alloy or intermetallic catalyst, while at the anode a fuel is oxidized, again using a Pt-based catalyst, generating the electrons that are used to perform work. Typically hydrogen is used as the fuel (since it is carbon free), but fuels such as methanol, formic acid, and perhaps ethanol are also of potential interest. Equations 1.2-1.6 below show these overall chemical reactions that ultimately determine the maximum theoretical potential for single fuel cell. Interestingly, all these have

single cell equilibrium potentials near 1.2 V– the standard potential of an alkaline Zn primary battery.

$$2\,H_2(g) + O_2\,(g) \xrightarrow[Cat.]{} 2\,H_2O\,(l) \qquad E^o=1.23\ V \qquad (1.2)$$

$$CH_4(g) + 2\,O_2\,(g) \xrightarrow[Cat.]{} 2\,H_2O\,(l) + CO_2(g) \qquad E^o=1.04\ V \qquad (1.3)$$

$$2\,CH_3OH(l) + 3\,O_2\,(g) \xrightarrow[Cat.]{} 4\,H_2O\,(l) + 2\,CO_2(g) \qquad E^o=1.21\ V \qquad (1.4)$$

$$2\,HCOOH(l) + O_2\,(g) \xrightarrow[Cat.]{} 2\,H_2O\,(l) + 2\,CO_2(g) \qquad E^o=1.20\ V \qquad (1.5)$$

$$CH_3CH_2OH(l) + 3\,O_2\,(g) \xrightarrow[Cat.]{} 3\,H_2O\,(l) + 2\,CO_2(g) \qquad E^o=1.15\ V \qquad (1.6)$$

Liquid fuels such as methanol and ethanol are much easier to distribute and handle from an engineering perspective; however, these fuels suffer from high oxidation overpotentials on present catalysts, as well as contribute to the poisoning of high surface area, nanoparticle catalysts with products from incomplete oxidation, such as carbon monoxide. Ethanol, for example, when fully oxidized yields 12 electrons per molecule as compared to methanol with only a 6-electron yield or hydrogen with only a 2-electron yield. Yet larger, more complex molecules often require more complicated (often multi-step) reaction mechanisms despite having a larger overall electron yield. Thus, both ethanol and methanol suffer from slow kinetics due to the need to break C-H bonds, and for the former C-C bonds. Because of the slow kinetics, cell potential must be sacrificed in order to drive the electrochemical process at a reasonable current density.

Hydrogen oxidation (HOR), on the other hand, is a relatively fast electrochemical process over a Pt catalyst and is capable of achieving reasonable current densities at low overpotentials.[27] The hydrogen, however, must be highly pure to avoid or at least reduce the occurrence of irreversible adsorption of contaminant species that poison the catalyst and drastically reduce or

destroy the electrochemically active surface area (ECSA). The presence of more than 0.1-10 ppm CO or even 10-100 ppb S (as H_2S or other organosulfur species) in a hydrogen stream is more than sufficient to effectively passivate a catalytically active surface. [5,28] Additionally, contaminants such as NH_3, HCN, and Cl^- may also be found in the fuel stream, especially when the hydrogen is formed by the reforming of methane, which can also affect cell performance.[29]

From a design point of view, the materials property requirements for an anode catalyst depend on the fuel being used. Generally, though, the catalyst must be synthesized as high surface area nanoparticles (3-5 nm) in order to achieve sufficiently high reaction rates.[30] Also, since only the surface of a catalyst is active and due to the fact that nanoparticles have a high surface to volume ratio, less of the expensive precious metal catalyst is required overall. Of course, the best catalyst would be that which oxidizes the fuel at the lowest overpotential (or has the best balance of cost versus performance as the industry dictates). The catalyst must be stable under fuel cell operating conditions (pH≤1 and at high potentials) and resist poisoning by impurities in the fuel stream as discussed earlier.

The stability of present catalysts has been widely studied and it has been shown that catalyst corrosion and loss of surface area occurs during both on-off and steady state operation. [31,32] Since, reaction kinetics are usually enhanced as temperatures increase, most common PEMFC stacks operate at 80 ºC. Heat management in a fuel cell stack would be easier if the reactions could proceed near 120 ºC, but water management and membrane dehydration then become significant problems.[33] Also, the theoretical cell efficiency drops as temperatures increases as was discussed previously.

Materials that have been investigated as anode electrocatalysts for hydrogen and small organic molecule oxidation are most commonly based on Pt and platinum group metals.

Typically, new materials are designed using two different modes of thinking, altering composition or morphology, with the aim being to retain the high activity for fuel oxidation and enhance the resistance to poisoning. $Pt_{0.5}Ru_{0.5}$ alloy, for example, is the standard electrocatalyst for methanol oxidation because it resists poisoning by CO. [34-36] The proposed mechanism for this poisoning tolerance uses enhanced water adsorption to the more oxophillic Ru centers near adsorbed CO molecules. The additional adsorbed water promotes the oxidation of CO to CO_2 and reduces poisoning markedly.[37] In addition to Ru, metals such as Ni, Co, Sn, Ti, W, Pb, and Bi have also been synthesized as alloy or intermetallic (ordered) phases with Pt, and tested as anode catalyst materials. [38-43]

From the morphology point of view, the objective has been to generate materials with preferential faceting. Here, only the most active crystalline faces of nanoparticles are exposed at the surface, leading to greater efficacy of catalytically active materials like Pt. Pt nanocubes, for example, may use the same amount of active material but can achieve higher overall current densities as compared to regular Pt nanoparticles. [44-47] Morphology control has also been applied to other Pt-M (M=transition metal) alloys. [44,48] Additionally, the dispersion of electrocatalyst particles in nanostructured architectures has been explored as a possible avenue to enhanced performance without the need for directly structuring the catalyst nanoparticles themselves. [49-52]

In contrast to the anode, which performs the oxidation reaction, the cathode is responsible for the reduction reaction. In PEMFCs the Oxygen Reduction Reaction (ORR, equation 1.7), has notoriously slow kinetics, leading to significant overpotential losses.

$$O_2(g) + 4\,H^+(aq) + 4\,e^- \rightarrow 2\,H_2O\,(g) \qquad (1.7)$$

Platinum or perhaps Pt_3Co is currently the best ORR catalyst available[53-57], but the slow reduction kinetics leads to large overpotentials in order to achieve reasonable current densities.

Figure 1.3, below, shows data obtained by General Motors while operating a fuel cell under *realistic* conditions.[58] (Reprinted from Applied Catalysis B: Environmental, 56(1), Hubert A. Gasteiger, Shyam S. Kocha, Bhaskar Sompalli, Frederick T. Wagner, Activity benchmarks and requirements for Pt, Pt-alloy, and non-Pt oxygen reduction catalysts for PEMFCs, 9-35, 2005, with permission from Elsevier).

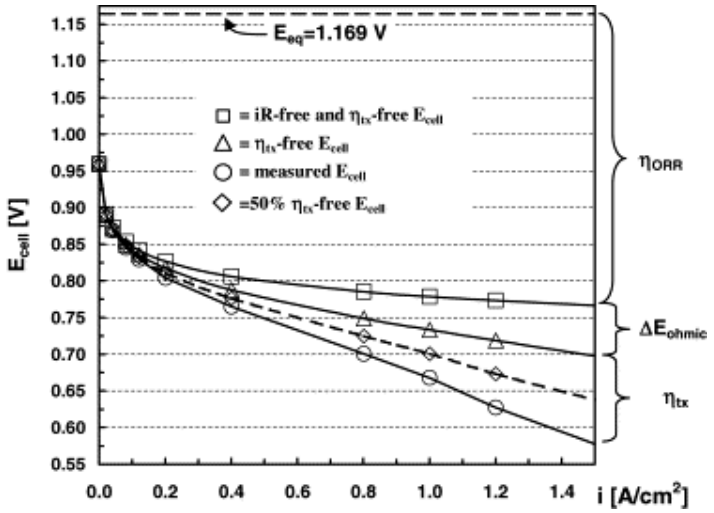

Figure 1.3 (a) Circular symbols: 50 cm^2 single-cell H_2/air performance at T_{cell} = 80 °C (80 °C dew points, i.e., 100% RH) at a total pressure of 150 kPa_{abs} and stoichiometric flows of s = 2.0/2.0 (controlled stoichiometric flows for i ≥ 0.2 A/cm^2; 0.2 A/cm^2 flows at i < 0.2 A/cm^2). Catalyst-coated membrane (CCM) based on a ca. 25-µm low-EW membrane (ca. 900 EW) coated with electrodes consisting of ca. 50 wt.% Pt/carbon (0.4/0.4 mgPt/cm^2 (anode/cathode)) and a low-EW ionomer (ca. 900 EW; ionomer/carbon ratio = 0.8/1). (b) Square symbols: E_{cell} vs. i for the mass-transport-free and ohmically corrected (i.e., iR-free) E_{cell}/i-curve shown in (a). In situ measurements of the high-frequency resistance vs. current density were obtained at 1 kHz (ranging from 45 to 55 mΩ cm^2) and used for the ohmic correction. (c) Triangular symbols: Addition of the ohmic losses, ΔE_{ohmic}, to the polarization curve shown in (b). (d) Diamond symbols: E_{cell}/i-curve shown in (a) corrected for 50% of the mass-transport losses. *Reproduced with permission under license.*

The theoretical potential of a working PEMFC when considering actual operating temperatures (80ºC) and partial pressures of H_2 and O_2 is +1.169 V. However, as shown in Figure 1.3, as soon as the device is switched on, approximately 400 mV of that working potential is sacrificed to drive the ORR at a sufficient current density. An additional 70 mV is lost to ohmic resistance and an additional 120 mV is lost to mass transport limitations (due to diffusion gradients in fuel and especially oxidant concentrations). Note that the overpotential for hydrogen

oxidation (the hydrogen oxidation reaction, HOR) is not shown - it is too small (a few 10's of mV) to show up on this scale. However, other fuels such as methanol, ethanol, and formic acid (all of which contain carbon) have significant overpotentials at these current densities (typically 300 mV or more). For automotive applications the overpotential needed for carbon containing fuels is too high to lead to a practical system. It is quite clear that better catalysts are needed for ORR and for carbon containing fuels. If these better catalysts cannot be discovered or invented, the potential impact of fuel cells in energy and transportation markets will not be realized.

Many of the design specifications discussed for the anode also apply to the cathode, although cathode materials must be able to sustain constant and cycling potentials between +0.8 V and +1.5 V vs. SHE (the Standard Hydrogen Electrode). Such a high potential in addition to a low pH causes most metals to oxidize and dissolve. Even Pt can dissolve and migrate to electrochemically inaccessible areas of the fuel cell or redeposit on other catalyst nanoparticles resulting in larger particle sizes and smaller overall catalyst surface area. [31,59] The extent to which Pt dissolves, however, is managed by the complex relationship between the dissolution of platinum, platinum oxide formation, and the dissolution of platinum oxide.[5]

The search for new ORR materials for PEMFCs has been a high priority for researchers, with a special emphasis on Pt-free catalysts.[60] Among the many different materials studied, Pd and Pd-M alloys[61-67], transition metal carbides[5], oxides/oxynitrides[5], and iron or corbalt-containing porphyrin complexes[58] have been the primary focus. Even though these catalysts have shown some activity for ORR, research has shown that significantly cheaper catalyst materials (like Fe or Co) would only be a viable option to replace Pt-based catalysts if their activities can reach, at minimum,10% that of Pt, a challenge which has yet to be met.[58] Additionally, pure Fe or Co themselves are known to oxidize and dissolve at relatively low

potentials, and their oxides are soluble at low pH[68]. Perhaps there are complex ternary or quaternary oxides or intermetallic compounds that would be suitable, but none have been reported so far.

Additional research has been conducted on new cathode catalysts for alkaline fuel cells since faster ORR kinetics have been reported under alkaline conditions. [69,70] Also, non-noble metal catalysts may *potentially* be used, making Alkaline Anion Exchange Membrane Fuel Cells (AAEMFC) of supreme interest to researchers.[71] Among the catalyst materials of interest, palladium-based catalysts[72], ruthenium-based catalysts[73], iron-porphyrin catalysts[74], nickel-cobalt-spinel catalysts[75-81], and manganese oxide-based catalyst[70 78-83] have emerged as potential alternatives to Pt-based cathode materials as well as elemental metals like Au, Ag, Co, and Ni[71]. Each of these materials presents its own unique challenges, the most important of which is the production of peroxide via a two-electron reduction step as opposed to the full four-electron reduction of oxygen to water. Despite this and other challenges, the caveat for full development of AAEMFCs continues to be the successful development of suitable membrane materials and ionomers that can handle hydroxide ion transport while standing up to fuel cell conditions.

It is clear that many challenges must be overcome for the development of new electrode materials for fuel cells. While many new materials have been explored, Pt and Pt-based catalysts endure as the most active catalytic materials for fuel cell reactions. Significant gains in performance or reduction in PEMFC cost may require a paradigm shift in how researchers think of and understand electrocatalysis. Despite these challenges, PEMFCs remain at the forefront of research while evolutionary (but not revolutionary) gains continue to be made in performance, durability, and cost of materials.

1.3.3 Catalyst Support Materials

The catalyst support is paramount for a working fuel cell because it provides electrical contact to the nanometer sized catalyst particles as well as provides the necessary open porosity that enables fast mass transport within the electrodes. Electrons generated at the catalyst move through the support material to an external circuit where they can be used to do work. Currently, amorphous carbon is used as the support material. However, carbon, in any form, is only thermodynamically stable up to approximately +0.2 V vs. SHE, and only kinetically stable above that. A fuel cell would optimally run at +1.2 V vs. SHE, with transient and on/off operation up to +1.5 V at the cathode (or under fuel starvation at the anode). [28,59] These high voltages lead to corrosion of the carbon support and loss of electrical contact to the catalyst, ultimately leading to device failure when as little as 10 wt.% of the support material is lost.[7] Recent developments have shown that support corrosion can be reduced to acceptable levels if appropriate control schemes and hardware are installed with the device[7]; however, these solutions ultimately limit the full potential achievable by a fuel cell and add levels of complexity in the design and operation of future generations of technology.

The use of nanoparticle platinum supported on carbon (Pt/C) catalysts for PEMFCs was largely developed in the late 1980s.[84] Since then, studies have shown that supported Pt and Pt-based catalysts have increased performance due to the higher achievable surface areas. [85,86] This higher overall surface area has also lead to a general lowering of the MEA catalyst loading, making PEMFCs cheaper without a loss in performance or durability. [87,88] As a result, Pt/C and other supported catalysts for PEMFCs have spurred great interest among researchers and engineers.[89]

The method in which a carbon support is prepared has a profound affect on its properties and thus its performance as a catalyst support material. Factors such as electronic conductivity[90,91], surface moieties[92-94], surface area[95], structure[96], graphitic/non-graphitic character[97], particle size[98] and morphology[95,99-101] may all be synthetically controlled. Much research has been done developing a variety of "carbon blacks" with different features for a variety of applications[87,102], with Vulcan® XC-72 (developed by Cabot Corporation) being the clear leader for supporting Pt catalysts in PEMFCs.[7,103,104]

In addition to Vulcan® XC-72, scientists have developed a variety of catalyst support materials based on both carbon and non-carbon building blocks. Besides carbon "blacks", several other nano-carbon materials have been studied for catalyst support applications including nanofibers[105], single and multi-walled carbon nanotubes[106,107], and graphene.[108] Non-carbon materials of interest include ceramics[109], polymers[110], and composite materials[111] as well as un-supported Pt catalysts (specifically the 3M® nano-structured thin film). [112-114] Several different catalyst supports based on TiO_2[115,116], SnO_2[117,118], SiO_2[119], and Ta_2O_5 [120]have also been studied. Additional studies of oxide and oxynitride support materials have been carried out in the DiSalvo group. [121-123] A more complete discussion of the reasoning and strategies for these oxide materials will be given in subsequent chapters.

From a design point-of-view, the property requirements for a catalyst support material depend on the exact operating parameters of the fuel cell system in which they are used. At a minimum, though, the potential suitability of a good catalyst support material can be determined by its stability (ideally thermodynamic) at high potentials in acidic solutions. Such supports need only a modest electrical conductivity (> 0.1 S/cm).[124] Additionally, a potential catalyst support material must be able to disperse a Pt or Pt-based catalyst and must be able to be

synthesized in an open-network, highly porous morphology to provide fast mass transport within a PEMFC. New support materials also need to be inexpensive and easy to manufacture, ideally.

1.4 Conclusions

The promise of high efficiency and significantly lower environmental impact have made fuel cells an attractive research goal for scientists and engineers, but it is clear that many challenges remain, slowing the development and deployment of fuel cell technology. PEMFCs show the most promise to replace internal combustion engines and revolutionize the transportation industry, yet materials durability and properties remain insufficient. In this thesis, the focus will be on addressing some of the materials challenges pertaining to catalyst supports and ORR catalyst for AAEMFCs. This work has been performed as part of the Energy Materials Center at Cornell (EMC^2), which has dedicated significant resources to advancing the state-of-the-art in fuel cell materials synthesis, characterization, and performance testing.

1.5 Outline of the Dissertation

This dissertation will now proceed into a total of 5 chapters, each of which is meant to stand-alone as a discussion of the project presented. In Chapter 2, catalyst support materials synthesized as bulk powders from the Nb-Ti-W-O system will be discussed. Here the goal was to synthesize new catalyst support materials by taking advantage of corrosion stable oxides like Nb_2O_5 while using doping techniques to induce conductivity. Additionally, this chapter focuses on a more traditional Solid State Chemistry approach to materials synthesis, which is also briefly discussed.

Chapter 3 will focus on the synthesis and characterization of mesoporous nanopowders of

Ti-M (M= Nb, W, and Cr) nitride materials as catalyst supports. Nitride materials have only recently been investigated for use as new PEMFC catalyst support materials, and this chapter represents some of the initial work that was done at Cornell for this specific application. A brief discussion of electrochemistry and experimental techniques will also be presented in this chapter. The work presented in Chapter 3 was performed in collaboration with two undergraduate researchers, whom I had the privilege of supervising, Joseph Singh (Spring 2010) and Mayra Hernández-Rivera (Summer 2010 REU).

Chapter 4 will discuss magnetron sputtering of thin-film nitride materials using Prof. Bruce van Dover's "Tubby" apparatus. The goal in transitioning from nanopowders to thin-films was to study the surface properties of nitrides on a more "well-defined" surface. Using thin-films, techniques such as conducting-probe atomic force microscopy (c-AFM) enable more meaningful measurements to be made in regards to surface processes and in elucidating the exact chemical nature of surface passivation and oxide layers. The ultimate goal in studying thin films of nitrides is to more fully understand corrosion properties and mechanisms of conducting materials. The work in Chapter 4 was done in collaboration with Dr. James O'Dea of the Marohn research Group, as well as Anna Legard and Abby van Wassen of the van Dover and Abruña groups with and HRTEM/EELS (High Resolution Transmission Electron Microscopy/Electron Energy Loss Spectroscopy) experiments performed by Meghan Holtz of the Muller Group.

Finally, in Chapter 5 the focus will shift from catalyst support materials, as I discuss the synthesis and characterization of rare-earth/transition metal perovskites for use as ORR catalysts for alkaline fuel cells. This work was originally inspired through a publication by Suntivich, *et al* in Nature in 2012[125] in which the authors aimed to describe the ORR activity for $LaMO_3$

catalysts (M is a 3rd row transition metal) using the electron count and orbital filling of the transition metal. Our efforts aimed at replicating these published results and building on them. However, conflicting results were obtained and will be discussed fully. The work in Chapter 5 was performed with another undergraduate researcher, Michael De Siena.

REFERENCES

(1) Singer, C.; Raper, R. *A History of Technology: The Internal Combustion Engine*; Singer, C., Ed. Clarendon Press, 1978; pp. 157–176.

(2) Langston, L. S. *Mechanical Engineering*. New York, NY June 1, 2004.

(3) Grove, W. *Phil. Mag. Ser.* **1839**, *3*, 127–130.

(4) Bagotsky, V. S. *Fuel Cells: Problems and Solutions*; Wiley: New York, 2009.

(5) Borup, R.; Meyers, J.; Pivovar, B.; Kim, Y. S.; Mukundan, R.; Garland, N.; Myers, D.; Wilson, M.; Garzon, F.; Wood, D.; Zelenay, P.; More, K.; Stroh, K.; Zawodzinski, T.; Boncella, J.; McGrath, J. E.; Inaba, M.; Miyatake, K.; Hori, M.; Ota, K.; Ogumi, Z.; Miyata, S.; Nishikata, A.; Siroma, Z.; Uchimoto, Y.; Yasuda, K.; Kimijima, K.-I.; Iwashita, N. *Chem. Rev. (Washington, DC, U. S.)* **2007**, *107*, 3904–3951.

(6) O'Hayre, R. P. *Fuel cell fundamentals*; John Wiley & Sons: Hoboken, N.J., 2009.

(7) Mathias, M. F.; Makharia, R.; Gasteiger, H. A.; Conley, J. J.; Fuller, T. J.; Gittleman, C. I.; Kocha, S. S.; Miller, D. P.; Mittelsteadt, C. K.; Xie, T.; Yan, S. G.; Yu, P. T. *Electrochem. Soc. Interface* **2005**, *14*, 24–35.

(8) Devanathan, R. *Energy Environ. Sci.* **2008**, *1*, 101–119.

(9) Zaidi, S. M. J.; Matsurra, T. *Polymer Membranes for Fuel Cells*; Javaid, Z. S. M.; Matsuura, T., Eds. Springer US: Boston, MA, 2009.

(10) Grot, W. *Fluorinated Ionomers*; William Andrew, 2011.

(11) Eisenberg, A.; Kim, J.-S. *Introduction to ionomers*; Wiley-Interscience, 1998.

(12) Mauritz, K. A.; Moore, R. B. *Chemical Reviews* **2004**, *{104}*, {4535–4585}.

(13) Adjemian, K. T.; Lee, S. J.; Srinivasan, S.; Benziger, J.; Bocarsly, AB *J. Electrochem. Soc.* **2002**, *{149}*, {A256–A261}.

(14) Jung, D. H.; Cho, S. Y.; Peck, D. H.; Shin, D. R.; Kim, J. S. *Journal of Power Sources* **2002**, *{106}*, {173–177}.

(15) Dimitrova, P.; Friedrich, K. A.; Stimming, U.; Vogt, B. *Solid State Ionics* **2002**, *{150}*, {115–122}.

(16) Zaidi, S.; Mikhailenko, S. D.; Robertson, G. P.; Guiver, M. D.; Kaliaguine, S. *Journal of Membrane Science* **2000**, *{173}*, {17–34}.

(17) Zaidi, S.; Ahmad, M. I. *Journal of Membrane Science* **2006**, *{279}*, {548–557}.

(18) Ahmad, M. I.; Zaidi, S.; Rahman, S. U. *DESALINATION* **2006**, *{193}*, {387–397}.

(19) Kim, Y. S.; Wang, F.; Hickner, M.; Zawodzinski, T. A.; McGrath, J. E. *Journal of Membrane Science* **2003**, *{212}*, {263–282}.

(20) Wu, H.; Wang, Y. X.; Wang, S. C. *JOURNAL OF NEW MATERIALS FOR ELECTROCHEMICAL SYSTEMS* **2002**, *{5}*, {251–254}.

(21) Xie, X. F. New Orleans, LA, 2002.

(22) Mikhailenko, S. D.; Zaidi, S.; Kaliaguine, S. *JOURNAL OF POLYMER SCIENCE PART B-POLYMER PHYSICS* **2000**, *{38}*, {1386–1395}.

(23) He, R. H.; Li, Q. F.; Xiao, G.; Bjerrum, N. J. *Journal of Membrane Science* **2003**, *{226}*, {169–184}.

(24) Savadogo, O.; Xing, B. *JOURNAL OF NEW MATERIALS FOR ELECTROCHEMICAL SYSTEMS* **2000**, *{3}*, {343–347}.

(25) Rikukawa, M.; Sanui, K. *PROGRESS IN POLYMER SCIENCE* **2000**, *{25}*, {1463–1502}.

(26) Mehta, V.; Cooper, J. S. *Journal of Power Sources* **2003**, *114*, 32–53.

(27) Lee, S. J.; Mukerjee, S.; Ticianelli, E. A.; McBreen, J. *Electrochimica Acta* **1999**, *44*, 3283–3293.

(28) Cheng, X.; Shi, Z.; Glass, N.; Zhang, L.; Zhang, J.; Song, D.; Liu, Z.-S.; Wang, H.; Shen, J. *Journal of Power Sources* **2007**, *165*, 739–756.

(29) Garzon, F.; Brosha, E.; Pivovar, B.; Rockward, T.; Springer, T.; Uribe, F.; Urdampilleta, I.; Valerio, J. **2006**.

(30) Mathias, M.; Gasteiger, H.; Makharia, R.; Kocha, S.; Fuller, T.; Xie, T.; Pisco, J. *Am. Chem. Soc. Preprints, Div. Fuel Chem* **2004**, *49*, 471.

(31) Xie, J.; Wood, D. L.; More, K. L.; Atanassov, P.; Borup, R. L. *J. Electrochem. Soc.* **2005**, *152*, A1011–A1020.

(32) Antolini, E. *J Mater Sci* **2003**, *38*, 2995–3005.

(33) Electrolysis, E. S. I.; Division, E. E.; Division, E. S. E. T.; Division, E. S. P. E. *Proton Conducting Membrane Fuel Cells III: Proceedings of the International Symposium*; Murthy, M., Ed. Electrochemical Society, 2005.

(34) Liu, H.; Song, C.; Zhang, L.; Zhang, J.; Wang, H.; Wilkinson, D. P. *Journal of Power Sources* **2006**, *155*, 95–110.

(35) Anderson, A. B.; Grantscharova, E. *The Journal of Physical Chemistry* **1995**, *99*, 9149–9154.

(36) Liu, S.-H.; Yu, W.-Y.; Chen, C.-H.; Lo, A.-Y.; Hwang, B.-J.; Chien, S.-H.; Liu, S.-B. *Chem. Mater.* **2008**, *20*, 1622–1628.

(37) Frelink, T.; Visscher, W.; Van Veen, J. *Surface science* **1995**, *335*, 353–360.

(38) de-los-Santos-Alvarez, N.; Alden, L. R.; Rus, E.; Wang, H.; Disalvo, F. J.; abruna, H. D. *JOURNAL OF ELECTROANALYTICAL CHEMISTRY* **2009**, *{626}*, {14–22}.

(39) Abe, H.; Matsumoto, F.; Alden, L. R.; Warren, S. C.; Abruña, H. D.; DiSalvo, F. J. *J. Am. Chem. Soc.* **2008**, *{130}*, {5452–5458}.

(40) Casado-Rivera, E.; Volpe, D. J.; Alden, L.; Lind, C.; Downie, C.; Vazquez-Alvarez, T.; Angelo, A.; Disalvo, F. J.; abruna, H. D. *J. Am. Chem. Soc.* **2004**, *{126}*, {4043–4049}.

(41) Ranjan, C.; Hoffmann, R.; Disalvo, F. J.; abruna, H. D. *J. Phys. Chem. C* **2007**, *111*, 17357–17369.

(42) Roychowdhury, C.; Matsumoto, F.; Zeldovich, V. B.; Warren, S. C.; Mutolo, P. F.; Ballesteros, M.; Wiesner, U.; abruna, H. D.; Disalvo, F. J. *Chem. Mater.* **2006**, *{18}*, {3365–3372}.

(43) Matsumoto, F.; Roychowdhury, C.; DiSalvo, F. J.; Abruña, H. D. *J. Electrochem. Soc.* **2008**, *{155}*, {B148–B154}.

(44) Habas, S. E.; Lee, H.; Radmilovic, V.; Somorjai, G. A.; Yang, P. *Nature Materials* **2007**, *6*, 692–697.

(45) Mazumder, V.; Lee, Y.; Sun, S. *Adv. Funct. Mater.* **2010**, *20*, 1224–1231.

(46) Chen, J.; Lim, B.; Lee, E. P.; Xia, Y. *Nano Today* **2009**, *4*, 81–95.

(47) Lu, L.; Yin, G. *Progress in Chemistry* **2010**, *22*, 338–344.

(48) Zhang, J.; Fang, J. *J. Am. Chem. Soc.* **2009**, *131*, 18543–18547.

(49) Kalra, V.; Lee, J.; Lee, J. H.; Lee, S. G.; Marquez, M.; Wiesner, U.; Joo, Y. L. *Small* **2008**, *4*, 2067–2073.

(50) Kamperman, M.; Burns, A.; Weissgraeber, R.; van Vegten, N.; Warren, S. C.; Gruner, S. M.; Baiker, A.; Wiesner, U. *Nano Lett.* **2009**, *9*, 2756–2762.

(51) Orilall, M. C.; Matsumoto, F.; Zhou, Q.; Sai, H.; Abruña, H. D.; DiSalvo, F. J.; Wiesner, U. *J. Am. Chem. Soc.* **2009**, *131*, 9389–9395.

(52) Li, Z.; Sai, H.; Warren, S. C.; Kamperman, M.; Arora, H.; Gruner, S. M.; Wiesner, U. *Chem. Mater.* **2009**, *21*, 5578–5584.

(53) Chen, S.; Ferreira, P. J.; Sheng, W.; Yabuuchi, N.; Allard, L. F.; Shao-Horn, Y. *J. Am. Chem. Soc.* **2008**, *130*, 13818–13819.

(54) Chen, S.; Sheng, W.; Yabuuchi, N.; Ferreira, P. J.; Allard, L. F.; Shao-Horn, Y. *J. Phys. Chem. C* **2009**, *113*, 1109–1125.

(55) Ruban, A. V.; Skriver, H. L.; Nørskov, J. K. *Phys. Rev. B* **1999**, *59*, 15990.

(56) Markovic, N. M.; Schmidt, T. J.; Stamenkovic, V.; Ross, P. N. *Fuel Cells* **2001**, *1*, 105–116.

(57) Stamenkovic, V.; Schmidt, T. J.; Ross, P. N.; Markovic, N. M. *J. Phys. Chem. B* **2002**, *106*, 11970–11979.

(58) Gasteiger, H. A.; Kocha, S. S.; Sompalli, B.; Wagner, F. T. *Applied Catalysis B: Environmental* **2005**, *56*, 9–35.

(59) Ferreira, P. J.; la O, G. J.; Shao-Horn, Y.; Morgan, D.; Makharia, R.; Kocha, S.; Gasteiger, H. A. *J. Electrochem. Soc.* **2005**, *152*, A2256–A2271.

(60) Wang, B. *Journal of Power Sources* **2005**, *152*, 1–15.

(61) Shao, M. H.; Sasaki, K.; Adzic, R. R. *J. Am. Chem. Soc.* **2006**, *{128}*, {3526–3527}.

(62) Zhang, J.; Mo, Y.; Vukmirovic, M. B.; Klie, R.; Sasaki, K.; Adzic, R. R. *JOURNAL OF PHYSICAL CHEMISTRY B* **2004**, *{108}*, {10955–10964}.

(63) Xiao, L.; Zhuang, L.; Liu, Y.; Lu, J.; Abruña, H. D. *J. Am. Chem. Soc.* **2009**, *{131}*, {602–608}.

(64) Yeh, Y.-C.; Chen, H. M.; Liu, R.-S.; Asakura, K.; Lo, M.-Y.; Peng, Y.-M.; Chan, T.-S.; Lee, J.-F. *Chem. Mater.* **2009**, *{21}*, {4030–4036}.

(65) Wang, W.; Huang, Q.; Liu, J.; Zou, Z.; Zhao, M.; Vogel, W.; Yang, H. *Journal of Catalysis* **2009**, *{266}*, {156–163}.

(66) Yang, J.; Lee, J. Y.; Zhang, Q.; Zhou, W.; Liu, Z. *J. Electrochem. Soc.* **2008**, *{155}*, {B776–B781}.

(67) Salvador-Pascual, J. J.; Citalan-Cigarroa, S.; Solorza-Feria, O. *Journal of Power Sources* **2007**, *{172}*, {229–234}.

(68) Pourbaix, M. *Atlas of Electrochemical Equilibria in Aqueous Solutions*; National Association of Corrosion Engineers, 1974.

(69) Wang, Y.; Li, L.; Hu, L.; Zhuang, L.; Lu, J.; Xu, B. *Electrochemistry Communications* **2003**, *5*, 662–666.

(70) Yang, C. *International Journal of Hydrogen Energy* **2004**, *29*, 135–143.

(71) Demarconnay, L.; Coutanceau, C.; Léger, J. M. *Electrochimica Acta* **2004**, *49*, 4513–4521.

(72) Yang, Y. F.; Zhou, Y. H.; Cha, C. S. *Electrochimica Acta* **1995**, *40*, 2579–2586.

(73) Prakash, J.; Joachin, H. *Electrochimica Acta* **2000**, *45*, 2289–2296.

(74) Gojković, S. L.; Gupta, S.; Savinell, R. F. *JOURNAL OF ELECTROANALYTICAL CHEMISTRY* **1999**, *462*, 63–72.

(75) Heller-Ling, N.; Prestat, M.; Gautier, J. L.; Koenig, J. F.; Poillerat, G.; Chartier, P. *Electrochimica Acta* **1997**, *42*, 197–202.

(76) Hu, Y.; Tolmachev, Y. V.; Scherson, D. A. *JOURNAL OF ELECTROANALYTICAL CHEMISTRY* **1999**, *468*, 64–69.

(77) Rashkova, V.; Kitova, S.; Konstantinov, I.; Vitanov, T. *Electrochimica Acta* **2002**, *47*, 1555–1560.

(78) Matsuki, K.; Kamada, H. *Electrochimica Acta* **1986**, *31*, 13–18.

(79) Ponce, J.; Rehspringer, J. L.; Poillerat, G.; Gautier, J. L. *Electrochimica Acta* **2001**, *46*, 3373–3380.

(80) Mao, L.; Sotomura, T.; Nakatsu, K.; Koshiba, N.; Zhang, D.; Ohsaka, T. *J. Electrochem. Soc.* **2002**, *149*, A504.

(81) Klápště, B.; Vondrák, J.; Velická, J. *Electrochimica Acta* **2002**, *47*, 2365–2369.

(82) Yang, J.; Xu, J. J. *Electrochemistry Communications* **2003**, *5*, 306–311.

(83) Mao, L. *Electrochimica Acta* **2003**, *48*, 1015–1021.

(84) Antolini, E.; Perez, J. *J Mater Sci* **2011**, *46*, 4435–4457.

(85) Fang, B.; Kim, M.; Yu, J. S. *Applied Catalysis B: Environmental* **2008**, *84*, 100–105.

(86) Yu, J. S.; Kang, S.; Yoon, S. B.; Chai, G. *J. Am. Chem. Soc.* **2002**, *124*, 9382–9383.

(87) Uchida, M.; Aoyama, Y.; Tanabe, M.; Yanagihara, N.; Eda, N.; Ohta, A. *J. Electrochem. Soc.* **1995**, *142*, 2572–2576.

(88) Taylor, E. J.; Anderson, E. B.; Vilambi, N. R. K. *J. Electrochem. Soc.* **1992**, *139*, L45–L46.

(89) Antolini, E. *Applied Catalysis B: Environmental* **2009**, *88*, 1–24.

(90) Decruppe, J. P.; Dujardin, F.; Charlier, M. F.; Charlier, A. *Carbon* **1979**, *17*, 237–241.

(91) Noda, T.; Kato, H.; Takasu, T.; Okura, A.; Inagaki, M. *Bull. Chem. Soc. Jpn.* **1966**, *39*, 829–&.

(92) Ehrburger, P.; Mahajan, O. P.; Walker, P. L. *Journal of Catalysis* **1976**, *43*, 61–67.

(93) Walker, P. L.; Janov, J. *J Colloid Interf Sci* **1968**, *28*, 449–&.

(94) Bartholo Ch; Boudart, M. *Journal of Catalysis* **1972**, *25*, 173–&.

(95) Pantea, D.; Darmstadt, H.; Kaliaguine, S.; Summchen, L.; Roy, C. *Carbon* **2001**, *39*, 1147–1158.

(96) W M Hess; C R Herd In *Carbon Black Science and Technology*; J B Donnet; R C Bansal; M Wang, B., Eds. Marcel Dekker: New York, USA, 1993.

(97) Pantea, D.; Darmstadt, H.; Kaliaguine, S.; Roy, C. *Appl. Surf. Sci.* **2003**, *217*, 181–193.

(98) Dicks, A. L. *Journal of Power Sources* **2006**, *156*, 128–141.

(99) Darmstadt, H.; Cao, N. Z.; Pantea, D. M.; Roy, C.; Summchen, L.; Roland, U.; Donnet, J. B.; Wang, T. K.; Peng, C. H.; Donnelly, P. J. *Rubber Chem. Technol.* **2000**, *73*, 293–309.

(100) Darmstadt, H.; Summchen, L.; Roland, U.; Roy, C.; Kaliaguine, S.; Adnot, A. *Surf. Interface Anal.* **1997**, *25*, 245–253.

(101) Pantea, D.; Darmstadt, H.; Kaliaguine, S.; Roy, C. *Journal of Analytical and Applied Pyrolysis* **2003**, *67*, 55–76.

(102) B R Corry, H. S. K. J. V. M. *Handbook of fillers for plastics*; Van Nostrand Reinhold, New York, 1987.

(103) Grolleau, C.; Coutanceau, C.; Pierre, F.; Léger, J. M. *Electrochimica Acta* **2008**, *53*, 7157–7165.

(104) Kumar, S. M. S.; Hidyatai, N.; Herrero, J. S.; Irusta, S.; Scott, K. *International Journal of Hydrogen Energy* **2011**, *36*, 5453–5465.

(105) Alvarez, G.; Alcaide, F.; Miguel, O.; Cabot, P. L.; Martinez-Huerta, M. V.; Fierro, J. L. G. *Electrochimica Acta* **2011**, *56*, 9370–9377.

(106) Wang, X.; Li, W.; Chen, Z.; Waje, M.; Yan, Y. *Journal of Power Sources* **2006**, *158*, 154–159.

(107) Long, D.; Li, W.; Qiao, W.; Miyawaki, J.; Yoon, S.-H.; Mochida, I.; Ling, L. *Chem. Commun.* **2011**, *47*, 9429–9431.

(108) Choi, J.-Y.; Higgins, D.; Chen, Z. *J. Electrochem. Soc.* **2012**, *159*, B87–B90.

(109) Antolini, E.; Gonzalez, E. R. *Solid State Ionics* **2009**, *180*, 746–763.

(110) Antolini, E.; Gonzalez, E. R. *Applied Catalysis A: General* **2009**, *365*, 1–19.

(111) Antolini, E. *Applied Catalysis B: Environmental* **2010**, *100*, 413–426.

(112) Debe, M. K.; Drube, A. R. *J. Vac. Sci. Technol. B* **1995**, *13*, 1236–1241.

(113) Liu, G. C.-K.; Stevens, D. A.; Burns, J. C.; Sanderson, R. J.; Vernstrom, G.; Atanasoski, R. T.; Debe, M. K.; Dahn, J. R. *J. Electrochem. Soc.* **2011**, *158*, B919–B926.

(114) van der Vliet, D.; Wang, C.; Debe, M.; Atanasoski, R.; Markovic, N. M.; Stamenkovic, V. R. *Electrochimica Acta* **2011**, *56*, 8695–8699.

(115) Huang, S.-Y.; Ganesan, P.; Popov, B. N. *Applied Catalysis B: Environmental* **2011**, *102*, 71–77.

(116) Rajalakshmi, N.; Lakshmi, N.; Dhathathreyan, K. S. *International Journal of Hydrogen Energy* **2008**, *33*, 7521–7526.

(117) Chhina, H.; Campbell, S.; Kesler, O. *Journal of Power Sources* **2006**, *161*, 893–900.

(118) Masao, A.; Noda, S.; Takasaki, F.; Ito, K.; Sasaki, K. *Electrochem. Solid-State Lett.* **2009**, *12*, B119–B122.

(119) Nam, K.; Lim, S.; Kim, S. K.; Yoon, S. H.; Jung, D. H. *International Journal of Hydrogen Energy* **2012**, *37*, 4619–4626.

(120) Baturina, O. A.; Garsany, Y.; Zega, T. J.; Stroud, R. M.; Schull, T.; Swider-Lyons, K. E. *J. Electrochem. Soc.* **2008**, *155*, B1314–B1321.

(121) Subban, C.; Zhou, Q.; Leonard, B.; Ranjan, C.; Edvenson, H. M.; Disalvo, F. J.; Munie, S.; Hunting, J. *Philosophical Transactions of the Royal Society a-Mathematical Physical and Engineering Sciences* **2010**, *368*, 3243–3253.

(122) Subban, C. V.; Zhou, Q.; Hu, A.; Moylan, T. E.; Wagner, F. T.; DiSalvo, F. J. *J. Am. Chem. Soc.* **2010**, *132*, 17531–17536.

(123) Wang, D.; Subban, C. V.; Wang, H.; Rus, E.; DiSalvo, F. J.; Abruña, H. D. *J. Am. Chem. Soc.* **2010**, *132*, 10218–10220.

(124) Wagner, F. T.; Yan, S. G.; Yu, P. T. In *Handbook of Fuel Cells: Fundamentals, Technology and Applications*; Vielstich, W.; Yokokawa, H.; Gasteiger, H. A., Eds. John Wiley &Sons, Ltd.,: Chichester, UK,, 2009; Vol. 5, pp. 250–263.

(125) Suntivich, J.; Gasteiger, H. A.; Yabuuchi, N.; Nakanishi, H.; Goodenough, J. B.; Shao-Horn, Y. *Nature Chem* **2011**, *3*, 546–550.

CHAPTER 2

CONDUCTING OXIDES OF Nb, W, AND Ti AS PEMFC CATALYST SUPPORTS

2.1 Introduction to Oxide Supports

Fuel cells may be poised to revolutionize the way we produce and consume energy, but many challenges must first be overcome for this technology to be fully realized. While some of these challenges are external to the device itself, such as developing and implementing a hydrogen fuel-dispensing infrastructure, many of the challenges involve the materials from which fuel cells are made. These challenges include limiting, or eliminating the need for expensive, precious metal catalysts such as platinum and its alloys, developing a more robust and stable membrane material that can handle additional fuels such as methanol and ethanol, and developing new, non-carbon based, catalyst support materials that are durable in long-term fuel cell operation. [1-7] In this chapter, I discuss my work on developing new catalyst support materials based on conducting oxides in the Nb-W-Ti-O system.

The catalyst support is paramount for a working fuel cell because it provides electrical contact to the nanometer sized catalyst particles, keeps the catalyst from agglomerating, and provides the necessary porosity that enables fast mass transport within the electrodes. Electrons generated at the catalyst surface move through the support material to an external circuit where they can be used to do work. Currently, amorphous carbon is used as the support material. However, carbon, in any form, is only thermodynamically stable up to approximately +0.2 V vs. the Standard Hydrogen Electrode (SHE), and only kinetically stable above that. A fuel cell optimally runs at +1.2 V vs. SHE, with transient and on/off operation at up to +1.5 V at the cathode (or under fuel starvation at the anode). [1-7] These high voltages lead to corrosion of the

carbon support, equation 2.1, and loss of electrical contact to the catalyst, ultimately leading to device failure when as little as 10 wt.% of the support material is lost. [2,8]

$$C(s) + 2H_2O \longrightarrow CO_2(g) + 4e^- + 4H^+ \quad E^o = +0.207\ V \tag{2.1}$$

Primarily, there are three properties that determine the potential suitability of a good catalyst support material: stability at high potentials in acidic (or possibly alkaline – for AAEMFCs) solutions, modest electrical conductivity when incorporated with the electrode (> 0.1 S/cm), and high porosity to facilitate fast mass transport.[9] Aside from carbon, other materials of interest such as sulfides, carbides, and nitrides are also thermodynamically driven to oxidize (corrode) or hydrolyze to oxides (or hydroxides), at least at the surface, under PEMFC conditions.[10] The extent and nature of surface oxidation or hydrolysis of any given material varies with its composition and the reaction conditions (pH, temperature, other species in solution, etc.). Some materials may form surface reaction layers just a few nanometers thick, while others may be completely converted or consumed. Therefore, when synthesized as nano- or meso-porous solids, new support materials (at least in the cathode) are likely to be some form of oxide or oxy/hydroxide, at least at the surface. This reasoning may lead one to believe that in order to achieve the desired stability (or sufficient metastability) in PEMFC conditions, oxides in which metallic elements are at or near their highest oxidation state (leaving no room for further oxidation/corrosion) are *potentially* suitable replacements for carbon catalyst supports, assuming that a composition with sufficient conductivity can be prepared. Conductivity usually occurs when some or all of the metal cations are partially reduced. The idea, then, is to look for materials in which the thermodynamic drive to complete oxidation is small and the kinetic

barriers to such oxidation, at least in the bulk material, are high. Of course, we do not known *a priori* if such a delicate balance is possible. This balance is what we begin to explore in this chapter.

2.1.1 Oxides and Stability

Oxides have been extensively used as catalysts and catalysts supports for a variety of applications,[11] with the surface structure and composition being of primary importance, especially when used as electrocatalysts. [12-14] Furthermore, when oxide materials are synthesized as nanoparticles or mesoporous solids (in order to achieve high surface areas) the large ratio of surface to bulk atoms often make chemical reactions (such as passivation, oxidation, adsorption, or dissolution) at the surface a concern.[15] It is important then to understand fully the behavior of metallic elements in an electrochemical environment like that of a PEMFC.

In looking at plots that describe the thermodynamic behavior of a metallic element as a function of changing pH and applied potential (so-called Pourbaix Diagrams[16]) it is found that no single metal is thermodynamically stable at PEMFC potentials in acidic, aqueous solutions. Although gold has the highest reduction potential at +1.5V vs. SHE, it dissolves at lower potentials when the concentration of gold cations in solution is low. Additionally, the cost of gold generally excludes it from being considered as a catalyst support for fuel cells. All other metals either dissolve as cations or form chemically passivating layers of electrically insulating oxide coatings at high potentials under acidic conditions. Similarly, under alkaline conditions, soluble metal-containing oxo-anions or passivating oxide/hydroxide layers are formed. Even metal alloys and intermetallics, despite generally having a small free energy of formation

compared to their respective oxides, are subject to leaching and oxidation of the more electropositive element under the highly oxidizing conditions found in a PEMFC.[17-19]

Very few single-metal oxides are insoluble at low pH and high potential. The list can be counted with one hand: TiO_2, Nb_2O_5, Ta_2O_5, and WO_3.[16] Furthermore, the stability of these oxides may vary based on the synthesis conditions as well as the presence of any other anionic or cationic species (such as NH_4^+, Cl^-, or SO_4^{2-}) in the electrochemical environment. Figure 2.1 below shows a calculated Pourbaix Diagram for the Nb-H_2O system at 25 ºC, with the red region indicating the conditions often found in a fuel cell. No other species are included in the calculated diagram. The dashed lines show the stability window for water as a function of pH and potential with a slope of -59 mV per pH unit change.

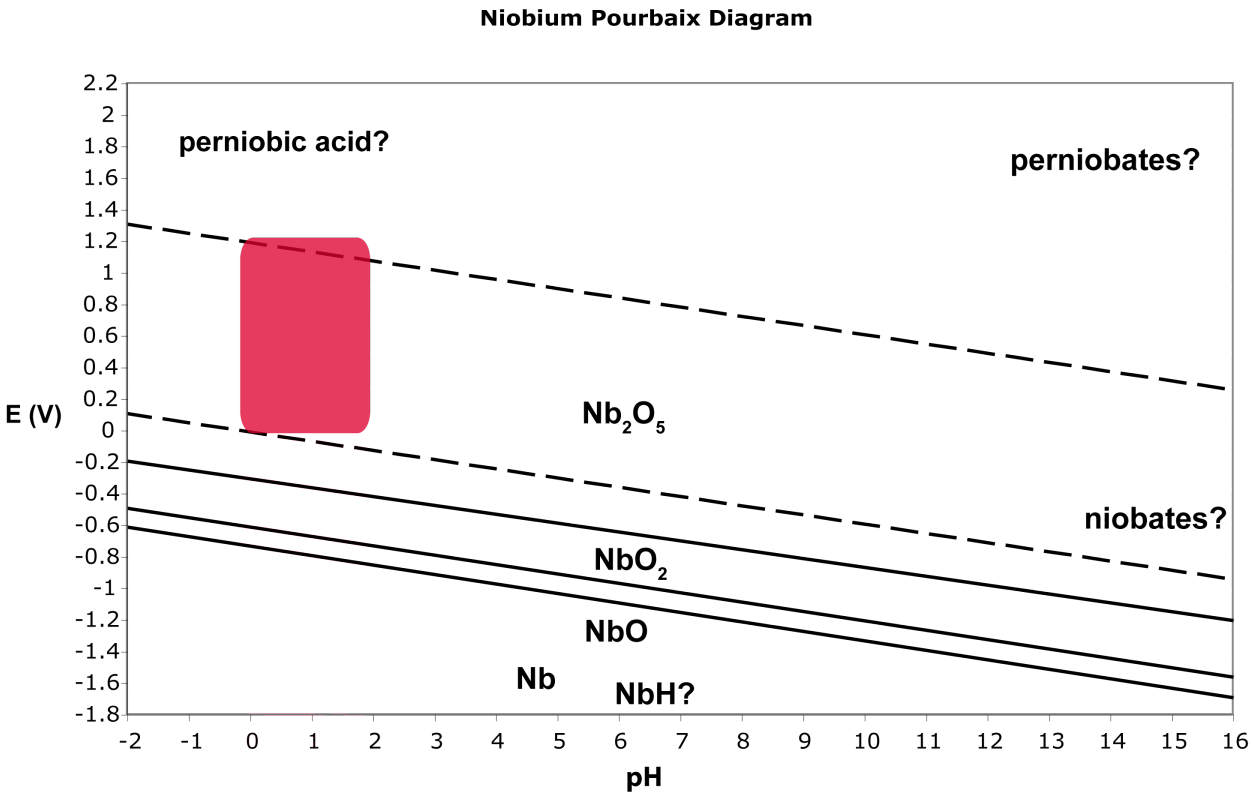

Figure 2.1 Pourbaix diagram for the Nb-H_2O system at 25 ºC. The red region applies to fuel cell conditions.

2.1.2 Oxides and Conductivity

Catalyst supports require a minimum conductivity of 0.1S/cm[9] and none of the previously mentioned oxides are electrically conducting. However, conductivity may be enhanced either by partially reducing the oxide[20,21], or by doping with aliovalent metal cations. [22-24] Titania, for example, has a band-gap between 3.0-3.5 eV, making pure samples practically insulating. [25,26] It is well documented, however, that rutile (TiO_2) can be doped with other cations to prepare materials with composition $Ti_{1-x}M_xO_2$, where M=Zr, Hf, V, Nb, Ta, Cr, Mo, W, Ru, Os, Ir and Sn induce electronic conductivity. Depending on the oxidation state and the valence shell electron configuration, this doping can modify the band-gap or lead to magnetism and/or conductivity. Many of these doped oxides have also been tested for stability under PEMFC conditions. [22,24,27-34]

Work by Chinmayee Subban and other former members of the DiSalvo group has shown that W-doped TiO_2 (rutile type: $Ti_{1-x}W_xO_2$) is conducting[35,36]and, as 50 nm nanoparticles, is stable in an environment resembling fuel cell conditions for more than 12 months.[35] Additionally, Subban has shown that at a doping level of 30 mole %, W-doped titania has co-catalytic properties that enhance the performance of Pt for the oxidation of impure (CO containing) hydrogen at the fuel cell anode. [35,37] Furthermore, when a group V metal, Mo or W are doped into TiO_2, a third dopant can be introduced, e.g. ($Ti_{1-x-y}W_xM'_yO_2$) where M' is Cr, Mn, Fe, Co, or Ni. Metal vacancies may also be generated in these materials, since they can be compensated by oxidizing W(IV) to W(V).[24,30,31,38,39] For some of these materials, enhanced corrosion resistance, conductivity, or catalytic behavior has been reported, while the addition of 3d transition metals such as Fe, Ni, Cu, and Co may yield a material with interesting catalytic or magnetic properties. Despite having significantly smaller catalytic activity for hydrogen

oxidation when compared to pure Pt, these materials may suggest a route to find more active catalysts, and can give insight for the design of future catalysts.[40]

2.2 Measuring Conductivity

As previously discussed, carbon black (Vulcan XC-72) is the current support material of choice, and in it's optimized form, has a reported conductivity of up to 8 S/cm.[41] However, it is also important to note that the *effective* conductivity of any material used in a PEMFC is highly dependent on the formulation and design of the MEA, balance of plant, and the internal (mechanical) pressure produced in assembling the device.[8] These factors play a major role in determining to what extent meso-porous or polycrystalline supports contact one another, which affects electronic percolation within the catalyst layers as well as the ability to overcome any surface insulating layers (either by physically breaking through them, or by electron tunneling). Therefore, the way in which one measures the conductivity of these materials is very important, and needs to mimic fuel cell conditions.

Measured conductivities depend on a variety of factors including particle size, degree of sintering, applied pressure, and temperature. For example, even the conductivity of copper powder grains changes with both applied pressure and sintering temperatures.[42] Such variation is not unexpected because the number and area of inter-particle contacts increases with applied pressure and with sintering. In some cases, especially for structurally anisotropic materials like the layered compound MoS_2, the electrical conductivity of powdered samples develops increasing anisotropy by aligning the layers through increasing applied pressure.[43] Studies on cubic ceria have demonstrated the effects of particle size on conductivity.[44] Impedance

spectroscopy has been used to characterize ceramic materials, and the effects of porosity and inter-grain contact resistance in the materials.[45]

The bulk conductivity of a material is generally measured using single crystals[46,47] but growing sufficiently large single crystals is not always possible or can be impractical. The highest value of conductivity measured is typically found in single crystals, since there are no grain boundaries and, in perfect crystals, few defects (both of which can add additional resistance at room temperature). In many polycrystalline metals, especially when the sample is sintered to increase grain size and contact area (and to eliminate voids) the measured conductivity at room temperature tends to be very close (typically within a few percent) to that of a single crystal of the same material.[48] Alternatively, statistical modeling can be used to estimate the effective conductivity of a sample of generic powder particles of some size, bulk conductivity, and density in a continuous matrix.[49] This method has also been used to estimate the DC electrical conductivities of metal nanoparticles prepared as films.[50,51]

In choosing a measurement technique, one must consider the physical nature of the sample of material being measured. Measurement methods applicable to single crystals may not be easily tailored to get meaningful results for a thin film or for an ensemble of nanoparticles. For example, if the sample is a thin film, commercially available four point probes can be used.[52,53] However, if the material is a polycrystalline powder, pressed pellet conductivity is a better choice.[43,48,54,55] The preferred techniques differ for different types of materials to allow for appropriate sample preparation and limitations imposed by certain assumptions about sample homogeneity, which are built into the calculation of conductivity from measured data (e.g. uniform film thickness for thin film measurements).[56,57]

In case of powders, the measured conductivity depends on how well the material is packed together and hence generally increases with increased pressure.[42] Among the methods for measuring the conductivity of powder samples, the two and four-point probe techniques are discussed here. A two-point probe uses a simple ohmmeter to measure the resistance across a portion of the sample (Figure 2.2 a and c). In this case we assure that resistance between the sample and the contact (so-called contact resistance) is negligible or acceptably small (say less than 10% of the total resistance). Of course, the contribution of particle-particle contact resistance cannot be determined and adds to the normal resistance. By controlling the cross-sectional area and overall length of the sample, the conductivity can be calculated with relative ease (Figure 2.2b). The two-point method is best suited for samples with high resistance (low conductivity), and is the only technique for measuring conductivity considered in this chapter.

A step up from the two-point probe is the four-point probe. In this technique, the potential across a portion of the sample (of known cross-sectional area) is measured using two "inside" probes (a known distance apart) while applying a constant current through two additional "outside" probes (Figure 2.2d).[52] Properly applied, these techniques can circumvent errors that might arise from contact resistance between the probes and the sample. When conducting the experiments presented in this chapter, only the two-point probe was available for measuring conductivity. As materials with higher conductivities were being developed, so too did the capability and equipment to perform four-point conductivity measurements. The four-point probe technique will be discussed further in Chapter 3.

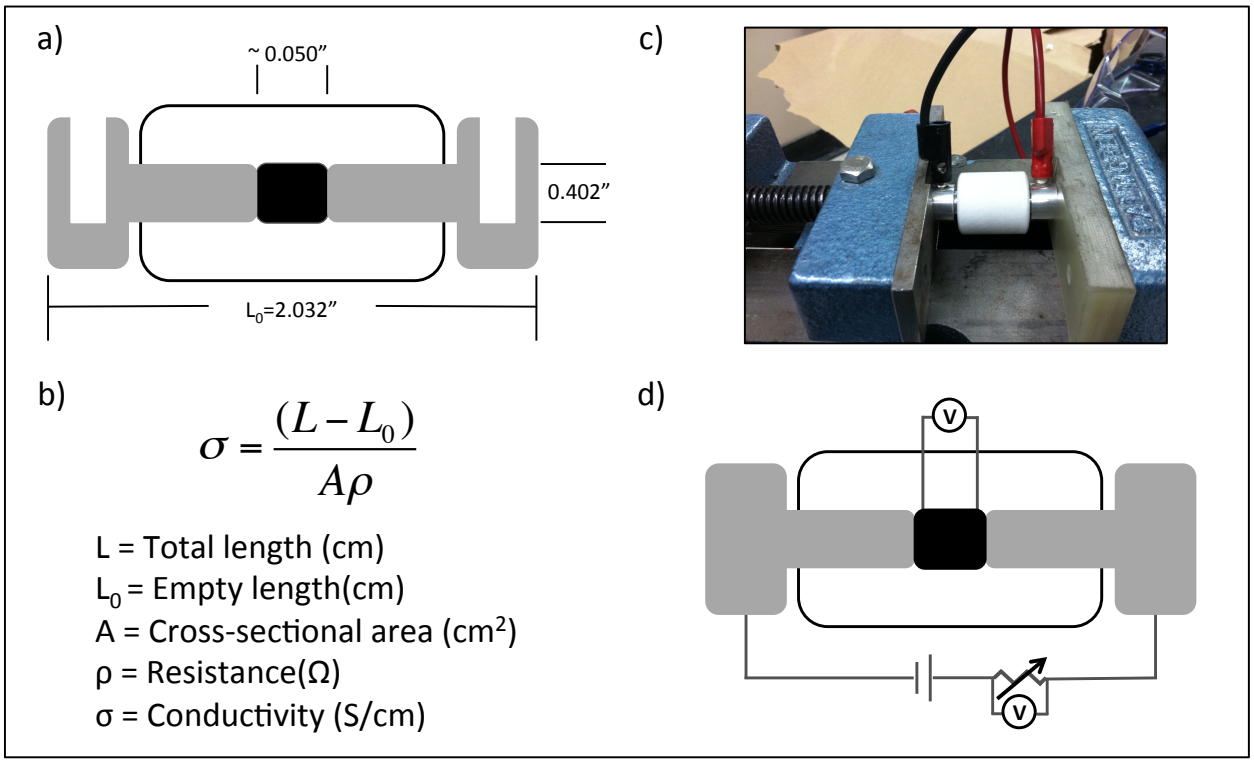

Figure 2.2 (a) Cross-sectional schematic of the two-point conductivity cell. (b) Equation to calculate conductivity. (c) Photo of the the experimental set up. (d) Schematic of the four-point conductivity cell.

2.2.1 The DiSalvo Two-Point Probe

The DiSalvo Group two-point powder conductivity probe consists of a cylindrical sample holder made from a Teflon® bar and two stainless steel pistons. To measure the conductivity of a sample, approximately 0.5g of the powder sample is loaded into the holder and the pistons are inserted into either end. The assembled sample holder is then placed into a modified bench vice which is tightened just enough to prevent the holder from falling through the vice jaws, but not enough to compress the sample in the holder. The modified vise has an insulating (Delrin®) jaw (to prevent short circuiting) with a slot milled to accept the piston head. The resistance of the sample is measured by measuring the resistance across the pistons using an ohmmeter (Fluke 75III Multimeter, Figure 2.2c). The vise is then tightened (to 25 in-lbs) using a torque wrench to increase the pressure on the sample, followed by measuring the resistance. The total length of the holder (from the outside edge of the piston heads) is also noted. The vise is tightened and the sample measured in this way in increments of 10 in-lbs to a maximum of 105 in-lbs.

While the conductivity can be measured as a function of applied pressure using this method (qualitatively at least), the "applied pressure" is actually the torque applied to the vise. While not explicitly a pressure, conducting subsequent measurements at benchmark torque settings does enable a qualitative comparison between samples of various compositions and morphologies. In virtually every case, the measured resistance value decreases with an increase in "applied pressure" and asymptotically approaches a minimum value, which does not significantly change with further increases in applied pressure. Using this minimum value with the area and length of the pellet the pressed powder conductivity of the sample can be calculated as shown in Figure 2.2b.

The two-point method is only suitable for materials that have relatively low conductivities. The multimeter used to measure the resistance has a detection limit of 0.1 Ω, which combined with the typical dimensions of the pellet with in the press makes the maximum detectible conductivity approximately 1 S/cm. Materials with conductivity greater than 1 S/cm will read 0.0 Ω on the meter and cannot be distinguished from samples with higher conductivities (up to 10^7 S/cm for silver or copper). Other methods, such as the modified four-point probe developed by Chinmayee Subban and I are better suited for more conducting materials.

2.3 Catalyst Supports Based on Nb_2O_5

Much of the previous work in the DiSalvo group focused on new catalyst support materials based on doped TiO_2. Often these material compositions consisted of solid solutions of rutile titania with dopant metal oxides that are isostructural (or possibly a distorted version of rutile). As an example, Subban[35,37,40] showed that tungsten dioxide (WO_2, a conductor) which has a distorted rutile structure type caused by W-W bond formation (the a-axis is extend and the c-axis is compressed)[58] reacted to form a solid solution with TiO_2 (an insulator) in a ratio of 7:3 Ti:W ($Ti_{0.7}W_{0.3}O_2$). This composition was shown to possess both acceptable conductivity and reasonable corrosion stability in fuel cell like conditions.

In addition to solid solutions, another approach may be to study "known" or reported phases with a stoichiometry and crystal structure independent of the parent oxides. In this strategy, ternary oxides comprised of the insoluble, stable oxides listed earlier are prepared followed by synthetically modifying their structures (via oxygen vacancy doping) to induce conductivity while retaining the stability predicted via Pourbaix Diagrams. For example in the

Nb_2O_5-WO_3 system, both the Nb and W are in their highest oxidation states (+5 for Nb and +6 for W) making any compound between the two fully insulating regardless of stoichiometry. It is known, however, that WO_2 possesses a relatively narrow stability window near the pH and potential conditions present in a fuel cell.[16] If the tungsten in reported Nb_2O_5-WO_3 compounds could be reduced from W(VI) to W(IV) (producing oxygen vacancies for charge balance), extra electrons, the two on W^{4+}(d^2), could lead to conductivity, if the bands at the Fermi level are sufficiently broad or if percolation "hopping" is possible.[59] If the parent crystal structure is also retained, then the only remaining challenge would be to find the compound(s) with the appropriate stoichiometry to allow for sufficient conductivity. Furthermore, in the Nb_2O_5-TiO_2 system if Ti could be reduced from Ti (IV) to Ti (III) an electron would be left in a Ti 3*d*-band, possibly allowing for conducting Ti centers. It is not clear, however, nor has it been reported in the literature to what extent oxygen vacancies may be introduced into these fully oxidized compounds or if such vacancy doping would make these materials unstable and cause them to phase segregate (disproportionate). The phase diagrams for the Nb_2O_5-WO_3 (above)[60] and Nb_2O_5-TiO_2 (below)[61] systems are shown in Figure 2.3.

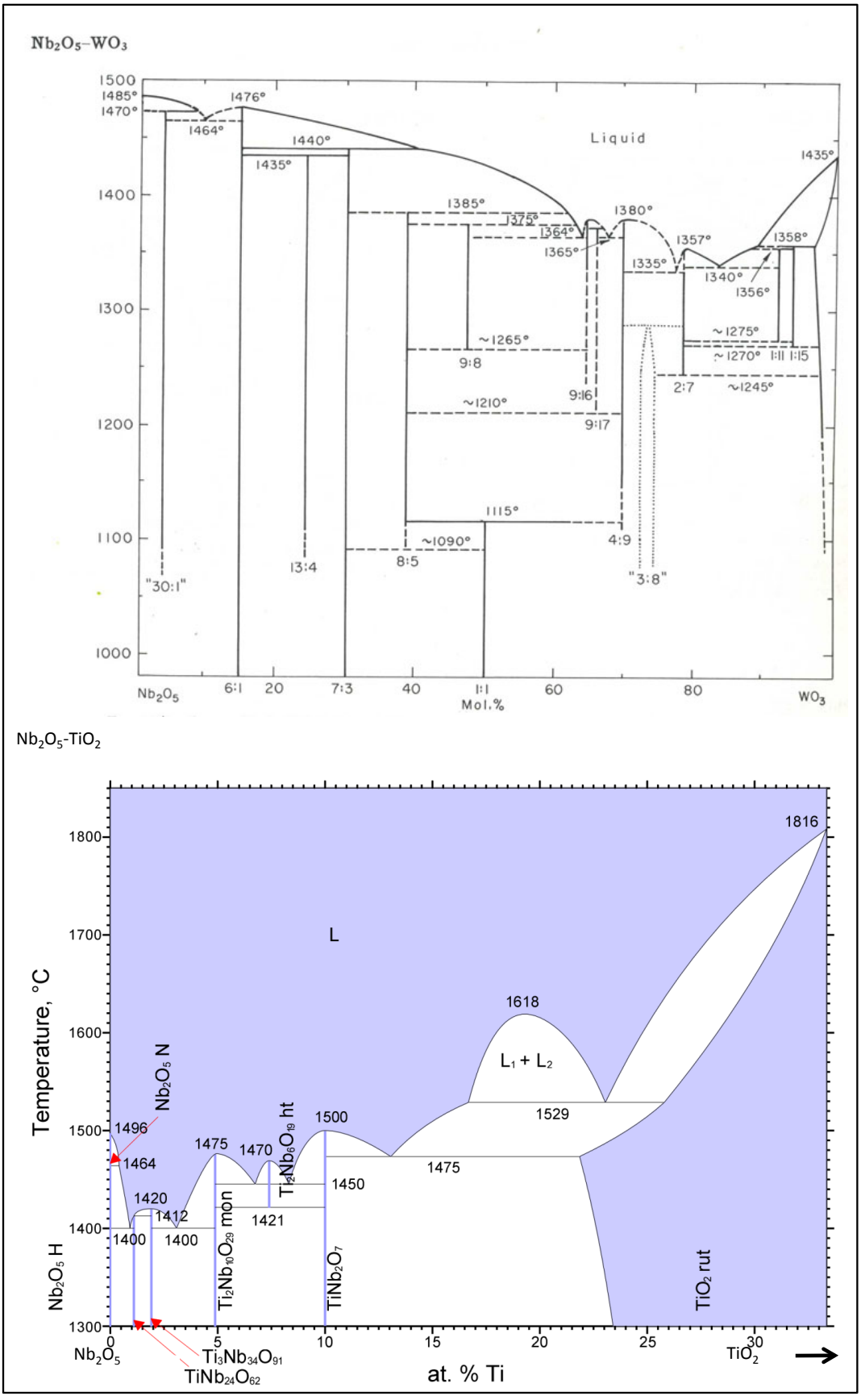

Figure 2.3 High temperature phase diagrams for the Nb_2O_5-WO_3 (above) and the Nb_2O_5-TiO_2 (below) systems.

2.3.1 Ellingham Diagrams

The spontaneity of any reaction is determined by the sign of the change in free energy (ΔG) arising from that reaction. Typically the free energy of formation for oxides is negative, meaning that most metals will oxidize (in the presence of oxygen). There may be kinetic barriers that make this process occur slowly (or perhaps not at all on a reasonable time-scale). For most metals, these barriers are easily overcome by increasing the temperature, above several hundred ºC. In addition to free energy, one must also consider the signs of the enthalpy (ΔH) and the entropy (ΔS) changes associated with metal oxidation (equation 2.2). Typically, ΔH is negative for metal oxidation, while ΔS is positive (overall reaction of gas phase oxygen into a solid oxide, thus lower entropy). Both ΔH and ΔS are *essentially* independent of temperature (the changes are negligible except when a phase change occurs); therefore, a plot of ΔG versus temperature (a so-called Ellingham Diagram[62]) is simply a series of straight lines with ΔH as the y-intercept and ΔS as the slope. At lower temperatures, ΔH has a larger affect on the available free energy of oxidation; however, as temperature increases entropy begins to play a larger role, consuming the available free energy. Because of the positive ΔS, the sign of ΔG can become positive causing the oxide to spontaneously reduce back to the metal at sufficiently high temperatures (e.g. Hg). Additionally, the partial pressure of oxygen in equilibrium with the metal and oxide at a given temperature can be calculated using equation 2.3.

$$\Delta G = \Delta H - T\Delta S \tag{2.2}$$

$$\Delta G = \Delta G^0 + RT \ln \frac{P_{O_2}}{P^0_{O_2}} \tag{2.3}$$

Ellingham diagrams are used extensively in metallurgy to predict equilibria between a metal, its oxide, and oxygen as a function of temperature. Such diagrams are also useful for determing the relative reducing power of the elements. For example, carbon can reduce a number of metal oxides, including Fe_2O_3, resulting in either CO or CO_2 as a coproduct. Any metal oxides with a free energy less negative than that of CO or CO_2 can be so reduced (Figure 2.4). Additional materials such as sulfides, nitrides, chlorides, and other non-metals may also be considered.[63]

Generally, the Gibbs free energy change for the oxidation reaction of a metal (per mole of oxygen) versus the temperature is plotted. Typically, the lower the position of a metal's line on the diagram, the more stable it's oxide (more negative ΔG). Hence, metals with a line lower on the diagram can act as a reducing agent for metal oxides that lay above them, and the further apart the lines, the greater the free energy change upon reduction (larger changes in free energy are more exothermic). This principle is often used in extractive metallurgy to isolate components from raw ore.[63] The thermite reaction is also an example. Aluminum lies below Fe_2O_3 on an Ellingham diagram (Figure 2.4). When Al and Fe_2O_3 are combined, and the reaction initiated, the Al is oxidized to Al_2O_3 and the Fe_2O_3 is reduced to Fe. The reaction is so exothermic, that the reduced Fe typically becomes molten.

The free energy of formation is negative for most metal oxides, and so a typical Ellingham Diagram is drawn with $\Delta G=0$ at the top of the diagram, with negative values of ΔG going down the y-axis. Temperatures where either the metal or oxide melt or vaporize may also be marked on a diagram or are indicated by a change in the slope of a line. Around the outside of the diagram is a scale that shows the equilibrium partial pressure of oxygen in contact with the metal and oxide (calculated by equation 2.3). To determine the partial pressure of oxygen at a

given temperature from the diagram, one simply constructs a line from the origin (typically the top-left corner of the plot) to the desired partial pressure of oxygen. This construction will intersect the line for a given metal, showing the required temperature to achieve that partial pressure of oxygen. Figure 2.4 shows a typical Ellingham Diagram for several metals of interest in this chapter as well as a sample construction for determining the oxygen partial pressure at a given temperature.

Note that in this case the constructed line intersects the oxygen scale at approximately 10^{-44} atm of oxygen partial pressure. To put this into perspective, 1 mole of an ideal gas occupies 22.4 L at standard temperature and pressure (1 atm, 298K). Therefore, a pressure of 10^{-24} atm is roughly equivalent to 1 molecule in a 22.4L volume (using Avagadro's Number). Typically achievable laboratory pressures (as in ultra-high vacuum systems) are only about 10^{-14} atm. At this pressure (10^{-14} atm), the time for a monolayer formation (derived from the Kinetic Theory of Gases) is about 300,000 sec (83 hours) assuming that all molecules in the gas phase stick or react when they strike a surface.[64] The time to monolayer formation increases by an order of magnitude per order of magnitude drop in pressure. Hence, if only oxygen is present in the vapor phase, and the equilibrium partial pressure is 10^{-44} atm, the time for just one monolayer to form on the surface is 300,000 x 10^{30} seconds, or 9.5×10^{27} years (that's longer than the Universe itself has existed!). This is a prime example of the limitations of kinetics. How then do these reactions take place at all? Any oxide exposed to air has physisorbed or chemisorbed species on the surface (especially water or hydroxide). Therefore, it is often these species that are responsible for oxidation by aiding in the transport of oxygen to and from the metal surface. These species also yield an overall larger partial pressure lending to faster kinetics.

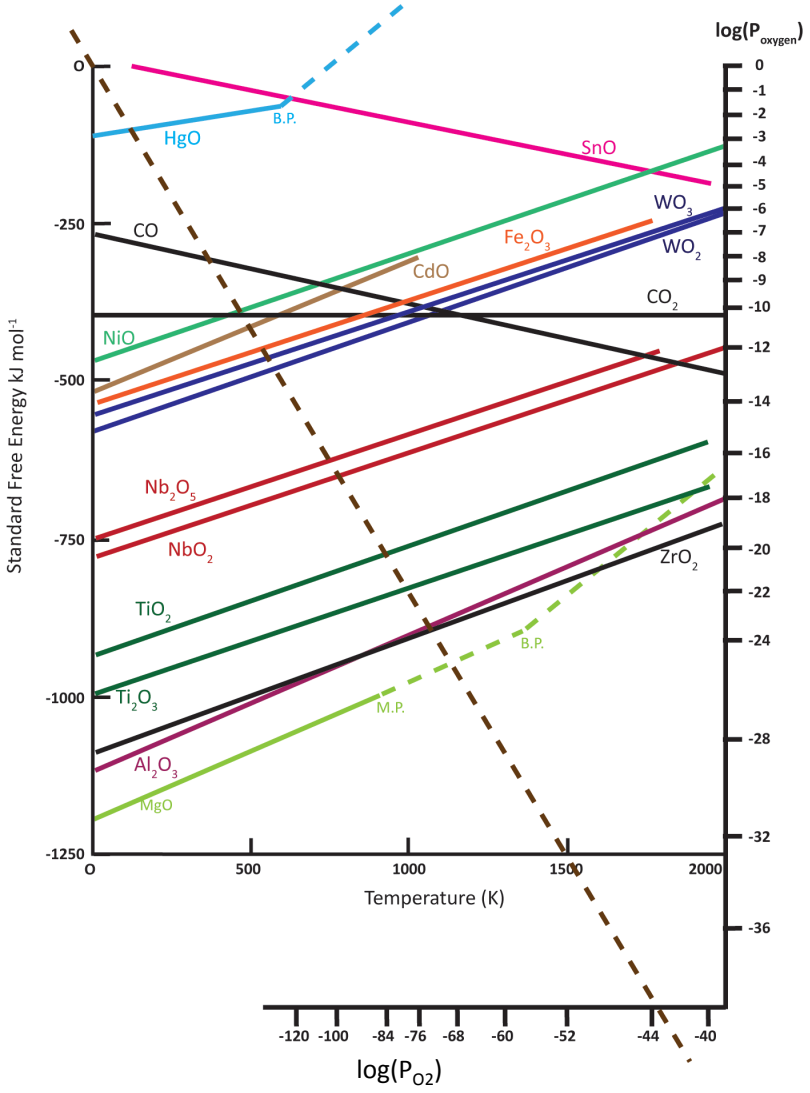

Figure 2.4 Ellingham Diagram for several metal oxidation reactions. Each line represents the free energy change as a function of temperature for the reaction between a metal in contact with oxygen to produce the noted metal oxide. The brown dashed line is a construction from the zero free energy change (top-left corner) to a specific partial pressure of oxygen noted on the scale along the right and lower edges. In this case, the constructed line shows that for the Nb_2O_5 line, at 750ºC the partial pressure of oxygen in equilibrium with the metal and oxide is approximately 10^{-44} atm.

It is interesting to see that not all of the lines in Figure 2.4 have a positive slope. Carbon is often a special case displayed on Ellingham diagrams. In the case of the full oxidation of carbon to carbon dioxide, one mole of O_2 reacts to form one mole of CO_2, since there is a zero net change in the number of moles of gas molecules, the entropy of oxidation is relatively small and the CO_2 line appears flat as a function of temperature. Conversely, the incomplete oxidation of C to CO yields an overall increase in the number of gas molecules (1 mole of O_2 yields two moles of CO). Here a large increase in entropy (ΔS is negative) is observed and the line slopes negative, the opposite of most metals (a positive slope for a positive ΔS). Additional versions of the Ellingham Diagram can be constructed for other gaseous species (NH_3, H_2, N_2, S, or H_2O) and are used most often by metallurgists to determine the appropriate ratios for reducing gas mixtures in processing raw ores.[63]

Ellingham diagrams are extremely useful tools, and allow for quick analysis of thermodynamic data with out the need for extensive calculations. They serve well as a first approximation of how multi-metal systems will behave from a thermodynamic perspective.

2.3.2 Oxygen Gettering

Gettering is a technique based on the ability of certain solids to collect free gases by adsorption, absorption, or occlusion. This effect is widely used in the electronics field to improve and maintain a high vacuum or to purify an atmosphere of noble gases. Generally, getters are found in three forms. Bulk getters are foils or wires of gas-absorbing metals, which usually are heated by resistive heating (in the case of vacuum tubes) or by a separate heating source. Coating getters are generally applied to the electrodes of vacuum tubes, which are maintained continuously at temperatures between 200-1200 ºC. Coating getters usually consist

of nonvolatile metal powders that are sintered together on an electrode surface. Finally, flash gettering involves the use of chemically active, volatile (typically alkaline earth) metals that are evaporated and recondensed trapping reactive species from the atmosphere. Flash gettering is typically used in vacuum tubes to trap non-noble gas species by precipitating them onto cold parts of the tube. The precipitates from the so-called "getter mirror" and is easily seen formed on the tip of halogen light bulbs.[65] Typical getter materials are those that have high enthalpies of formation of their oxide or nitride, and include Zr, Ta, Nb, Al, Ti, Mg, Ba, P, and others.

Apart from the manufacture and operation of vacuum components, gettering has been used extensively in the study of semi-conductors and superconductors. [35,66]. For oxide materials, gettering techniques have been used to control the oxygen stoichiometry and vacancy ordering in the study of YBCO superconductors[67,68] and other oxide materials.[69] Gettering of metal impurities has also been observed in the manufacture of silicon-based semiconductors (n and p type) and other wafer processing operations.[70]

In our work, we use the approach developed by Cava[66,67] and others[69] in which gettering is used to control oxygen stoichiometry. This approach is derived from observable behavior on the Ellingham Diagram (Figure 2.4). In a closed system, when a metal oxide is heated, some equilibrium partial pressure of oxygen is produced (although it may be very low) as a function of temperature. We've already discussed that unless other species (water vapor and hydroxide especially) are present, the kinetics of oxidation can be very slow. In those cases, adventitious water and/or hydroxide species (which form water and an oxide anion upon heating) often acts as a shuttle, moving oxygen from the metal oxide to a getter metal (Zr in this case) with a more negative free energy of oxide formation. Of course, this is only a thermodynamic treatment; and there may be kinetic barriers to this process. Additionally, the equilibrium of the system will

also contribute to the (reducing/oxygen absorbing) action of the getter metal (Zr in our case) via Le Châtelier's principle. If an appropriate amount of getter material is placed in the system to remove a prescribed amount of oxygen, one simply needs to apply a sufficient temperature and allow enough reaction time for complete conversion of the getter metal to its oxide. For example, if 0.5 moles of Zr foil are placed into an evacuated tube with 1 mole of WO_3, after heating at 750 ºC for 48 hours, the Zr foil will be oxidized fully to ZrO_2 and the WO_3 will be reduced to WO_2. Hence, Zr gettering was used in the preparation of oxide supports to affect reduction of W(VI) to W(IV) and Ti(IV) to Ti(III) with the hopes of yielding a stable, conducting material (discussed in sections 2.5 through 2.7 of this chapter).

2.4 Synthetic Strategies

Synthetic methods to produce oxide materials for a wide range of applications has been extensively reported.[71-76] Apart from traditional solid-state synthesis (so-called "shake-n-bake" or ceramic synthesis)[77 78], methods such as sol-gel[79-81], spray pyrolysis[82], combustion synthesis[72,83], and chemical vapor transport (CVT) [84-86] have also been developed to produce oxide materials of various morphologies (i.e. thin-films, micron and nano sized powders, and mesoporous solids). In an initial approach, compounds in the Nb-W-O system were synthesized using traditional ceramic methodologies. This strategy allows for the study of changes in phase behavior from reported phases in the Nb_2O_5-WO_3 system to ones with different oxygen stoichiometries.

2.4.1 A Few Notes on Ceramic and Chemical Vapor Transport Methods

Ceramic syntheses have been used extensively for the preparation of oxide materials.[68,78] Principally, this technique relies on simple solid-state diffusion (governed by Fick's Law,

equation 2.4) making reaction time and reaction temperature the primary synthetic "control-knobs". Generally, reaction temperatures and/or reaction times can be significantly decreased by making the starting materials very fine powders and pressing these precursors into a pellet or "pill" prior to heating. Pressing the precursors increases inter-particle contact and smaller size allows for overall smaller diffusion distances. In the standard ceramic method, pressed pellets of reactant oxides are typically heated in static or flowing air in an appropriate non-reactive crucible (often alumina or platinum) to temperatures between 500˚C to 1500˚C for several days.[72]

$$x(t) \propto (D(T)t)^{1/2} \tag{2.4}$$

Another approach to decreasing reaction times may be to forego diffusion in the solid-state and to utilize transport of the constituent elements through the vapor phase. To achieve vapor transport, either the reaction must reach sufficiently high temperatures to develop an adequate vapor pressure of the precursors (typically 10^{-6} torr to several atmospheres), or a "transport agent" must be added. Typically, this transport agent operates by producing trace amounts of high vapor pressure intermediates. This method is referred to as Chemical Vapor Transport (CVT) and may be used to prepare single crystals or epitaxial films of many different substances, including oxides. [84,87]

Typically the transporting agent is chosen such that, when combined with the precursor oxide, the reaction is reversible and the free energy of formation is small and temperature dependent. Because the transport is occurring in the vapor phase, these reactions are carried out in a sealed container that is heated in a manner to induce a temperature gradient. This temperature gradient causes the transporting agent to reversibly generate, and deposit precursor

species in the temperature region which allows for the lowest free energy.[86] It is important to note also that the transporting agent is not consumed in this reaction, and therefore relatively small amounts are needed when compared to the amount of oxide material being synthesized.[88]

2.5 Preparation of Compounds in the Nb-W-O and Nb-Ti-O Systems

The Nb_2O_5-WO_3 and Nb_2O_5-TiO_2 systems have several known phases, some of which are congruently melting and some of which decompose at high temperatures (Figure 2.3). In a series of experiments, several examples of these known phases were prepared using traditional, high-temperature solid-state chemistry techniques.

2.5.1 Materials

Niobium Oxide (Nb_2O_5 99.999%, 325 mesh white powder) was purchased from Sigma-Aldrich; Tungsten Oxide ($WO_{2.9}$ 99.99%, dark blue powder) was purchased from Alfa Aesar and heated in air at 800 ºC for 4 days to fully oxidize the powder to WO_3; Titanium Dioxide (TiO_2, 99.8%, white powder) was purchased from Sigma Aldrich; Titanium Trioxide (Ti_2O_3, 99.99%, black powder) was purchased from Fluka Scientific; Zirconium foil (Zr, 99.8%, 0.025 mm thick, annealed) was purchased from Alfa Aesar; Hexachlorobenzene (C_6Cl_6, 97%, white crystals) was purchased from Aldrich; 14 mm x 16 mm silica tubing was purchased from Quartz Scientific.

2.5.2 Synthesis

Typically, stoichiometric mixtures of Nb_2O_5 and WO_3 (or Nb_2O_5 and TiO_2) powders were mixed and finely ground in an agate mortar followed by pressing into a 10 mm diameter x 5mm thick pellet at 4000 PSI using a Carver laboratory hydraulic press. The pellets were then heated

in air between 1050ºC and 1100ºC for 3 to 8 days. Often a single phase of the target composition was obtained, while some samples required multiple heating cycles to reach equilibrium. Typically the pellets remained intact through their heating cycles and were reground and repressed if they required multiple heat treatments. The as-synthesized compounds were typically white to off-white in color, and possessed metal centers that were in their highest oxidation state, thus requiring subsequent processing to hopefully prepare a conducting material.

By the reasoning explained earlier, oxygen vacancy doping is achieved by reducing the tungsten (or titanium) in these compounds from W(VI) to W(IV) (or Ti(IV) to Ti(III)). In order to do this without solution based methods, Zr foil was used as an oxygen getter following the method developed by Cava *et al*.[68] Zirconium is a highly oxophilic metal that will react with any available oxygen to produce ZrO_2, especially at high temperatures (oxygen gettering). Furthermore, Zr will act as a reducing agent for W and Ti oxides simply because of thermodynamic considerations as predicted by Ellingham Diagrams (Figure 2.4).[62] For example, to reduce all of the W(VI) to W(IV) (or Ti(IV) to Ti(III)) a stoichiometric amount of Zr foil (equations 2.5 and 2.6) was placed into a silica ampoule and then placed into a larger silica tube with the as-made, fully oxidized compounds (powders in this step were not pressed into a pellet). The tube was then evacuated while heating the in-process material to drive off any adsorbed water. Care was taken not to heat the Zr foil in order to avoid premature oxygen gettering. The silica tube was then sealed under vacuum and heated at 750 ºC for 48 hours. This tube-within-a-tube approach is used to keep the Zr foil separated from the in-process oxide, as well as to prevent the reacted ZrO_2 from contaminating the reduced product. Generally, a dark blue to black powder was obtained, with full oxidation of the Zr foil.

$$xNb_2O_5 \bullet yWO_3 + \frac{y}{2}Zr \xrightarrow[48hrs]{750°C} xNb_2O_5 \bullet yWO_2 + \frac{y}{2}ZrO_2 \quad (2.5)$$

$$xNb_2O_5 \bullet yTiO_2 + \frac{y}{4}Zr \xrightarrow[48hrs]{750°C} xNb_2O_5 \bullet \frac{y}{2}Ti_2O_3 + \frac{y}{4}ZrO_2 \quad (2.6)$$

2.5.3 Discussion of Nb-W-O results

There are several phases in the Nb_2O_5 -WO_3 system that are expected to exist at room temperature. Since the goal in producing a new catalyst support material is to synthesize a material that is both conducting and stable, and because the conducting component (WO_2) is only narrowly stable under PEMFC conditions, compositions that are richer in Nb_2O_5 were synthesized first. To begin, the 1:1 Nb_2O_5:WO_3 (Nb_2WO_8) and the 7:3 Nb_2O_5:WO_3 ($Nb_{12}W_3O_{44}$) phases were synthesized by the ceramic method with heating at 1050ºC for 3 days with subsequent reduction by zirconium foil. Figure 2.5 shows powder X-ray Diffraction (pXRD, using a Scintag XDS 2000 diffractometer with Cu Kα radiation) patterns for the as prepared and the reduced compounds for the 1:1 phase (PDF # 04-009-3209, orthorhombic (*Pbcm*) a=3.949, b=17.622, c=16.626 Å).

The most obvious change in the pXRD pattern in the reduced sample is the emergence of peaks at approximately 40.4º, 58.2º, and 73.2º (starred in Figure 2.5a). These peaks index to elemental tungsten (PDF# 00-001-1203, cubic (*Im-3m)*, a=3.155 Å), indicating that it phase segregates from the parent compound. The remaining peaks in the reduced sample (a dark blue/black powder) belong to the parent compound Nb_2WO_8 (a white powder) with no evidence in the powder pattern of other phases present (i.e. Nb_2O_5). It is not necessarily surprising that some of the tungsten was fully reduced rather then all of the tungsten being partly reduced to WO_2. Considering that WO_2 is prepared by reacting WO_3 with W metal at high temperatures, it

is reasonable that the process is reversible at high temperatures, especially in the presence of a reducing agent like Zr.[89] The reaction stoichiometry for this disproportionation process is shown by equation 2.7.

$$WO_2 \rightarrow \frac{2}{3}WO_3 + \frac{1}{3}W \tag{2.7}$$

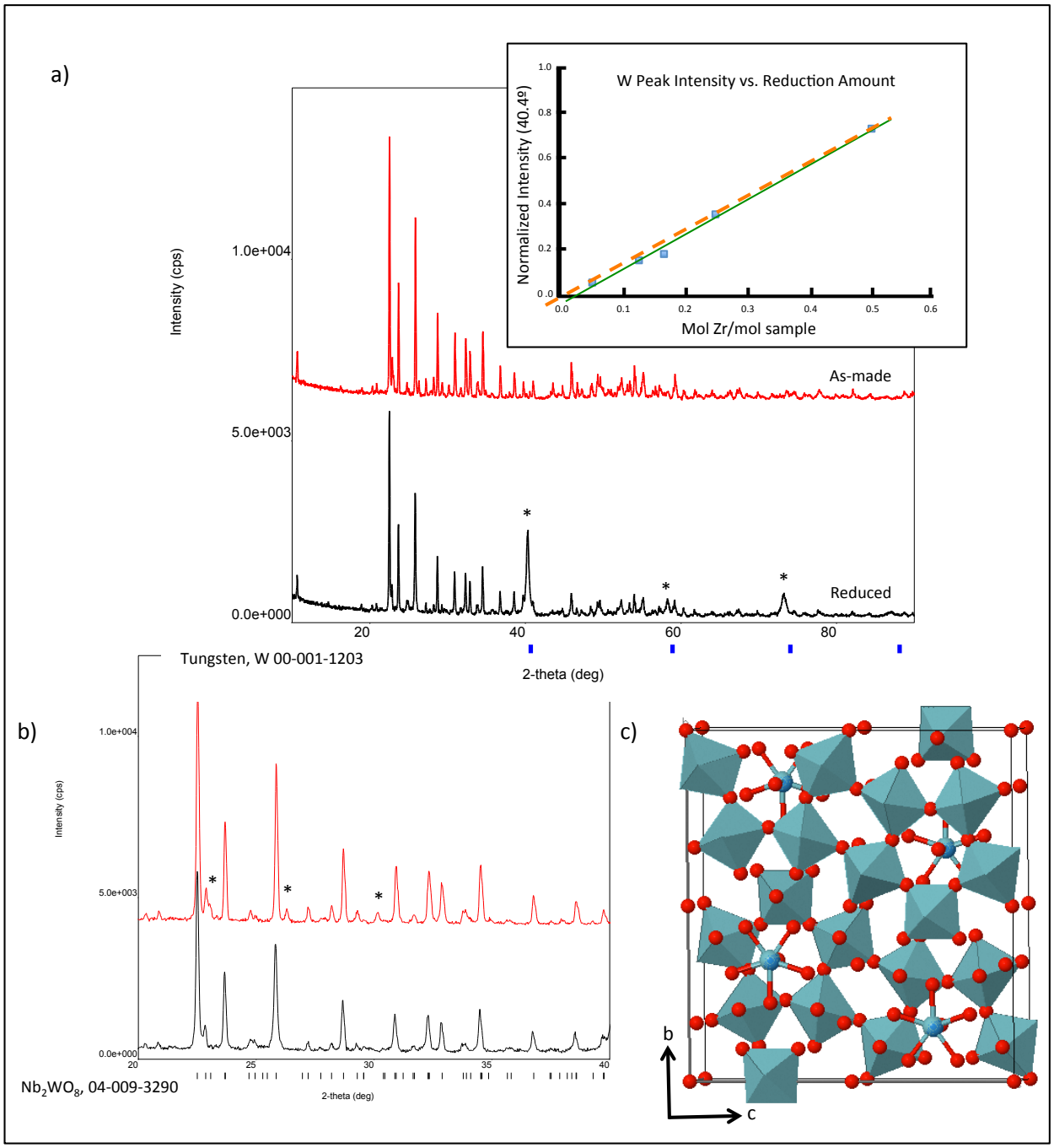

Figure 2.5 (a) pXRD pattern of oxidized (red line) and reduced (black line) Nb_2WO_8. Notice the elemental W peaks in the reduced sample (starred). (Inset,a) Plot of W peak intensity vs amount of Zr reduction, 0.5 mol equivalent is full reduction of WO_3 to WO_2. The dashed (orange) line is a forced linear fit through the origin (y=ax) while the solid (green) line is a regular linear fit (y=ax+b). There is not a very significant difference between the two. (b) Blown-up pXRD pattern in the 20-40º region. The starred peaks are present in the oxidized compound but disappear in the reduced compound. This may indicated some impurities in the parent compound, which may have contributed to W disproportionation. (c) Crystal structure of Nb_2WO_8. Orthorhombic (*Pbcm*) a=3.949, b=17.622, c=16.626 Å.

It is surprising, however, as there is evidence of pure W in the sample, there is no evidence of Nb_2O_5 in the reduced product, as would be predicted by simple mass balance. To investigate this further, a series of reactions were performed which varied the amount of the Zr foil used to reduce the sample. The inset in Figure 2.5 shows a plot of the normalized (to the strongest peak of Nb_2WO_8, 22.6º) intensity of the strongest W peak (at 40.4º) in the reduced sample versus the mole ratio of Zr used (note that a mole ratio of 0.5 means full reduction of WO_3 to WO_2). This plot is linear, and extrapolates to about 0.03. This indicates that there is likely not a second, meta-stable phase which is generated before W begins to segregate from the sample (i.e. there would be a larger x-intercept), but rather that there is a relatively wide composition window for the 1:1 phase, which allows for some W non-stoichiometry. An additional possibility is that there is a second phase, but it is amorphous and non-detectable using pXRD. This, however is unlikely due to the temperatures to which the materials are heated. Additionally, amorphous phase behavior is not typically observed in this system.[90]

Additional synthetic routes to the 1:1 phases were explored in order to circumvent the need for reduction by Zr. In a first attempt Nb_2O_5 was mixed with a stoichiometric amount of WO_3 and W metal (in a 1: 0.66 : 0.33 ratio) and sealed in a silica tube under vacuum prior to heating at 1050ºC for 3 days. A small amount (3.5 mg for a 1 g batch) of Hexachlorobenzene (C_6Cl_6) was also added to generate Cl_2 (upon decomposition at high temperatures), a CVT transporting agent, prior to sealing. The resulting product showed significant reaction with the silica tube (as evidenced by SiO_2 peaks visible in the pXRD pattern) and was a gray to off white powder. In another attempt, Nb_2O_5 was mixed with WO_2 in order to directly synthesize the targeted product. As before, a stoichiometric ratio was pressed into a pellet at 4000 PSI, and sealed in a silica tube under vacuum prior to heating at 1050ºC for 4 days. The resultant powder

was dark blue to black, as before, and showed identical phase behavior to the 1:1 compounds synthesized via Zr reduction (i.e. W metal peaks in the pXRD pattern)

The 7:3 Nb_2O_5:WO_3 ($Nb_{12}W_3O_{44}$, PDF# 04-009-3726, tetragonal (*I-4*), a=21.020, c=3.820 Å) phase was initially prepared in exactly the same way as was the 1:1 phase. Figure 2.6a shows the pXRD patterns for the as made and reduced product, as well as a scanning electron microscope image (obtained with a Leo 1550 FESEM at 5 keV) of the reduced powder (Figure 2.6b).

Figure 2.6b shows obvious phase segregation of highly faceted octahedral (or hexagonal) crystals from the bulk compound. The pXRD pattern of the reduced (dark blue/black) sample shows evidence of pure crystalline WO_2 (PDF# 00-005-0431, monoclinic ($P2_1$), a=5.567, b=4.892, c=5.550 Å, β=118.19º) as a secondary phase not present in the fully oxidized (white) powder, with the remaining peaks belonging to the parent compound and no evidence of other secondary phases. Again it is surprising that no Nb_2O_5 is observed in the reduced product pXRD pattern as would be predicted by mass balance.

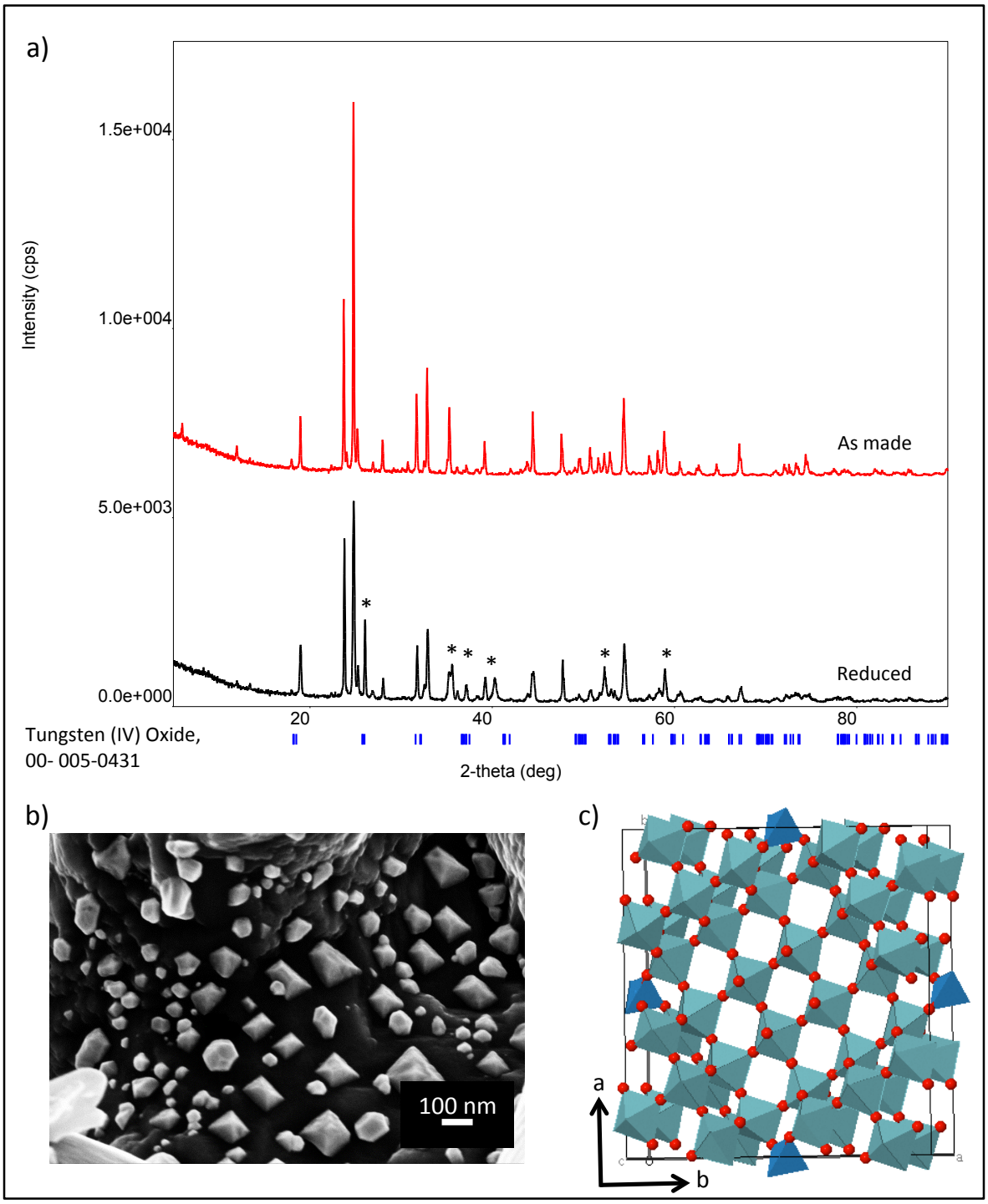

Figure 2.6 (a) pXRD pattern of as made(red line) and reduced (black line) $Nb_{14}W_3O_{44}$. Notice the presence of WO_2 peaks (starred) in the reduced sample. (b) SEM image of reduced sample, the powder grains are coated with faceted crystallites segregated from the bulk compound. (c) Crystal structure of $Nb_{14}W_3O_{44}$. Tetragonal (*I-4*) a= 21.020, c=3.820 Å.

Additionally, it is interesting that the relative intensity of the two strongest peaks in the parent compound pattern (23.8º and 24.8º) changes when the product is reduced. This can be due to a few different things. Fundamentally, this change in relative intensity may indicate a difference in the scattering power of the crystallographic planes that give rise to those reflections. Tungsten is a heavy element with a high X-ray scattering cross-section, therefore it is likely that these reflections are from plains rich in tungsten. Furthermore, if the parent compound is being depleted of tungsten upon reduction it may indicate that there is an unreported, fairly wide window of non-stoichiometry or phase width within the Nb_2O_5-WO_3 system for this previously reported[60] line phase. Secondly, if the crystalline domains are large (> 10μm), it is possible that the powder mixture is not truly a randomly oriented mixture of all possible crystallographic orientations (a necessary conditions for repeatable intensities in pXRD measurements), which would give rise to changes in the relative intensity. This reason is unlikely when looking at SEM images of the powder grains. The largest powder grains are on the order of 15-20 μm, which are made up of many much smaller crystallites. Lastly, if the crystallites have a preferred shape (such as needles), it is possible to have changes in the pXRD pattern due to preferred orientation on the X-ray sample holder (e.g. needles all lay down rather than randomly distributed at different angles). Again, in looking at SEM images of the powder grains, this reason for the observed changes in peak intensity is unlikely.

In order to investigate the formation of WO_2 crystallites in the 7:3 compound a series of reactions were prepared in which a sub-stoichiometric amount of Zr foil was used to reduce the sample, the aim being to discover at what composition WO_2 crystallites begin to form. A 4g batch of the oxidized 7:3 compound was prepared and split into 4 1g fractions. Each fraction was sealed in a silica tube, under vacuum with a prescribed amount (1, 0.5, 0.25, and 0.2 times

the stoichiometric amount) of Zr foil followed by heating at 750º C for 48 hours. Figure 2.7, below, shows SEM images of the prepared products.

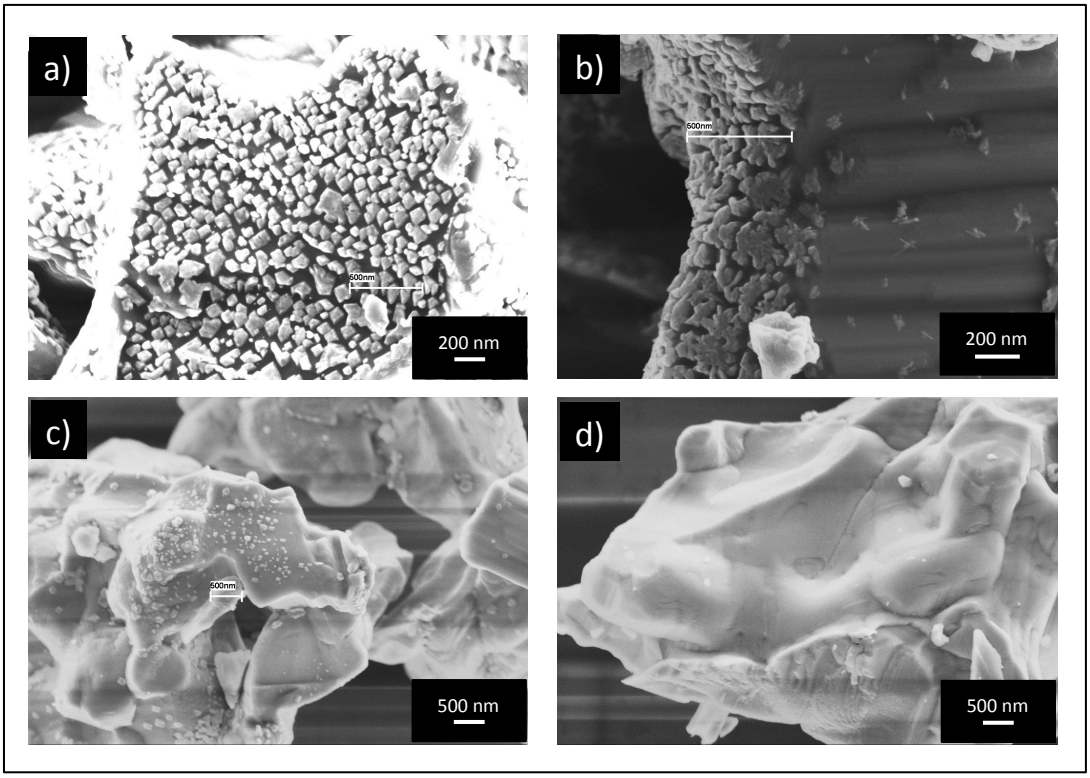

Figure 2.7 SEM images of 7:3 Nb_2O_5:WO_3 reduced with various fractions of the required Zr for reduction. (a) Stoichiometric, (b) half stoichiometric, (c) one quarter stoichiometic, (d) one fifth stoichiometric. Notice the decrease In density and faceting of the surface crystallites with decreasing amount of Zr.

As the amount of Zr reducing agent is decreased, the density and faceting of the WO_2 crystallites decreases. Between half and one quarter the stoichiometric amount, the density of WO_2 crystallites appears to fall below the percolation limit (the WO_2 crystallites are no longer in direct contact). This will have an effect on the conductivity of these compounds, which will be discussed later. Another interesting feature of these images is to notice where the surface crystallites appear to nucleate and grow. In images c and d there are several surfaces that have no crystallite formation, with additional images (not shown) showing what appears to be pitting

of the surface in regions with higher concentrations of WO_2 crystallites. These phenomena beg the question of whether or not there are preferential faces of the 7:3 grains that enable the nucleation and growth of WO_2.

Other synthetic approaches to the 7:3 phase were also attempted, as with the 1:1 phase, including direct reaction of Nb_2O_5 with WO_2 and combining Nb_2O_5 with WO_3 and W using CVT. Both approaches showed similar results to the 1:1 compound synthesis including the significant tube reaction in the CVT case, and the appearance of W metal in using WO_2 to bypass reduction by Zr.

Additional compounds in the Nb_2O_5-WO_3 system were investigated using similar syntheses described previously. Both the 30:1 and 13:4 phases were unable to be obtained despite several attempts with numerous heating cycles at 1050º and 1100ºC for 8 days. Both the 6:1 and the 4:9 phases were successfully prepared, while the 6:1 phase had evidence of WO_2 present by pXRD just as the 7:3 phase.

The 4:9 (Nb_2O_5:WO_3) phase (PDF# 04-009-6278, orthorhombic (*Pbam*), a=36.57, b=36.69, c=3.945 Å) was synthesized by heating stoichiometric amounts of the parent oxides at 1050 ºC for 4 days, and showed no evidence of any second phase generation after reduction with Zr despite a shift in the pXRD pattern to slightly higher angles (22.6º to 22.8º in the strongest peak) which propagated throughout the pXRD pattern. The reduced powder was black to dark blue (as compared to white for the oxidized compound). The shift in peaks to higher angles likely indicates slight zero-offset differences or height aberration from the X-ray measurement. Notwithstanding the observed phase behavior, this phase is W rich, which may make it less stable, and thus less desirable for PEMFC catalyst supports.

The conductivity of each Nb-W-O sample was measured as described previously section 2.2. Table 2.1, summarizes the results of the conductivity measurements.

Table 2.1 Summary of conductivities of Nb-W-O samples.

Reported Compound	Nb:W Oxide Ratio	WO_3 Mol%	Amount of Zr reducing agent	Secondary Phases Present (by pXRD)	Conductivity at 105 in-lbs (S/cm)
Vulcan XC-72	-	-	-	-	**> 1**
Nb_2WO_8	1:1	50.0	S*	W	0.0757
Nb_2WO_8	1:1	50.0	1/2 S	W	4.38×10^{-4}
Nb_2WO_8	1:1	50.0	1/3 S	W	1.43×10^{-4}
Nb_2WO_8	1:1	50.0	1/4 S	W	1.66×10^{-4}
Nb_2WO_8	1:1	50.0	1/10 S	W	2.14×10^{-4}
$Nb_{14}W_3O_{44}$	7:3	30.0	S	WO_2	0.12
$Nb_{14}W_3O_{44}$	7:3	30.0	1/2 S	WO_2	0.0508
$Nb_{14}W_3O_{44}$	7:3	30.0	1/4 S	WO_2	6.26×10^{-4}
$Nb_{14}W_3O_{44}$	7:3	30.0	1/5 S	WO_2	3.75×10^{-4}
$Nb_8W_9O_{47}$	4:9	69.2	S	None	0.0142
$Nb_{60}WO_{153}$	30:1	3.2	--	Many	--
$Nb_{26}W_4O_{77}$	13:4	23.5	--	Many	--

* S means a stoichiometric amount of Zr was used
Vulcan XC-72 measured using the same conductivity cell

The most important result displayed here is that only one reduced material could be synthesized as a single phase, specifically the reduced 4:9 Nb_2O_5:WO_3 compound. Even as a single phase however, the best conductivity is only .014 S/cm at 105 in-lbs (Vulcan XC-72 is at 105 in-lbs), 10-times lower than the minimum of 0.1 S/cm. Other phases, such as the 7:3, when fully reduced have conductivities that approach the minimum, but have a significant presence of secondary phases (in this case WO_2). The observed conductivity is most likely due to the surface WO_2 crystallites and not the parent phase itself. This is evidenced by no changes to the parent phase pXRD pattern (as one might expect if vacancy doping was occurring) and the fact that as sub-stoichiometric amounts of Zr are used for reduction, fewer WO_2 crystallites are formed and the conductivity drops. This same logic applies to the 1:1 phase as well, in this case W being the

primary cause for conductivity. It is clear from these results that compounds in the Nb_2O_5-WO_3 system by themselves do not meet the necessary conductivity requirements for use as catalyst supports in PEMFCs. Even as nanoparticles or mesoporous solids the conductivities would be expected to drop due to a larger number of grain boundaries, non-conducting pores, and greater overall contact resistance. Furthermore, the segregated phases that are lending to conductivity are unstable in fuel cell environments and would likely oxidize in a fuel cell system, this is certainly true for elemental W.[16]

2.5.4 Discussion of Nb-Ti-O Results

The 1:1 (Nb_2TiO_7, PDF#00-070-2009, monoclinic (*I2/m*), a=17.684, b=3.804, c=11.890 Å, β=95.33°) and 5:2 ($Nb_{10}Ti_2O_{29}$, PDF# 00-013-0316, orthorhombic (*Bbmm*), a=20.510, b=28.500, c=3.805) phases were prepared by grinding stoichiometric amounts of Nb_2O_5 and TiO_2 in an agate mortar, pressing them into a pellet at 4000 PSI, and heating in air (on Pt foil) at 1050 ºC for a total of 8 days (with regrinding and repressing on day 4) . At the end of the heating cycle, the pXRD patterns for both phases (white-yellow powders) showed multi-phase products; therefore the powders (unpressed) were sealed into silica tubes with 4mg of hexachlorobenzene (a precursor for the CVT transporting agent Cl_2) and heated at 1050ºC for 3 days to attempt to obtain a single-phase product. Upon conclusion of the heating program, the previously white-yellow powders appeared dark blue to black. Typically, black metal oxides are conducting. While no Zr foil was used to cause a reduction of the sample, residual carbon from the hexachlorobenzene decomposition may have acted as a reducing agent, partially reducing the Ti in both compositions. The conductivity of these samples was measured using the two-point

probe technique described in section 2.2. The 1:1 (Nb_2O_5:TiO_2) compound had a conductivity of $2.1x10^{-5}$ S/cm while the 5:2 compound had a conductivity of $3.18x10^{-5}$ S/cm.

Additionally, the 1:1 compound was prepared as before by grinding and pressing a stoichiometric amount and heating at 1300 ºC for 4 days. The prepared product was single-phase, and was reduced with Zr foil. The finished product was black and showed both the 1:1 and 5:2 phases present by pXRD. The conductivity of the parent ($4.47x10^{-8}$ S/cm) and reduced samples ($4.75x10^{-4}$ S/cm) was also measured.

In an attempt to by-pass the Zr reduction step, Ti_2O_3 was mixed directly with Nb_2O_5 using the CVT method. A 1:1 mole ratio mixture of Ti_2O_3 and Nb_2O_5 (this is off Ti stoichiometry for the Nb_2TiO_7 phase) was ground and placed in a silica tube with 3.5mg hexachlorobenzene before being sealed under vacuum and heated at 1000ºC for 4 days. The product was a highly crystalline, black powder that was identified as $NbTiO_4$ by pXRD (Figure 2.8, below). $NbTiO_4$ (PDF# 01-081-0911, tetragonal (*$P4_2/mnm$*), a=4.743, c=2.994 Å) has a rutile structure type and represents a compound with mixed valent Ti and Nb centers (the Nb has both 4+ and 5+ character, while the Ti has both 3+ and 4+ character).[91] The mixed valency in this compound yields an overall larger number of charge carriers when compared to other compounds in this system giving this compound a significantly higher conductivity (measured >1 S/cm, i.e. too conducting to be measured with the two-point probe). Despite the higher conductivity, sol-gel prepared nanoparticles (by Chinmayee Subban) of a 50:50 rutile Ti:Nb oxide showed limited chemical stability in acid solutions.[92]

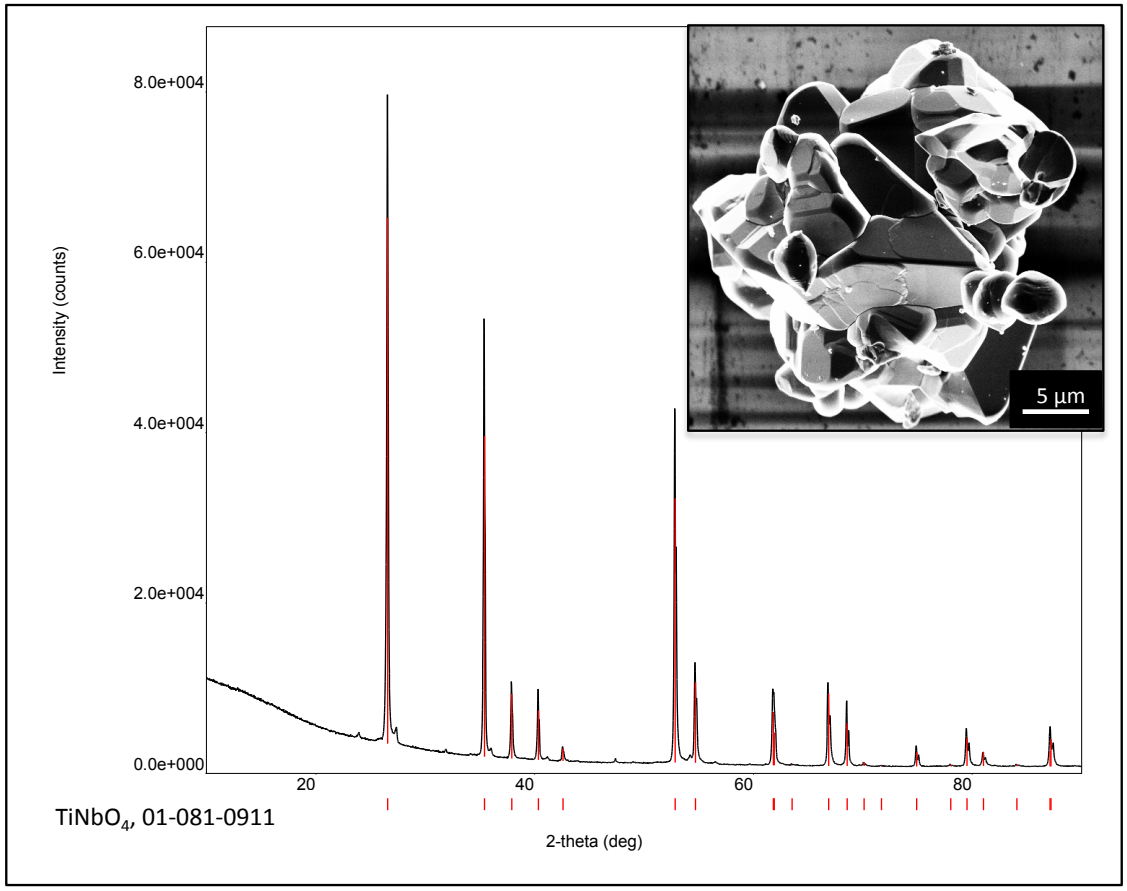

Figure 2.8 pXRD pattern for CVT prepared NbTiO4. (Inset) SEM image of the highly faceted powder grains

2.6 Preparation of Compounds in the Nb-Ti-W-O System

For the compounds discussed thus far, the approach has been to synthesize known oxide compounds and chemically modify their structures via oxygen vacancy doping to achieve a conducting material. Possible stability to corrosion then had to be assessed. Alternatively, another approach pursued by members of the DiSalvo group has been to explore solid solutions of Ti and W oxides (since some of their oxides possess similar structure types). In this section, combining these two approaches will be discussed. Specifically, W-doped rather than pure

titania will be used to synthesize Nb_2O_5-TiO_2 compounds in the hopes of synthesizing a conducting material in the structure type of a reported phase. Additionally, synthesis of these compounds will enable the exploration of the previously unreported phase space between niobia, titania, and tungsten oxides.

Figure 2.9 shows a pseudo-ternary phase diagram for the Nb_2O_5-TiO_2-WO_2 system constructed from experimental results. Each of the compositions were prepared via the CVT technique in which the prescribed stoichiometric amounts of the constituent oxides were ground in an agate mortar and sealed with 3.5mg of hexachlorobenzene in an evacuated silica tube before heating at 1000ºC for 8 days. The green circles represent samples that showed moderate to severe interaction with the silica tube during heating.

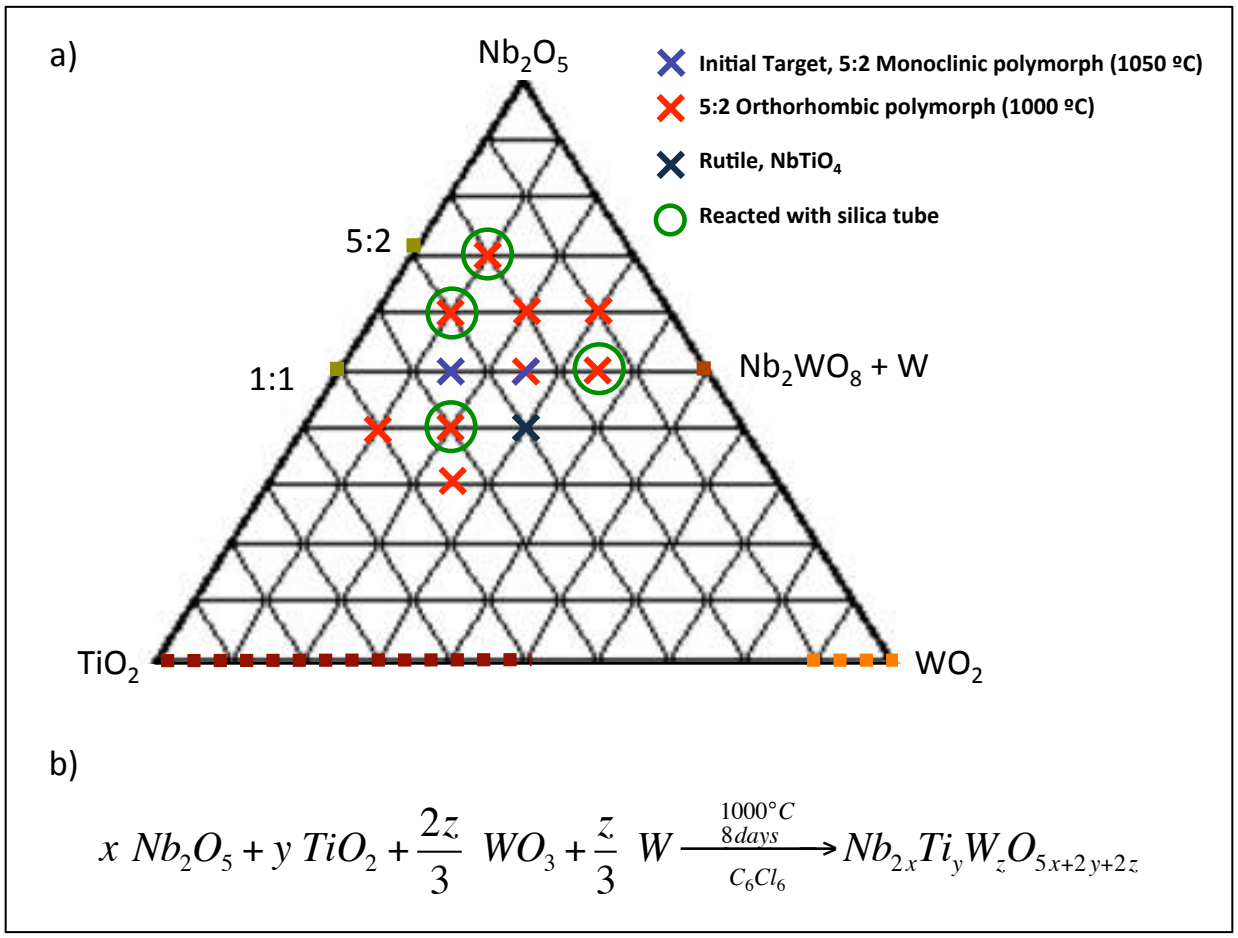

Figure 2.9 (a) A partial pseudo-ternary phase diagram constructed from experimental results. The X's indicate the structure type of the material identified by pXRD. Note however that the material at that position has the correct stoichiometry as confirmed by Energy Dispersive X-Ray Spectroscopy (EDX). (b) A balanced chemical equation for the synthesis of these compounds. Note x, y, and z represent the mole fraction (or mole ratio) of Nb_2O_5, TiO_2, and WO_2 respectively.

The most interesting feature of this system is that the structure type of the 5:2 Nb_2O_5:TiO_2 compound ($Nb_{10}Ti_2O_{29}$) seems to be the preferred structure for a variety of compositions (even though they also include W). There are two distinct polymorphs of the 5:2 structure, a monoclinic cell (red X's) and an orthorhombic cell (purple X's) (Figure 2.10). The dark blue X at the center represents a 40:30:30 (Nb_2O_5:TiO_2:WO_2) ratio of the constituent oxides, which resulted in a single-phase compound with a rutile structure type.

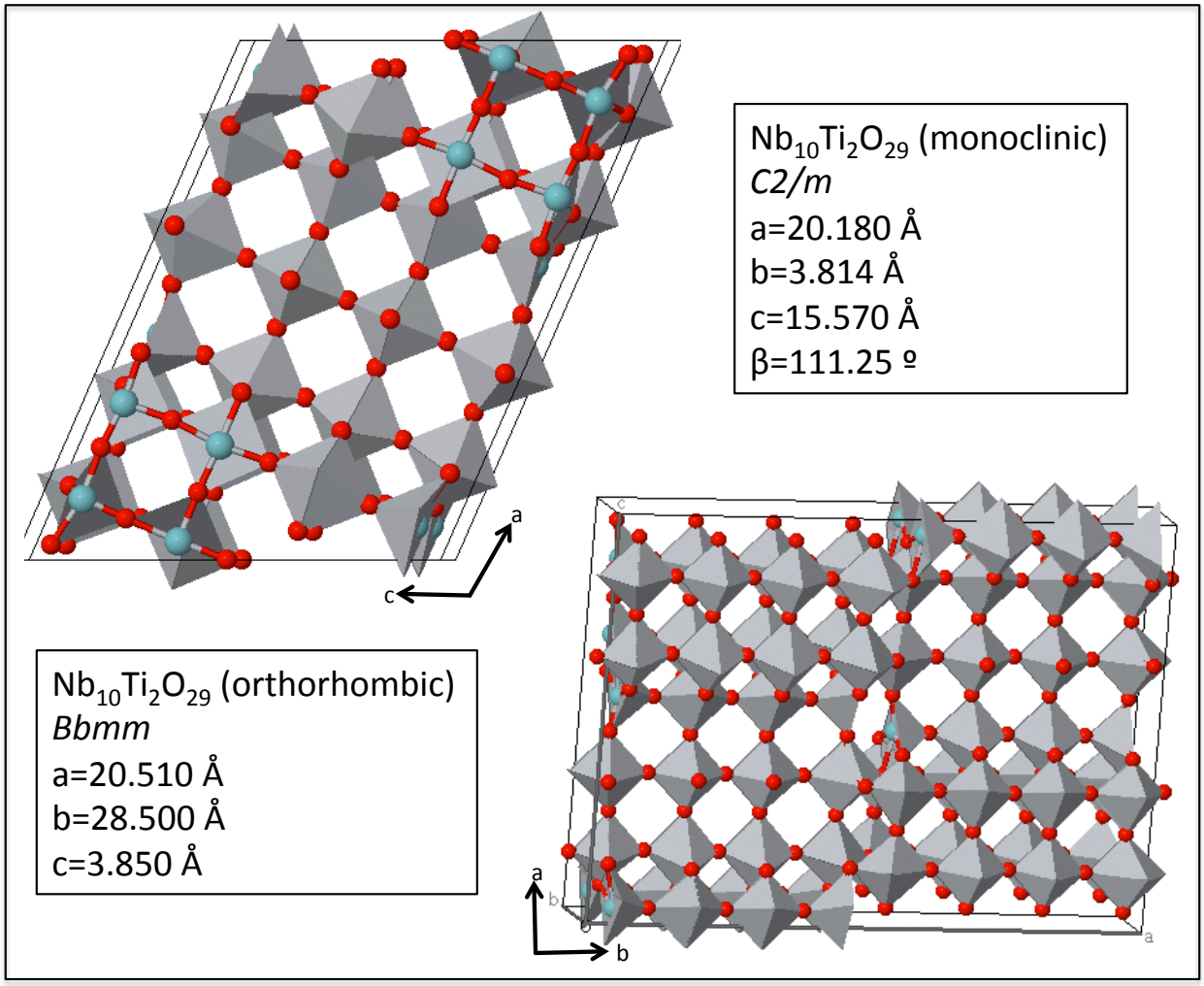

Figure 2.10 Crystal structures of the $Nb_{10}Ti_2O_{29}$ monoclinic (above) and orthorhombic (below) polymorphs.

The conductivity of some Nb-Ti-W-O samples is summarized in Table 2.2. Other samples described in Figure 2.9 were not measured for conductivity. Several had evidence of significant tube reaction (frosting of the tube and the presence of SiO_2 (PDF# 00-39-1425, tetragonal ($P4_12_12$), a=4.978, c= 6.948 Å) peaks in the pXRD pattern). Additionally, similar compounds were being synthesized by Chinmayee Subban in the DiSalvo group, and we felt that generally these compounds were not well suited, in their present state, for catalyst support

applications: their conductivities were too low, and their stability was yet to be fully studied. Nonetheless, the adoption of the 5:2 structure-type by such a wide range of compositions has never been reported. The exact nature of the W environment and chemical state has yet to be fully characterized.

Table 2.2 Summary of conductivities of Nb-Ti-W-O samples.

Nb:Ti:W Oxide Ratio	Structure Type (by pXRD)	Conductivity at 105 in-lbs (S/cm)
Vulcan XC-72	**-**	**> 1.0**
50:35:15	5:2 Nb_2O_5:TiO_2	0.00205
50:35:15	5:2 Nb_2O_5:TiO_2	0.00702
50:35:15	5:2 Nb_2O_5:TiO_2	0.01290
50:25:25	5:2 Nb_2O_5:TiO_2	0.00443
40:30:30	Rutile	> 1.0

2.7 Conclusions

Compounds in the Nb-Ti-W-O system have a rich chemistry and interesting phase behavior that has previously been unreported. While sufficiently conducting compounds for PEMFC applications were not successfully obtained, several new ideas about using conducting oxides for fuel cell catalyst supports were identified. As is the nature of research, one does not always know the appropriate questions to ask when embarking on previously unexplored research topics. Future work in the system should include more fully characterizing the chemical nature and phase behavior of these compounds. While it is known that PEMFC conditions are not ideal for material stability, perhaps these compounds would be suited to other applications or processes (oxygen anion conductors?). Compounds in the Nb-Ti-W-O system should be

synthesized as single crystals and fully characterized by X-ray diffraction techniques. Some single crystal syntheses were attempted, but were ultimately unsuccessful.

While conducting these studies, additional ideas were generated regarding new materials that may be of potential interest for PEMFC supports. Many nitrides, for example, are significantly more conducting than oxides and may be of use as catalyst support materials if they can be made sufficiently stable. This idea will be discussed further in Chapter 3. Ultimately, the oxide support materials discussed in this chapter were set aside in order to focus research efforts on nitride and other materials for use as catalysts and supports.

REFERENCES

(1) Borup, R.; Meyers, J.; Pivovar, B.; Kim, Y. S.; Mukundan, R.; Garland, N.; Myers, D.; Wilson, M.; Garzon, F.; Wood, D.; Zelenay, P.; More, K.; Stroh, K.; Zawodzinski, T.; Boncella, J.; McGrath, J. E.; Inaba, M.; Miyatake, K.; Hori, M.; Ota, K.; Ogumi, Z.; Miyata, S.; Nishikata, A.; Siroma, Z.; Uchimoto, Y.; Yasuda, K.; Kimijima, K.-I.; Iwashita, N. *Chem. Rev. (Washington, DC, U. S.)* **2007**, *107*, 3904–3951.

(2) Cheng, X.; Shi, Z.; Glass, N.; Zhang, L.; Zhang, J.; Song, D.; Liu, Z.-S.; Wang, H.; Shen, J. *Journal of Power Sources* **2007**, *165*, 739–756.

(3) Gasteiger, H. A. *Electrochemistry* **2007**, *75*, 103.

(4) Gasteiger, H. A.; Kocha, S. S.; Sompalli, B.; Wagner, F. T. *Applied Catalysis B: Environmental* **2005**, *56*, 9–35.

(5) Ferreira, P. J.; la O, G. J.; Shao-Horn, Y.; Morgan, D.; Makharia, R.; Kocha, S.; Gasteiger, H. A. *J. Electrochem. Soc.* **2005**, *152*, A2256–A2271.

(6) Dresselhaus, M. S.; Thomas, I. L. *Nature* **2001**, *414*, 332–337.

(7) Dresselhaus, M.; Crabtree, G.; Buchanan, M.; Mallouk, T. *Basic Research Needs for the Hydrogen Economy: Report of the Basic Energy Sciences Workshop on Hydrogen Production, Storage and Use*; 2nd ed. US Department of Energy Office of Science, Basic Energy Sciences, 2004.

(8) Mathias, M. F.; Makharia, R.; Gasteiger, H. A.; Conley, J. J.; Fuller, T. J.; Gittleman, C. I.; Kocha, S. S.; Miller, D. P.; Mittelsteadt, C. K.; Xie, T.; Yan, S. G.; Yu, P. T. *The Electrochemical Society: Interface* **2005**, *14*, 24–35.

(9) Wagner, F. T.; Yan, S. G.; Yu, P. T. In *Handbook of Fuel Cells: Fundamentals, Technology and Applications*; Vielstich, W.; Yokokawa, H.; Gasteiger, H. A., Eds. John Wiley &Sons, Ltd.,: Chichester, UK,, 2009; Vol. 5, pp. 250–263.

(10) Zhang, H. Z.; Gilbert, B.; Huang, F.; Banfield, J. F. *Nature* **2003**, *424*, 1025–1029.

(11) Keane, M. A. *J Mater Sci* **2003**, *38*, 4661–4675.

(12) Henrich, V. E.; Cox, P. A. *The Surface Chemistry of Metal Oxides*; Cambridge University Press: Cambridge, UK, 1994.

(13) Kung, H. H. *Transition Metal Oxides: Surface Chemistry and Catalysis*; Elsevier: Amsterdam, 1989.

(14) Noguera, C. *Physics and Chemistry at Oxide Surfaces*; Cambridge University Press: Cambridge, UK,, 1996.

(15) Lucas, E.; Decker, S.; Khaleel, A.; Seitz, A.; Fultz, S.; Ponce, A.; Li, W. F.; Carnes, C.; Klabunde, K. J. *Chem-Eur J* **2001**, *7*, 2505–2510.

(16) Pourbaix, M. *Atlas of Electrochemical Equilibria in Aqueous Solutions*; National Association of Corrosion Engineers, 1974.

(17) Erlebacher, J.; Sieradzki, K. *Scripta Materialia* **2003**, *49*, 991–996.

(18) Rugolo, J.; Erlebacher, J.; Sieradzki, K. *Nature Materials* **2006**, *5*, 946–949.

(19) Wagner, K.; Brankovic, S. R.; Dimitrov, N.; Sieradzki, K. *J. Electrochem. Soc.* **1997**, *144*, 3545–3555.

(20) Inglis, A. D.; Page, Y. L.; Strobel, P.; Hurd, C. M. *J. Phys. C: Solid State Phys.* **2000**, *16*, 317–333.

(21) Ioroi, T.; Senoh, H.; Yamazaki, S.-I.; Siroma, Z.; Fujiwara, N.; Yasuda, K. *J. Electrochem. Soc.* **2008**, *155*, B321.

(22) CHANG, L. L. *Journal of the American Ceramic Society* **1968**, *51*, 295–295.

(23) Horkans, J.; Shafer, M. W. *J. Electrochem. Soc.* **1977**, *124*, 1202–1207.

(24) Murata, Y.; Fukuta, S.; Ishikawa, S. *Corrosion Engineering* **2000**, *7*, 412–419.

(25) Ashour, A. *Surface Review and Letters* **2006**, *13*, 87–92.

(26) Mikami, M.; Nakamura, S.; Kitao, O.; Arakawa, H.; Gonze, X. *Jpn J Appl Phys 2* **2000**, *39*, L847–L850.

(27) Chen, G.; Waraksa, C. C.; Cho, H.; Macdonald, D. D.; Mallouka, T. E. *J. Electrochem. Soc.* **2003**, *150*, E423.

(28) Colomer, M. T.; Velasco, M. J. *Journal of the European Ceramic Society* **2007**, *27*, 2369–2376.

(29) García, B. L.; Fuentes, R.; Weidner, J. W. *Electrochem. Solid-State Lett.* **2007**, *10*, B108.

(30) Pejryd, L. *Journal of the American Ceramic Society* **1986**, *69*, 717–720.

(31) Roy, A.; Dey, S.; Ghose, J. *Indian Journal of Physics, A* **2000**, *74A*, 191–193.

(32) Sakata, K.; Nishida, I.; Matsushima, M.; Sakata, T. *J. Phys. Soc. Jpn.* **1969**, *27*, 506.

(33) Sasaki, K.; Zhang, L.; Adzic, R. R. *Phys. Chem. Chem. Phys.* **2007**, *10*, 159.

(34) Smith, J. R.; Walsh, F. C.; Clarke, R. L. *J. Appl. Electrochem.* **1998**, *28*, 1021–1033.

(35) Subban, C. V.; Zhou, Q.; Hu, A.; Moylan, T. E.; Wagner, F. T.; DiSalvo, F. J. *J. Am. Chem. Soc.* **2010**, *132*, 17531–17536.

(36) Aryanpour, M.; Hoffmann, R.; DiSalvo, F. J. *Chem. Mater.* **2009**, *21*, 1627–1635.

(37) Wang, D.; Subban, C. V.; Wang, H.; Rus, E.; DiSalvo, F. J.; Abruña, H. D. *J. Am. Chem. Soc.* **2010**, *132*, 10218–10220.

(38) Colomer, M. T.; Jurado, J. R. *Chem. Mater.* **2000**, *12*, 923–930.

(39) Sasaki, Y.; Tokuyasu, Z.; Ono, Y.; Iwasaki, M.; Ito, S. *Research Letters in Materials Science* **2009**, *2009*, 1–4.

(40) Subban, C.; Zhou, Q.; Leonard, B.; Ranjan, C.; Edvenson, H. M.; Disalvo, F. J.; Munie, S.; Hunting, J. *Philosophical Transactions of the Royal Society a-Mathematical Physical and Engineering Sciences* **2010**, *368*, 3243–3253.

(41) Pantea, D.; Darmstadt, H.; Kaliaguine, S.; Summchen, L.; Roy, C. *Carbon* **2001**, *39*, 1147–1158.

(42) Piszczek, T.; Stolarz, S. *Powder Metallurgy International* **1986**, *18*, 9–11.

(43) Sánchez, V.; Benavente, E.; Lavayen, V.; O'Dwyer, C.; Sotomayor Torres, C. M.; González, G.; Santa Ana, M. A. *Appl. Surf. Sci.* **2006**, *252*, 7941–7947.

(44) Tschope, A.; Birringer, R. *J. Electroceram.* **2001**, *7*, 169–177.

(45) Brailsford, A. D.; Hohnke, D. K. *Solid State Ionics* **1983**, *11*, 133–142.

(46) Carr, V. M.; Chadwick, A. V.; Saghafian, R. *J. Phys. C: Solid State Phys.* **1978**, *11*, L637–L641.

(47) Cronemeyer, D. C. *Phys. Rev.* **1952**, *87*, 876–886.

(48) Maier, J. *Ber. Bunsen-Ges. Phys. Chem. Chem. Phys.* **1986**, *90*, 26–33.

(49) Batchelor, G. K.; Obrien, R. W. *Proc. R. Soc. London Ser. A-Math. Phys. Eng. Sci.* **1977**, *355*, 313–333.

(50) Roy, S.; Chakravorty, D. *J. Phys.-Condes. Matter* **1994**, *6*, 8599.

(51) Fujita, T.; Ohshima, K.; Wada, N. *J. Phys. Soc. Jpn.* **1969**, *27*, 1459–&.

(52) Bowler, N. *Res. Nondestruct. Eval.* **2006**, *17*, 29–48.

(53) Bowler, N. *Meas. Sci. Technol.* **2011**, *22*.

(54) McLachlan, D. S.; Sauti, G. *Journal of Nanomaterials* **2007**, *2007*, 9.

(55) Patro, L. N.; Hariharan, K. *Materials Chemistry and Physics* **2009**, *116*, 81–87.

(56) Ahmed, S. R.; Saka, M. *Res. Nondestruct. Eval.* **2007**, *18*, 69–100.

(57) Yamashita, M.; Nishii, T.; Kurihara, H. *Jpn J Appl Phys 2* **1996**, *35*, 1948–1953.

(58) Palmer, D. J.; Dickens, P. G. *Acta Cryst* **1979**, *B35*, 2199–2201.

(59) Strelniker, Y. M.; Havlin, S.; Berkovits, R.; Frydman, A. *Phys Rev E Stat Nonlin Soft Matter Phys* **2005**, *72*, 016121.

(60) Roth, R. S.; Waring, J. L. *J Res Natl Bur Stand A* **1966**, *70*, 281.

(61) Fedorov, F. N.; Mel'nikova, O. V.; Saltykova, V. A.; Pivovarova, A. P.; Dib, M.; Strakhov, V. I. *Russian Journal of Inorganic Chemistry* **1989**, *34*, 741–744.

(62) Ellingham, H. *Journal of the Society of Chemistry and Industry* **1944**, *63*, 125.

(63) Ishizaki, K. *Acta Metallurgica et Materialia* **1990**, *38*, 2059–2066.

(64) Harrison, I. *Why is the a need for UHV?*; 2006.

(65) van de Walle, J. *About the Use of Getters*; Emmision Laboratories: Czech Republic, 2002.

(66) Cava, R. J.; Batlogg, B.; Chen, C. H.; Rietman, E. A.; Zahurak, S. M.; Werder, D. *Nature* **1987**, *329*, 423–425.

(67) Cava, R.; Batlogg, B.; Chen, C.; Rietman, E.; Zahurak, S.; Werder, D. *Phys. Rev. B* **1987**, *36*, 5719–5722.

(68) Cava, R. J.; Krajewski, J. J.; Peck, W. F.; Batlogg, B.; Rupp, L. W.; Fleming, R. M.; James, A.; Marsh, P. *Nature* **1989**, *338*, 328–330.

(69) Chailout, C.; Remeika, J. P. *Solid Sate Communications* **1985**, *56*, 833–835.

(70) Ferré, R.; Martín, I.; Trassl, R.; Alcubilla, R.; Brendel, R. *Appl. Phys. Lett.* **2011**, *98*, 022102.

(71) Chen, Z. W.; Jiao, Z.; Wu, M. H.; Shek, C. H.; Wu, C. M. L.; Lai, J. K. L. *Progress in Materials Science* **2011**, *56*, 901–1029.

(72) Rao, C. N. R. *Materials Science and Engineering B-Solid State Materials for Advanced Technology* **1993**, *18*, 1–21.

(73) Rao, C. N. R.; Vivekchand, S. R. C.; Biswasa, K.; Govindaraja, A. *Dalton Transactions* **2007**, 3728–3749.

(74) Ashkarran, A. A. *Journal of Cluster Science* **2011**, *22*, 233–266.

(75) Gupta, S. M.; Tripathi, M. *Cent. Eur. J. Chem* **2012**, *10*, 279–294.

(76) NIEDERBERGER, M.; GARNWEITNER, G. *Chem-Eur J* **2006**, *12*, 7282–7302.

(77) Kingery, W. D. *Introduction to Ceramics*; John Wiley & Sons, 1960.

(78) Sigmund, W. M.; Bell, N. S.; Bergstrom, L. *Journal of the American Ceramic Society* **2000**, *83*, 1557–1574.

(79) Livage, J.; Henry, M.; Sanchez, C. *Progress in Solid State Chemistry* **1988**, *18*, 259–341.

(80) Lev, O.; Wu, Z.; Bharathi, S.; Glezer, V.; Modestov, A.; Gun, J.; Rabinovich, L.; Sampath, S. *Chem. Mater.* **1997**, *9*, 2354–2375.

(81) Brinker, C. J.; Scherer, G. W. *Sol-Gel Science: The Physics and Chemistry of Sol-gel Processing*; Academic Press: San Diego, CA, 1990.

(82) Messing, G. L.; Zhang, S. C.; Jayanthi, G. V. *Journal of the American Ceramic Society* **1993**, *76*, 2707–2726.

(83) Carp, O.; Patron, L.; Reller, A. *Revue Roumaine De Chimie* **2003**, *48*, 513–520.

(84) van Arkel, A. E.; de Boer, J. H. *Z. anorg. allg. Chem.* **1925**, *148*, 345–350.

(85) Schafer, H. *Chemical transport Reactions*; Academic Press: New York, 1964.

(86) Schafer, H. *Erläuterungen und Ausgewählte Praktikumsaufgaben zum chemischen Transport*; Univ. Münster, 1989.

(87) Schafer, H. *Z. anorg. allg. Chem.* **1973**, *400*, 242–252.

(88) Gruehn, R.; Glaum, R. *Angewandte Chemie-International Edition* **2000**, *39*, 692—.

(89) Wells, A. F. *Structural Inorganic Chemistry*; OUP Oxford, 2012.

(90) Roth, R. S.; Wadsley, A. D. *Acta Cryst* **1965**, *19*, 26–32.

(91) Antonio, M. R.; Song, I.; Yamada, H. *Journal of Solid State Chemistry* **1991**, *93*, 183–192.

(92) Subban, C. V. Synthesis and Characterization of Mixed-Metal Oxides for Catalyst Support Applications in Proton Exchange Membrane Fuel Cells, Cornell University, 2012.

CHAPTER 3

SYNTHESIS AND CHARACTERIZATION OF MESOPOROUS MIXED METAL NITRIDES AS PEM FUEL CELL CATALYST SUPPORTS

Work in this chapter was performed in collaboration with two undergraduate researchers: Joseph Singh and Mayra Hernández-Rivera

In Chapter 2 we discussed the need for new catalyst supports for PEMFCs, as well as our reasoning for attempting to use conducting oxide materials. Ultimately, we found that the conducting oxides of interest to us did not possess sufficient conductivity or chemical stability. It was clear at that time that a new approach was needed.

The DiSalvo group has a rich history of studying nitride materials. While not specifically for PEMFC applications, the synthetic expertise and experience with nitride chemistry in the group prompted us to consider nitride materials as new catalyst support materials. Again the principle criteria for a good nitride support material would be one that possesses sufficient conductivity and chemical stability under fuel cell conditions, as well as possessing high porosity and surface area. In this chapter, I will discuss my work on the preparation of mesoporous mixed-metal nitride materials and the characterization of their properties for potential use as PEMFC catalyst supports.

3.1 Introduction to Nitrides

Nitrides were first investigated in the 1940's by Juza.[1,2] These early studies focused mostly on lithium compounds due to their relatively simple structures and ease of preparation. Over the next several decades, several groups around the world expanded on these studies by preparing other binary and ternary nitride compounds. By the late 1980's, with the advent of several new preparation techniques, the synthesis of new nitride materials had accelerated, and

systematic approaches to compound discovery were being developed. Today, complex nitrides remain a rapidly growing field in Solid-State Chemistry, with specific focuses on understanding their crystal chemistry and structure-property relationships.[3]

Strictly defined, a nitride is a solid-state compound that contains nitrogen as the lone monatomic anionic unit, N^{3-}. Using this definition, materials such as nitrates are excluded from the class of nitrides since the nitrate anion contains N^{5+}. Moreover, materials such as $Y_2Si_3O_3N_4$ are not *pure* nitrides since they contain both O^{2-} and N^{3-} anions (such materials are so-called *oxynitrides)*. Instead, only materials such as Mg_3N_2, GaN, or $CaTiN_2$ can be considered *pure* nitrides as nitrogen is the sole anion.[4]

This strict definition aside, even including "mixed" anionic nitrides (oxynitrides, halonitrides, carbonitrides, etc.), the family of solid-state materials that contain anionic nitrogen is quite small. For comparison, the Inorganic Crystal Structure Database (which catalogues nearly all of the inorganic chemical compounds currently known) has only 9,777 entries for compounds containing N^{3-} and 74,783 entries for compounds containing O^{2-} (compounds with both O^{2-} and N^{3-} are excluded).[5] Perhaps even more startling is the number of naturally occurring nitrides: there is only one, TiN (and it is only found in meteorites from space!).[4]

At first, the difference between the number of known nitride phases and the number of known oxide phases seems odd. There is far more nitrogen than oxygen available in the atmosphere (78% nitrogen versus 21% oxygen roughly), so one might expect that most minerals should be nitrides as opposed to oxides. However, the prevalence of oxide compounds in nature has little to do with stoichiometry and significantly more to do with thermodynamics. We've already considered that the free energy change of any process is related to the associated enthalpy and entropy changes. Generally, the entropy change for the formation of an oxide or

nitride compound should be similar since the dominating contribution to entropy would be reaction of gas phase molecules into a solid (ΔS^{o}_{O2}=161.1 J K^{-1} mol^{-1} versus ΔS^{o}_{N2}=191.6 J K^{-1} mol^{-1}).[6] This results in a negative entropy change per mole of gas, and a relatively small contribution to the free energy change ($\Delta G \sim -T\Delta S \approx$ -45 kJ mol_{gas}^{-1} @ 300K). The dominating factor, then, for the difference in the formation energy for nitrides and oxides is the difference in the enthalpy of formation.[7]

The enthalpy of formation is equal to the difference in energy between the bonds formed and the energy of the bonds broken in transforming the reactants to the product. The triple bond of N_2 (945 kJ mol^{-1}) is significantly stronger than the double bond of O_2 (498 kJ mol^{-1}). Hence, the free energy of formation for nitride compounds tends to be lower (more positive) than oxides. Furthermore, because ΔG_f^{o} is lower (more positive), decomposition of nitride compounds upon heating (through loss of N_2) is more likely than for compounds containing other anions (oxides, sulfides, etc.). Additionally, despite the large electronegativity of nitrogen (3.04 on the Pauling Scale), the contribution of ionic bonding to the stability of nitride compounds is likely to be small, due to the high energy of formation of N^{3-} from atomic N (+2,300 kJ mol^{-1}) compared to the formation of O^{2-} or S^{2-} from atomic O or S (700 kJ mol^{-1} and 331 kJ mol^{-1}, respectively).[8] Thus M-N bonds in nitride compounds tend to be more covalent in nature than M-O bonds in analogous compounds.

From this basic thermodynamic understanding, one can derive two very important points. First, in order to spontaneously form a nitride compound (under conditions such that $\Delta G_f < 0$), the synthesis temperature must be as low as possible. This is due to the fact that, since ΔS is already negative, ΔG can become positive at higher temperatures. Temperature may be less of a concern if alternative N sources are used which do not require breaking a triple bond, for

example ammonia. Secondly, when compared to an oxide material, the corresponding nitride will always be less thermodynamically stable. As a result, it is necessary to carefully control the synthesis conditions to exclude oxygen and water. Some nitrides rapidly decompose into oxides or hydroxides (at least at the surface) in the presence of air or water. In fact, "air stable" nitrides form a protective surface *passivation* (oxide) layer, which inhibits further oxidation of the bulk nitride at low temperatures.[9] Therefore, "air stable" nitrides are only kinetically stable, not thermodynamically stable.

In addition to these thermodynamic considerations, nitrides are an interesting class of materials due to the variety of structural features they adopt due to more covalent nature of the M-N bond. Many of these structural features are not seen in other types of compounds (e.g. oxides). For example, in the compound $Ba_5Si_2N_6$, SiN_4 tetrahedra share edges to form $Si_2N_6^{10-}$ dimers. Similar edge sharing SiO_4 tetrahedral units are rarely found in silicate containing oxides (silicates mostly feature corner sharing tetrahedra).[10] Additionally, the more covalent nature of the M-N bond is also believed to stabilize unusual oxidation states of other metals in the same compound. This is demonstrated in the case of $Ba_3Ge_2N_2$, where the average oxidation state of Ge is zero; half as Ge^{2+} in GeN_2^{4-} units and the other half as Ge^{2-} which form infinite zigzag chains along the [010] direction.[11]

While the chemistry of nitrides is incredibly rich and interesting from an academic perspective, the properties of nitrides are of specific interest to many researchers developing new devices and studying other applications. To date, the majority of nitride materials that have been successfully integrated into devices or other applied technologies has been limited to simple binary nitrides. Perhaps the most famous of these is gallium nitride (GaN), which is a wide band gap semiconductor (E_g=3.4 eV).[4] Gallium nitride is primarily used in electronics in light

emitting diodes (LEDs) as an efficient emitter in the near ultraviolet (UV).[12] GaN can also be alloyed with InN to lower the band gap to produce strong blue emission around 460nm.[13] The tunability of the emission for GaN based materials is the foundation for many new technologies including solid-state lighting and laser materials for Blu-ray disc players.[4] Titanium nitride (TiN) is another nitride material that has found an application niche, and is used as a coating material for tools and medical equipment due to its high hardness and corrosion inhibition properties. Additionally, both binary and ternary nitrides (Mo_2N[14,15] and Co_3Mo_3N[16], for example) and oxynitrides (γ-$Mo_2O_yN_{1-y}$[17], for example) have been investigated for use as both catalysts and supports for a variety of industrially significant processes.[18]

It is clear that nitrides hold a unique position at the frontier of materials science and solid-state chemistry research. While ternary and quaternary nitrides offer scientists a unique perspective on the exotic structural features and elegant chemistry of nitrogen compounds, a majority of the research has focused on nitride materials with a demonstrated industrial utility.

3.2 Synthesis of Nitrides

Much of the early nitride work involved synthesizing materials using traditional Solid-State methods.[18] These include High-Pressure High-Temperature syntheses[19,20], direct reaction of metal powders with flowing or static N_2 gas,[7,15,21], solid state metathesis reactions,[22-26] and using molten metal fluxes for preparing single and polycrystalline nitride compounds.[27-29] Typically each of these techniques were carried out under a nitrogen atmosphere, and the relatively harsh reaction conditions were necessary to effect N_2 bond activation. Alternative nitrogen sources (other than N_2 gas) such as NH_3[30], hydrazine[30], NaN_3[26,31,32], or urea[33,34] were also used in the preparation of nitride compounds using ceramic techniques (e.g. sealed tube

reactions). Additionally, microwave radiation was used to generate N_2 plasma, which was reacted with metal and metal oxide powders to synthesize several binary nitride compounds, including TiN, NbN, VN, BN, AlN, and GaN.[35,36] Microwave-assisted carbothermal reduction of metal precursors has also been reported.[37] Quite often these preparation techniques produced bulk nitride compounds with low surface areas and negligible porosity.[18,21]

In addition to bulk nitride compounds, nitride thin-films are useful for a variety of industrial and electronic applications.[38] Nitride thin films have been prepared using a variety of techniques including both chemical and physical vapor deposition. Chemical vapor deposition involves the chemical reaction of a gas phase species with a heated substrate surface, and can be assisted by a reactive gas (such as NH_3), a plasma, or UV and laser radiation.[21] Typically films applied by CVD are free of impurities and have low porosity with a small number of defects. This makes this technique ideal for applications in the electronic, tooling, and aerospace industry where high-performance well-defined surfaces are required.[39] Physical vapor deposition (PVD) is distinguished from CVD by the absence of surface chemical reactions that release ligands or other byproducts that are not part of the end-composition of the film. More simply put, PVD involves the simple condensation of oligomeric units of the same composition as the film onto a surface. PVD is used primarily in the tooling industry to apply nitride coatings to cutting and grinding tools to improve wear resistance.[39] Thin-film nitrides are discussed further in Chapter 4.

Recently, many new technologies are emerging which require materials with high surface areas and porosity. This has pushed researchers to study and develop techniques for synthesizing nanoparticles and mesoporous materials with a variety of properties and applications. For nitride materials, only within the last decade or so has the synthesis of particles with nanometer domain sizes been investigated. Often these syntheses involve the reaction of molecular metal precursors

or mesoporous metal oxides with flowing ammonia via temperature programmed heating to moderate temperatures (≤ 1000 ºC).[18] Generally in these types of reactions, high flow rates of ammonia are used (typically several hundred mL/min), and the driving force of the reaction is the production of water (equation 3.1, for the case of a metal oxide reacting with ammonia).[40] These high flow rates sweep the generated water out of the system, which forces the partial pressure of water in the system to remain low. A low partial pressure of water promotes the spontaneous formation of the nitride compound from a precursor (e.g. a metal oxide) by lowering ΔG_f (making it more negative). Thermodynamic calculations for the formation of several nitride compounds have been published by former DiSalvo group member Scott Elder.[40]

$$MO_x + \frac{2}{3x}NH_3 \rightarrow MN_y + xH_2O + (\frac{x}{3} - \frac{y}{2})N_2 \quad (3.1)$$

A number of studies have shown that nitrides prepared via temperature programmed ammonolysis contain various surface adsorbed NH_x species (partially dehydrogenated surface ammonia).[41,42] In temperature programmed ammonolysis, samples are generally cooled in flowing nitrogen, argon, or ammonia – the choice of which can affect the composition and structure of these surface moieties.[43] Following cooling, the nitride materials are passivated by exposure to oxygen or air. Some studies use dilute oxygen in an inert carrier gas (typically ≤ 1% O_2) which flows over the sample at room temperature,[44,45] while other studies report filling the sample chamber with an inert gas and using diffusion of oxygen from room air through a small opening to limit the partial pressure of oxygen exposed to the sample over time.[46,47] In addition to the O_2 content, the partial pressure of water in the passivation gas is an important consideration, as this can affect the structure and chemical nature the surface passivation

layer.[9,45,48] In this passivation stage, an oxynitride (or oxide or oxyhydroxide) surface skin is formed which facilitates handling the material in air and protects the bulk nitride from further oxidation or reaction with air. Significant amounts of oxygen may be incorporated into the near surface region of bulk materials and nanoparticles by this method (so much so that nanoparticles which are smaller than a few nm may be fully oxidized).[44,49] The surface passivation layer may be removed by reduction with hydrogen (in the case of catalytic applications) or left to impart chemical and oxidative kinetic stability to the nitride compound.[42,49,50] Using this synthetic motif, nanoparticles and sintered mesoporous networks of binary and ternary nitrides and oxynitrides are obtainable for several binary and ternary metal nitrides consisting of group IV, V, VI metals and main group elements.[51-58]

3.3 Nitrides as PEMFC Catalyst Supports

In contrast to the oxide materials discussed in Chapter 2, the exploration of transition metal nitrides as corrosion resistant, conducting materials for catalyst supports is just beginning. Most literature reports for nitrides as PEMFC catalyst supports focus on simple binary nitrides, with the large emphasis on titanium nitride.[59] Titanium nitride (TiN), has a number of desirable properties which make it uniquely suited as a potential replacement for carbon based catalyst supports in fuel cells (in fact, TiN as a PEMFC catalyst support was patented by General Motors in 2009).[60] In addition to its high hardness and reasonable oxidation and acid corrosion stability, bulk TiN has a higher electrical conductivity than carbon (4000 S cm^{-1} for TiN versus 1190 S cm^{-1} for carbon).[21] Other studies have reported even higher conductivities for TiN, up to 55,000 S cm^{-1} for single crystals.[61] These properties have pushed TiN and other binary nitrides to the forefront of research on this class of materials.

Many of the properties of TiN arise from its electronic structure. Studies have shown that electron deficiencies in the Ti *d*-band near the Fermi level inhibit adsorption to the surface of TiN, and make the surface more electron accepting.[62] Additionally, the mixed *p* and *d* characteristics of the Ti-N bond have been shown to be responsible for its inert nature, mechanical hardness, and high melting point.[61] The high conductivity of TiN has also been shown to arise from one unpaired electron that populates a metal-localized *pd*-hybrid orbital on Ti, which results in a non-zero density of states at the Fermi level. [61,63]

TiN is well known for its oxidation resistance, and is used in many industrial cutting and grinding tools to improve their strength and durability. This oxidation resistance has been well studied, and has been shown to arise from the native passivation layer that is created when the TiN is exposed to oxygen.[61,64-66] As discussed previously, the structure and composition of the oxide/oxynitride passivation layer is highly dependent on the exact conditions and methods of the exposure of the material to oxygen. Several studies have also reported that quite often the surface passivation layer is non-uniform in structure or composition, and that both amorphous and crystalline domains can be observed.[61,64,65] The degree to which the passivation layer is amorphous or crystalline greatly depends on the conditions of exposure to oxygen or air.[67-70] Despite this demonstrated passivation behavior, Avasarala and Haldar[71] showed that platinum supported on TiN nanoparticles was only stable up to 60 ºC when tested in PEMFC-like conditions (900 cycles in sulfuric and perchloric acid electrolytes from 0 to 1.2 V vs. SHE at 50 mV/s). Above 60 ºC the surface passivation layer became dominated by Ti-OH species, which significantly reduced the conductivity and led to a significant loss in electrochemically active surface area. Since current PEMFCs operate at 80 ºC (preferably higher if suitable materials can be found), TiN nanoparticles alone may not possess the necessary stability to replace carbon-

based supports.

In addition to TiN, other nitrides of the group IV, V, and VI metals are also of interest for use as fuel cell catalyst supports because of their similar properties to TiN. Most of these metals form simple cubic phases (with the NaCl structure type) such as TiN, NbN, TaN , WN and CrN. These phases can be prepared at relatively low temperatures, and most have high solid solubility with each other enabling the formation pseudo-ternary, mixed-metal nitride compounds. It has been shown that some mixed-metal nitrides posses superior properties to their binary nitride parents. For example, work by Gao and Li[58] showed that solid solutions of NbN and CrN had higher hardness and corrosion resistance than NbN or CrN alone. Furthermore, there are several recent reports that discuss the properties of Ti-M nitrides (M=Nb, Cr, Mo) for use as a catalyst supports in PEMFCs.[72-82]

Several of these studies focus on bulk or thin-film nitride materials, while mesoporous solids (nanopowders) with a pore size of approximately 50 nm are needed for use in an actual fuel cell. As a nanopowder, each of the nanocrystalline domains needs to be sintered into a connected network with open porosity. This morphology is ideal for a fuel cell because it provides not only a highly porous network for fast mass transport, but also provides an electronically conducting pathway throughout the entire material. Therefore, for the remainder of this chapter, I will discuss my work on the synthesis and characterization of some mixed-metal nitride compounds of the form $Ti_{1-x}M_xN$ (M=Nb, Cr, W). In addition to conductivity, the corrosion resistance properties of these materials will be discussed.

3.4 Preparation of Mesoporous $Ti_{1-x}M_xN$ Nanopowders (M=Cr, Nb, W)

Nanopowder nitrides can be prepared by a variety of methods, with the simplest being the reaction of a nanopowder metal oxide with ammonia at temperatures between 600ºC to 1000ºC.[72] One approach, used in the preparation of our compounds, is to synthesize nanopowder mixed-metal oxides and treat them with ammonia at 800ºC. The nanopowder oxides can be prepared by a variety of methods described in the literature including spray pyrolysis[83-85], combustion syntheses[86-88], freeze drying[89,90], sol-gel[91-97], and soft chemical techniques[98]. Many of these methods, such as sol-gel chemistry[99] and co-precipitation[56-58], involve the use of molecular metal-organic precursors that undergo hydrolytic condensation by reaction with water. By controlling parameters such as total metal ion concentration, pH, temperature, and the use of polymerizing or chelating agents one can tune the size and morphology of the generated oxides.[91] Here we use the co-precipitation method to form amorphous mixed-metal oxides as precursors for mesoporous, Ti-based, mixed-metal nitrides.

Often, the as-synthesized materials form as amorphous particles that are tens of nanometers in size, and which agglomerate into larger (micron-size) powder grains. Upon reaction with ammonia at high temperatures (800º in this case) the amorphous particles crystalize into NaCl-type mixed-metal nitrides that sinter within the larger powder grains. Because the nitridation reaction involves an overall decrease in the number of atoms per unit cell (3 atoms in TiO_2 to 2 atoms in TiN, for example), the formation of porosity throughout the powder grains is promoted and the surface area is increased.

3.4.1 Materials

Titanium(IV) tetra-butoxide (TBOT, 97%, clear viscous liquid) was purchased from Sigma-Aldrich; Niobium penta-ethoxide ($Nb(OEt)_5$, 99.999%, yellow viscous liquid) was purchased from GFS chemicals; Tungsten (VI) hexa-ethoxide $W(OEt)_6$, 99.99%, white crystalline solid) was purchased from Gelest; Chromium Nitrate, Nonahydrate ($Cr(NO_3)_3 \bullet 9\ H_20$ (99.8%, green, crystalline solid) was purchased from Sigma Aldrich; Hexachloroplatinic Acid ($H_2PtCl_6 \bullet 6\ H_2O$, ACS grade, orange hydroscopic powder) was purchased from Sigma Aldrich; Potassium Hydroxide and Sodium Hydroxide (ACS, reagent grade, white pellets) were purchased from Malinckrodt; Anhydrous ethanol (200 Proof, ACS grade) was purchased from Pharmco Aaper; Ethylene Glycol (spectroscopy grade, clear liquid) was purchased from Sigma Aldrich; Anhydrous Ammonia (99.99%, < 50 ppm H_2O) was purchased from Airgas; Argon (Analytical grade, < 50 ppm H2O) was purchased from Airgas; 22mm x 25 mm silica tubing was purchased from Quartz Scientific.

As most of the metal precursors are moisture sensitive (all but the chromium nitrate), the syntheses of the nanopowder mixed metal oxides were carried out using air and water free techniques. For the liquid precursors (TBOT and $Nb(OEt)_5$), the as received bottles were fitted with a septum under an Ar blanket to allow for measuring precise volumes of the precursor liquid with a syringe without exposing the remaining precursor to air. These bottles were also kept in a desiccator while not in use. The $W(OEt)_6$ was pumped into an Ar filled glove box, and small amounts were removed as needed. The $Cr(NO_3)_3 \bullet 9\ H_2O$ precursor was stored at ambient conditions as it was already hydrated. A Schlenck line was also used to enable the mixing and manipulation of the precursor materials under flowing Ar.

Anhydrous ammonia and argon were used during the nitridation process. I designed and built a flow-through reactor manifold that allows one to select different process gasses with out

breaking any connections to the sample chamber. Both NH_3 and Ar are purified by in-line gas purifiers from MicroTorr (Model# SPG-MC190-902F and SPG-MC400-702F), which remove trace contaminants to part-per-billion levels. Specifically the O_2 and H_2O levels were of concern, and the in-line MicroTorr purifiers should remove both of these contaminants to < 1 ppb.

3.4.2 Synthesis

In a typical synthesis, stoichiometric amounts of TBOT and an additional metal precursor were dissolved in absolute ethanol using standard techniques to exclude water and air. Liquids were transferred via a syringe to a degassed, Ar filled 3-neck round bottom flask (a typical degassing procedure involves three cycles of evacuation and back-filling with Ar). Solid precursors were added to the round bottom flask before degassing and filling with Ar (for $W(OEt)_6$, the 3-neck round bottom flask was pumped into the Ar glove box, charged with the appropriate amount of $W(OEt)_6$, and sealed with septa).

Once the metal precursors were added to the 3-neck round-bottom (in the appropriate stoichiometric ratio), an appropriate amount of anhydrous ethanol (200 proof) was added to form a precursor solution with a total metal concentration of 0.5 M (following the method described by Ran[57]). For example, to form the nanopowder, metal oxide precursor for $Ti_{0.5}Nb_{0.5}N$, equimolar amounts of TBOT (2.07 mL) and $Nb(OEt)_5$ (1.5 mL) were mixed in absolute ethanol (20 mL). Each of the precursors readily dissolved in ethanol (in the case of $W(OEt)_6$, the required solvent volume contained 20% dry THF to aid in solubility), and the solutions were allowed to stir for 10 minutes in order to fully dissolve the precursors and to insure a homogeneous solution.

The homogeneous precursor solution (yellow colored for Ti-Nb samples, clear for Ti-W, and green for Ti-Cr) was then added to a rapidly stirring (1100 RPM), aqueous precipitating solution (25 mL) using the cannulation technique (Figure 3.1). Several different precipitating solutions were studied in order to investigate their effect on the materials properties. These solutions included 0.2 M KOH, 0.2 M NaOH, DI water, and conc. NH_4OH (18 M).

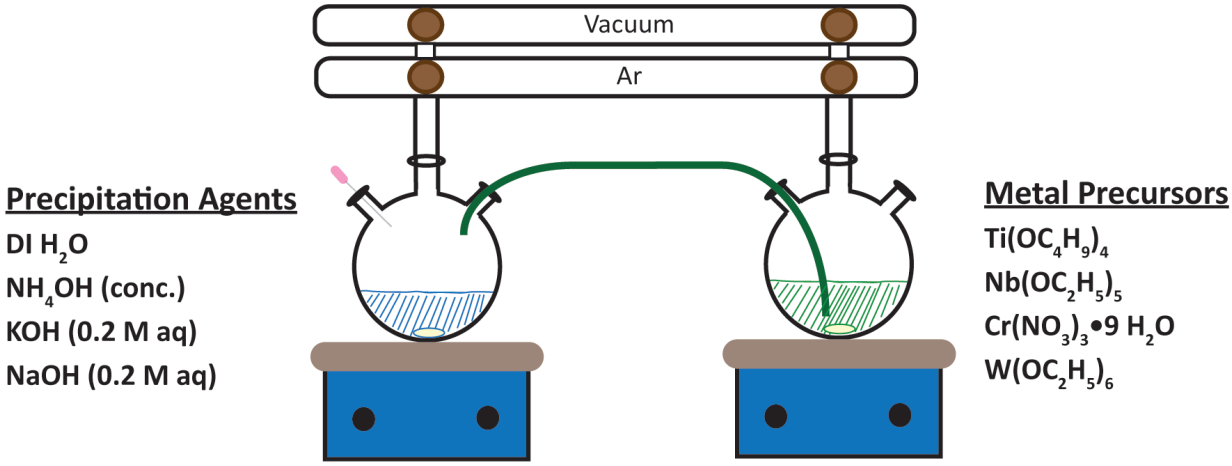

Figure 3.1 Schematic of co-precipitation experimental set-up. The green precursor solution on the right (for a Ti-Cr sample) is transferred to the precipitating solution on the left using cannulation (green tube). A needle is inserted though a septum in the receiving flask (precipitating solution, above) which reduces the pressure in the flask, allowing a higher pressure in the transfer flask (precursor solution, above) to push the solution through the tube. Cannulation enables the transfer of liquids without exposing them to air.

Immediately upon mixing, a white (Ti-W), off-white (Ti-Nb) or light green (Ti-Cr), fine suspension formed. When the liquid precursors were directly injected into the precipitating solution (without first dissolving in ethanol) several seconds passed before any precipitate was formed, indicating that there is some kinetic barrier associated with ligand dissociation from the metal. Furthermore, both the TBOT and $Nb(OEt)_5$ precipitated at different rates (TBOT took almost 30 seconds, while $Nb(OEt)_5$ took approximately 5 seconds). The solid precursors displayed similar behavior taking several seconds to dissolve, and then precipitate as metal

oxides. Therefore, in order to form a truly co-precipitated, homogeneous mixed-metal powder, the precursors must be dissolved and the concentration controlled such that the hydrolysis rate for both precursors is fast, and they hydrolyze essentially simultaneously.

The precipitated precursor was allowed to stir for 2 minutes during which time the fine suspension became somewhat more viscous (evidenced by the magnetic stirrer slowing down). The suspended powder and supernatant solution were exposed to air (by removing the septa from the 3-neck round bottom flask), poured into a petri dish (125 mL capacity), and dried for 12 hours at 120 ºC. The dried powder was then washed with deionized water, isolated by centrifugation at 2000 RPM for 5 minutes (the rinsate was decanted off), and re-dried at 120ºC for 12 hours. The washed and dried product was then calcined in a box furnace at 450 ºC for 6 hours in air in order to fully oxidize the powder and remove any residues (carbon species, nitrate species, etc.) left from the co-precipitation. The calcined product was a free-flowing, white (Ti-W), light tan (Ti-Nb), or light green (Ti-Cr) powder. Powder fractions that dried to the sides and bottom of the petri dish were scrapped off and retained as well.

A portion of the fully oxidized nanopowder was then nitrided using temperature programmed ammonolysis. In a typical process, the oxidized nanopowder was placed into an alumina boat, which was then placed into a 25 mm (outer diameter) silica tube. The silica tube was placed in a clamshell furnace, and fitted with compression caps that allow gas to flow through the tube, as well as to prevent the ingress of air. The tube was purged with flowing Ar for 5 minutes, and then anhydrous ammonia gas was introduced into the tube at a flow rate of 300 mL min^{-1}. The furnace temperature was then ramped from room temperature to 800 ºC at a rate of 100 ºC hr^{-1}, and held at 800ºC for 14 hours. The furnace was allowed to cool with ammonia continuing to flow over the sample until the furnace reached room temperature (this typically took 3-4 hours). Once cool, the tube was purged with Ar for 10 min, and a slight

positive pressure of Ar was isolated in the tube to keep out any air that might otherwise leak in. The tube was removed from the furnace, and pumped into an Ar filled glove box where the product (which had changed color to black in all cases) was removed from the silica tube and alumina boat, and was packaged in a septum-capped vial.

As discussed previously, the method by which a nitride material is exposed to oxygen significantly affects the chemical nature and morphology of the surface passivation layer. While other researchers have performed post-nitridation annealing in dilute oxygen, I chose to use slow diffusion of oxygen into the septum-capped sample vial to limit the partial pressure of oxygen the nitride product was exposed to. Typically the Ar-filled, septum-capped sample vial was brought out of the glove box and a small-bore needle (22 ga.) was pierced into the septum. Because Ar is heavier than air it tended to sit at the bottom of the vial over the sample, and several hours were required for air from the atmosphere to diffuse through the needle and equilibrate with the vial atmosphere. The needle-pierced vial was allowed to sit at ambient for 24 hours. The relative humidity of the air fluctuates from day to day. This aspect of the air – exposure was not controlled, but it is important to note that the water partial pressure in the passivating atmosphere is important to the final morphology and structure of the passivating layer. After passivation, the material was found to be "air-stable" by Powder X-ray Diffraction (pXRD) and sample color, and was fully characterized (SEM, conductivity measurements, electrochemistry, and thermogravimetric analysis).

3.5 Material Characterization

3.5.1 Composition and Morphology

Figure 3.2a shows powder X-ray diffraction (pXRD) patterns for the calcined, co-precipitated oxide nanopowders before (black curve) and after (red, blue, and green curves) ammonolysis. For each of the $Ti_{1-x}M_xN$ (M=Nb, W, or Cr) compounds, the pXRD pattern changes from the amorphous pattern of the nanopowder oxide to the pattern for the crystalline, NaCl structure. Only one phase can be identified in the pXRD pattern, indicating that solid solutions of TiN and MN were obtained. The peaks in each of the crystalline nitride patterns appear slightly shifted to higher angles, indicating a shrinking of the lattice parameter. Figure 3.2b-d shows Reitveld refinements[100] of the pXRD pattern, which were obtained using the GSAS software package. Table 3.1 summarizes the results of the GSAS refinements as well as Energy Dispersive X-ray Sepctroscopy (EDS) and Wavelength Dispersive X-Ray Spectroscopy (WDS) results for the elemental composition of each of the nitride compounds.

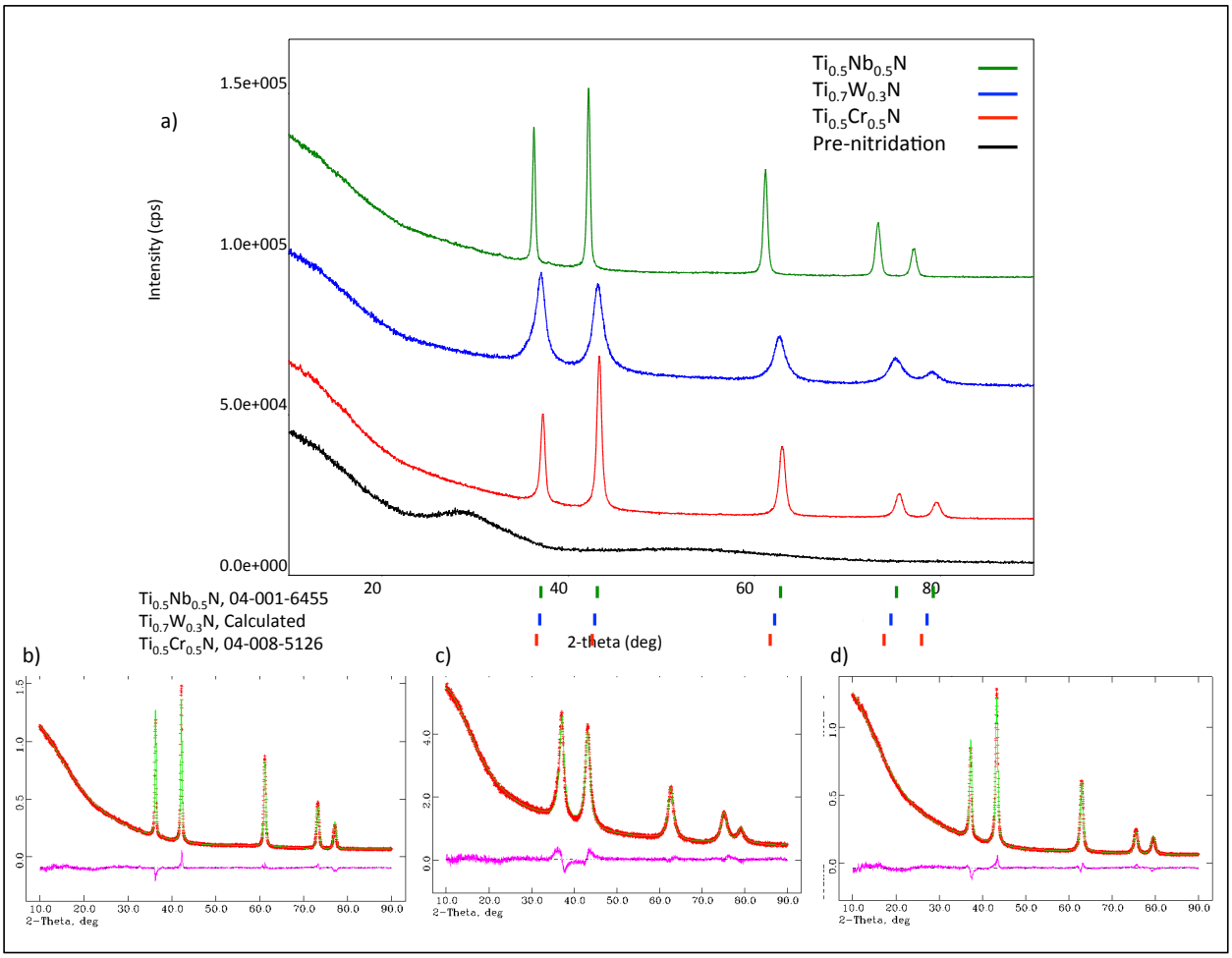

Figure 3.2 (a) pXRD patterns for the amorphous oxide precursor (black curve) and the crystalline nitride compounds (red, blue and green curves) for $Ti_{1-x}M_xN$ (M=Nb, W, and Cr). Each compound adopts the NaCl–type nitride structure. (b-c) Reitveld structural refinements with difference curves potted for for $Ti_{0.5}Nb_{0.5}N$ (b), $Ti_{0.7}W_{0.3}N$ (c), and $Ti_{0.5}Cr_{0.5}N$ (d). Refinements typically led to wRp values of approximately 5% indicating good fit convergence. Refined lattice parameters were a=4.283 Å (b, $Ti_{0.5}Nb_{0.5}N$, lit. a=4.341 Å), a=4.192Å (c, $Ti_{0.7}W_{0.3}N$, lit. a= 4.307 Å), and a =4.175Å (d, $Ti_{0.5}Cr_{0.5}N$, lit a=4.184 Å). Generally, the wider peaks correspond to smaller crystalline domain sizes, with refined domain sizes of 43.77nm (b, $Ti_{0.5}Nb_{0.5}N$), 6.67 nm (c, $Ti_{0.7}W_{0.3}N$), and 21.12 nm (d, $Ti_{0.5}Cr_{0.5}N$). NB: The peak position lines in (a) may be slightly misaligned due to formatting, and serve more as a guide for the eye.

Table 3.1 Summary of Reitveld Refinement of and EDS Measurements for $Ti_{1-x}M_xN$

Target compound	Structure type	Literature lattice paramter (Å)	Refined lattice parameter (Å)	Refined crytalline domain size (nm)	wRp %	Ti/M compostion by EDS (at.%)	Oxygen detected by WDS (mol %)	Oxygen by Combustion Analysis (mol %)
$Ti_{0.5}Nb_{0.5}N$	NaCl	4.341	4.283	43.77	5.55	49/51	22	23
$Ti_{0.7}W_{0.3}N$	NaCl	4.307	4.192	6.67	5.17	71/29	26	
$Ti_{0.5}Cr_{0.5}N$	NaCl	4.184	4.175	21.12	5.08	52/48	23	
TiN	NaCl	4.242						
NbN	NaCl	4.393						
WN	NaCl	4.460						
CrN	NaCl	4.148						

The refined lattice parameters for each of the mixed-metal nitride compounds are smaller than values reported in the literature[5] by 1% (Ti-W), 2% (Ti-Nb), and 0.3% (Ti-Cr). These values were approximately the same for nitride compounds prepared from the various precipitating solutions described earlier. Table 3.1 also shows WDS results, which indicate that a relatively large amount of oxygen is present in these compounds. The oxide ion is approximately 19% smaller than the nitride ion[101] (140 pm versus 171 pm, respectively) therefore a shrinking of the lattice parameter from the values reported for the pure nitride compounds is not surprising.

The fact that approximately 20 mol% oxygen was detected in these compounds is somewhat surprising. As discussed previously, the driving force for nitride formation by ammonolysis is the production of water. As water is removed from the system (by using high flow rates, and by starting with very dry ammonia) one would expect to drive the nitridation reaction and incorporate less oxygen. It is possible that because small domain size (6-20 nm) nitrides are being synthesized, a significant amount of the nitride at the surface is oxidized (upon exposure to air) to generate the protecting passivation layer. It is difficult, however, to conclude that the oxygen is limited to the surface layer since X-ray spectroscopies (such as WDS) typically probe approximately 1 μm^3 of the sample (thus several, whole nanoparticles are

analyzed simultaneously). Analysis techniques that are more surface-sensitive, such as X-ray Photoelectron Spectroscopy (XPS), would be required to draw firm conclusions as to the nature and location of the detected oxygen.

Additionally, the time and temperature of nitridation may affect the amount of oxygen remaining in the sample, although the parameters described above gave the best results in terms of surface area and single phase products (higher temperatures reduced surface areas and longer times didn't seem to have a significant effect on the amount of oxygen). While the exact cause of the residual oxygen is likely a combination of these issues, it is clear that each of these compounds is actually an oxynitride rather than pure nitride. Hence, a more exact chemical description is, for example, $Ti_{0.5}Nb_{0.5}N_{1-x}O_x\ \square_z$ (where $\square$=anion vacancy, and z is expected to be small). However, for convenience we shall continue to write $Ti_{0.5}Nb_{0.5}N$ for the products studied here.

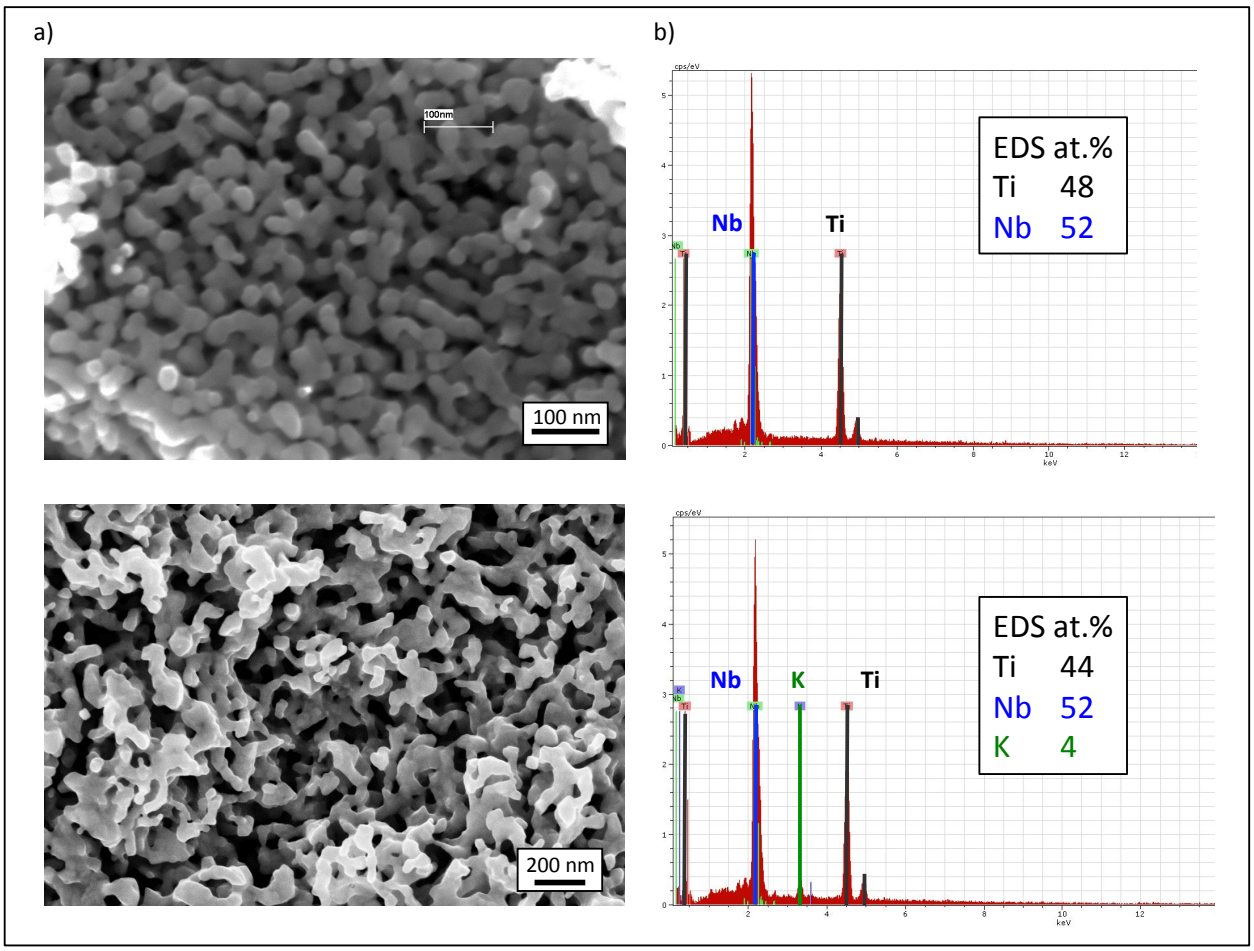

Figure 3.3 (a) SEM images of $Ti_{0.5}Nb_{0.5}N$ prepared from oxides co-precipitated in DI water (above) and 0.2M KOH (below). Note that the crystallinity and morphology are similar. $Ti_{0.5}Nb_{0.5}N$ produced form the water precipitated oxide has crystallites of approximately 25-30 nm in size , while crystallites of $Ti_{0.5}Nb_{0.5}N$ produced form the 0.2M KOH precipitated oxide are slightly bigger at approximately 50-70 nm. (b) Energy Dispersive X-ray Spectroscopy (EDS) of $Ti_{0.5}Nb_{0.5}N$ (above-from DI water, below-from 0.2M KOH). Note that despite washing the precipitated oxide, approximately 4% K is can still be detected by EDS. Samples of of $Ti_{0.5}Nb_{0.5}N$ prepared from oxides precipitated in 0.2 M NaOH are similar to those precipitated in 0.2M KOH, while 3-4 at.% Na was detected by EDS.

Figure 3.3 shows Scanning electron microscopy images (a) and Energy Dispersive X-Ray Spectra (b) for the $Ti_{0.5}Nb_{0.5}N$ compound prepared from oxides precipitated in DI water (above) and 0.2 M KOH (below). While the crystallinity and morphology are similar for both samples, the crystallite size for the sample prepared using DI water (25-30 nm) is slightly smaller than the sample prepared from 0.2 M KOH (50-70 nm). EDS shows that the Ti:Nb ratio is approximately

1:1 for both precipitating solutions; while for the 0.2 M KOH, approximately 4% K remains post-nitridation. This finding was surprising. The nanopowder oxide was washed prior to calcination, and it was believed that any residual species from the precipitating solution would be removed. While it is true that EDS results contain a certain amount of error (typically ± 5%), the K signal is out of the noise, clearly indicating that *some* K is present in the sample. Similar results were obtained for $Ti_{0.5}Nb_{0.5}N$ prepared from 0.2 M NaOH precipitated oxides, with typically 3-4% Na detected. Both K^+ (152 pm) and Na^+ (116 pm) are significantly larger than Ti^{3+} (81 pm) and Nb^{3+} (86 pm) meaning that K and Na are likely not included in the lattice of the nitride compound. Therefore the any residual Na or K would likely exist as some oxide either included in the surface passivation layer, or covering the outside of the sintered particles. Na_2O and K_2O (if they existed in the surface layer) would be converted to the hydroxide (and thus would be fully soluble upon washing) upon exposure to moisture in the air, therefore the residual K (or Na) in the sample likely exists as some K-M-O compound (M= Ti and/or Nb) that may be either crystalline or amorpohous; however, if the compound is crystalline, the fact that no peaks for a 2nd phase are visible in the pXRD indicates that the phase fraction is very low (< 1 %). It is more likely that the residual K exists as an amorphous K-M-O compound as part of the surface passivation layer. Additionally, the formation of K-Al-Ca oxides (although crystalline) in the surface passivation layer of iron nitride (FeN_x x=0 – 0.5) catalysts for the production of ammonia has been reported.[102]

In addition to the elemental composition (Figure 3.3b), Figure 3.3a shows that using the co-precipitation/ammonolysis synthesis produces highly sintered, random network morphology (I call it a funnel cake) with a pore size of approximately 30-50 nm. Nitrogen physisorption measurements showed that these materials have a BET[103] surface area of 30-60 $m^2\ g^{-1}$. The

measured surface area did not seem to vary with any specific experimental parameter, and was similar for each of the $Ti_{1-x}M_xN$ samples. The mesoporous network was sintered into larger powder grains of several microns in size, which may occlude some porosity, especially near the core of the powder grains. Higher surface areas may be achievable if smaller overall powder grains can be obtained either synthetically, or by mechanical means (grinding or ball-milling).

3.5.2 Conductivity

Measuring the conductivity of polycrystalline powders was discussed in Chapter 2. In that discussion, a variety of methods for measuring conductivity were introduced, as well as several measurement parameters that contribute to the *apparent* value of the measured conductivity. Specifically, the degree to which porous, polycrystalline powders are sintered and compacted can greatly affect the measured conductivity value, and additional resistance from interparticle contact can reduce the *effective* conductivity one can measure. Furthermore, the idea that insulating surface layers can also contribute to lower observed conductivities was also introduced. It is clear from the discussion presented in Chapter 2, that the method used to measure the conductivity can have a considerable affect on the measured value, and one must strive to measure the conductivity in a context that most closely resembles the operating conditions under which the material will be used. In this section the 4-point probe technique will be described and measured conductivities for the $Ti_{1-x}M_xN$ (M=Cr, Nb, W) will be presented.

A schematic of the modified four-point powder conductivity apparatus is shown in Figure 3.4. Much like the two-point probe discussed in Chapter 2, the device consists of a cylindrical, Teflon® sample holder with brass pistons fitted on each end. Additionally, two W-leads (a known distance apart) span a middle section of the sample holder and make contact with the

sample. Furthermore, in-order to more quantitatively apply pressure to the sample as it is measured, a guide rod and spring were added to one end of the device. The guide rod only functions as a guide for the spring, and is does not contribute to the electronic circuit. From the spring constant, the total compressed length of the spring, and the dimensions of the sample holder, the approximate pressure (minus any friction forces) applied to the sample during measurement can be calculated.

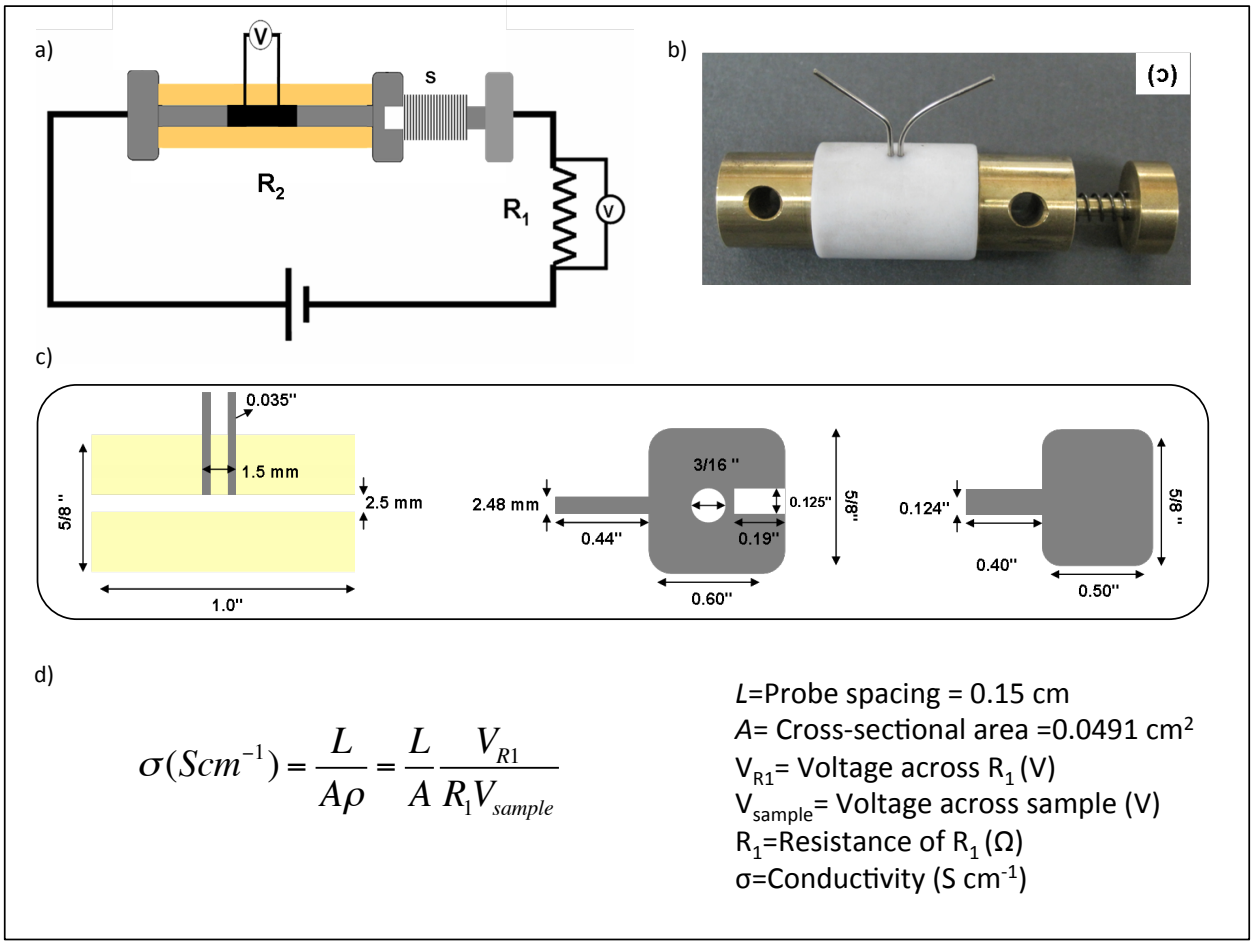

Figure 3.4 (a) Schematic for the 4-point probe device designed by Chin Subban and myself. The resistance of R_1 and R_2 (the sample) should be similar, and R_1 should be rated for high power to avoid changes in resistance due to heating. (b) picture of the assembled conductivity cell. The W-leads just touch the surface of the sample, and are not pressed into the "pellet" which forms under compression. (c) Dimensions of the conductivity cell. (d) Equation to calculate conductivity. Note that for this cell design L/A is ~ 3. Other designs for which L/A is significantly higher (≥100) may not uniformly compress the powder and can lead to spurious results. Schematics courtesy of Chin Subban

In a general measurement, a small quantity of sample (~100-200 mg) is introduced into the sample holder and the two bass pistons are inserted. The device is then inserted into the same modified vise used for the two-point measurements. As the vise is closed, the spring begins to compress. Once the spring is compressed to the appropriate length for the required applied pressure, current is passed through the sample from the two pistons. A variable power supply was used to supply the current, and the exact current was determined by measuring the voltage across a resistor (R_1, Figure 3.4) in series with the conductivity cell. Typically the resistance of R_1 should be close to the expected resistance of the sample. Also, resistors that are rated for high power should be used so to avoid temperature affects on the conductivity from resistive heating at high currents.

As current is passed, the voltage drop across the sample is measured. Since no current is being passed at the W-leads, the contact resistance from the pistons is not included in the measured sample resistance (as in the two-point measurement). The voltage drop across the sample is measured for several currents, and the average conductivity calculated as shown in Figure 3.4.

Through discussions with DiSalvo group member Chin Subban and collaborators at General Motors, it was determined that the internal pressure in a typical fuel cell is approximately 200 PSI. Therefore a spring with spring constant k=1.125 N/mm was selected and compressed from 0.625” to 0.260” to apply 200 PSI to the sample. A more complete discussion of spring selection and the four-point method can be found in Chapter 9 of Chin Subban’s PhD thesis.[104]

Table 3.2 summarizes the results of the conductivity measurements for $Ti_{1-x}M_xN$ (M=Cr, Nb, W) powders prepared by co-precipitation from several precipitating solutions.

Table 3.2 Summary of conductivity measurements for $Ti_{1-x}M_xN$ compounds

Compound	Precipitating solution	Washed	Conductivity at 200 PSI (S cm^{-1})
Vulcan XC-72			1.5
TiN	DI Water	N	27.4
NbN	DI Water	N	14.7
CrN*	DI Water	N	1.4
$Ti_{0.5}Nb_{0.5}N$[1]	DI Water	N	74.5
$Ti_{0.5}Nb_{0.5}N$[2]	DI Water	N	11.2
$Ti_{0.5}Nb_{0.5}N$	conc. NH_4OH	Y	16.4
$Ti_{0.5}Nb_{0.5}N$[1]	0.2M KOH	Y	3.9
$Ti_{0.5}Nb_{0.5}N$[2]	0.2 M KOH	Y	1.8×10^{-2}
$Ti_{0.5}Nb_{0.5}N$	0.02 M KOH	N	0.15
$Ti_{0.5}Nb_{0.5}N$	0.2 NaOH	N	1.3×10^{-2}
$Ti_{0.5}Cr_{0.5}N$	0.2 M KOH	Y	2.8
$Ti_{0.7}W_{0.3}N$	DI Water	N	0.55

* Approximately 15% phase fraction of Cr_2O_3 was also present by pXRD which reduced the measured conductivity

[1] Initial Measurement

[2] 2 years at ambient conditions

In analyzing the conductivity data, one immediately notices that the measured conductivities for many of the nitrides are higher than that of carbon black (Vulcan XC-72). While the value measured for carbon black (1.5 S cm-1) is in good agreement with the literature value[105] (2.1 S cm-1), several of the mixed-metal nitride conductivities are lower than one might expect. This is most likely due to the degree of sintering and level of porosity of these compounds. As was previously mentioned, interparticle contact can have a significant affect on the *apparent* conductivity that one can measure. 200 PSI is not a very high pressure and may not be sufficient to fully compact the nitride to negate effects from the porosity. This is not necessarily a bad thing, however, since these materials must be porous to function in an actual

fuel cell. It is important to note however that higher conductivities may be measured if these materials were pressed to higher pressures. This behavior was observed and documented for several oxide and nitride compounds by Chin Subban in Chapter 9 of her dissertation.[104] However, as 200 PSI was generally agreed upon as being the closest to PEMFC conditions, higher pressures were not investigated in this work.

An additional feature illustrated in Table 3.2 is that the way in which the nitride compounds were prepared had a significant effect on the conductivity. $Ti_{0.5}Nb_{0.5}N$ for example had conductivities that ranged from 74.5 S cm^{-1} when precipitated in DI water, to $1.3x10^{-2}$ S cm^{-1} when precipitated in 0.2 M NaOH and left unwashed. Two reasons for this large swing in conductivity are possible. One explanation may be that there is greater porosity in the sample precipitated in NaOH and the larger pore volume and greater inter-particle resistance reduced the effective conductivity. This is not likely, however, because there was not a significant difference in the BET surface area of these samples (45.6 m^2 g^{-1} versus 32.7 m^2 g^{-1} for the DI water precipitated sample and 0.2 M NaOH sample respectively), nor was there a significant difference in porosity or morphology as observed in SEM images (Figure 3.5).

The second explanation has to do with the oxide passivation layer. As was previously discussed, both Na and K can still be detected in the samples post-nitridation. Both of these ions are much larger than Ti or Nb ions in the nitride compound, therefore it's most likely that the K and Na species exist in the surface passivation layer as some amorphous oxide (since no 2nd phases were detected by pXRD it is most likely amorphous). The presence of Na or K likely makes that passivation layer more rich in O and can make it thicker, reducing the ability of electrons to tunnel through the oxide, thus lowering the effective conductivity of the compound.

This reasoning is also bolstered by looking at the oxygen content by combustion analysis, where 48 mol% oxygen was detected in samples that were precipitated in 0.2 M NaOH and not washed.

It is clear that the preparation technique can have a significant affect on the conductivity of the nitride compound. Despite the adverse affects that K and Na species have on conductivity, including these species in the synthesis may have beneficial affects in terms of oxidation stability. These affects will be discussed later. It is also clear from these results that mixed-metal nitride compounds can be prepared with conductivities significantly higher than current carbon-based supports, let alone the 0.1 S cm^{-1} that is required. The true test for these materials, however, must be when they are placed in an operating fuel cell, only then will their full potential and limitations be fully understood.

One disconcerting feature of Table 3.2 is that $Ti_{0.5}Nb_{0.5}N$ prepared from 0.2 M KOH shows a significant drop in conductivity after sitting at ambient conditions for two years. While the initial conductivity of 3.9 S cm^{-1} is quite good, the conductivity of this material dropped to $1.8x10^{-2}$ S cm^{-1}. This drop in conductivity is also observed for $Ti_{0.5}Nb_{0.5}N$ prepared from DI water which has an initial conductivity of 74.5 S cm^{-1} that drops to 11.2 S cm^{-1} after two years at ambient conditions The pXRD patterns for both of these compounds are not different from those shown in Figure 3.2, nor are their morphology or particle size significantly different from the images in Figure 3.3. This drop in conductivity is likely due to partial oxidation of the sample, or thickening of the oxide passivation layer to a level that significantly inhibits electron tunneling. While the exact cause of the loss of conductivity may be due to many factors, it is clear that the long term stability of these types of materials is be dependent on several factors including how they are prepared, how they are passivated, and the presence of any species in the passivation layer which may promote oxidation over long time scales (years).

3.5.3 Oxidative Stability

The chemical stability (or durability, corrosion resistance, or thermal oxidation rate) of a material can be defined and measured in a variety of ways. Often the stability is quoted in reference to some condition or set of parameters of the determination (e.g. stable in 0.1 M perchloric acid for 3 weeks at 80 ºC). As with conductivity, the context of determining chemical stability should, as closely as possible, mimic the operating environment the material must endure to ensure that a useful measure of a material's stability is obtained. Determining the appropriate parameters or method is not always intuitive, and full scale fuel cell testing is not always available. Thus alternative tests have been developed and implemented to serve as semi-quantitative, relative measures for material stability. In the DiSalvo lab, a standard chemical stability test involves soaking a perspective material in an acidic or basic solution 80ºC for some time (typically 3 weeks or more). The selection and concentration of the stability test liquid is key. For example it is well known that Ti in the presence of a high concentration of sulfate ions will form soluble titanyl sulfate.[106,107] Therefore the stability of Ti containing compounds in concentrated sulfuric acid is not as high as in perchloric acid or in solution of Nafion (sulfonated polymer). A thorough discussion of stability tests of several Ti-M oxides and nitrides can be found in Chapter 6 of Chin Subban's dissertation.[104] Because others in the lab were conducting chemical stability tests of this type on similar compounds, Ti-M nitrides prepared by the co-precipitation technique were generally not tested using this method, and complimentary techniques (such as TGA studies, discussed next) were explored instead. Those few samples that were tested by this method will be discussed with the results of electrochemical measurements in the section 3.6 of this chapter.

In addition to soaking a material in an acid or basic solution, one can measure the oxidative stability by monitoring changes in weight, for example by using a thermogravimetic analyzer (TGA). Such techniques have been used to investigate oxidation mechanisms for nitride thin-films. For example, one study suggests that NbN thin-films are stable upon heating up to ~200ºC, and that the mechanism of oxidation is grain boundary diffusion of O into the nitride lattice.[108] Furthermore, TGA studies have been used to find that the oxidation of NbN thin-films follows a linear rate law ($[-\ln(1-\alpha)]^{1/3} = kt$, where k is the rate constant (s^{-1}), t is the time (s), and α is the mol fraction of the nitride unreacted) at low temperatures (200-500 ºC).[109]

One can see that the formula weight of a nitride and its corresponding oxide are different (for example 125.45 g mol^{-1} for 7:3 TiO_2:WO_3 versus 102.66 g mol^{-1} for $Ti_{0.7}W_{0.3}N$). Therefore if one can measure small changes in weight as a function of environment, one can more quantitatively analyze a material's stability. Furthermore, if a TGA measurement using air or oxygen is performed, one can measure the "onset temperature" of oxidation, with a higher onset temperature indicating a more stable nitride. The onset temperature is roughly defined as the point at which the sample mass increases by ~0.5%. That point is dependent upon the heating rate, and generally increases as the rate increases.

Figure 3.5 shows the results of TGA measurements performed in air for $Ti_{0.5}Nb_{0.5}N$ prepared from several precipitating solutions. Figure 3.5a shows that for an ideal sample one would expect a 26% increase in sample weight upon oxidizing a fully nitrided $Ti_{0.5}Nb_{0.5}N$ to a 50:50 mixture of fully oxidized TiO_2:Nb_2O_5. Typically weight increases of approximately 21% are observed. This is not surprising, as it has been already noted that some oxygen exists in the sample. For $Ti_{0.5}Nb_{0.5}N$ approximately 22 mol% oxygen was detected by WDS, which

corresponds to 4 wt% oxygen. Therefore a weight increase of 21 wt% agrees well with the WDS result of 4 wt% oxygen already in the sample.

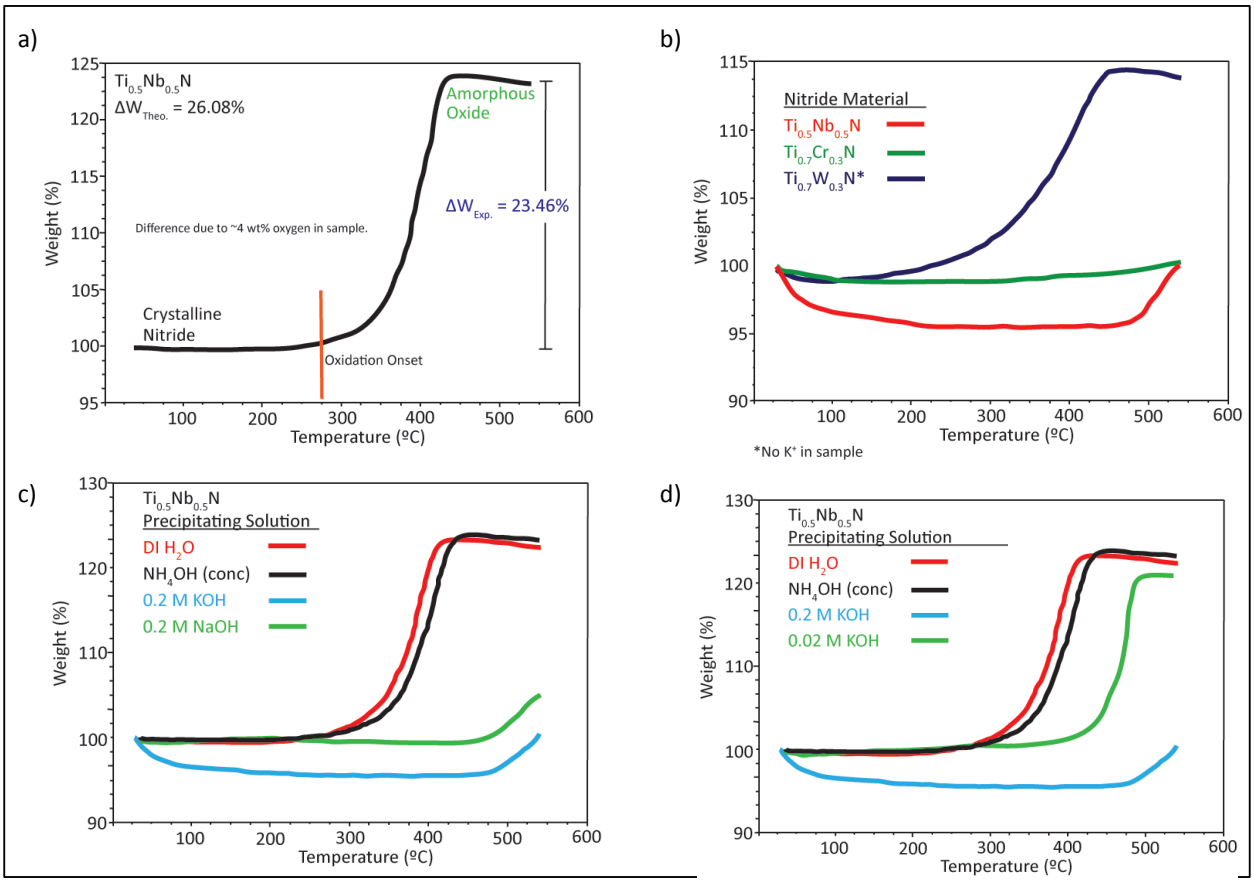

Figure 3.5 (a)TGA of typical oxidation experiment. The sample is heated in flowing air (90 mL/min) from room temperature to 550ºC at a rate of 5ºC min^{-1}. As the sample is heated, it begins to react with oxygen in the flowing air and gain weight. Nitrogen from the nitride is lost as N_2 and swept away. The onset of oxidation is taken as approximately 275-300ºC for the sample shown in a. (b) TGA data for several $Ti_{1-x}M_xN$ (M=Cr, Nb, W) compounds. Here both the Ti-Nb and and Ti-Cr samples were precipitated in 0.2M KOH while the Ti-W sample was precipitated in DI water. For the Ti-W sample it is interesting to note that the slope of the weight increase is more shallow than for Ti-Nb samples, this may indicate that the kinetics of oxidation are different for compounds which contain different metals. (c)TGA plots for $Ti_{0.5}Nb_{0.5}N$ as a function of precipitating solution. Precipitating in 0.2 M KOH or NaOH has a significant affect on the oxidation stability of the nitride, extending the oxidation onset by approximately 200ºC. (d) TGA plots for $Ti_{0.5}Nb_{0.5}N$ as a function of precipitating solution concentration. The green curve is for a sample precipitated in 0.02M KOH, which shows intermediate performance for a sample precipitated with no K and one precipitated with 0.2M KOH.

Figure 3.5b showed TGA results for several Ti-M nitride compounds. Both Ti-Cr and Ti-Nb samples were precipitated in 0.2 M KOH while the Ti-W sample was precipitated in DI water. Despite the obvious differences in oxidation onset, an interesting feature is the slope of the Ti-W oxidation curve. This curve appears much more shallow than the curve in Figure 3.5a. This indicates that the kinetics of oxidation for Ti-M compounds are different. Additionally, upon oxidation one would expect a 22% increase in weight (125.45 g mol^{-1} for 7:3 TiO_2:WO_3 versus 102.66 g mol^{-1} for $Ti_{0.7}W_{0.3}N$). Since only an increase of ~13% is observed for $Ti_{0.7}W_{0.3}N$ there is likely already ~8-9 wt% (49 mol%) oxygen in the sample. This increased oxygen content likely implicates a thicker passivation layer, which contributes to the potentially slower oxidation kinetics of the Ti-W samples.

Figure 3.5c showed TGA data for Ti-Nb nitride for various precipitating solutions. The most striking feature of this data is that preparing samples in 0.2 M KOH or NaOH has a significant effect on the onset of oxidation, shifting it to higher temperatures by almost 200ºC. This finding is quite interesting and has not been reported for these compounds before. As stated previously, K and Na ions are significantly larger in size than Ti or Nb, and hence would not fit into the NaCl type lattice that the nitride compound assumes. It is more likely that K and Na participate as part of amorphous oxide species in the surface passivation layer.

Figure 3.5d showed the effects of different K concentrations on the oxidation behavior. Ti-Nb nitride precipitated in 0.02 M KOH shows intermediate performance between samples precipitated with no K and with 0.2 M KOH. It is clear from these results that K indeed is primarily responsible for the enhanced oxidation resistance observed for these samples. Furthermore, it is clear that careful control of the amount of residual K can give one an additional synthetic knob to tune the properties of nitride supports.

3.5.4 Passivation Layer Characterization

It is important to note, however, that despite the increased oxidation resistance, samples precipitated in KOH or NaOH showed much lower conductivities (up to 4 orders of magnitude) than samples precipitated in DI water or ammonium hydroxide. This is likely due to thicker, more oxidized surface layers, which inhibit electron transport from the conducting nitride at the core of the sintered, mesoporous network. In order to characterize the surface layers, High Resolution Transmission Electron Microscopy (HRTEM) images and Electron Energy Loss Spectroscopy (EELS) measurements were made on samples precipitated with and without residual K. Figure 3.6 shows data obtained by Julia Mundy and Houlin Xin of the Muller Group at Cornell University, a collaboration fostered through the Energy Materials Center at Cornell (EMC^2).

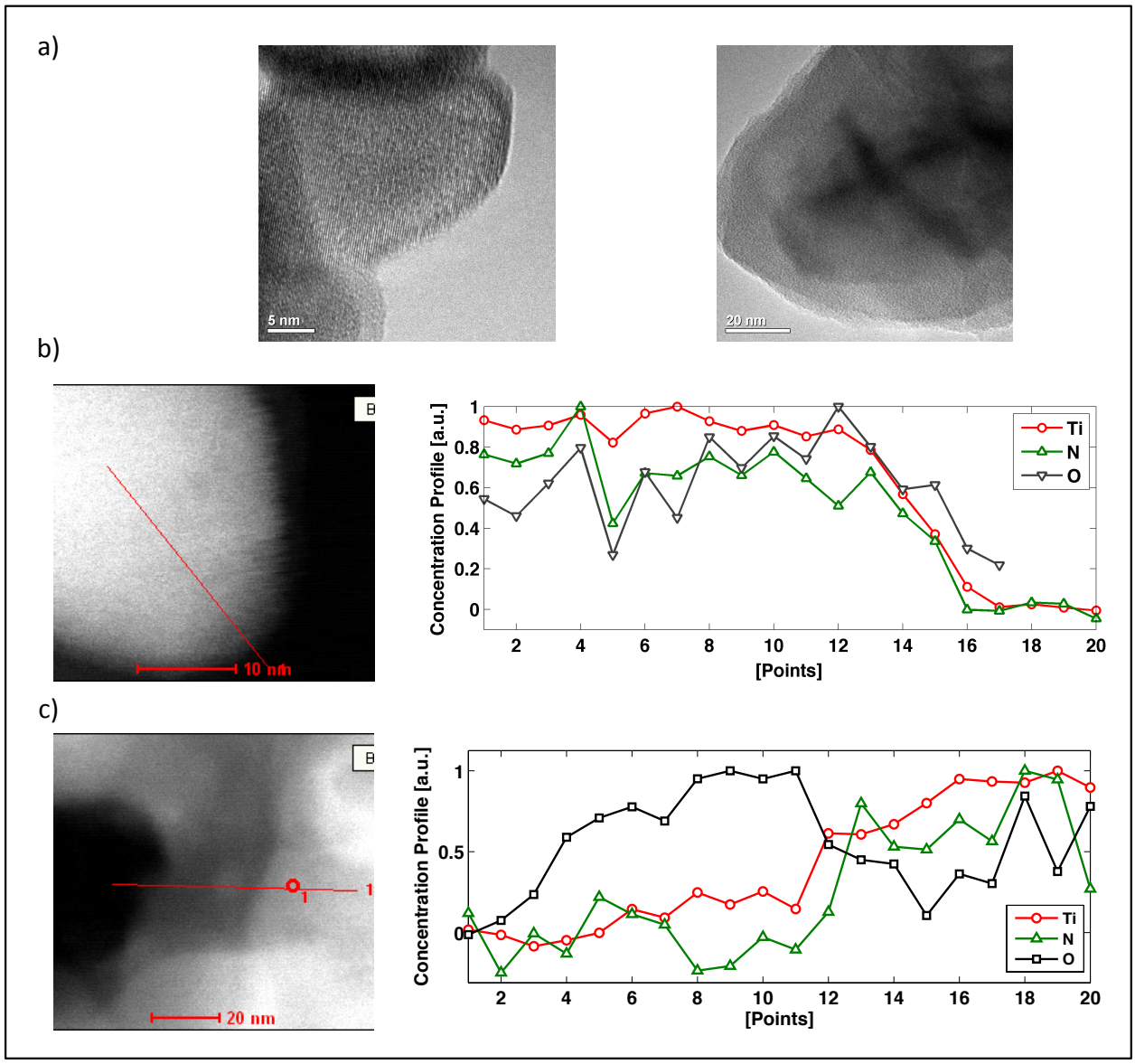

Figure 3.6 (a) HRTEM images of Ti-Nb nitride. Note that both amorphous and crystalline features can be seen. (b) EELS line scan for Ti-Nb nitride precipitated from DI water. Note that there is a small region (~1 nm) near the surface of the particle with a higher O content than N (point 12 on the line scan). Also note that O is detected throughout, further indicating that these are oxynitrides and that O is not purely detected on the surface. (c) EELS line scan for Ti-Nb nitride precipitate from 0.2M KOH. Note that there is a significantly larger region at the surface where predominantly O is present. Note also that each of these EELS scans suffered from carbon contamination for the instrument during analysis, this artifact (contamination followed be renormalization of the signal) caused the N to have a negative concentration at some points. It is clear from this data that qualitatively, the potassium in the samples leads to a thicker oxide layer. N.B. K was not quantified due to the carbon contamination as their EELS edges correspond.

Figure 3.6a showed HRTEM images of $Ti_{0.5}Nb_{0.5}N$. Both amorphous and crystalline regions are visible, and there does appear to be some contrast changes near the edges of the sintered particles, which suggest a surface layer. While contrast in bright-field TEM can be due to a number of factors (including atomic number and thickness), the fact that the contrast follows the contours of the particle are interesting. Furthermore, edges tend to be darker in TEM due to thickness effects, so the fact that these edges are lighter may be indicative that the layers are less dense and amorphous as opposed to crystalline.

Figure 3.6b and c showed EELS line-scans for $Ti_{0.5}Nb_{0.5}N$ precipitated in DI water (b) and 0.2 M KOH (c). In image b, there is a thin (~1 nm) region near the surface (at point 12 in the line scan) that has a higher O content than throughout the rest of the sample. The fact that the O signal follows the N signal closely, except at this point, is evidence of the surface passivation layer, which is richer in O. In c, the O signal is much higher, and there is a significantly higher surface region richer in O. Potassium was also detected in this sample, however quantification was not possible due to carbon contamination from the TEM grid (K and C EELS edges overlap and make quantification very difficult). It is important to note, also that the EELS scans represent relative concentrations, and are not quantitatively accurate. Despite the lack of quantitative accuracy, it is clear from a qualitative perspective that incorporating K or Na into the synthesis of the nitride compounds leads to a thicker passivation layer. Furthermore, samples with K and Na seem to incorporate more O throughout, leading to lower overall conductivities but higher oxidation resistance.

It is clear from these results that there are several synthetic parameters that enable the properties of mesoporous nitrides to be tuned. Some of these parameters seem to affect particle size and morphology (precipitating solution pH, precursor choice, mixing speed), while others

more greatly affect the end-product properties (precipitating solution, nitridation conditions). Despite the synthetic variability, it is clear that mesoporous mixed-metal nitrides can be prepared by the co-precipitation method, and their properties meet the minimum criteria for potential replacements for carbon-based catalyst supports: they are mesoporous, oxidation resistant, and have sufficient conductivities.

3.6 Electrochemical Characterization

The electrochemical stability of $Ti_{1-x}M_xN$ (M=Nb, W) nanopowders was examined under pH and applied potential conditions similar to those found in a PEMFC using standard electrochemical techniques (i.e. cyclic voltammetry (CV) and Rotating Disk Electrode (RDE) experiments). Generally, these experimental techniques involve a Teflon wrapped, 5 mm glassy carbon disk (GC) electrode which is mounted onto a stainless steel arbor and held stationary (CV) or rotated by an electric motor (RDE). In order to apply the nitride nanopowder to the electrode, a suspension (or ink) of the nanopowder was prepared by mixing the nanopowder and a suitable binder in an appropriate solvent. The concentration of the suspension is also important for accurate loading of the active material onto the glassy carbon electrode. An typical ink recipe is as follows: 10 mg nitride nanopowder, 3.98 mL DI water, 1 mL isopropyl alcohol, and 20 µL of Nafion ® solution (5 wt% in aliphatic alcohol/water). Typically, the ink ingredients are added to a glass vial and mixed using a sonicating water bath (or an ultrasonicating wand) for 30 minutes. Once mixed, 20µL of ink suspension is drop cast onto a cleaned and polished GC electrode (for a loading of 200 µg nitride/ cm^2_{geo}).

This standard ink recipe is derived from typical ink preparations for Pt/C catalysts.[110-112] It is important to note, however, that these "standard" ink recipes are not necessarily appropriate for all materials, and oxide/nitride materials often require modifications to form stable suspensions, and to adequately apply them to the GC electrode. One such modification, is to add 20 wt% Vulcan XC-72 to the suspension. Often the added carbon aides in binding the larger, sintered oxide/nitride particles to the glassy carbon disk as well as facilitating greater electrical contact to the GC disk. An additional approach developed in the DiSalvo lab has been to use Au disk electrodes and Au foil rather than GC. Au is a soft metal, and oxide or nitride nanopowders can be mechanically pressed into the surface, which eliminates the need for adding carbon or other binders to aid with conductivity. The results of these experiments are discussed more fully in Chapter 9 of Chin Subban's PhD dissertation.

Ultimately, the take home message is that "standard" techniques do not always apply when new materials are introduced for a specific application. Oxides and nitrides are harder and denser than carbon blacks, therefore typical techniques which rely on these physical features (such as forming homogenous ink suspensions, and accurately loading catalysts) do not always directly apply, and modifications for sample preparation and analysis often must be developed along with the new materials.

3.6.1 Electrochemical Stability

To investigate the electrochemical stability of the Ti-M nitride supports chemical stability and cyclic voltammetry experiments were preformed. Typical chemical stability tests use concentrated test liquids (often 3M acid or base). While such solutions do enable the accelerated aging of materials, it is not clear that such aging adequately mimics long-term operation in a fuel

cell. It's possible that 3M acid solutions are much too strong, and overestimate the conditions that a material must endure while operating in a fuel cell. The role of the anion in corrosion is also important. There are no free anions in a fuel cell – only anions that are bound to the polymer membrane. In the electrochemical tests, anions such as SO_4^{2-} and ClO_4^- are present. The former is well known to accelerate the dissolution of TiO_2 to form $TiO(SO_4)$.[107] For this reason, tests in acid solutions are very likely to be more aggressive than the fuel cell environment. Chemical stability tests using 3M test solutions have been conducted for a variety of oxide and nitride compounds and are discussed elsewhere.[104]

Figure 3.7 shows pXRD patterns of $Ti_{0.5}Nb_{0.5}N$ before, and after soaking in 0.1 M KOH at 80ºC for 1 month. There is virtually no observable change in the pXRD pattern before and after the stability test. Furthermore, materials co-precipitated in DI water and 0.2 M KOH showed identical behavior. It is possible that small amounts of K-Nb-O ternary oxides are present in the original and stability tested sample (as discussed previously) given that there is a small peak at 28.5º, however such identification is difficult to make from only one peak. However, if some K-M-O phase is present and crystalline, it represents a relatively minor phase fraction (< 1 % based on the intensity of the peaks), or is amorphous (and thus invisible by pXRD).

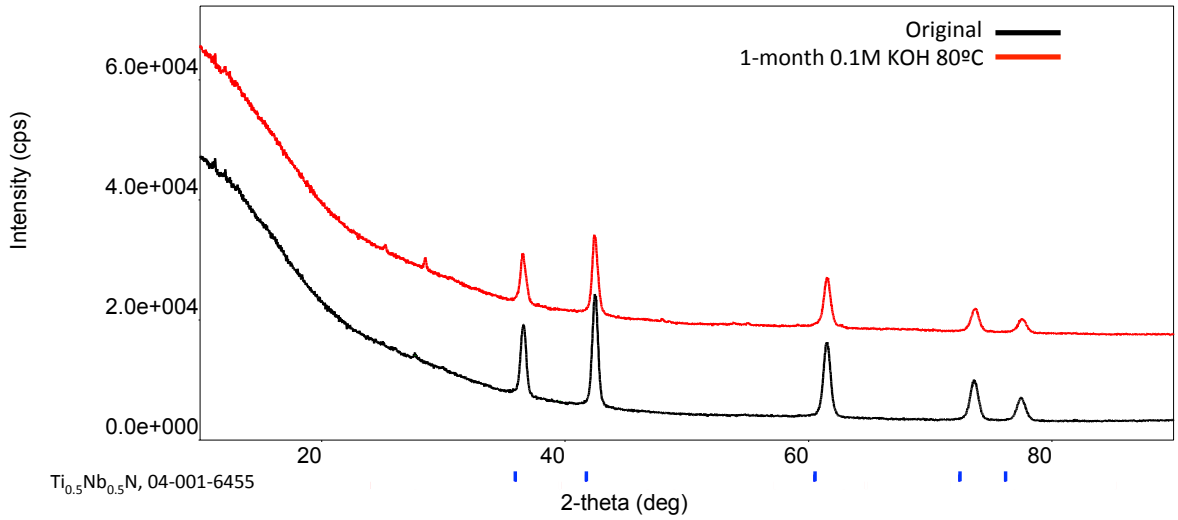

Figure 3.7 pXRD pattern of $Ti_{0.5}Nb_{0.5}N$ before (black) and after (red) a chemical stability test. The chemical stability test consisted of soaking the material in 0.1M KOH at 80ºC for 1-month. Samples precipitated in DI water and in 0.2M KOH showed identical chemical stabiity for 0.1M KOH.

Figure 3.8 shows cyclic voltammetry of $Ti_{0.5}Nb_{0.5}N$ (without any platinum) precipitated from DI water (a) and 0.2 M KOH (b). In a standard measurement, the material is prepared as a suspended "ink", as previously described, and drop cast onto a 5mm GC electrode. The prepared electrode is then placed in a 3-chamber electrochemical cell filled with 0.1 M H_2SO_4. A NaCl saturated Ag/AgCl reference electrode and carbon counter electrode are added to the working electrode to complete the standard 3-electrode cell. The acid electrolyte is then degassed, and saturated with Ar, H_2, or O_2 prior to potential cycling from -1 V to +1.2 V versus SHE with electrode rotation at 2000 RPM.

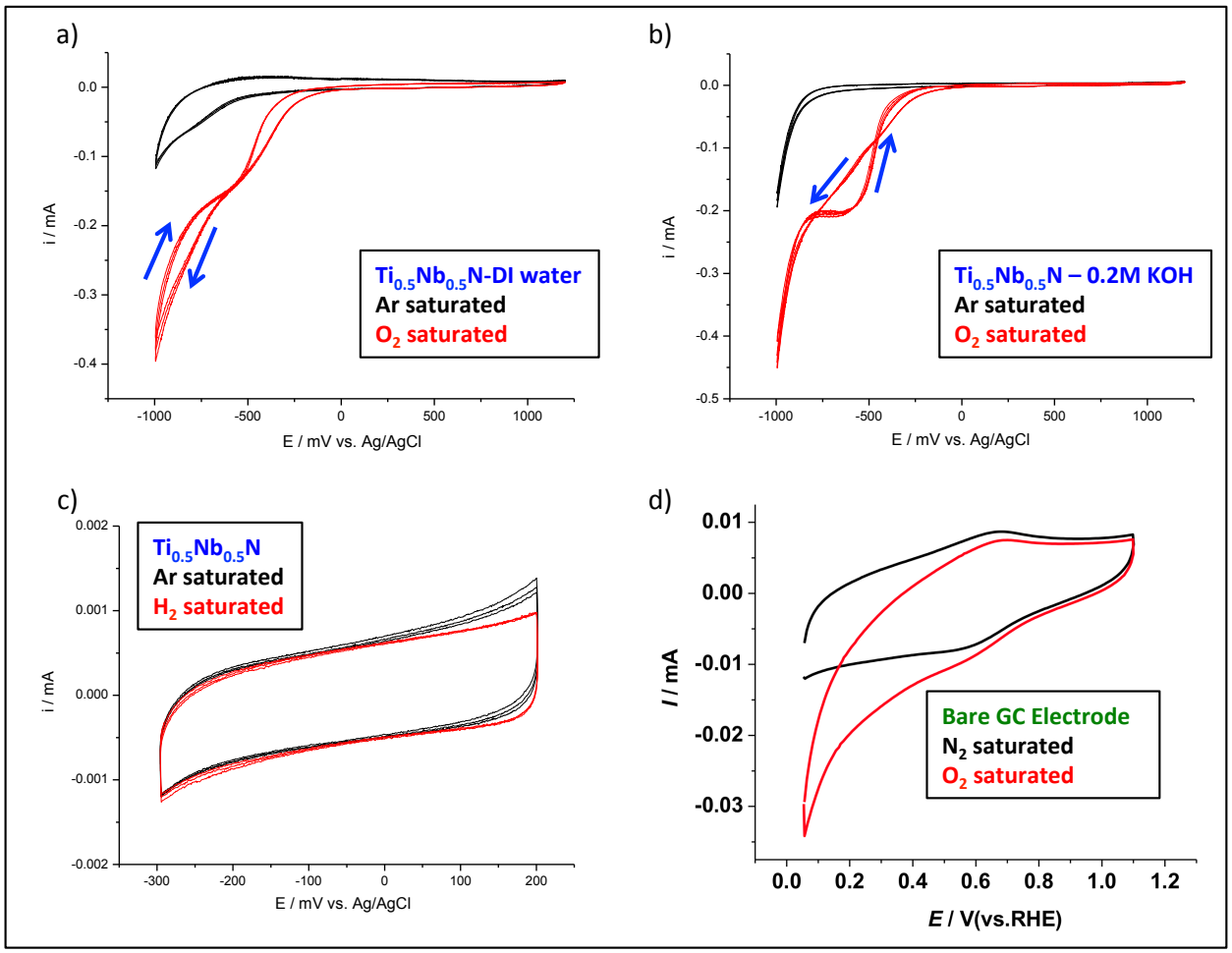

Figure 3.8 (a) Ar and O_2 saturated CV of $Ti_{0.5}Nb_{0.5}N$ precipitated from DI water. Note the ORR wave near -500mV and the HOR wave at -1000 mV. (b) Ar and O_2 saturated CV of $Ti_{0.5}Nb_{0.5}N$ precipitated from 0.2M KOH. Note that the wave at -500 mV is different than in (a). This is likely due to some surface process arising from K residue from the precipiation. There are no other differences between these samples. (c)) Ar and H_2 saturated CV of $Ti_{0.5}Nb_{0.5}N$ precipitated from DI water. This CV covers a smaller potential window, but gives detail in the double layer region. Note that there are no observable redox waves. (d) CV in N_2 (black) and O_2 (red) saturated electrolyte of the bare GC electrode. Each of these scans were taken at sweep rates of 10 mV s^{-1}

Figure 3.8a and b showed CVs for Ti-Nb nitride precipitated in DI water(a) and 0.2 M KOH(b) obtained in 0.1 M H_2SO_4 at room temperature by Dr. Qin Zhou. Both the temperature and acid concentration are lower than traditional chemical stability tests, and since a typical electrochemical experiment takes only a few hours, no evidence of corrosion or oxidation of the nitride material was observed. In the potential region from 0-1.5 V versus RHE, no redox waves

appear which suggests a stable surface. Admittedly, however, the reduction process between -300 mV and -1000 mV dwarfs any small processes that may be occurring in this potential region. Figure 3.8c, shows a CV over a smaller potential window to look at any double layer features. Both the Ar and H_2 saturated scans overlap indicating no significant changes, and no activity for the nitride support for Hydrogen Oxidation (such activity was not expected, but would have been a nice surprise). The lack of any waves is indicative that the material is stable (or possible not electrically connected to the electrode, however observing behavior below -300 mV suggests otherwise).

Figure 3.8d shows a CV for the bare GC electrode in both N_2 and O_2 saturated electrolyte. The most prominent feature is the redox wave at ~600 mV due to quinone moieties on the surface of the GC. Additionally, the GC itself shows activity for ORR below 400 mV. It is important to note that any observed ORR would be a combination of the activity from the material under study, and the GC electrode. An additional observation is the double layer current for the bare GC electrode (GCE). The double layer current for the bare GCE is about 5 μA, while figure 3.8c shows the double layer current for the nitride is ~0.5μA. One would expect that as higher surface area material is added to the GC (such as the drop-cast nitride), the observed double layer current would increase proportionally with the surface area. However, the opposite is observed in this case. In this case different GCEs for both the nitride ink and bare CVs were used, therefore it is difficult to draw firm conclusions from a direct comparison; however, the drop in double layer current is indicative that there are issues in applying the drop cast ink to the GCE. The Nafion binder (as well as nitride particle size) in the ink may be inhibiting full electrical contact of the support material to the GCE. Furthermore, an identical set of experiments performed by Dr. Zhiming Cui showed CVs (not shown) that had identical

double layer currents for the nitride and the bare GCE. It is clear that sample preparation of nitride supports for electrochemical testing represents and on-going challenge in the characterization of these materials.

Figure 3.8 a and b showed low-level oxygen reduction onset at approximately -300 mV. This is far too high an overpotential for these nitride materials to be of interest for applications as electrocatalysts rather than as supports. What's more interesting is that the ORR wave is different for $Ti_{0.5}Nb_{0.5}N$ precipitated in DI water and 0.2 M KOH. The positive-going sweep produces a higher current for the reduction process (crossing over the negative-going sweep). As the only difference between the two samples is the precipitating solution, this change in the CV must be due to the K residue left behind from the co-precipitation. It has already been noted that the K exists on the surface as part of the amorphous passivation layer. As the current does not change upon cycling, it does not appear that the redox wave is due to the oxidation and dissolution of ions, but rather is a reversible redox couple of a surface bound species. K has a standard reduction potential of -2.925 V which means that the wave is not due to potassium it self. Ti(III) reduction to Ti (II) has a standard reduction potential of -0.37V, which is much closer. However if the wave was due solely to a Ti redox couple, why is it only observed for the sample precipitated from 0.2 M KOH? The exact nature of this redox wave is unknown, however it lies at a significantly negative potential that would not be present in a fuel cell, therefore it is of limited concern.

These data confirm at least short-term (meta) stability of $Ti_{0.5}Nb_{0.5}N$ in the potential range of fuel cell operation. Complications from past experiments have led many in the DiSalvo group to wonder if the material is actually electrically connected to the GC electrode since the behavior resembles that of bare GC. This points out a challenge: if the material was totally inert

over the potential range examined, one would expect to see just the characteristics of the GC electrode. It is important then to verify that the observed behavior is intrinsic to the nitride material and not due to experimental artifacts such as poor electrical contact. As different features are seen for samples prepared from different precipitating solutions, it is clear that at least *some* of the nitride is electrically connected. Additionally, the currents observed in Figures 3.8 a and b for ORR on the nitride support are significantly higher than for just bare GC, indicating again that at least *some* of the nitride is in electrical contact with the GC. Furthermore, adding carbon black to the ink suspension does aid in enhancing the electrical contact of the nitride to GC. This will be demonstrated when discussing the platinized samples in section 3.6.3.

Figure 3.9 shows electrochemical data obtained by Dr. Deli Wang for $Ti_{0.7}W_{0.3}N$ prepared by co-precipitation in DI water. Each of the CVs was obtained in 0.5 M H_2SO_4 at a sweep rate of 50 mV s^{-1}.

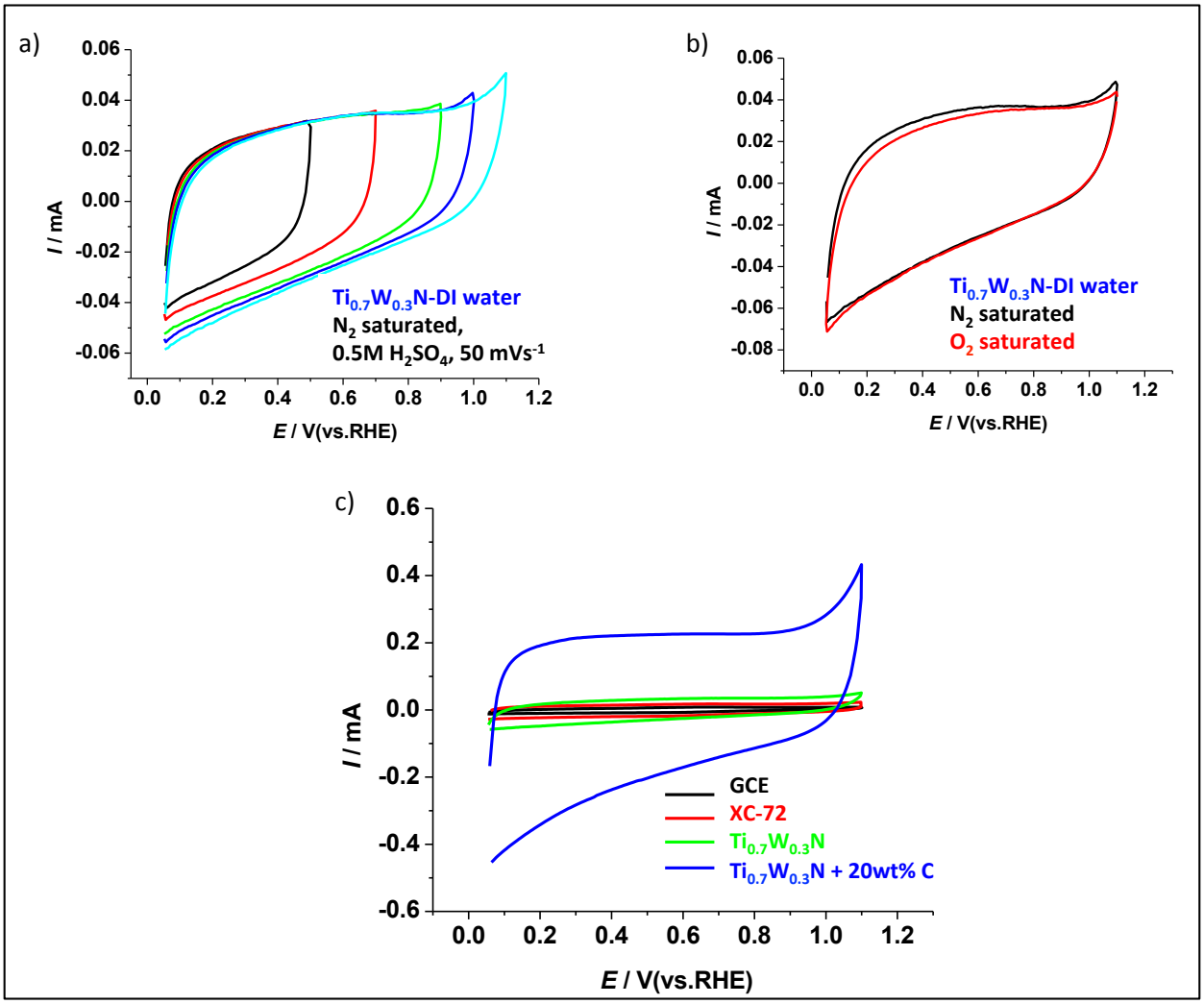

Figure 3.9 (a) Window opening CV of $Ti_{0.7}W_{0.3}N$ co-precipitated in DI water. The high double layer current is due to the 50 mV s^{-1} sweep rate. (b) ORR activity for $Ti_{0.7}W_{0.3}N$. Note that the material shows no activity for ORR in the potential region for fuel cell operation. (c) Comparison $Ti_{0.7}W_{0.3}N$ (green) to GC (black), Vulcan XC-72 (red), and$Ti_{0.7}W_{0.3}N$ with 20wt% Carbon black added (blue). Note that significantly higher double layer current is achieved when adding 20 wt% C. This is likely due to increasing the electrical contact of the nitride to the GC electrode. No other electrochemical processes are observed indicating the material is (meta) stable in the potential region of fuel cell operation.

Figure 3.9a showed window opening CVs of $Ti_{0.7}W_{0.3}N$ from 0 to 1.2 V versus SHE. It is important to note that the large double layer current arises somewhat from the fast sweep rate and somewhat due to the larger, surface area-dependent double layer capacitance of the material. Generally, however, the material appears stable over the potential window. Figure 3.9b shows CVs of $Ti_{0.7}W_{0.3}N$ in N_2 (black) and O_2 (red) saturated electrolyte. There is no apparent activity for ORR between 0 to 1.2 V, although it is possible that the nitride is not fully connected to the electrode. This idea is bolstered somewhat by the fact that the N_2 and O_2 curves in Figure 3.9b virtually overlap. Figure 3.9c further bolsters this observation. Figure 3.9c shows a comparison of GC (black), Vulcan XC-72 (red), $Ti_{0.7}W_{0.3}N$ (green), and $Ti_{0.7}W_{0.3}N$ with 20 wt% C added to the ink (blue). The blue curve shows a significantly higher double layer current that any of the other samples (although the surface area of the added carbon black also contributes to this higher double layer current). This indicates that adding C to the nitride inks is likely necessary to ensure electrical contact of the material to the GC electrode. Additionally, there does appear to be a reduction current (of unknown origin) in the blue curve of Figure 3.9c below 500 mV. On a positive note, no oxidation behavior is observed, which indicates that $Ti_{0.7}W_{0.3}N$ is stable over the potential region 0 to 1.2 V versus SHE.

It is clear that testing oxide and nitride support materials is not necessarily straightforward. While some of these results bare further confirmation, the nitride materials do appear stable under simulated fuel cell conditions. It is unclear however how nitride materials will fare during transient load and on/off fuel cell operations when the potential can be driven quite positive, or under fuel starvation conditions when no other species are present to sustain the imposed current demand. Future testing of the nitride material stability should include testing in

an actual fuel cell as well as continued development of electrochemical methods and sample preparation techniques.

3.6.2 Platinization of Ti-M Nitrides (M=Nb, W)

As previously discussed, Pt and Pt-based catalysts supported on carbon are the currently used catalysts for both the anode and cathode in PEMFCs. As Pt is very expensive, several studies have been performed on optimizing Pt utilization to enable lower amounts of catalyst to be used.[113-119] These studies focus on altering the size, shape, and disperisty of Pt in an effort to maximize the electrochemically active surface area (ECSA). From these studies, several methods have been developed for depositing Pt and Pt-based nanoparticles on catalyst supports.[120,121] Often these methods focus on the platinization of carbon supports, however reports of platinizing non-conducting oxides and other ceramic supports for high temperature applications are also available.[122,123] Additionally, a method developed in the DiSalvo group traps Pt-M nanoparticles in a salt matrix during the synthesis. The salt matrix serves to control the size and dispersal of the nanoparticles which are then transferred from the salt onto a carbon support.[124] From the variety of techniques reported in the literature, it is clear that the method by which one deposits a catalyst onto a support can have a significant impact on the performance of that material.

An additional consideration is that typical Pt loadings do not directly translate from carbon to ceramic supports. Typically Pt (or any catalyst) loading is quoted as weight percent and is determined relative to the weight of the catalyst. Loading the same weight percent of catalyst on two supports that have different densities and pore morphologies typically results in different amounts of active Pt surface area and degree of dispersity, while the actual Pt surface

area depends on factors such as nanoparticle size and their degree of aggregation. Since the surface area for a given mass of the support material is a function of the density of the bulk support material and the pore size distribution, a higher surface area per gram of support material results in a lower surface density (higher dispersity) of Pt nanoparticles. Vulcan XC-72, for example, has a high BET surface area of ~235 $m^2 g^{-1}$ that arises from the low density of the material, the small particles size of the carbon building blocks (approximately 50 nm), and high porosity. [125,126] If one assumes that a nitride support has identical particle/pore size and morphology to carbon black, then the matching Pt loading per unit surface area of the support is determined as the ratio of the theoretical bulk density of the nitride support to that of Vulcan XC-72. In most cases this assumption is not valid (as the pore size distribution and support particle size and degree of sintering are in-fact not the same), however this method allows for a crude, "apples-to-apples" way to compare Pt catalysts on different supports. In reality, a specific definition of performance for comparable catalyst loadings is needed. Typically this takes the form of quoting the mass (or cost) of the catalyst per watt of power generated under a specific set of operating conditions.

Several different methods for platinizing oxide and nitride supports are discussed in Chapter 7 of Chin Subban's thesis. Among those discussed is the Microwave Polyol technique.[127] At the time these nitride samples were prepared, the Microwave Polyol technique was popular in the DiSalvo Lab for adding Pt to newly developed support materials. Since then we have moved away from this technique due to it's limited ability to control Pt particle size and the adverse affects of microwave heating on the support porosity and particle size.[104] Despite these detrimental effects, the Microwave Polyol technique provides a quick and easy way to load Pt onto a catalyst support. In the technique, ethylene glycol is used as both a surfactant and as a

precursor to the reducing agent that is generated *in-situ* during microwave heating. As a result, the microwave polyol technique has greater control of the catalyst particle size and distribution as compared to reduction by other means (e.g. borohydride or hydrazine).[128] However, the Microwave Polyol reaction is very pH sensitive, and requires the use of KOH. If the solution is heterogeneous, increased local concentrations of KOH leads to larger Pt particle sizes and non-uniform distribution, especially for high Pt loadings.[129-133]

A typical platinization procedure using the microwave polyol technique is as follows. Ethylene glycol (12.92 mL), 0.05M H_2PtCl_6 (aq, 0.646 mL), 0.4M KOH (aq 0.254 mL), and Ti-M nitride (M=Nb, W) prepared by co-precipitation (93.7 mg) were added to a small glass beaker and sonicated for 30 min. These amounts of reagents were calculated to yield a platinized support with 6.34 wt% Pt loading, which is comparable to 20 wt% Pt/C by a ratio of the theoretical bulk density of the supports. The mixture was then heated in a modified kitchen microwave (900 watts) for a total of 90 seconds in 30-second intervals. Using short intervals prevents the ethylene glycol from boiling over. After microwave heating, the sample was separated by centrifugation at 4500 RPM for 10 min and decanting of the supertenant liquid. The sample was washed with acetone 3 times, and was dried in air at 80ºC for 12 hours. The platinized sample was then characterized by pXRD, electron microscopy, and was prepared for electrochemical measurements.

Figure 3.10 shows pXRD (a) and SEM images (b) of the platinized support. From the SEM images (b) Pt nanoparticles of ~5 nm appear to be dispersed on the nitride support. Using the Scherrer equation, the FWHM of the Pt peaks in the pXRD pattern confirm that the average crystalline domain size is 4.6 nm indicating that many of the Pt particles are likely single crystals. However, in Figure 3.10b one can see that there are areas that contain well dispersed Pt

nanoparticles, next to areas that have none. A second challenge (unaddressed, as yet) is to determine the distribution of the catalyst *inside* the porous particles. These are persistent problems for several oxide and nitride materials, as the only controllable parameter is the duration of heating. While other microwave apparti are available which enable the user to control many parameters, including power, time, pressure, etc. using the modified kitchen microwave offered a quick and simple method for platinizing the oxide supports. The platinized $Ti_{0.7}W_{0.3}N$ showed similar behavior to the Ti-Nb sample and had an average Pt particle size of 4.9 nm.

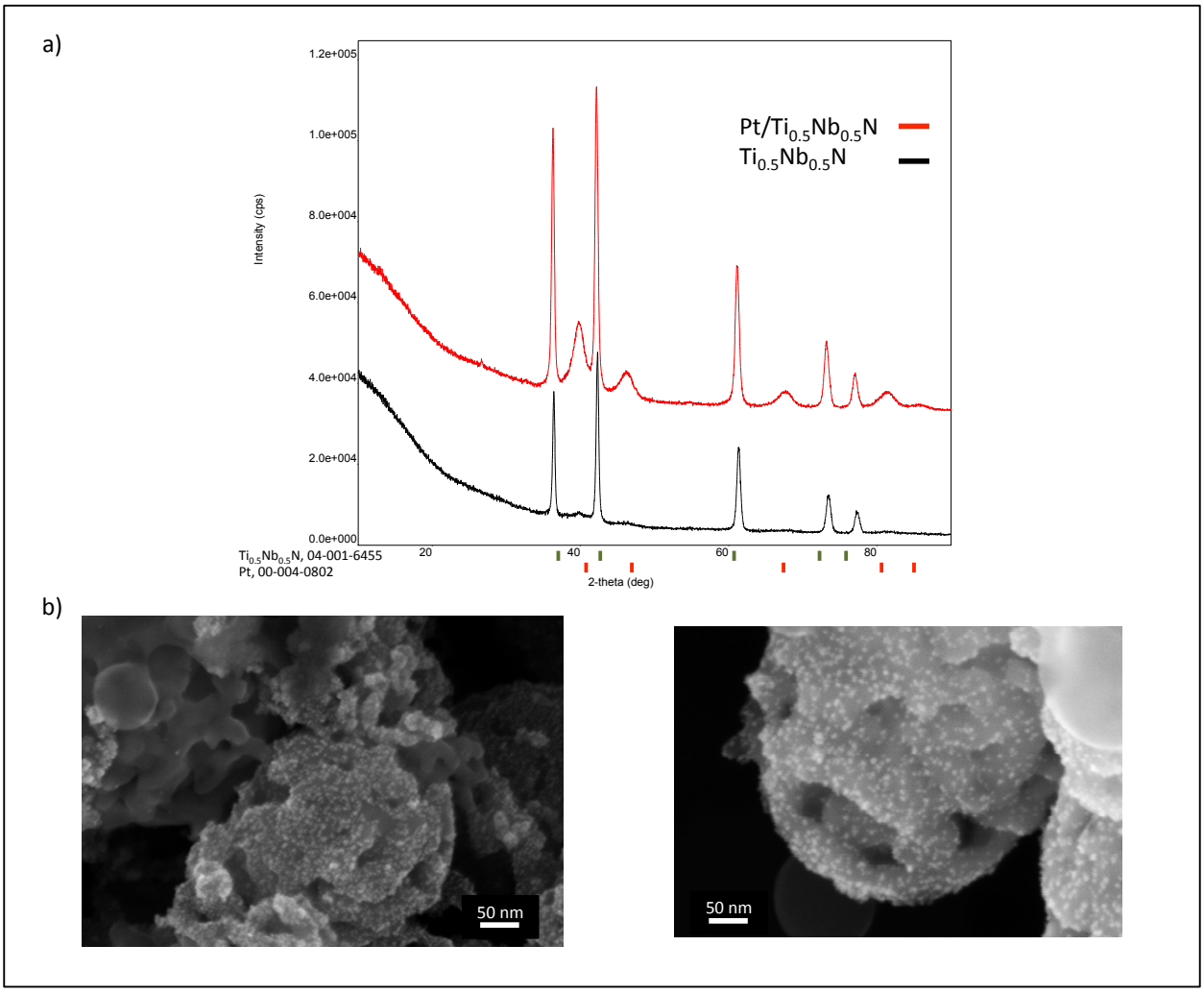

Figure 3.10 (a) pXRD patterns for the platinized (red) and unplatinized (black) $Ti_{0.5}Nb_{0.5}N$. Using the FWHM of the Pt peak, the crystalline domain size is 4.6 nm by the Scherrer Equation. (b) SEM images of the platinized nitride support. Note that in several areas the Pt nanoparticles seem well dispersed while in others, there appear to be no particles (left).

In addition to the microwave polyol technique, $Ti_{0.5}Nb_{0.5}N$ was also platinized using a standard polyol synthesis (a method which does not require KOH). Dr. Zhiming Cui of the DiSalvo group performed this work, following the method presented by Bock *et al*.[134] In a typical preparation, 40 mg of mesoporous $Ti_{0.5}Nb_{0.5}N$ was suspend in 50 mL of ethylene glycol, and 1 mL of H_2PtCl_6 solution (aq 0.025 M) was added. The mixture was heated in an oil bath at 140 ºC for 3 hours with constant stirring, followed by filtering and washing with DI water. The platinized support was then dried at 80 ºC for 6 hours. The resulting, platinized support had a Pt loading of 20 wt% (relative to the nitride support). Figure 3.11 shows a pXRD pattern of the platinized support. The crystalline domain size for the as-deposited Pt nanoparticles is 5.0 nm calculated using the Scherrer equation. Figure 3.11 also shows an inset SEM image of the as-deposited Pt particles. While the dispersity of the Pt particles appeared somewhat better than the microwave polyol technique, Pt particle agglomerations and areas with little to no Pt particles were visible. The particle size also appears to vary somewhat between 5-10 nm. Overall, the standard polyol technique offers slightly more control in Pt particle deposition than the microwave polyol technique (in terms of heating rate and duration). Also, local temperature variations (hot-spots), which are more prone in microwave heating, can be avoided which is reported to lead to greater particle size uniformity.[134]

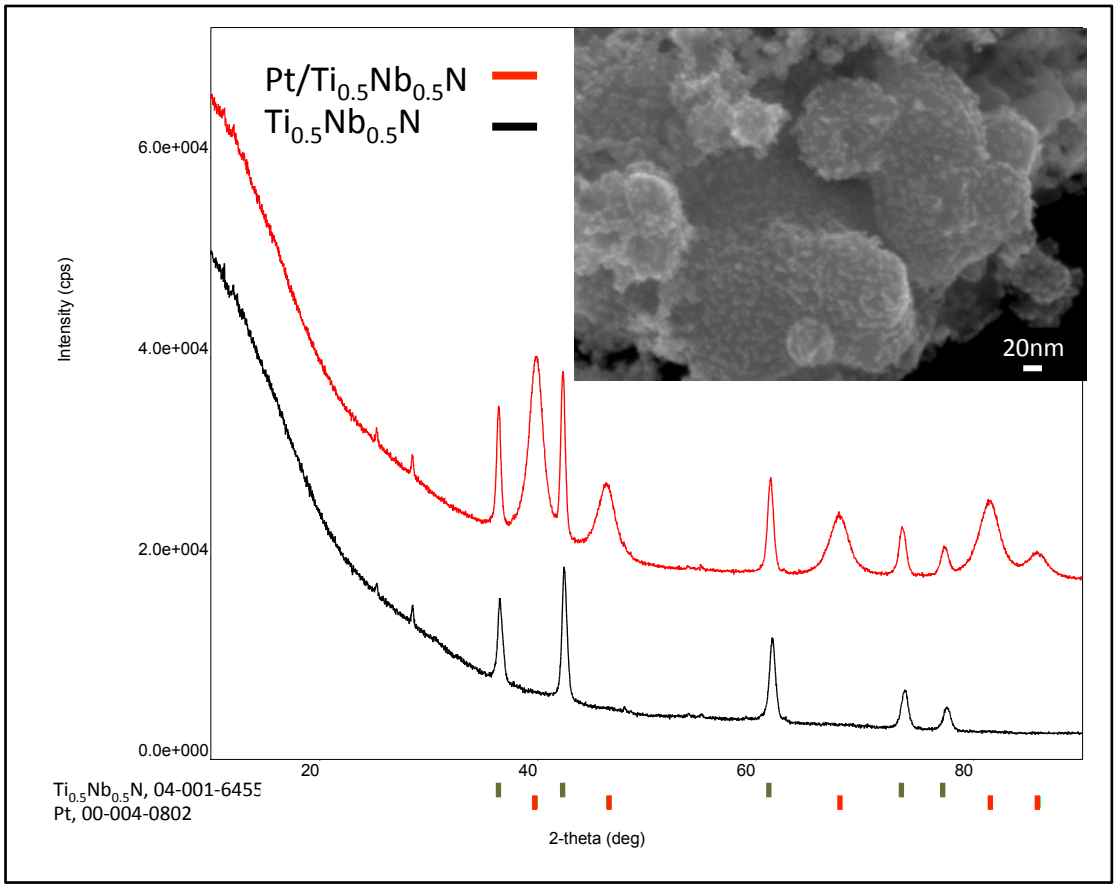

Figure 3.11 pXRD pattern of $Pt/Ti_{0.5}Nb_{0.5}N$ (red) and $Ti_{0.5}Nb_{0.5}N$ (black). The crystalline domain size was calculated from the FWHM of the Pt peaks to be 5.0nm using the Scherrer Equation. (inset) SEM image of the platinized catalyst. The Pt particles appear more dispersed compared to the microwave polyol technique, although agglomerations of Pt particles and some bare areas of the support are visible.

3.6.3 Electrochemical Performance of Pt/$Ti_{1-x}M_xN$ (M=Nb, W)

The platinized nitride supports were prepared as suspended inks as described previously. 20wt% carbon black was also added to the ink suspensions to aid in electrically connecting the nitride supports to the GC electrode. Figure 3.12 shows window-opening CVs obtained by Dr. Deli Wang for 12 wt% Pt/$Ti_{0.7}W_{0.3}N$ (prepared by the Microwave Polyol technique) between 0 and 1.2 V versus RHE in N_2-purged, 0.5M H_2SO_4 at a sweep rate of 50 mV s^{-1}.

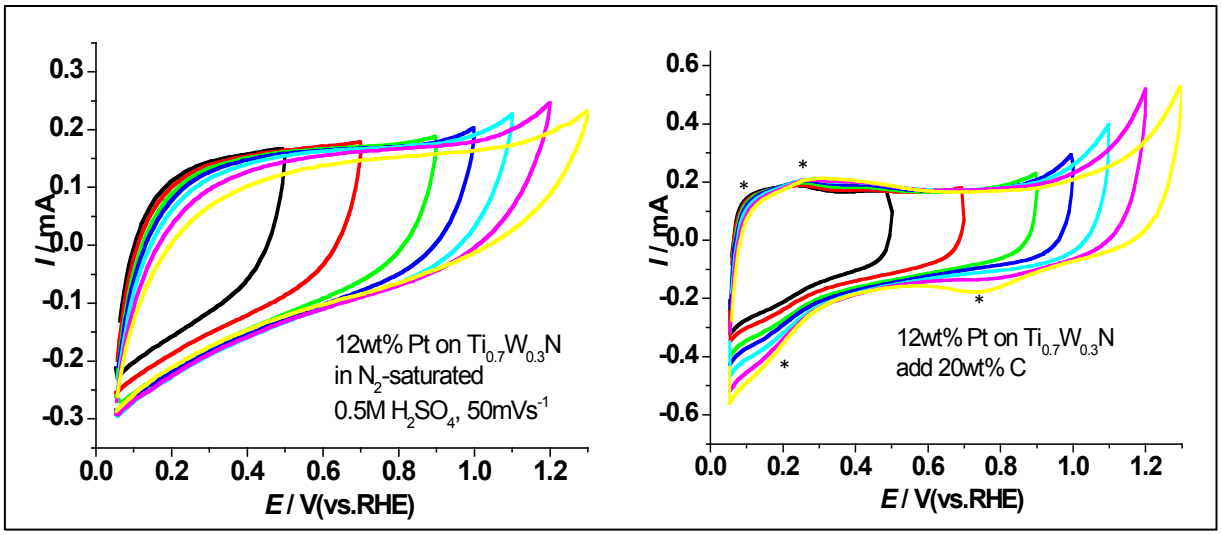

Figure 3.12 Window-opening CVs for 12wt% Pt/$Ti_{0.7}W_{0.3}N$ with no carbon added (left) and 20wt% carbon black added (right) to the ink suspension. Adding carbon black produced the expected CV for Pt (starred waves), indicating that it is necessary for electrically connecting the nitride supported Pt particles to the GC. Note the Pt-hydride formation peaks near 0.2V and the Pt-oxide reduction wave near 0.8V. The CVs were obtained in N_2-purged 0.5M H_2SO_4 at a sweep rate of 50 mV s^{-1}.

The left CV in Figure 3.12 was obtained from ink drop-casting on a GC electrode that contained no added carbon black. The CV loops are very similar to the CV shown in Figure 3.9 for the unplatinized support. Upon adding 20wt% carbon black (CV on the right in Figure 3.12), typical features of Pt are just barely visible (namely the hydrogen adsorption peaks near 0.2V and the Pt-oxide reduction wave near 0.8V, starred in figure 3.12). It is apparent from these

results that adding carbon to the ink recipe improves electrical contact of the support catalyst to the GC electrode. The larger particle sizes of the nitride supports, and perhaps contact resistance between the Pt and the nitrides that arises from the insulating passivation layer are likely contributing factors to problems in making good electrical contact without carbon black. While smaller particle sizes may be achievable using ball-milling or by ultrasonication, passivating interfaces *may* still be a problem.

Indeed when carbon black is added, it may be that some Pt migrates to or is contacted by the carbon back and that the low level of activity seen in the CV is due only to Pt on the carbon black. Developing methods and techniques to be sure that activity is due to catalyst bound to the non-carbon support is clearly needed. Without such advances it will be difficult to draw firm conclusions from electrochemical data. Further engineering and synthesis optimization for catalyst deposition and support particle size control will be necessary for these materials to be suitable replacements for carbon-based supports. Nonetheless, it is apparent that $Ti_{0.7}W_{0.3}N$ can support Pt nanoparticles, which is confirmation that nitrides can function as catalyst supports under PEMFCs-like conditions. Future work on $Pt/Ti_{0.7}W_{0.3}N$ should include testing the material as an anode catalyst for hydrogen oxidation and investigate its CO tolerance. $Pt/Ti_{0.7}W_{0.3}O_2$ was previously reported to have enhanced CO-tolerance[112], and as the surface layer is an oxide, similar behavior may be expected for the nitride catalyst. A central challenge is to invent a process for the uniform deposition of the catalyst in all the pores as well as the external surface of the particles.

Figure 3.13 shows CVs comparing 20 wt% $Pt/Ti_{0.5}Nb_{0.5}N$ and E-Tek 50 wt% Pt/C prepared by Dr. Zhiming Cui. To prepare the ink cast GCE, Dr. Cui added 5mg of the platinized support to 1 mL of ethanol and 50 μL of 5% Nafion solution (in aliphatic alcohols) and sonicated

the suspension for 30 min. A 10 µL aliquot of the ink suspension was then drop-cast on a cleaned and polished GCE. It is important to note that the nitride of the catalyst ink contains ***no*** added carbon black in this case.

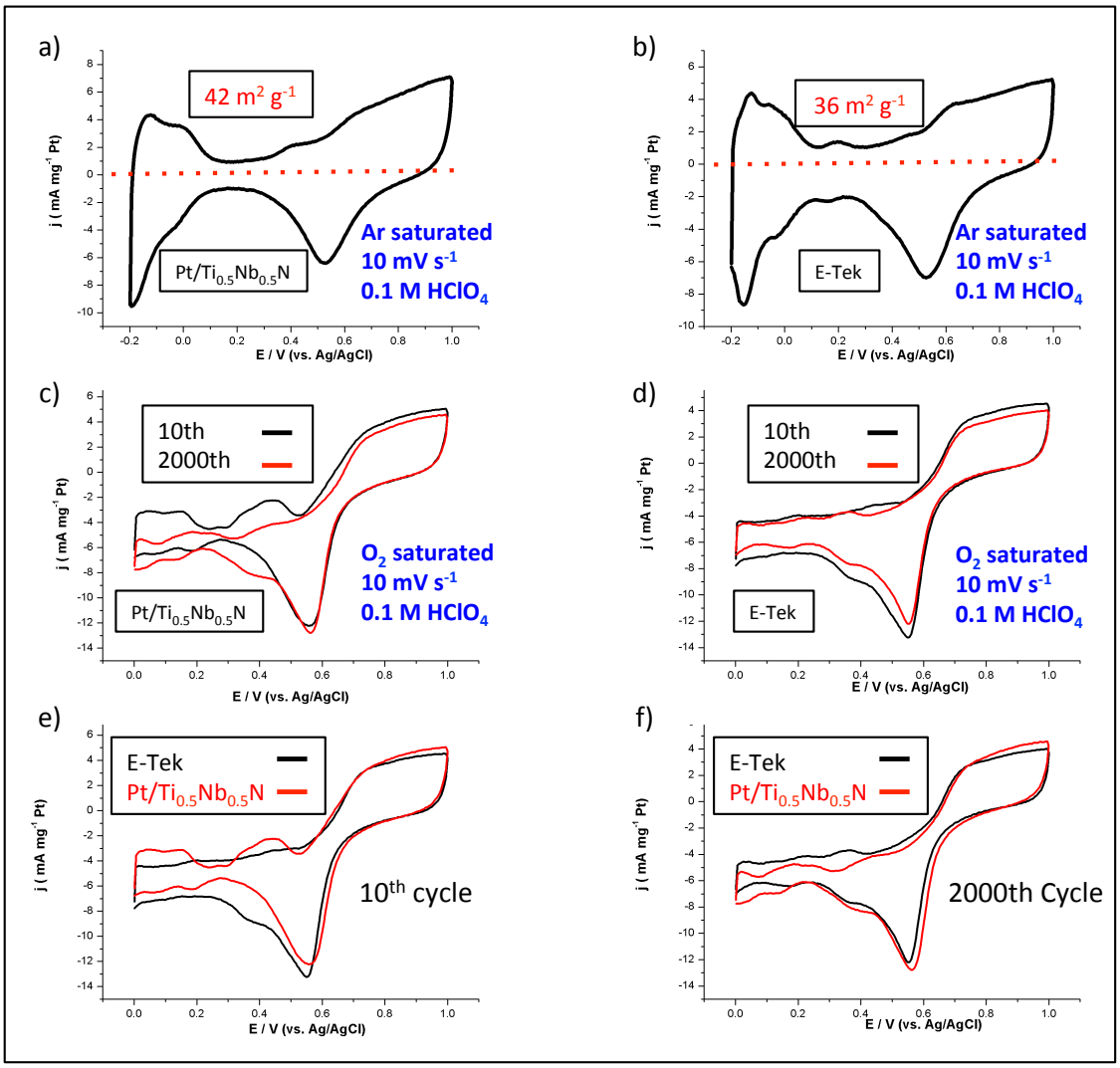

Figure 3.13 (a) CV of 20 wt% $Pt/Ti_{0.5}Nb_{0.5}N$ in Ar saturated 0.1 M $HClO_4$. The Pt ECSA was calculated to be 42 $m^2\ g^{-1}$ by integrating the hydrogen adsorption peaks and assuming 210 µC cm^{-2}. (b) CV of 50 wt% Pt/C (E-Tek) in Ar saturated electrolyte. Note that the Pt ECSA is similar to the nitride at 36 $m^2\ g^{-1}$. (c-d) Stability tests of $Pt/Ti_{0.5}Nb_{0.5}N$ (c) and Pt/C (d, E-Tek) in O_2 saturated electrolyte. Each material was subjected to 2000 cycles with continuously bubbling O_2. Note the ORR activity for both materials (peak at 0.6V). The activity for Pt/C (E-Tek) drops somewhat after 2000 cycles, while the activity for $Pt/Ti_{0.5}Nb_{0.5}N$ slightly increases. (e-f) Comparison of Pt/C and $Pt/Ti_{0.5}Nb_{0.5}N$ before and after a 2000 cycle stability test. The $Pt/Ti_{0.5}Nb_{0.5}N$ catalyst has a slightly more positive $E_{1/2}$ for ORR as well as higher activity (normalized to the mass of Pt) than E-Tek Pt/C.

Figure 3.13 a and b showed CVs for 20 wt% Pt/$Ti_{0.5}Nb_{0.5}N$ (3.13a) and E-Tek 50 wt% Pt/C(3.13b) obtained in Ar saturated 0.1 M $HClO_4$ at a sweep rate of 10 mV s^{-1}. Typical CVs for Pt were obtained with hydrogen adsorption peaks between 100 mV and -200 mV (versus a Ag/AgCl reference electrode) and Pt-oxide formation and reduction waves near 600 mV. Using 210 μC cm^{-2}, the Pt electrochemical surface area (ECSA) was calculated, by integrating the hydrogen adsorption region, to be 42 m^2 g^{-1} for Pt/$Ti_{0.5}Nb_{0.5}N$ and 36 m^2 g^{-1} for Pt/C (E-Tek). An additional redox wave is visible in the Pt/C CV(3.13b) at approximately 0.2 V versus Ag/AgCl, which is not visible in the Pt/$Ti_{0.5}Nb_{0.5}N$ CV (3.13a). The origin of this redox wave is unknown, and is not believed to arise from the Pt. It is possible that this wave is due to functional groups on the carbon support. Nonetheless, both Pt/$Ti_{0.5}Nb_{0.5}N$ (prepared using the standard polyol technique) and Pt/C (prepared commercially) behave similarly.

Figure 3.13 c and d shows an electrochemical stability test for Pt/$Ti_{0.5}Nb_{0.5}N$ (3.13c) and Pt/C (3.13d) after 2000 cycles in O_2 saturated 0.1 M $HClO_4$ at a sweep rate of 10 mV s^{-1}. The primary feature of these CVs is the ORR wave at approximately 0.6 V versus Ag/AgCl. For Pt/$Ti_{0.5}Nb_{0.5}N$ the peak current for ORR slightly improves after 2000 cycles, while for E-Tek Pt/C the peak current diminishes somewhat. Additionally, the $E_{1/2}$ for ORR on the Pt/C CV shifts slightly negative upon cycling (from 0.61 V to 0.59 V,) while Pt/$Ti_{0.5}Nb_{0.5}N$ remains stable (0.63 V). For Pt/$Ti_{0.5}Nb_{0.5}N$ (Figure 3.13c), the current in the region 0 mV to 400 becomes noticeably more negative after 2000 cycles. This indicates a possible enhancement of ORR (or another reduction process) upon cycling that is not observed for Pt/C in Figure 3.13d. Further experiments will be required to fully elucidate the nature of the reduction waves in this region.

Figure 3.13 e and f shows a side-by-side comparison of Pt/$Ti_{0.5}Nb_{0.5}N$ and Pt/C before (3.13e) and after (3.13f) 2000 cycles. While, Pt/C has a slightly higher peak current for ORR

before cycling, the ORR peak current for $Pt/Ti_{0.5}Nb_{0.5}N$ surpasses Pt/C after cycling. Additionally, $Pt/Ti_{0.5}Nb_{0.5}N$ has a more positive $E_{1/2}$ for ORR, possibly indicating that it is a better catalyst for ORR than commercially prepared Pt/C.

Finally, Figure 3.14 shows a preliminary measurement of $Pt/Ti_{0.5}Nb_{0.5}N$ compared to Pt/C (E-Tek) for ORR activity in basic electrolyte. Here, $Pt/Ti_{0.5}Nb_{0.5}N$ and Pt/C were drop-cast on a GCE as previously described and were cycled at 10 mV s^{-1} in O_2 saturated 0.1 M KOH. The most dramatic feature of Figure 3.14 is the significantly higher peak current for ORR at approximately -250 mV versus Ag/AgCl. This measurement is very preliminary, but indicates that $Pt/Ti_{0.5}Nb_{0.5}N$ is *potentially* a better catalyst than Pt/C for ORR in base. Future work should include RDE studies of $Pt/Ti_{0.5}Nb_{0.5}N$ in base and acid electrolytes to more completely understand the source of the observed enhanced activity, as well as to determine if any synergy between the catalyst and support may enable superior performance.

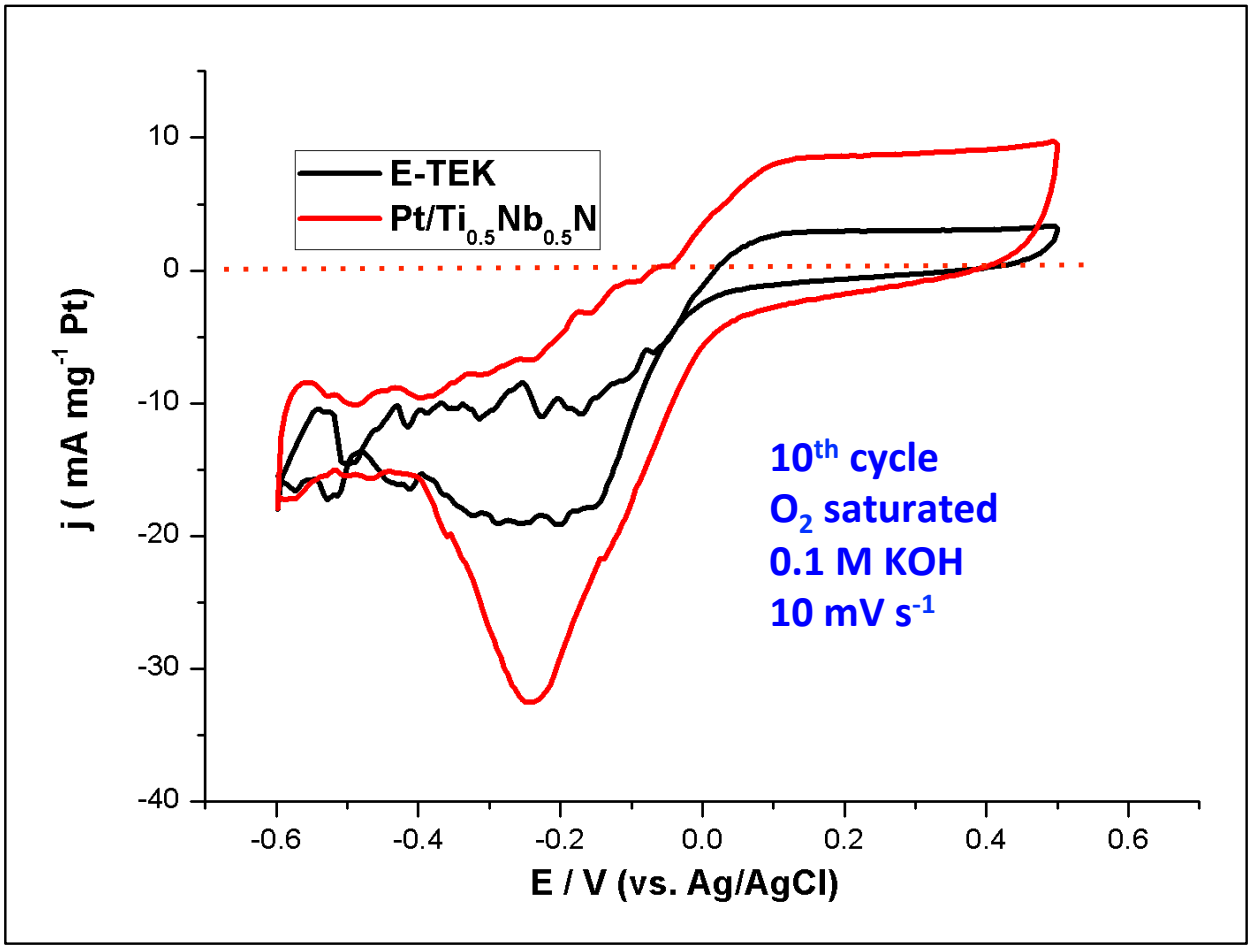

Figure 3.14 CV of $Pt/Ti_{0.5}Nb_{0.5}N$ and Pt/C (E-Tek) in O_2 saturated 0.1 M KOH. Note the higher ORR activity for $Pt/Ti_{0.5}Nb_{0.5}N$ indicated by the higher peak current at approximately -250 mV.

3.7 Conclusions

So far, binary mixed-metal nitrides look promising to potentially replace carbon-based catalyst supports; however, further testing is required to draw firm conclusions. While it is clear that several questions regarding oxidative and chemical stability remain, mesoporous, conducting nitride compounds can be produced with relative ease. It is clear form the work presented in this chapter that further investigation of these materials is warranted, and necessary to fully understand the oxidation behavior and possible corrosion mechanisms of nitride supports. Extensive characterization of Pt/Ti-M nitride supports was not performed; therefore, future studies should more fully characterize Pt/Ti-M nitride catalyst systems as well as Pt-M alloys and intermetallics. Nevertheless, the preliminary measurements presented above indicate that Pt/C and Pt/Ti-M nitride possess similar ORR activity, and that Pt/$Ti_{0.5}Nb_{0.5}N$ out performs E-Tek Pt/C after 2000 cycles in acid electrolyte, and in alkaline electrolyte for at least 10-20 cycles.

In order to better understand the chemical nature and behavior of the passivation layer, transitioning from mesoporous solids (with a lot of interfaces) to thin films (with many fewer interfaces, ideally one) was the next evolution of studying nitride supports for PEMFC applications. Chapter 4 will focus on combinatorially prepared, nitride thin-films that have been deposited by magnetron sputtering. The focus of this project was to synthetically control and then characterize the passivation layer of nitride compounds on well-defined interfaces. Additionally, using a combinatorial approach allowed us to study a variety of compositions on a single sample simultaneously.

REFERENCES

(1) Juza, R. *Advances in Inorganic Chemistry and Radiochemistry* **1966**, *9*, 81–131.

(2) Juza, R.; Langer, K.; Benda, Von, K. *Angewandte Chemie-International Edition* **1968**, *7*, 360–370.

(3) Niewa, R.; Disalvo, F. J. *Chem. Mater.* **1998**, *10*, 2733–2752.

(4) Reiherzer, J. Synthesis and Photoluminescent Properties of Rare Earth Activated Nitride Phosphors, Cornell University: Ithaca, NY, 2009.

(5) Inorganic Crystal Structure Database **2012**.

(6) Lide, D. R.; Bruno, T. J. *CRC Handbook of Chemistry and Physics*; 87 ed. CRC Press, 2012.

(7) Bailey, M. S. The Synthesis and Characterization of Nitrides and Other Non-oxide Materials, Cornell University: Ithaca, NY, 2005.

(8) DiSalvo, F. J.; Clarke, S. J. *Current Science* **2001**, 241–249.

(9) Kal'ner, V. D.; Verner, A. K. *Metal Science and Heat Treatment* **1994**, *36*, 196–199.

(10) Yamane, H.; Disalvo, F. J. *J. Alloy. Compd.* **1996**, *240*, 33–36.

(11) Yamane, H.; Disalvo, F. J. *J. Alloy. Compd.* **1996**, *241*, 69–74.

(12) Mueller-Mach, R.; Mueller, G. O.; Krames, M. R.; Trottier, T. *IEEE J. Sel. Top. Quantum Electron.* **2002**, *8*, 339–345.

(13) Nakamura, S.; Mukai, T.; Senoh, M. *Appl. Phys. Lett.* **1994**.

(14) Marchand, R. J.; Gouin, X.; Tessier, F.; Laurent, Y. *MRS Proc.* **2011**, *368*, 15.

(15) Marchand, R.; Tessier, F.; Disalvo, F. J. *J. Mater. Chem.* **1999**.

(16) Shi, C.; Zhu, A. M.; Yang, X. F.; Au, C. T. *Catalysis letters* **2004**, *97*, 9–16.

(17) He, H.; Dai, H. X.; Ngan, K. Y.; Au, C. T. *Catalysis letters* **2001**.

(18) Hargreaves, J. S. J.; Mckay, D. *Catalysis* **2005**, *19*, 85–109.

(19) Boćkowski, M. *Physica B: Condensed Matter* **1999**, *265*, 1–5.

(20) Horvath-Bordon, E.; Riedel, R.; Zerr, A.; McMillan, P. F.; Auffermann, G.; Prots, Y.; Bronger, W.; Kniep, R. D.; Kroll, P. *Chem. Soc. Rev.* **2006**, *35*, 987.

(21) Oyama, S. T. *Chemistry of Transition Metal Carbides and Nitrides*; Blackie Academic & Professional: London, 1996.

(22) Cumberland, R. W.; Blair, R. G.; Wallace, C. H.; Reynolds, T. K.; Kaner, R. B. *JOURNAL OF PHYSICAL CHEMISTRY B* **2001**, *{105}*, {11922–11927}.

(23) Parkin, I. P. *Chem. Soc. Rev.* **1996**, *{25}*, {199–}.

(24) Parkin, I. P.; Nartowski, A. M. *POLYHEDRON* **1998**, *{17}*, {2617–2622}.

(25) Song, B.; Jian, J. K.; Wang, G.; Lei, M.; Xu, Y. P.; Chen, X. L. *Chem. Mater.* **2007**, *19*, 1497–1502.

(26) Gillan, E. G.; Kaner, R. B. *Inorg. Chem.* **1994**, *33*, 5693–5700.

(27) Clarke, S. J.; Disalvo, F. J. *Inorg. Chem.* **1997**, *36*, 1143–1148.

(28) Cario, L.; Gál, Z. A.; Braun, T. P.; DiSalvo, F. J.; Blaschkowski, B.; Meyer, H. J. *Journal of Solid State Chemistry* **2001**, *162*, 90–95.

(29) Gál, Z. A.; Cario, L.; DiSalvo, F. J. *Solid State Sciences* **2003**, *5*, 1033–1036.

(30) Jacob, K. T.; Verma, R.; Mallya, R. M. *J Mater Sci* **2002**, *37*, 4465–4472.

(31) Hu, J.; Lu, Q.; Tang, K.; Yu, S.; Qian, Y.; Zhou, G.; Liu, X. *Journal of the American Ceramic Society* **2000**, *83*, 430–432.

(32) Gál, Z. A.; Mallinson, P. M.; Orchard, H. J.; Clarke, S. J. *Inorg. Chem.* **2004**, *43*, 3998–4006.

(33) Podsiadło, S. *Thermochimica acta* **1995**, *256*, 367–373.

(34) Gomathi, A.; Rao, C. N. R. *Materials Research Bulletin* **2006**, *41*, 139.

(35) Houmes, J. D.; Loye, zur, H.-C. *Journal of Solid State Chemistry* **1997**, *130*, 266–271.

(36) Houmes, J. D.; Loye, zur, H.-C. *Chem. Mater.* **1996**, *8*, 2551–2553.

(37) Vaidhyanathan, B.; Rao, K. J. *Chem. Mater.* **1997**, *9*, 1196–1200.

(38) Hultman, L. *Vacuum* **2000**, *57*, 1–30.

(39) Podob, M. *Surface Modification Technologies XII* **1998**, 15–24.

(40) Elder, S. H.; Disalvo, F. J.; Topor, L.; Navrotsky, A. *Chem. Mater.* **1993**, *5*, 1545–1553.

(41) Haddix, G. W.; Jones, D. H.; Reimer, J. A.; Bell, A. T. *Journal of Catalysis* **1988**, *112*, 556–564.

(42) Wei, Z.; Xin, Q.; Grange, P.; Delmon, B. *Journal of Catalysis* **1997**, *168*, 176–182.

(43) Hargreaves, J. S. J.; Mckay, D. *Journal of Molecular Catalysis A: Chemical* **2009**, *305*, 125–129.

(44) Markel, E. J.; Van Zee, J. W. *Journal of Catalysis* **1990**, *126*, 643–657.

(45) Tompkins, H. G. *J. Appl. Phys.* **1991**, *70*, 3876.

(46) Subban, C. V.; Smith, I. C.; DiSalvo, F. J. *Small* **2012**, *8*, 2824–2832.

(47) Yang, M.; MacLeod, M. J.; Tessier, F.; DiSalvo, F. J. *Journal of the American Ceramic Society* **2012**, *95*, 3084–3089.

(48) Demczyk, B. G.; Choi, J.-G.; Thompson, L. T. *Appl. Surf. Sci.* **1994**, *78*, 63–69.

(49) Colling, C. W.; Choi, J.-G.; Thompson, L. T. *Journal of Catalysis* **1996**, *160*, 35–42.

(50) Choi, J.-G.; Curl, R. L.; Thompson, L. T. *Journal of Catalysis* **1994**, *146*, 218–227.

(51) Jaggers, C. H.; Michaels, J. N.; Stacy, A. M. *Chem. Mater.* **1990**, *2*, 150–157.

(52) Neylon, M. K.; Bej, S. K.; Bennett, C. A.; Thompson, L. T. *Applied Catalysis A: General* **2002**, *232*, 13–21.

(53) Zhang, Y.; Li, Y.; Raval, R.; Li, C.; Zhai, R.; Xin, Q. *Journal of Molecular Catalysis A: Chemical* **1998**, *132*, 241–253.

(54) Korlann, S.; Diaz, B.; Bussell, M. E. *Chem. Mater.* **2002**, *14*, 4049–4058.

(55) Yu, C. C.; Ramanathan, S.; Oyama, S. T. *Journal of Catalysis* **1998**, *173*, 1–9.

(56) Gao, Q.; Giordano, C.; Antonietti, M. *Small* **2011**, *7*, 3334–3340.

(57) Ran, S.; Gao, L. *Journal of the American Ceramic Society* **2008**, *91*, 2378–2381.

(58) Li, Y.; Gao, L. *Journal of the American Ceramic Society* **2002**, *85*, 3090–3092.

(59) Avasarala, B.; Haldar, P. *Electrochimica Acta* **2010**, *55*, 9024–9034.

(60) Halalay, I. C.; Merzougui, B.; Carpenter, M. K.; Swathirajan, S.; Garabedian, G. C.; Mance, A. M.; Cai, M. **2009**.

(61) Milošv, I.; Strehblow, H. H.; Navinšek, B.; Metikoš Huković, M. *Surf. Interface Anal.* **1995**, *23*, 529–539.

(62) Ham, D. J.; Lee, J. S. *Energies* **2009**, *2*, 873–899.

(63) Neckel, A.; Rastl, P.; Eibler, R.; Weinberger, P. *Journal of Physics C: ...* **1976**, *9*, 579–592.

(64) Saha, N. C.; Tompkins, H. G. *J. Appl. Phys.* **1992**, *72*, 3072.

(65) Massiani, Y.; Medjahed, A.; Gravier, P.; Argème, L.; Fedrizzi, L. *THIN SOLID FILMS* **1990**, *191*, 305–316.

(66) Ernsberger, C. *Journal of Vacuum Science & Technology A: vacuum, Surfaces and Films* **1986**, *4*, 2784.

(67) Esaka, F. *Journal of Vacuum Science & Technology A: vacuum, Surfaces and Films* **1997**, *15*, 2521.

(68) Francois, J. C.; Massiani, Y.; Gravier, P.; Grimblot, J.; Gengembre, L. *THIN SOLID FILMS* **1993**, *223*, 223–229.

(69) Chyou, S. D.; Shih, H. C.; Chen, T. T. *Corrosion Science* **1993**, *35*, 337–347.

(70) Vesel, A.; Mozetic, M.; Kovac, J.; Zalar, A. *Appl. Surf. Sci.* **2006**, *253*, 2941–2946.

(71) Avasarala, B.; Haldar, P. *International Journal of Hydrogen Energy* **2011**, *36*, 3965–3974.

(72) Avasarala, B.; Murray, T.; Li, W.; Haldar, P. *J. Mater. Chem.* **2009**, *19*, 1803.

(73) Castro, D. T.; Ying, J. Y. *NanoStructured Materials* **1997**, *9*, 67–70.

(74) Drygaś, M.; Czosnek, C.; Paine, R. T.; Janik, J. F. *Chem. Mater.* **2006**, *18*, 3122–3129.

(75) Ran, S.; Gao, L. *Materials Letters* **2009**, *63*, 94–96.

(76) Guo, Q.; Xie, Y.; Wang, X.; Lv, S.; Hou, T.; Bai, C. *Journal of the American Ceramic Society* **2005**, *88*, 249–251.

(77) Kim, H. S.; Shin, C. H.; Bugli, G.; Bureau-Tardy, M.; Djega-Mariadassou, G. *Applied Catalysis A: General* **1994**, *119*, 223–240.

(78) Lee, J.-M.; Han, S.-B.; Song, Y.-J.; Kim, J.-Y.; Roh, B.; Hwang, I.; Choi, W.; Park, K.-W. *Applied Catalysis A: General* **2010**, *375*, 149–155.

(79) Mantyla, T. A.; Helevirta, P. J.; Lepisto, T. T.; Siitonin, P. T. *THIN SOLID FILMS* **1985**, 275–281.

(80) Schwartz, V.; Oyama, S. T. *Chem. Mater.* **1997**, *9*, 3052–3059.

(81) Xiang, D.; Liu, Y.; Zhao, Z.; Gao, S.; Tu, M. *J Mater Sci* **2007**, *42*, 4630–4635.

(82) Yuan, B.; Yang, M.; Zhu, H. *Journal of Materials Research* **2009**, *24*, 448–451.

(83) Messing, G. L.; Zhang, S. C.; Jayanthi, G. V. *Journal of the American Ceramic Society* **1993**, *76*, 2707–2726.

(84) Chamberlin, R. R.; Skarman, J. S. *J. Electrochem. Soc.* **1966**, *113*, 86–89.

(85) Kodas, T.; Datye, A.; Lee, V.; Engler, E. *J. Appl. Phys.* **1989**, *65*, 2149–2151.

(86) Carp, O.; Patron, L.; Reller, A. *Revue Roumaine De Chimie* **2003**, *48*, 513–520.

(87) Rao, C. N. R. *Materials Science and Engineering B-Solid State Materials for Advanced Technology* **1993**, *18*, 1–21.

(88) Chick, L. A.; Pederson, L. R.; Maupin, G. D.; Bates, J. L.; Thomas, L. E.; Exarhos, G. J. *Materials Letters* **1990**, *10*, 6–12.

(89) Sale, F. R. *Metall. Mater. Technol.* **1977**, *9*, 439.

(90) Anderton, D. J.; Sale, F. R. *Powder Metall.* **1979**, *22*, 8–13.

(91) Brinker, C. J.; Scherer, G. W. *Sol-Gel Science*; Academic Pr, 1990.

(92) Hench, L. L.; West, J. K. *Chem. Rev. (Washington, DC, U. S.)* **1990**, *90*, 33–72.

(93) Giordano, C.; Antonietti, M. *Nano Today* **2011**, *6*, 366–380.

(94) Cushing, B. L.; Kolesnichenko, V. L.; O'Connor, C. J. *Chem. Rev. (Washington, DC, U. S.)* **2004**, *104*, 3893–3946.

(95) Macwan, D. P.; Dave, P. N.; Chaturvedi, S. *J Mater Sci* **2011**, *46*, 3669–3686.

(96) NIEDERBERGER, M.; GARNWEITNER, G.; PINNA, N.; NERI, G. *Progress in Solid State Chemistry* **2005**, *33*, 59–70.

(97) Pinna, N.; Niederberger, M. *Angewandte Chemie-International Edition* **2008**, *47*, 5292–5304.

(98) Topnani, N.; Kushwaha, S.; Athar, T. *International Journal of Green Nanotechnology: Materials Science & Engineering* **2010**, *1*, M67–M73.

(99) Subban, C. V.; Zhou, Q.; Hu, A.; Moylan, T. E.; Wagner, F. T.; DiSalvo, F. J. *J. Am. Chem. Soc.* **2010**, *132*, 17531–17536.

(100) Rietveld, H. M. *J. Appl. Cryst.* **1969**, *2*, 65–71.

(101) Gillespie, R. J.; Humphreys, D.; Baird, C.; Robinson, E. A. *Chemistry*; Allyn and Bacon, Inc.: Newton, Massachusetts, 1986.

(102) Arabczyk, W.; Zamlynny, J. *Catalysis letters* **1999**, *60*, 167–171.

(103) Brunauer, S.; Emmett, P. H.; Teller, E. *J. Am. Chem. Soc.* **1938**, *60*, 309–319.

(104) Subban, C. V. Synthesis and Characterization of Mixed-Metal Oxides for Catalyst Support Applications in Proton Exchange Membrane Fuel Cells, Cornell University, 2012.

(105) Pantea, D.; Darmstadt, H.; Kaliaguine, S.; Summchen, L.; Roy, C. *Carbon* **2001**, *39*, 1147–1158.

(106) Pourbaix, M. *Atlas of Electrochemical Equilibria in Aqueous Solutions*; National Association of Corrosion Engineers, 1974.

(107) Mehta, S. M.; Patel, S. R. *J. Am. Chem. Soc.* **1951**, *73*, 224–226.

(108) Frankenthal, R. P.; Siconolfi, D. J.; Sinclair, W. R.; Bacon, D. D. *J. Electrochem. Soc.* **1983**, *130*, 2056–2060.

(109) Gallagher, P. K.; Sinclair, W. R.; Bacon, D. D.; Kammlott, G. W. *J. Electrochem. Soc.* **1983**, *130*, 2054–2056.

(110) Kakinuma, K.; Wakasugi, Y.; Uchida, M.; Kamino, T.; Uchida, H.; Watanabe, M. *Electrochemistry* **2011**, *79*, 399–403.

(111) McGovern, M. *Journal of Power Sources* **2003**, *115*, 35–39.

(112) Wang, D.; Subban, C. V.; Wang, H.; Rus, E.; DiSalvo, F. J.; Abruña, H. D. *J. Am. Chem. Soc.* **2010**, *132*, 10218–10220.

(113) Lee, H. J.; Habas, S. E.; Somorjai, G. A.; Yang, P. D. *J. Am. Chem. Soc.* **2008**, *130*, 5406–5407.

(114) Solla-Gullon, J.; Vidal-Iglesias, F. J.; Rodriguez, P.; Herrero, E.; Feliu, J. M.; Clavilier, J.; Aldaz, A. *J. Phys. Chem. B* **2004**, *108*, 13573–13575.

(115) Tian, N.; Zhou, Z. Y.; Sun, S. G.; Ding, Y.; Wang, Z. L. *Science* **2007**, *316*, 732–735.

(116) Wang, C.; Daimon, H.; Lee, Y.; Kim, J.; Sun, S. *J. Am. Chem. Soc.* **2007**, *129*, 6974–6975.

(117) Sasaki, K.; Wang, J. X.; Naohara, H.; Marinkovic, N.; More, K.; Inada, H.; Adzic, R. R. *Electrochimica Acta* **2010**, *55*, 2645–2652.

(118) Bonnemann, H.; Waldofner, N.; Haubold, H. G.; Vad, T. *Chem. Mater.* **2002**, *14*, 1115–1120.

(119) Borup, R.; Meyers, J.; Pivovar, B.; Kim, Y. S.; Mukundan, R.; Garland, N.; Myers, D.; Wilson, M.; Garzon, F.; Wood, D.; Zelenay, P.; More, K.; Stroh, K.; Zawodzinski, T.; Boncella, J.; McGrath, J. E.; Inaba, M.; Miyatake, K.; Hori, M.; Ota, K.; Ogumi, Z.; Miyata, S.; Nishikata, A.; Siroma, Z.; Uchimoto, Y.; Yasuda, K.; Kimijima, K.-I.; Iwashita, N. *Chem. Rev. (Washington, DC, U. S.)* **2007**, *107*, 3904–3951.

(120) Fang, B.; Kim, M.; Yu, J. S. *Applied Catalysis B: Environmental* **2008**, *84*, 100–105.

(121) Yu, J. S.; Kang, S.; Yoon, S. B.; Chai, G. *J. Am. Chem. Soc.* **2002**, *124*, 9382–9383.

(122) Fu, Q.; Saltsberg, H.; Flytzani-Stephanopoulos, M. *Science* **2003**, *301*, 935–938.

(123) Joo, S. H.; Park, J. Y.; Tsung, C.-K.; Yamada, Y.; Yang, P.; Somorjai, G. A. *Nature Materials* **2008**, *8*, 126–131.

(124) Chen, H.; Yu, Y.; Xin, H. L.; Newton, K. A.; Holtz, M. E.; Wang, D.; Muller, D. A.; Abruña, H. D.; DiSalvo, F. J. *Chem. Mater.* **2013**, *25*, 1436–1442.

(125) Grolleau, C.; Coutanceau, C.; Pierre, F.; Léger, J. M. *Electrochimica Acta* **2008**, *53*, 7157–7165.

(126) Ducampsanguesa, C.; Herreraurbina, R.; Figlarz, M. *Solid State Ionics* **1993**, *63-5*, 25–30.

(127) Yu, W. Y.; Tu, W. X.; Liu, H. F. *Langmuir* **1999**, *15*, 6–9.

(128) Fang, B.; Chaudhari, N. K.; Kim, M.-S.; Kim, J. H.; Yu, J.-S. *J. Am. Chem. Soc.* **2009**, *131*, 15330–15338.

(129) Brinas, R. P.; Hu, M. H.; Qian, L. P.; Lymar, E. S.; Hainfeld, J. F. *J. Am. Chem. Soc.* **2008**, *130*, 975–982.

(130) Chen, Z. W.; Xu, L. B.; Li, W. Z.; WAJE, M.; Yan, Y. S. *Nanotechnology* **2006**, *17*, 5254–5259.

(131) Ji, X. H.; Song, X. N.; Li, J.; Bai, Y. B.; Yang, W. S.; Peng, X. G. *J. Am. Chem. Soc.* **2007**, *129*, 13939–13948.

(132) Liu, Z. L.; Lee, J. Y.; Chen, W. X.; Han, M.; Gan, L. M. *Langmuir* **2004**, *20*, 181–187.

(133) Ullah, M. H.; Chung, W. S.; Kim, I.; Ha, C. S. *Small* **2006**, *2*, 870–873.

(134) Bock, C.; Paquet, C.; Couillard, M.; Botton, G. A.; MacDougall, B. R. *J. Am. Chem. Soc.* **2004**, *126*, 8028–8037.

CHAPTER 4

COMBINATORIALLY SPUTTER DEPOSITED THIN FILMS FOR DISCOVERY OF NEW POLYMER ELECTROLYTE MEMBRANE FUEL CELL CATALYST SUPPORTS

Work in this chapter was performed in collaboration with Dr. James O'Dea, Anna Legard, Megan Holtz, and Abigail Van Wassen as part of the Energy Materials Center at Cornell.

4.1 Origin of the Project

In Chapter 3 binary, mesoporous metal nitrides were investigated as potential replacements for carbon based catalyst supports in polymer electrolyte membrane fuel cells. It was clear from the results of these studies that nitrides could be prepared with the required porosity and conductivity, and that synthetic conditions play a role in the oxidation stability of these compounds. Despite these initial positive results, several questions regarding the oxidation stability and surface passivation layer thickness of the nitride compounds remained.

It was hypothesized that using scanned probe microscopy, specifically Atomic Force Microscopy (AFM), may enable a more quantitative understanding of the roughness and thickness of the surface oxide layer on the nitride nanoparticles. Furthermore, using conductive probe-AFM (cp-AFM) would enable one to monitor the conductivity of individual particles, and correlate conductivity with oxide layer thickness and morphology. The main idea of this strategy was to use a stiff AFM cantilever with a hard, conducting tip to probe the surface of the nitride particles. The cantilever would be slowly pressed into the surface, and the conductivity monitored. Once a sharp increase in conductivity was observed, the height change of the cantilever would correspond to the thickness of the oxide layer. This strategy, in principle, seemed reasonable; however, the DiSalvo group's experience with scanned probe techniques was limited, and we quickly learned that performing AFM imaging (using instrumentation in the

CCMR facilities) on porous solids with large particle sizes was difficult and non-intuitive.

Following some initial failed experiments, I (in collaboration with Dr. James O'Dea) proposed that we move away from synthesizing nitride nanoparticles, and begin studying co-sputtered metal nitride thin-films. The benefit to studying thin films is that there are fewer interfaces, and significantly less porosity to contend with. While it is true that thin films have some roughness, it was believed that looking at the "well-defined" surface of a thin film would circumvent many of the problems associated with imaging mesoporous solids. Furthermore, using co-sputtered combinatorial libraries, an approach pioneered by the van Dover group (a collaboration fostered through EMC^2), the effect of composition on conductivity and oxidative stability could also be studied simultaneously.

The work in this chapter represents a large collaborative effort between the DiSalvo, Abruña, van Dover, and Marohn groups as part of the Energy Materials Center at Cornell (EMC^2). Additionally, Megan Holtz of the Muller group provided technical expertise for STEM imaging and EELS spectroscopy. Each participant contributed to the project in different ways. Dr. James O'Dea was responsible for all of the AFM imaging, Abby Van Wassen and Anna Legard for electrochemical measurements, Anna Legard (and to some extent, I) was responsible for producing the thin films under study, and as stated Megan Holtz was responsible for STEM and EELS experiments. My roll in this project was to analyze the films using XPS to more quantitatively measure film composition, as well as serving as a subject matter resource and general project coordinator.

4.2 Preparation of Nitride Thin Films

Over the last several years, a large number of studies have focused on the preparation of transition metal nitrides because of their numerous technological applications. Nitride thin films are particularly interesting for applications in integrated circuits[1], corrosion resistant coatings[2], and as hard surface layers in cutting and grinding tools.[3]

Nitride thin films can be prepared in many ways including by deposition from a plasma, by chemical vapor deposition (CVD), by physical vapor deposition (PVD), or by electrochemical reduction of a precursor material (electroplating).[4] Each of these techniques has its own merits, and is suited for different applications depending on the material requirements; however, this discussion will focus only on physical vapor deposition.

Physical vapor deposition (PVD) may be viewed as the simple condensation of gaseous, oligomeric units onto a substrate. Typically these oligomeric units have the same composition as the final deposited films. PVD can be distinguished from chemical vapor deposition, in that there are no chemical processes (such as the releasing of ligands from a precursor or production of by-products) involved as the film is deposited.[4] A simple analogy would be to think of spray painting. Some examples of PVD techniques include Pulsed Laser Deposition (PLD), Molecular Beam Epitaxy (MBE), and sputtering.

One specific type of PVD is sputtering. Here, a biased metal target plate is bombarded by energetic ions (typically Ar^+) generated from a plasma created in front of the target. The impact of these energetic ions causes the removal (or "sputtering") of target atoms, which may then condense on a substrate placed some distance away (a few cm) as a thin film. Because the ejected atoms must travel some distance, the background sputtering gas pressure is an important parameter to control as it affects the mean free path of the sputtered atoms. Secondary electrons

are also emitted from the target surface as a result of the ion bombardment, and these electrons play an important role in maintaining the plasma.[5] Historically, the sputtering process has been somewhat limited by low deposition rates, low ionization efficiencies in the plasma, and high substrate heating effects. Several of these limitations have been overcome, however, with the introduction of magnetron sputtering.[6,7]

Magnetrons make use of the fact that a magnetic field oriented parallel to the target surface can confine secondary electron motion to near the target. Magnets are arranged in such a way that one pole is positioned at the central axis of the target and the second pole is formed by a ring of magnets around the outer edge of the target. Trapping the electrons in this way substantially increases the probability of an ionizing electron-atom collision occurring. This increased ionization efficiency results in a more dense plasma in the target region, which leads to increased ion bombardment of the target. Magnetron sputtering has the benefit of higher sputtering rates and, therefore, higher deposition rates at the substrate. In addition, the increased ionization efficiency achieved by using magnetrons allows the discharge to be maintained at lower operating pressures (typically 10^{-4} Torr) and lower operating voltages (typically 500 V) than is possible without them.[8] A generalized schematic for the reactive magnetron sputtering process is shown in Figure 4.1.

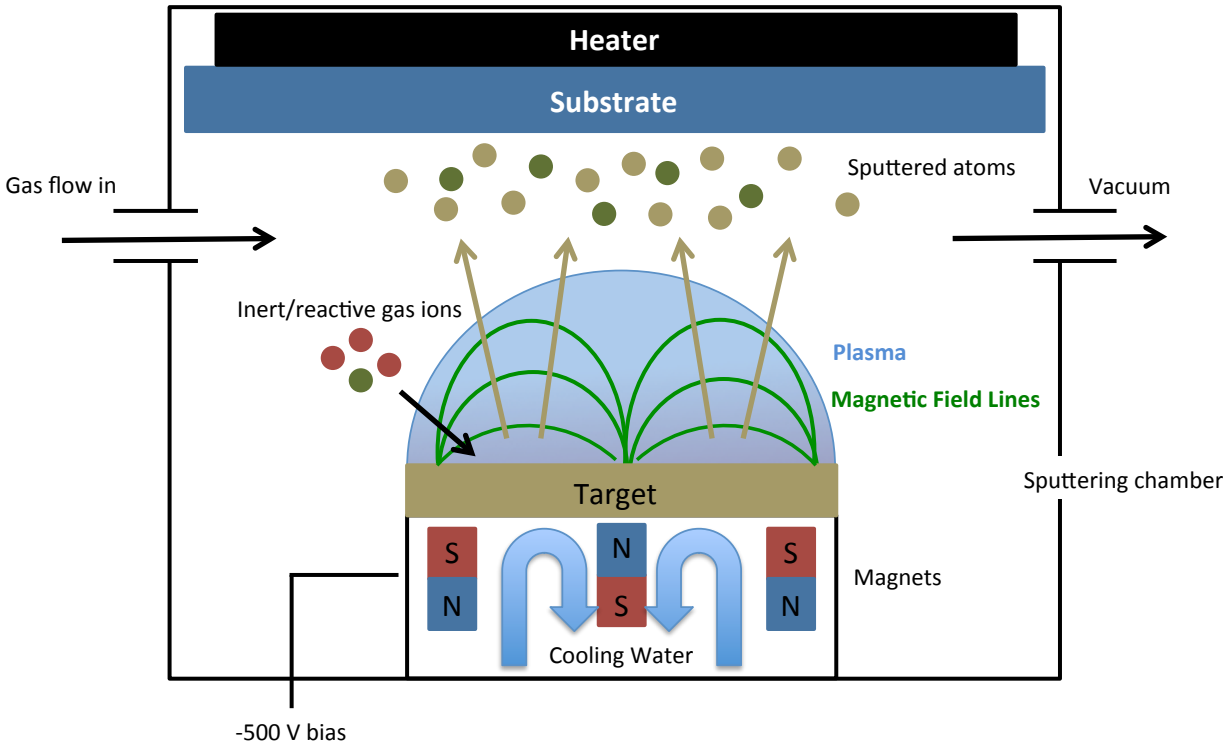

Figure 4.1. Schematic of reactive magnetron sputtering. Inert and reactive sputtering gases (Ar and N_2, respectively) are flowed into the sputtering chamber (red and green dots) and drawn to the biased magnetron sputtering gun. These gaseous atoms are ionized and impact the target, ejecting target atoms which travel to the heated substrate and are deposited. Reactive sputtering gas ions are co-deposited with the target atoms to generate the nitride compound. The magnets in the magnetron control the plasma which is generated and aid in control of secondary electron generation and some target contamination. The magnetron bias can be tuned to control sputtering rate, which can ultimately affect film quality and density.

Specifically for the preparation of nitride films, a reactive sputtering gas (typically N_2) is introduced into the sputtering chamber at a specified mole fraction (or partial pressure) in addition to the inert sputtering gas (typically Ar). Both gases are continuously flowed into and pumped out of the chamber to achieve a sputtering pressure typically on the order of 10^{-3} Torr. By controlling the fraction of the reactive gas (N_2) the stoichiometry of the films can be controlled, and to some extent the amount of time needed for depositing a film of a certain thickness can be modified. A more detailed discussion of the physics and experimental parameters of reactive sputtering is available elsewhere.[9-12]

An important concern in any deposition technique is the purity of the deposited material. For PVD techniques, the most common cause of film contamination is the incorporation of reactive gaseous species in the deposited film. For nitrides, this takes the form of residual oxygen in the chamber generating oxygen impurities in the film. While performing depositions in an ultra-high vacuum (UHV) practically eliminates this concern, common UHV practices such as using load-locks and performing long pump downs and bake-outs after system venting are impractical for many studies. Furthermore, using combinatorial, high-throughput methods, which require frequent substrate and sputter target changes makes traditional UHV work highly impractical.[13]

Getter sputtering was developed in the 1960s by Theuerer and Hauser and eliminated the need for UHV chambers for thin film preparation.[14] In this technique, a "shroud" was cooled with liquid nitrogen and was placed around the sputtering source. During sputtering, any reactive gases within the sputtering chamber were physisorbed to the shroud and remained there due to the cryogenic temperature of the metal. Using this technique enabled the production of high-quality, low-impurity films in sputtering chambers with a base pressure of only 10^{-6} Torr

(UHV chambers typically have a base pressure on the order of 10^{-11} Torr). Getter sputtering was further advanced by van Dover[15,16] who expanded the "shroud" technique to a three-source deposition system for studying linear composition spreads of amorphous transition metal/rare-earth alloys. Using getter sputtering ultimately generates an *effectively* UHV environment "where it counts", locally around the substrate.

Using the concept of getter sputtering, a former Graduate student and EMC^2 collaborator Dr. John Gregoire developed and built a customized DC magnetron sputtering system called "Tubby". The ins-out-outs of Tubby's design are described elsewhere.[17] Most importantly, Tubby was designed to prepare combinatorially sputtered metal thin films for discovery of new catalyst compositions for PEMFC anode catalysts. Tubby features a 4-gun magnetron sputtering array (featuring 2" magnetron sputtering guns, three oriented 120º apart at a 15º "take off angle", the fourth oriented parallel to the substrate) which allows for the synthesis of ternary and quaternary metal thin films that have a spread in composition of approximately 1 at% mm^{-1}. Depositing such a film on a typical 3" Si wafer substrate enables one to simultaneously synthesize compounds that have compositions that span a large portion of their ternary or quaternary phase diagrams. Additionally, if a reactive sputtering gas is introduced, compounds with up to 5 different elements could potentially be synthesized, further expanding the versatility of such an apparatus. In addition to the 2" guns, Tubby is also outfitted with an ion gun (for cleaning substrates) and a 4" magnetron sputtering gun (used to deposit Ti or Ta adhesion layers to the substrates before film deposition). Surrounding the 4-gun array is a liquid N_2-cooled cryoshroud, which removes impurities in the sputtering gases and enables getter sputtering as previously described. Furthermore, Tubby is outfitted with a 3-substrate sample stage each fitted with custom substrate heaters, enabling the simultaneous annealing and deposition of up to 3

films per pump down. A schematic of the insides of Tubby is shown in Figure 4.2[17]. (Reprinted with permission from Gregoire, J. M., van Dover, R. B., Jin, J., DiSalvo, F. J., et al. Getter sputtering system for high-throughput fabrication of composition spreads. *Rev. Sci. Instrum.* **2007**, 78(7), 072212. Copyright 2007, American Institute of Physics.)

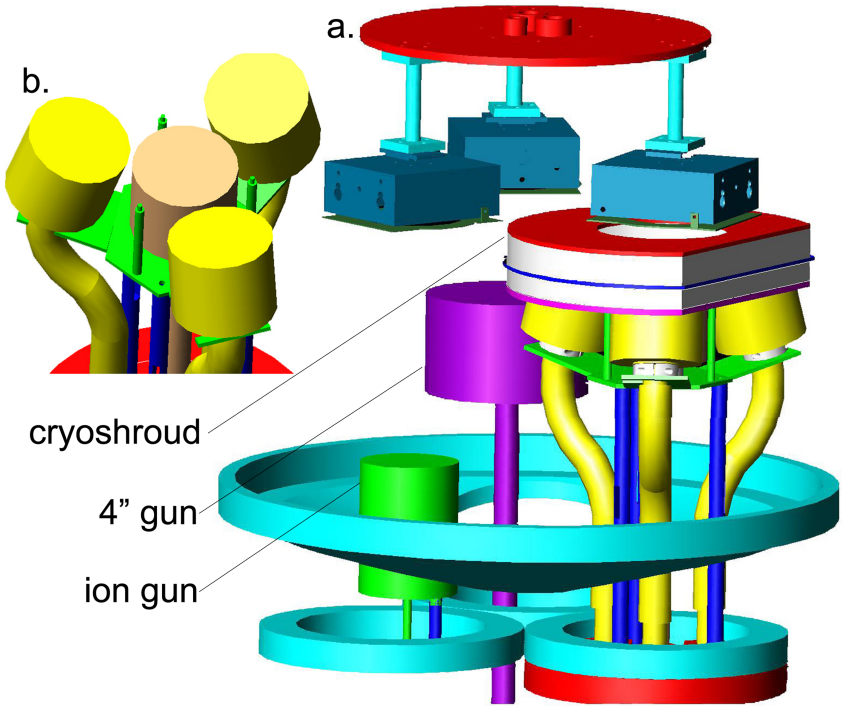

Figure 4.2 (a) The three custom substrate heaters on their rotating mounting plate are pictured with the ion gun, 4" gun, and four-gun assembly as positioned in the deposition system. (b) A detailed look at the arrangement of the four-gun assembly. *Reprinted with permission.*

4.3 Scanned Probe Microscopy

As discussed in Chapter 3, nitride compounds are stabilized by an oxidized surface passivation layer, and the structure, composition, and morphology of this passivation layer is important for oxidation stability in electrocatalyst applications.[18-22] While Chapter 3 focused on measurement techniques that give ensemble properties, accurately describing the oxidation behavior of nitride based supports requires the application of surface sensitive analytical techniques. Among these techniques are scanned probe methods, and variety of spectroscopic techniques including: X-ray absorption, X-ray photoelectron spectroscopy (XPS), Surface Enhanced Raman (SERS), Optical, IR and other photoemission spectroscopies. [23-25]

Applying surface analysis techniques that probe by excitation of sample surface-atoms with photon or particle beams (such as X-rays, ion beams, or electron beams) can limit sample analysis time and data resolution.[26] Often, to obtain high-quality data, such techniques may cause destruction of the sample or a significant change in the probed property (so-called "beam damage").[27] Scanned probe microscopy (SPM), on the other hand, is useful for limiting sample damage while obtaining quality images of sample surfaces with high-resolution.[28]

The popular types of SPM are scanning tunneling microscopy (STM) and atomic force microscopy (AFM).[29] STM can be used to obtain electrical characteristics of individual nanoparticles or film domains, while AFM is generally useful for determining the shape, texture, and roughness of a surface.[29,30] Several reports for AFM imaging of nanoparticles and mesoporous solids are available[30-39], but measuring such highly textured sample morphologies is non-ideal.[31,40] AFM is best suited for the imaging of low roughness, nearly atomically flat samples.[41] Such imaging studies are standard practice for AFM experiments, and atomic scale resolution is often achievable.[29,42]

Several different AFM modes (or measurement techniques) are available and are selected based on the material-property of interest, as well as the size and shape of the sample. One such mode is conductive probe AFM (cp-AFM), which is used to measure the conductivity in correlation to the spatial features of the sample.[29,43,44] A thorough discussion of cp-AFM technical specifications, experimental parameters, and methods for interpreting results is available in the literature.[44] Generally though, a sample is placed on an actuated XY stage and electrically connected with the cp-AFM probe head. A small negative bias (typically – 50 mV) is placed on the sample; the probe tip is lowered, makes contact with the sample surface, and a constant tip-sample force (10 nN in this case) is maintained by measuring the deflection of the cantilever (thus completing the circuit, with the insulating oxide layer acting as a "resistor" between the probe tip and the sample). The tip is then rastered in X and Y over a small sample area (typically 1 μm^2). The current between the sample and cp-AFM tip is measured and plotted with false-color intensity as an "image" or XY map. It is important to note that in this mode of operations, the tip closely approaches the surface (within a few nm) but does not "contact" the surface. Under the appropriate bias, electrons tunnel through the intervening space between the tip and the film surface, thus the measured current is a tunneling current. Simultaneous topography or phase imaging is also possible due to the tip-height feed back control available on most commercial AFM instruments.[44] Comparing the conductivity "image" with a topography "image" allows one to compare electrical properties with surface morphology or topology.

The technique has been extensively used to study surface oxidation on a variety of thin film oxide and nitride materials for applications in the semi-conductor industry.[45-56] Additional reports for cp-AFM studies of oxide layer thickness on metal nanoparticles are also available.[57,58] Because of its reported utility in studying the characteristics of oxide layers, cp-AFM was

employed in our study of transition metal nitride thin films. A schematic of a generalized cp-AFM experiment is shown in Figure 4.3 (courtesy of Dr. James O'Dea and Dr. Chinmayee Subban).

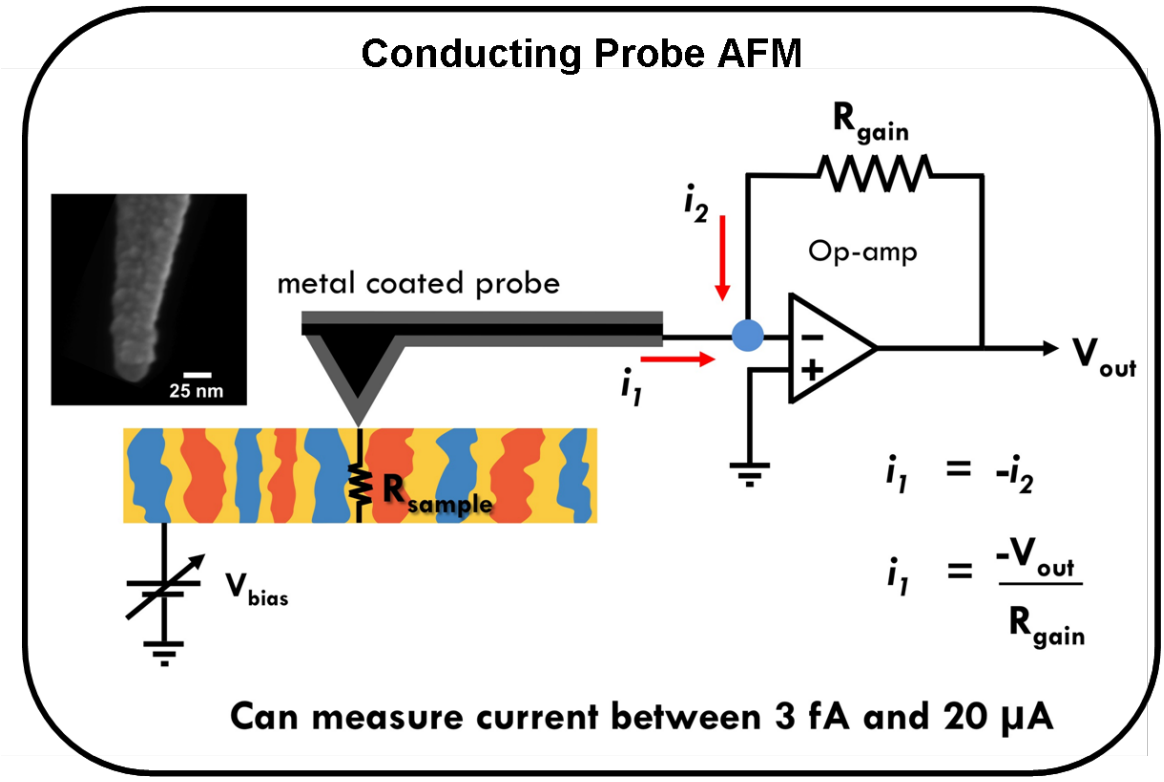

Figure 4.3 A cartoon schematic depicting the general conductive AFM set-up used to measure conductivity in correlation to the spatial features of the sample. An SEM image of a c-AFM tip is shown in the inset. (Figure courtesy of Dr. James O'Dea and Dr. Chinmayee Subban)

4.4 Preparation and Characterization of Ti-Al-Ta Nitride Thin Films

The material requirements for new PEMFC catalyst supports have already been discussed. To review, new catalyst support materials must be conducting (at least 0.1 S cm^{-1}), porous, and stable under PEMFC operating conditions (pH < 1 up to 1.5 V versus SHE).[59,60] Oxides[61-63], nitrides[64,65], and carbides[66-68] have been extensively studied as potential replacements for carbon-based catalyst supports, and have been shown to catalyze hydrogen oxidation[67] and oxygen reduction[69-71] without the addition of Pt (or other catalysts). These findings are significant as supports based on catalytically active oxide or nitride materials may enable the lowering of Pt (or other catalyst) loadings, which may potentially lower the cost of PEMFCs to commercially viable levels (Pt still accounts for 20-24% of PEMFC cost).[72] Furthermore, oxide and nitride materials with suitable durability, catalytic activity, and electrical conductivity for catalyst support applications have been observed independently, yet developing a material with a combination of these properties has rarely been achievable[73,74] (although the DiSalvo group recently reported a conducting, doped-oxide material which reduced CO poisoning on Pt catalysts but was not stable upon repeated cycling[63]).

It was hypothesized that because of the passivation behavior observed for early transition metal nitrides, titanium nitride-based compounds containing Ta and Nb (which would convert to Nb and Ta surface oxides upon passivation) may be more oxidatively stable due to the thermodynamic stability of the Nb and Ta oxides (ΔG_f^o = -1766.0 kJ mol^{-1}, ΔG_f^o= -1911.2 kJ mol^{-1} for Nb_2O_5 and Ta_2O_5 respectively).[75] Furthermore, Ta oxynitrides (TaO_xN_y) have been reported to possess activity for ORR without a need for Pt.[76,77] Therefore incorporating Ta may increase catalytic activity for Pt/Ti-Ta-Al-N films or catalysts (assuming an appropriate composition of Ti-Ta-Al nitride can be discovered).

In addition to Ta and Nb, Al was also predicted to enhance the corrosion stability of TiN-based thin films. Aluminum nitride (AlN), unlike its early transition metal cousins, is an "insulating" nitride (E_g= 6.2 eV, direct) with a hexagonal (rather than cubic) structure.[78] However, upon passivation AlN has a reported thermal stability up to 1370 ºC in air.[78,79] This high temperature stability is attributed to the formation of Al_2O_3 (ΔG_f = -1582.3 kJ mol^{-1})[75] in a "thick" surface passivation layer (~10 nm).[79,80] There have also been reports of enhanced oxidation stability of TiAlN coatings for corrosion resistant steels.[81,82] Additionally, Al (as well as Si, B, and perhaps Cr) may selectively diffuse to grain boundaries in the nitride films, resulting in increased mechanical strength and reduced ability of O_2 to diffuse along grain boundaries causing further oxidation.[83-89]

Guided by these principles, thin films of Ti-Ta-Al nitride were prepared using the combinatorial magnetron sputtering chamber, "Tubby". The goal was to combinatorially prepare and screen a variety of compositions of ternary metal nitrides to find the composition(s) that yielded the best mix of properties (conductivity, corrosion stability, catalytic activity). Furthermore, the formation of the passivating oxidation layer was "controlled" by introducing a small amount of oxygen into the deposition chamber and annealing the sputtered thin films after nitride film deposition. By keeping the passivation layer thin, the high conductivity of the nitride film could be exploited by electron tunneling while being protected by the insulating passivation layer. Figure 4.4 shows the general scheme of the film preparation and screening using conductive probe AFM.

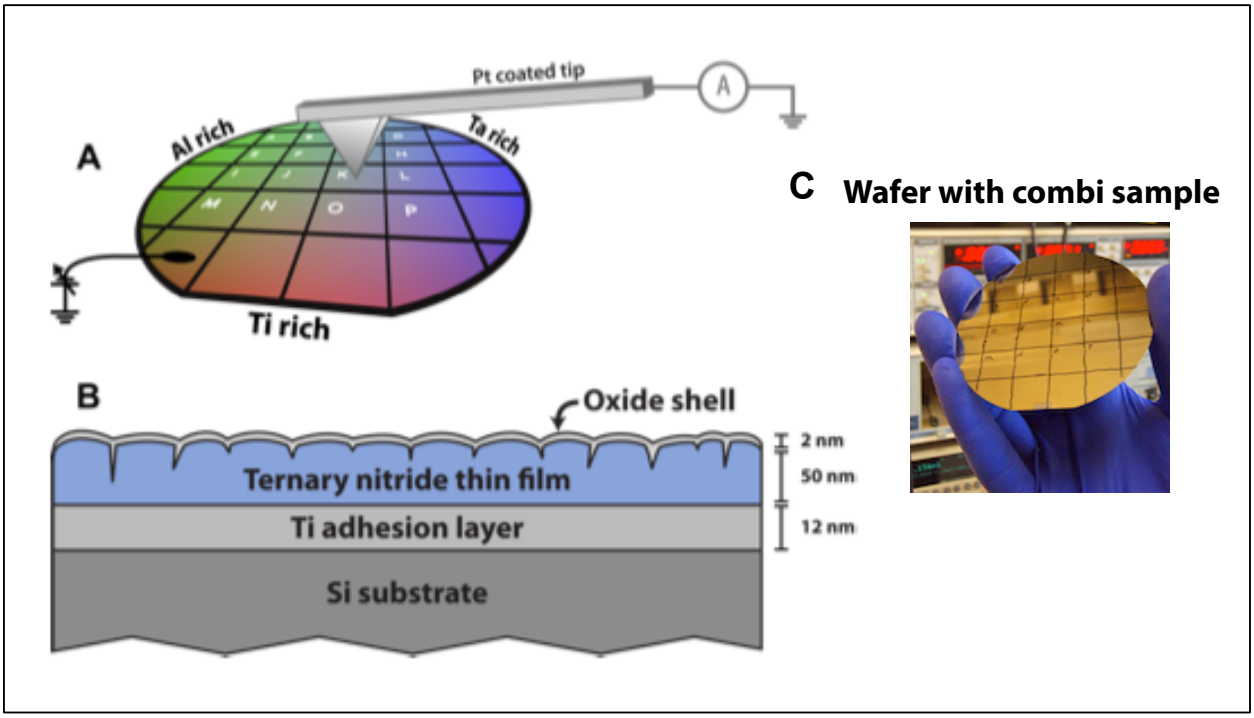

Figure 4.4 (A) Illustration of a combinatorially sputter deposited nitride thin film showing the composition gradient over the sample. Note the Al-rich (green), Ta-rich (blue), and Ti-rich (red) regions. The color mixing across the film is a visual analogy for the compositional gradient that is created by sputtering from the specially designed sputter system. The tip illustrates the cp-AFM tip used to prove the sample surface. (B) Cross-sectional view showing pertinent dimensions of the nitride films studied in this work. (C) Photo of deposited film prepared for cp-AFM analysis. *Image courtesy of Dr. James O'Dea.*

4.4.1 Film Deposition

(This section represents work conducted by Anna Legard, Abigail Van Wassen and Raymond Burns, and was written by Anna Legard as part of a manuscript in preparation for publication.)

Nitride thin films (50 nm thick) were prepared in a custom built combinatorial sputter deposition system.[17] Films were deposited on a 12 nm thick Ti adhesion layer on a 76.2 mm diameter Si substrate in an atmosphere of 0.67 Pa Ar. The substrate was radiatively heated at 400 ºC during the deposition. Elemental Ta, Ti, and Al (>99.9% purity) were co-deposited from separate magnetron sputter sources (Angstrom Sciences) in an atmosphere of 1.0 Pa Ar/N_2 (13% N_2). During deposition, the background pressure remained approximately 10^{-5} Pa through use of a cryoshroud.[17] The geometric relation of the deposition sources with respect to the Si substrate provided a deposition gradient from each source that upon co-deposition resulted in a continuous variation in composition across the substrate. Prior to film deposition, the deposition rate of each element was measured at the center of the substrate using a quartz crystal monitor. After film deposition, the sputtering chamber was evacuated, and the substrate cooled to 250 ºC. Oxygen was introduced into the chamber to a total pressure of 1 mTorr. The sample was held at 250 ºC for 1 hour in the oxygen atmosphere. The films were removed form the sputtering chamber, and immediately stored in an Ar filled glovebox pending further characterization.

4.4.2 Material Characterization

(This section represents work conducted by Anna Legard (electrochemistry), Abigail Van Wassen (electrochemistry), Raymond Burns (XPS), Megan Holts (EELS) and Dr. James O'Dea (cp-AFM) and was co-written as part of a manuscript in preparation for publication.)

Electrochemical stability measurements were performed using a small Teflon electrochemical cell (the so-called "scanning mini-cell") that isolated a 0.32 cm^2 area of the thin film for localized testing, as described by Gregoire et al.[90] The 6-mm inner diameter cell included a GRAFOIL® counter electrode and a Ag/AgCl reference electrode. Window-opening cyclic voltammograms (CVs) were performed on select regions of the film, revealing film stability from −0.5 V to 0.9 V vs. Ag/AgCl in 0.1 M H_2SO_4 (Sigma-Aldrich, 99.999% pure). Subsequent electrochemical stress testing involved cycling between these ranges at 50 mV/s. Four regions of the film were selected for such durability testing: three regions corresponding to areas rich in either Al, Ti, or Ta and one region in the center of the film, corresponding to an equal composition of each element. Each region was subjected to continuous electrochemical cycling for 2 hours.

Conductive probe atomic force microscopy (cp-AFM) images were taken with Pt coated cantilevers (MikroMasch, DPE17) with a +50 mV sample bias and tip-sample force of 10 nN (Veeco, D3100). Current amplifier gains of 1 nA/V and 100 nA/V were used to image regions with a current response below and above 10 nA, respectively.

Cross sectional TEM specimens were prepared by focused ion beam (FIB) lift out. Spectroscopic images were performed on a 100 keV Nion UltraSTEM, a 5th order aberration corrected microscope optimized for electron energy loss spectroscopy (EELS) imaging with a probe size of 1 Å, an EELS energy resolution of 0.6 eV, and a high usable beam current. Dual EELS allowed collection of two different energy ranges, allowing for simultaneous maps of C, N,

Ti, O, Al, and Ta, which were acquired with a 0.25 eV/channel energy dispersion.

X-ray Photoelectron Spectroscopy was performed on a Surface Science Instruments model SSX-100 with monochromated Al Kα X-rays (1486.6 eV), an operating pressure of 10^{-9} Torr, and a beam diameter of 1mm. Photoemitted electrons were collected at a 55º emission angle using a hemispherical analyzer with 150 V pass energy. Survey scans from 0-1000 eV were collected from a 7 x 7 spot square grid on the nitride film (49 total scans) to determine film composition (as a function of position) using the Ti 2*p*, Ta 4*d*, and Al 2*s* peaks. The collected data was analyzed using the CasaXPS software package, and the imbedded image processing algorithms were used to generate metal composition maps of nitride films.

4.5 Results and Discussion

(This section represents work conducted by Anna Legard (electrochemistry), Abigail Van Wassen (electrochemistry), Raymond Burns (XPS), Megan Holts (EELS) and Dr. James O'Dea (cp-AFM) and was co-written as part of a manuscript in preparation for publication.)

4.5.1 Conducting Probe AFM Studies

Using conductive probe atomic force microscopy as a high throughput tool to screen electrical conductivity, we have found that conductivity varies significantly with nitride film composition (Figure 4.5, courtesy of Dr. James O'Dea). For each sample, conductivity screening involved imaging sixteen 1 μm x 1 μm regions located approximately 12 mm apart, where the atomic % of each element is expected to change at ~1 at% mm^{-1}. Ti- rich regions exhibit the highest conductivity, and conductivity decreases as the amount of Al and Ta increases. These results agree with cp-AFM measurements of single element nitrides (Figure 4.5 bottom) where Ti-nitride thin films exhibit high electrical conductivity, while Al and Ta nitride thin films show insulating behavior.

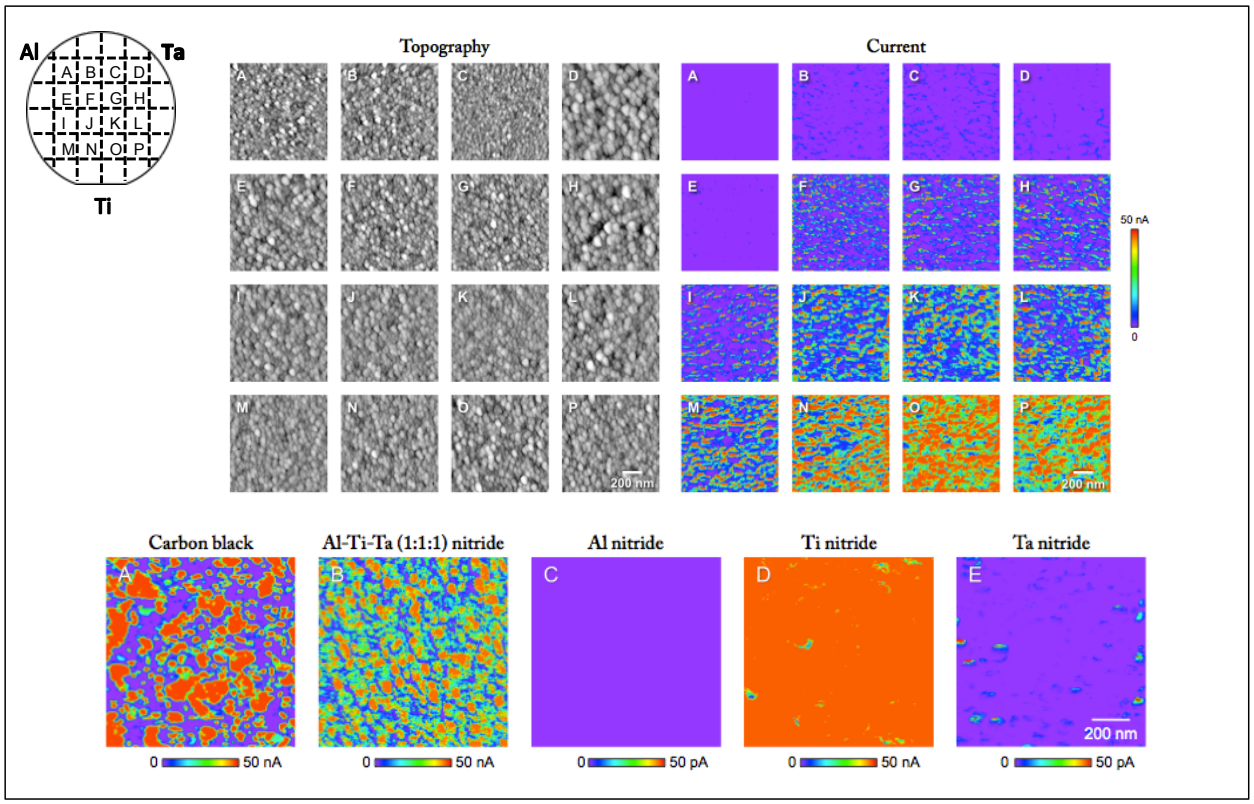

Figure 4.5 (top) Topography (left) and current (right) images of a combinatorial spread of Al-Ti-Ta nitride. Images were acquired in the center of the areas lettered in Figure 4.4, at a constant tip-sample force (contact mode) of approximately 10 nN, and at a sample bias of +50 mV. The inset in the top-left corner shows the orientation of the film with respect to the current and topography images as well as the location of the specified element rich regions of the film (i.e. Ti-rich near the Ti label, etc.). (Bottom) Current images of (A) carbon black (Vulcan XC-72) and (B) Al-Ti-Ta (1:1:1) nitride. (C)-(E) Current images of single element Al (C), Ti (D), and Ta (E) nitrides showing the insulating behavior of Al and Ta nitrides and the high electrical conductivity of Ti nitride. *Images courtesy of Dr. James O'Dea*

It is important to note that the color scale images show the relative amount of current passed at a given point rather than the conductivity of the film at that point. Several factors play a role in the observed current including the topology of the sample, tip-sample force, and the current amplifier gain of the cp-AFM instrument. The current images in Figure 4.5 were taken at the highest gain setting, meaning that 50 nA of current results in saturation of the current detector. The conductivity can be roughly calculated from this current using equation 4.1, which is derived from general sheet resistance theory.[91]

$$\rho = \frac{\pi}{\ln(2)} \times \frac{\mathrm{V}}{\mathrm{I}} \times t \times k \tag{4.1}$$

Equation 4.1 is typically used for 4-point probe measurements of semi-conductor thin film resistivity (ρ). However, the general terms necessary for a 1st order calculation are included. V is the applied voltage, and I the measured current. There are also geometric terms for the film thickness (*t*) and for the ratio of the probe size to the size of the film (*k*). The dimensionless term *k* can be approximated as the ratio of the wafer diameter to the probe diameter, and approaches a value of 1 in the infinite limit.[92] As the tip-size is small (a few nm) relative to the wafer (~75 mm diameter), a value of 1 was assumed for k . Plugging 50 nA and 50 mV into equation 4.1 for a film thickness of 50 nm gives a conductivity (simply the inverse of the resistivity) of approximately 4.5 S cm^{-1} for the most conducting regions of the film. Although using this formula does not fully describe the conductivity characteristics of the nitride films, it is important to understand that regions of the film that appear red in the cp-AFM current images can not be resolved into areas of higher or lower conductivity with the currently available instrumentation.

Importantly, even a small amount of Ti in the combinatorial sample imparts significant conductivity in regions otherwise rich in Al and Ta. This finding has considerable implications in designing materials with multiple functionalities by allowing incorporation of conductive materials with components that impart durability and/or catalytic enhancement, yet may not possess high electrical conductivity. We have found that even Al-Ti-Ta nitride compositions with equal atomic fractions of each metal has a conductivity $\geq$4.5 S cm^{-1} (as does carbon black) using cp-AFM (Figure 4.5, again realizing that red regions have saturated the detector), indicating these materials may be suitable for incorporation into fuel cells in terms of electrical conductivity.

Areas of low current in the image of carbon black (Figure 4.5A) correspond to low lying regions in the topography of the powder, where electrical contact between the tip and sample was insufficient for passage of current. Such influences of topography are expected for a powder with grains <100 nm in diameter. Additionally, up to 250 nm variations in topography maybe expected for the nanoparticle powder over the 1 μm x 1 μm region imaged. A wide swing in topography is not observed for the nitride thin film (they are much less rough as shown in the topography image of Figure 4.5), hence submicron variations in the current image of Al-Ti-Ta nitride in Figure 4.5 are not readily explained by variations in tip-sample contact. Therefore differences in conductivity must be due to variations in composition on the 10s to 100s of nm scale.

4.5.2 X-ray Photoelectron Spectroscopy

Figure 4.6 shows an XPS survey spectrum and 7 x 7 point composition maps for the Ti-Ta-Al nitride thin film. Figure 4.6 a-c shows single element composition maps for Ti (a), Ta (b)

and Al (c) using a 7 x 7 point grid across the 3" nitride film. Note that the areas of highest intensity (white color) are approximately 120º apart which corresponds well with the orientation of the magnetron sputtering guns from the film deposition. The orientation of the substrate for XPS analysis is not the same as for cp-AFM (the Ti-rich region of the film is in the top right corner, rather than along the bottom of the image). It is important to note that the composition does not appear to change at 1 at% mm^{-1}, as was previously predicted, and observed for ternary metal thin films. While the general trend of a concentration gradient is preserved, each concentration gradient is non-uniform (at least at the surface). As XPS only probes the top 1-2 nm of the surface, it's possible that deeper into the film the composition gradient is preserved, and is more uniform in nature. Figure 4.7 shows the quantified composition of the film at each point, and demonstrates the relative rates of change across the film (the distance between each point is 12 mm).

Figure 4.6d shows a wide band survey spectrum from one of the 7 x 7 grid points. Each peak in the spectrum is accounted for, while only the Ti 2*p*, Ta 4*d*, and Al 2*s* peaks were used for quantification. Note that O 1*s* and N 1*s* peaks are also visible. Including the N 1*s* signal in data quantification was performed; however, generating the composition images is currently limited to three simultaneous comparisons (hence the metals are shown here for clarity). The O 1*s* and C 1*s* signals are generally observed in all XPS experiments due to carbonaceous species and water vapor that is adsorbed on to the sample. Because of these artifacts, quantifying O or C in a sample is difficult using XPS, without first ion milling the sample to remove the first 2-3 nm of the surface. Because of the difficulty in quantifying O, accurate measures of surface oxidation and nitrogen content are difficult by XPS and were not performed. Future XPS measurements on these films should include ion milling (so-called "depth profiling") and high energy resolution

scans over the Ti, Ta, and Al signals to more quantitatively understand their oxidation state and associated O or N as a function of position on the film (i.e. composition).

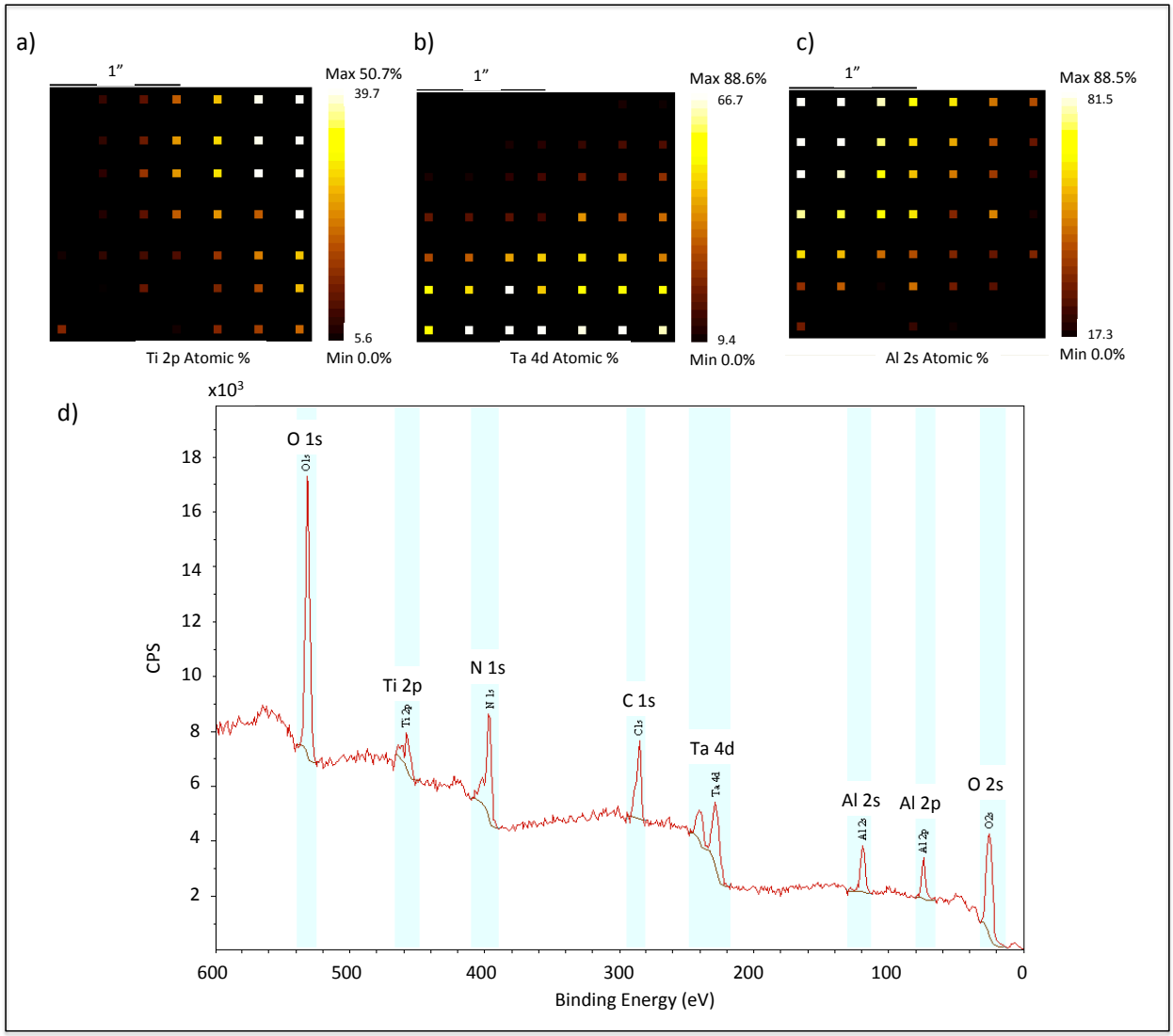

Figure 4.6 X-ray Photoelectron Spectroscopy of a Ti-Ta-Al nitride thin film. (a-c) Single element XPS maps on a 7 x 7 point grid across the 3" nitride film. Note the areas of highest intensity for each element (white colored) are 120 º apart matching the orientation of the sputtering guns from film deposition. The orientation is different form the current images due to sample mounting in the different instruments. The false color intensity represents the Atomic % of each element at that point, normalized to 100% composition (each element is analyzed simultaneously). (d) A representative XPS survey spectrum from one of the 7 x 7 grid points. Note that all the peaks can be identified, but only the Ti 2*p*, Ta 4*d*, and Al 2*s* were used for quantification. The C 1*s* signal is typical of XPS signals and arises from carbonaceous species in the air that adsorb to the sample surface prior to analysis.

Figure 4.7 a and b shows a convolution of the Ti 2*p*, Ta 4*d*, and Al 2*s* signals from the 7 x 7 point grid. The color at each point represents a weighted RGB color combination, with the color weights corresponding to the composition of the film surface at that point. It is important to note that the composition at each point is normalized to 100%. Figure 4.7b (courtesy of Dr. James O'Dea) shows the normalized metals content at each point in the grid. The most important feature of this plot is that that composition of the metals does not change at the expected 1 at% mm^{-1} that has been observed for metal films. The exact reason for this departure from the previously observed composition gradient[93,94] is unknown, but may be partially due to differing sputter rates from Ti, Ta, and Al, and diffusion within (or at the surface) the film upon deposition.

Since only the metals are compared (and not oxygen or nitrogen), the composition at each point is more semi-quantitative, and does not reflect the true composition of the film. Overall, however, the expected behavior is observed, in that there are three distinct regions of the film that are more rich in one element than the others (red, green, and blue regions of the image in Figure 4.7) and areas near the middle that combine all three. Using this information in combination with the current image shown in Figure 4.5 may give important insights into the necessary (metals) composition of a nitride material that yields the best mix of corrosion stability and conductivity at the surface.

a)

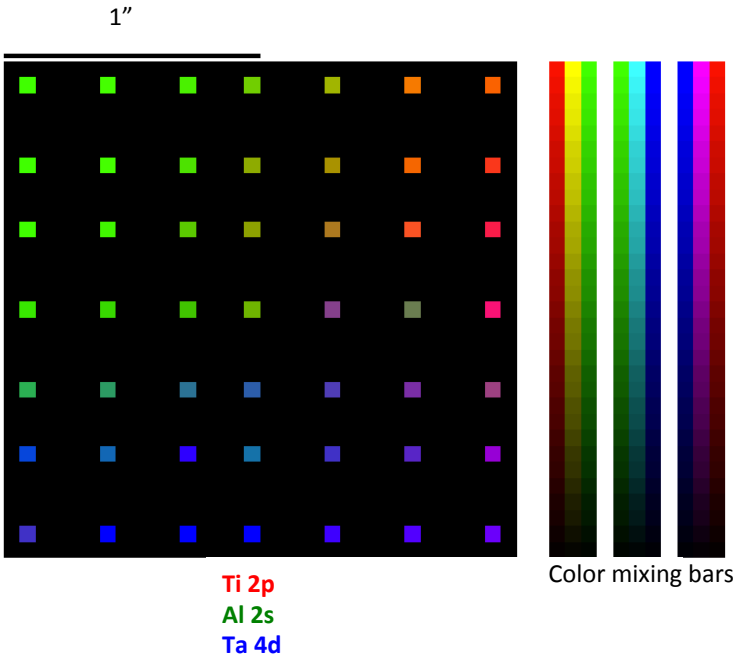

b)

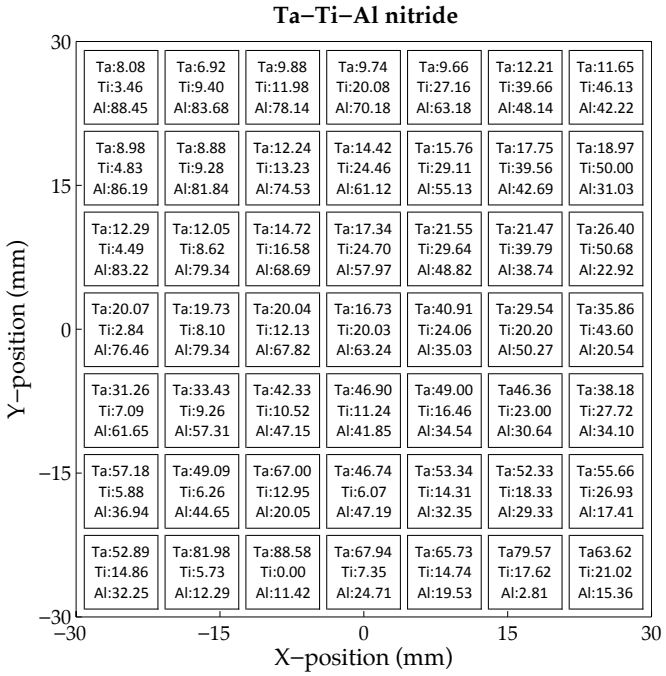

Figure 4.7 (a) Convolution of Ti, Ta, and Al signals for the 7 x 7 point grid. The color is derived from the fraction of each element detected at that point on the sample and applied to a fraction of red, green, and blue for Ti, Ta, and Al respectively. The color mixing bars to the right of the image may aid in visualizing changes in composition across the film. (b) Data from (a) with atomic % of each metal at each point. NB each point is normalized to 100%. *Image courtesy of Dr. James O'Dea*

4.5.3 Elemental Mapping

Electron Energy Loss Spectroscopy (EELS) can be applied to two-dimensional imaging, and allows for the point-by-point mapping of elemental composition at the atomic scale. Using a 5th order aberration corrected STEM, EELS maps of Ti, Ta, Al, O, and N signals from a cross-section of the nitride thin film (obtained by Focused Ion Beam (FIB) milling) were plotted (Figure 4.8, Image courtesy of Dr. James O'Dea and Megan Holtz).

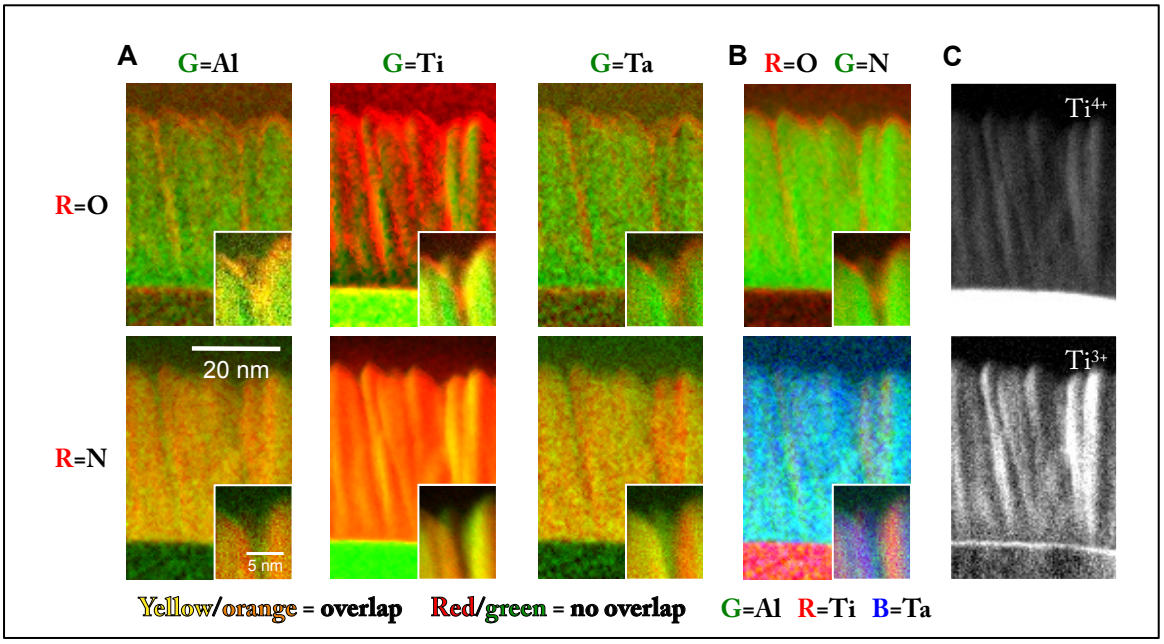

Figure 4.8 Two-dimensional electron energy loss spectroscopic (EELS) imaging on a 5th order aberration corrected electron microscope. (A) EELS maps showing the correlation between each metal and oxygen and nitrogen. (B) EELS maps showing correlation between oxygen and nitrogen (top) and AL, Ti, and Ta (bottom). (C) EELS maps of Ti4+ and Ti3+. All images in (A)-(C) correspond to the same area of the film. *Images courtesy of Dr. James O'Dea and Megan Holtz*

Figure 4.8A showed false color overlays of the metal (Ti, Ta, or Al in green) overlaid with the oxygen or nitrogen signal (in red). Pixels where both the metal and O (top) or N (bottom) were detected appear yellow. It is important to note that one can not conclude that chemical bonds exist between the metal and non-metal from the images shown in A, but simply that both are detected in that same pixel. Higher energy resolution EELS images (like those shown in Figure 4.8C) are required to determine chemically specific information such as bonding.

Several important features can be observed in Figure 4.8A. Firstly, the columnar grain structure of the film is readily visible. Furthermore, it appears that there is a significantly higher O concentration at the surface and at the grain boundaries of the film. This makes since, as the primary mechanisms for the oxidation of nitride thin films have been reported to proceed by diffusion of oxygen along grain boundaries.[95,96] Additionally, the significant overlap of N and metal signals in Figure 4.8A (bottom) indicates that the film has more nitride than oxide character, and that the oxygen content is limited to the surface and grain boundaries. This is further bolstered by looking at Figure 4.8B (top) where the O (red) and N (green) signals are overlaid. Here there is very little (if any) overlap (would be yellow if observed), and a majority of the O signal is isolated to the surface and grain boundaries of the film. It is interesting that very little yellow is observed in the N/O overlay. This indicates limited oxynitride character of the bulk film, while the surface does have mixed oxide/oxynitride character.

Figure 4.8B (bottom) shows an overlay of the three metal signals from the EELS images. The most interesting feature here is that there does appear to be some phase segregation among the different columnar grains of the film. Some grains appear richer in Ti (red colored) than in Ta or Al (blue-green color). The large red band near the bottom of Figure 4.8B (bottom) is due to the Ti adhesion layer that was deposited before the nitride film. An additional observation one

can make is that the surface oxidation layer appears to be richer in Al and Ta than Ti. This, too, make sense because of the higher oxophilicity of Ta and Al relative to Ti, and because of the predicted thermodynamic stability these oxide coatings would provide to nitrides of Ta and Al.

Finally, Figure 4.8C shows high-energy resolution EELS images for Ti. Small shifts in the EELS energy allow Ti^{4+} and Ti^{3+} to be distinguished in the image. It can be seen that the bulk of the film exists as Ti^{3+} (the nitride), while the surface and grain boundaries have more Ti^{4+}. Ti^{4+} can still be observed in the bulk of the film, yet the intensity of the signal is much lower than Ti^{3+}. Overall, the higher concentration of Ti^{3+} in the bulk of the film lends to higher conductivities observed in cp-AFM, while changes in composition for different grain boundaries and the higher O content for Al and Ta rich domains may explain areas of low current in the cp-AFM images (because such domains are more insulating that Ti rich domains).

High-resolution EELS line profiles were also conducted, and reveal that oxygen concentrated at the surface is limited, spatially, to the top 2 nm of the film surface (Figure 4.9). This finding represents the first evidence our group has obtained showing the limited oxidation of a nitride support material. As the line scan enters the film, the FWHM of the O signal is 1.6 nm, and fluctuates only between 1.5 – 2 nm in each of the 16 regions shown in Figure 4.5. The C signal is an artifact from the sample preparation. The spike in concentration at the surface is unmistakable, and validates previous literature reports of the passivating oxide layer that forms on the surface of nitride materials. Additionally, the fact that the O is limited to the top ~2 nm indicates that the post-deposition annealing of the sample in O_2 may be important to control the thickness of this layer. Further experiments are required (such as annealing without O_2 and having no additional anneal at all) however, before firm conclusions can be drawn.

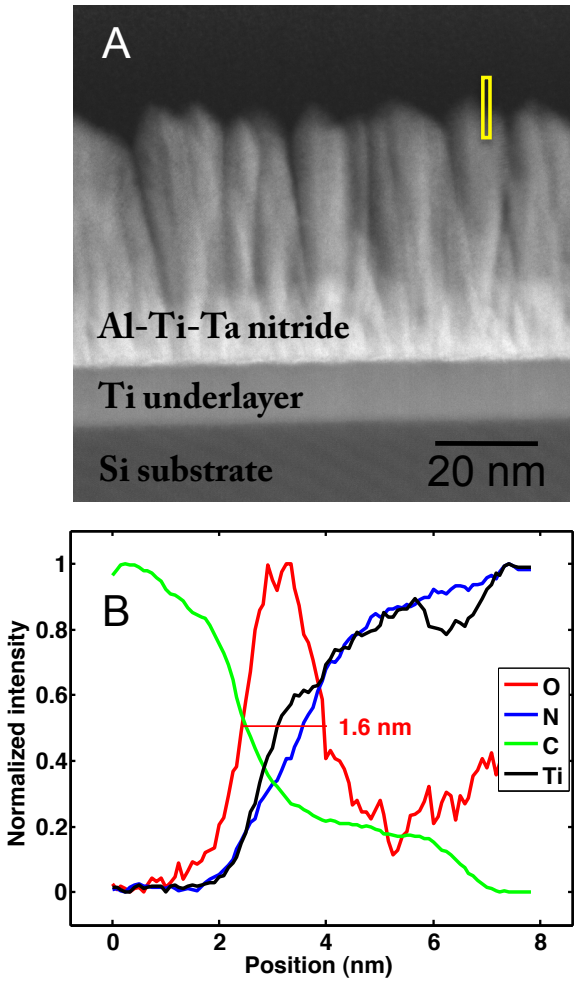

Figure 4.9 (A) HAADF STEM image of a cross section of a al-Ti-Ta (1:1:1) nitride thin film. (B) Composition line profiles acquired from electron energy loss spectra taken in the region covered by the yellow box. The oxygen signal has a FWHM of 1.6nm, indicating oxidation is limited to the outermost region of the Al-Ti-Ta nitride film. Composition line profiles acquired over several other areas indicate an oxide thickness of 1.5-2.0nm. *Image courtesy of Dr. James O'Dea and Megan Holtz*

4.5.4 Durability Testing

In an effort to simulate the potentials and pH experienced by catalyst supports in PEM fuel cells, Al-Ti-Ta nitride films were electrochemically cycled in 0.1 M H_2SO_4 from −0.5 V to 0.9 V vs. Ag/AgCl at 50 mV/s for 2 hours using the "scanning mini-cell" which isolates a 0.32 cm^2 area of the film. Four regions of the film were subjected to this durability testing: three regions rich in Al, Ti, or Ta and one region in the center of the film, corresponding to an equal composition of each element (Figure 4.10).

The lighter colored scans in Figure 4.10 represent the initial cycles, while the darker scans represent the activity after 2 hours of cycling. In all but the Ti-rich region, current at the positive region of the sweep decreased over time indicating further oxidation of the thin film. It is important to note however, that the decreased current does not indicate that metals are dissolving from the film, but rather that the oxide layer is growing thicker. If metals were dissolving the currents would be expected to increase. Furthermore, each region of the film appears to remain conducting as there is not a significant change in the double layer capacitance or a change in slope of the CV indicating increased resistivity.

Abigail Van Wassen is conducting additional electrochemical experiments on these films, while these preliminary results indicate that Ti-rich compositions are the most stable toward PEMFC-like conditions. Furthermore, experiments with Ti-rich films in alternative electrolytes and at higher temperatures should be investigated due to the leaching of Ti in SO_4^{2-} containing electrolytes[97,98], and the limited stability of TiN-based catalyst supports in SO_4^{2-} and ClO_4^- electrolytes above 60 ºC.[18]

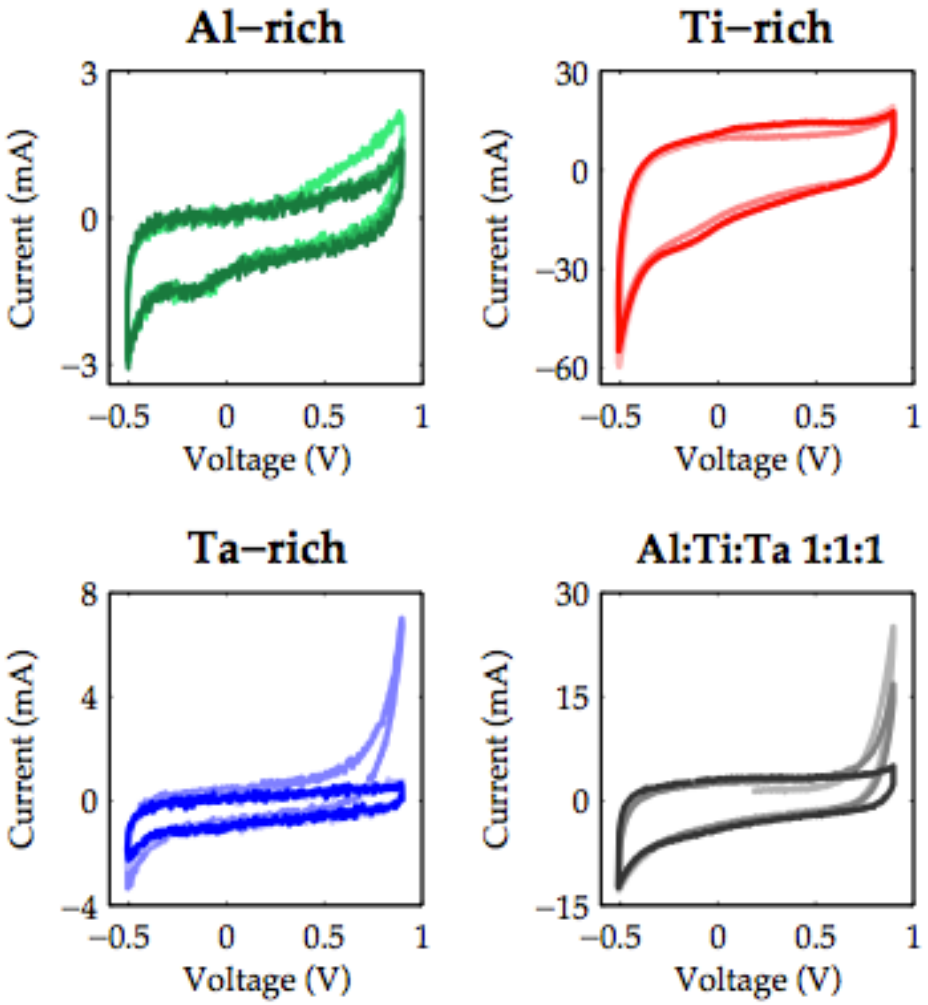

Figure 4.10 Cyclic voltammograms (CVs) taken over four different 0.32 cm^2 areas of the combinatorially prepared Al-Ti-Ta nitride thin film. Each location of the film was cycled continuously for 2 hr from -0.5 V to 0.9 V versus Ag/AgCl at 50 mV s^{-1} in 0.1 M H_2SO_4. Light colored scans correspond to the current response in the initial sweep and dark colored scans to sweeps made after 2 hr. of cycling. *Image courtesy of Abigail Van Wassen, Anna Legard, and Dr. James O'Dea*

4.6 Summary of Additional Experiments

In addition to Ti-Ta-Al nitride films, several other metal combinations are currently being investigated using the techniques described in this chapter. A few preliminary results from these experiments are presented in this section for completeness without an extensive discussion. Again this section represents the collaborative efforts of the researchers already mentioned in this chapter.

4.6.1 Ti-Nb-Al and Ti-Cr-Nb Nitride Films

In addition to Al-Ti-Ta nitride films, nitride films of Al-Nb-Ti and Cr-Ti-Nb were also prepared and studied by cp-AFM. Figure 4.11 shows current (top) and topography (bottom) images of each of the films (the data for Al-Ti-Ta nitride is the same as that shown in Figure 4.5). Interestingly, Ta and Nb behave differently, in that there is a wider range of compositions that are more conducting for Nb containing compositions than for the Ta. Furthermore, Cr-Ti-Nb has an even wider range of compositions that appear conducting by cp-AFM. The topography images are not significantly different for either of the films (the Al-Ti-Nb film may be slightly less rough), indicating that the differences in conductivity are not due film grain morphology. It is important to note again that the red regions of the current images represent a saturated current detector and convert to a conductivity of roughly 4.5 S cm^{-1}. Compositions in red may be significantly more conducting, but must be studied by other techniques to draw firm conclusions. Experiments on these films are on going, yet Cr-Ti-Nb nitrides appear to be the most promising in terms of high conductivity. Corrosion stability testing of these films has also been planned.

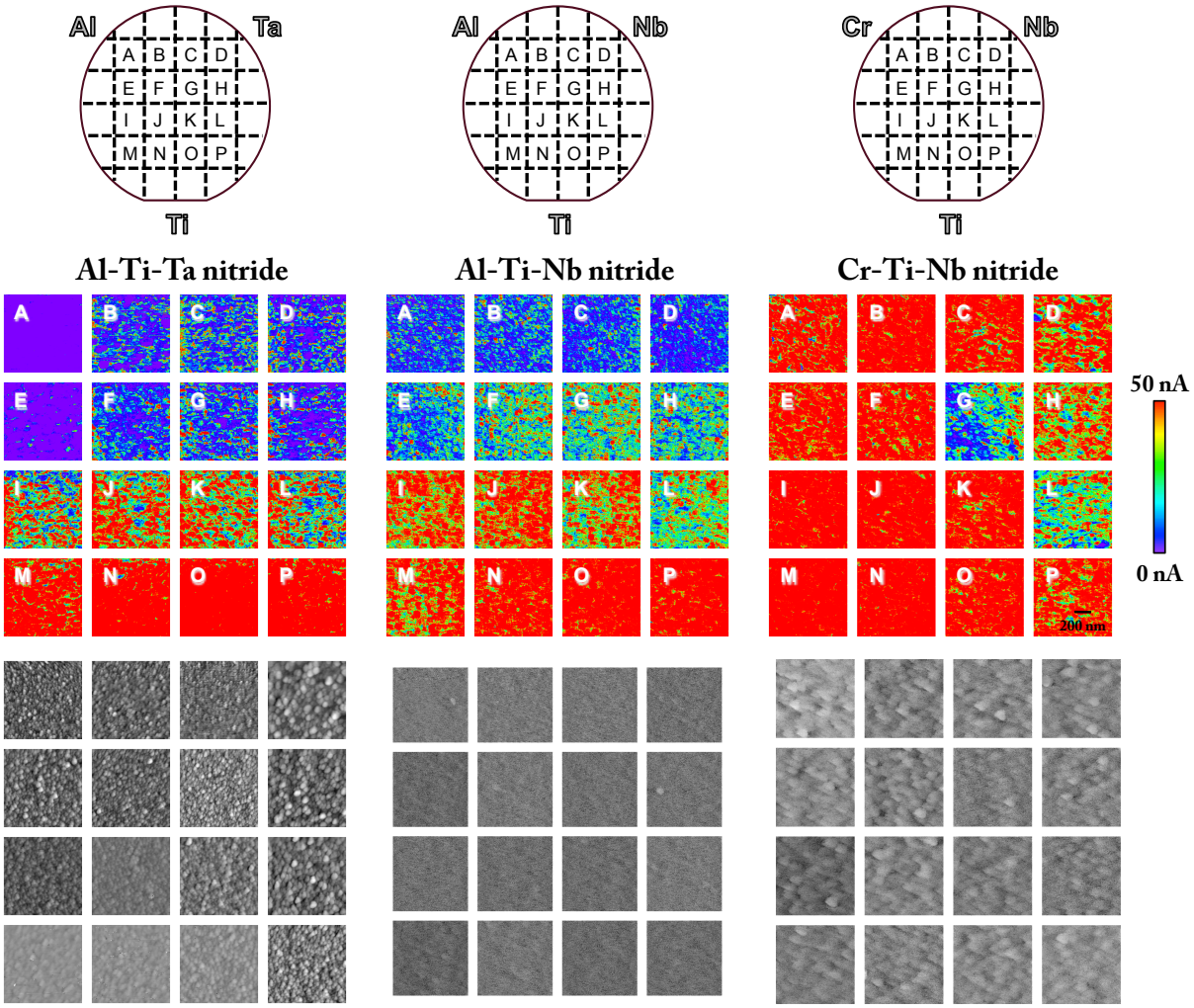

Figure 4.11 Current (top) and Topography (bottom) cp-AFM images of Al-Ti-Ta (left), Al-Ti-Nb (center), and Cr-Ti-Nb (right) nitride films. Nb appears more conducting than Ta, and Cr-Ti-Nb seems to have the highest coductivity over the widest composition range. It is important to note again, however, that the red color indicates a saturation of the current detector, meaning that all of these areas appear to have a conductivity of 4.5 S cm^{-1} that may be higher for some compositions. *Images courtesy of Dr. James O'Dea.*

4.6.3 Pt deposited on Ti-Ta-Al nitride thin films.

In order to investigate the suitability of these materials as catalyst supports, a 2.5 nm layer of Pt was deposited on the O_2 annealed films. The Pt deposition was performed in such a way that the Pt tends to form small islands rather than a conformal film, thus approximating nanoparticles deposited on the surface of the film. Figure 4.12 shows CVs obtained using the scanning mini-cell for the single element rich regions of the film and for the center of the film. CVs were obtained in 0.1 M H_2SO_4 over -0.2 to 1.2 V vs. Ag/AgCl at 50 mV s^{-1}. Typical features for Pt (starred peaks in Figure 4.12) are visible in each of the regions of the film, while the Ti-rich region seems to give the highest currents. Additionally, the double-layer current (between -50 mV and + 300 mV) is different for each region of the film. This suggests non-uniformity in the film roughness and Pt surface area. This behavior is not surprising since the Pt was deposited as a discontinuous, 2.5 nm layer. It is important to note that the Ti-rich region shows the greatest performance from a Pt-utilization point-of-view. Further electrochemical experiments are required to fully characterize the activity of Pt/nitride film catalysts, but these initial results suggest that Pt can be supported and characterized while supported on Ta-Ti-Al nitride films.

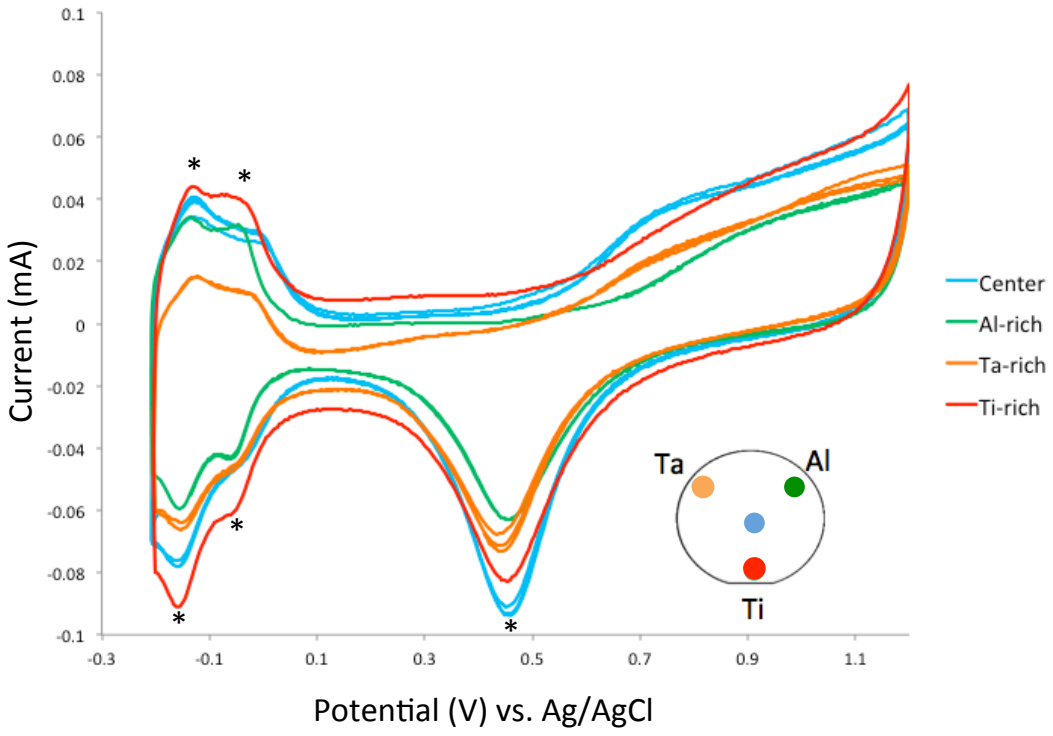

Figure 4.12 CVs of 2.5 nm Pt film deposited on a Ta-Ti-Al nitride film. Each scan was performed on a different region of the film, shown in the inset film diagram. Note the typical features of Pt (starred) are visible indicating that nitride film is capable of acting as a support for Pt.

Figure 4.13 shows results from methanol (MeOH) oxidation studies of the 2.5 nm Pt layer deposited on the Ta-Ti-Al nitride film. This data was taken in 1 M MeOH and 0.1 M H_2SO_4 over the range -0.2 to 0.7 V vs. Ag/AgCl at 50 mv s^{-1}. The maxium current (typically near 0.6 V vs. Ag/AgCl) is plotted vs. cycle number, and is taken as a measure of MeOH oxidation activity. Importantly, the Pt thin film was deposited in the same system, but is 10 nm thick and continuous, whereas the Pt deposited on the nitride film is only 2.5 nm thick and is not continuous. The Pt film shows approximately 2x the current for MeOH oxidation, yet the Pt/nitride film shows significantly less drop in current after the 1^{st} 5 cycles, with the Ti-rich region of the film performing the best in these experiments. These initial results may indicate that CO poisoning is less of a challenge on nitride supports, since the performance of Pt/nitride film is less affected upon cycling, however further experiments are required to draw firm conclusions. Nonetheless, these initial results are exciting and suggest that ternary nitride compounds (as nanoparticles) should be developed as supports for Pt-based catalysts, and their potential co-catalytic (or poisoning inhibiting properties) studied.

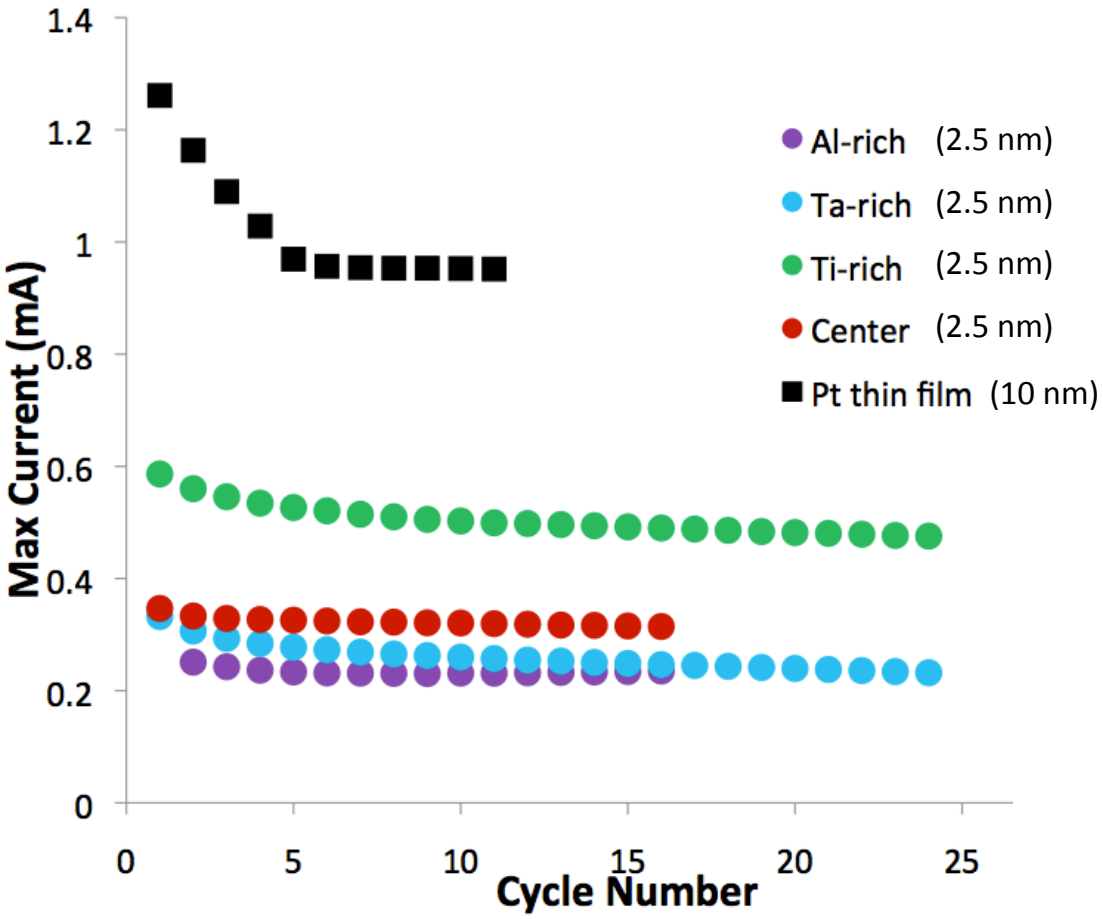

Figure 4.13 Plot of MeOH oxidation maximum current vs. cycle number for Pt/Ti-Ta-Al nitride film and a Pt thin film. Note that the Pt thin film is a continuous 10 nm film, while the Pt/Ti-Ta-Al nitride is comprised of small Pt islands on the nitride film. Although the current is almost half the Pt film, the nitride supported Pt film has a lower loss of current during the initial 5 cycles. This may indicate that Pt/Nitride films are more resistant to poisoning by CO. *Image courtesy of Abigail Van Wassen and Anna Legard*

4.7 Conclusions

Using magnetron sputtering, thin films of Ti-Ta-Al nitride (and other metals) have been prepared and studied using a variety of surface sensitive techniques. We have shown that nitrides are capable of supporting Pt catalysts for fuel cell reactions, and have shown that a surface oxide layer that is approximately 2.0 nm thick stabilizes the nitride supports. Using cp-AFM we observed that the conductivity of the nitride film varies significantly with composition, and that Ti-rich nitrides are likely of the most interest for nanoparticle studies based solely on conductivity.

The work presented in this chapter summarizes the results of our experiments to date, while further investigations are forthcoming. In addition to Ti-Ta-Al nitride films, Nb and Cr containing films have been prepared and films with W and V have been planned. The ultimate aim is to use the combinatorial approach to discover new nitride compounds that have a host of desirable properties, and to use the insights gained through high-throughput studies to synthesize nanoparticles of the identified active compositions.

4.8 Catalyst Support Conclusions

Chapters 2 through 4 of this dissertation have focused on my efforts to develop new catalyst support materials for PEMFCs. While oxide based materials, due to their limited conductivities, have fallen somewhat out of favor in our group, nitride materials are of burgeoning interest. I have shown that mixed metal, Ti-based nitrides possess unique oxidative stability when prepared correctly, and that some nitride compounds surpass carbon-based supports when tested in fuel cell like conditions. It is my hope that the results presented here will inform future researchers in the DiSalvo and other groups who are interested in the properties of nitride compounds and their utility as catalyst supports.

REFERENCES

(1) Hahlbohm, H.-D. *Superconducting Quantum Interference Devices and Their Applications*; De Gruyter: Berlin, 1985.

(2) Karlsson, B.; Sundgren, J.-E.; Johansson, B.-O. *THIN SOLID FILMS* **1982**, *87*, 181–187.

(3) Danroc, J.; Aubert, A.; Gillet, R. *THIN SOLID FILMS* **1987**, *153*, 281–286.

(4) Oyama, S. T. *Chemistry of Transition Metal Carbides and Nitrides*; Blackie Academic & Professional: London, 1996.

(5) *Opportunities for Innovation*; Sproul, W. D.; Legg, K. O., Eds. Technomic Publishing Company: Switzerland, 1995.

(6) Behrisch, R. *Sputtering by particle bombardment I. Physical sputtering of single-element solids, Vol. 47*; Springer-Verlag,New York, NY, 1981; Vol. 47.

(7) Townsend, P. D.; Kelly, J. C.; Hartley, N. E. W. *Ion implantation, sputtering and their applications*; Academic Press: London, 1976.

(8) Kelly, P. J.; Arnell, R. D. *Vacuum* **2000**, *56*, 159–172.

(9) Sundgren, J.-E.; Johansson, B.-O.; Karlsson, S.-E. *THIN SOLID FILMS* **1983**, *105*, 353–366.

(10) Sundgren, J.-E.; Johansson, B.-O.; Karlsson, S.-E.; Hentzell, H. *THIN SOLID FILMS* **1983**, *105*, 367–384.

(11) Berg, S.; Nyberg, T. *THIN SOLID FILMS* **2005**, *476*, 215–230.

(12) Gregoire, J. M. High-Throughput Materials Science for Discovery of Energy Related Materials, Cornell University: Ithaca, NY, 2009.

(13) Gregoire, J. M.; van Dover, R. B.; Jin, J.; DiSalvo, F. J.; Abruña, H. D. *Rev. Sci. Instrum.* **2007**, *{78}*.

(14) Theuerer, H. C.; Hauser, J. J. *J. Appl. Phys.* **1964**, *35*, 554.

(15) van Dover, R. B.; Hong, M.; Gyorgy, E. M.; Dillon, J. F.; Albiston, S. D. *J. Appl. Phys.* **1985**, *57*, 3897.

(16) van Dover, R. B.; Hessen, B.; Werder, D.; Chen, C. H.; Felder, R. J. *Chem. Mater.* **1993**, *5*, 32–35.

(17) Gregoire, J. M.; van Dover, R. B.; Jin, J.; DiSalvo, F. J.; Abruña, H. D. *Rev. Sci. Instrum.* **2007**, *78*, 072212.

(18) Avasarala, B.; Haldar, P. *International Journal of Hydrogen Energy* **2011**, *36*, 3965–3974.

(19) Saha, N. C.; Tompkins, H. G. *J. Appl. Phys.* **1992**, *72*, 3072.

(20) Ernsberger, C. *Journal of Vacuum Science & Technology A: vacuum, Surfaces and Films* **1986**, *4*, 2784.

(21) Massiani, Y.; Medjahed, A.; Gravier, P.; Argème, L.; Fedrizzi, L. *THIN SOLID FILMS* **1990**, *191*, 305–316.

(22) Noguera, C. *Physics and Chemistry at Oxide Surfaces*; Cambridge University Press: Cambridge, UK,, 1996.

(23) Kung, H. H. *Transition Metal Oxides: Surface Chemistry and Catalysis*; Elsevier: Amsterdam, 1989.

(24) Henrich, V. E.; Cox, P. A. *The Surface Chemistry of Metal Oxides*; Cambridge University Press: Cambridge, UK, 1994.

(25) Al-Abadleh, H. A.; Grassian, V. H. *Surface Science Reports* **2003**, *52*, 63–161.

(26) Fernandez-Garcia, M.; Martinez-Arias, A.; Hanson, J. C.; Rodriguez, J. A. *Chem. Rev. (Washington, DC, U. S.)* **2004**, *104*, 4063–4104.

(27) Baer, D. R.; Amonette, J. E.; Engelhard, M. H.; Gaspar, D. J.; Karakoti, A. S.; Kuchibhatla, S.; Nachimuthu, P.; Nurmi, J. T.; Qiang, Y.; Sarathy, V.; Seal, S.; Sharma, A.; Tratnyek, P. G.; Wang, C. M. *Surf. Interface Anal.* **2008**, *40*, 529–537.

(28) Park, J. Y.; Maier, S.; Hendriksen, B.; Salmeron, M. *Materials Today* **2010**, *13*, 37–44.

(29) *Electrical Characterization with Scanning Probe Microscopes*; 1st ed. AN79; Veeco Instruments: Santa Barbara, CA, 2008; pp. 1–12.

(30) Baer, D.; Gaspar, D.; Nachimuthu, P.; Techane, S.; Castner, D. *Analytical and Bioanalytical Chemistry* **2010**, *396*, 983–1002.

(31) Klapetek, P.; Valtr, M.; Necas, D.; Salyk, O.; Dzik, P. *Nanoscale Research Letters* **2011**, *6*, 514.

(32) Wallace, J. M. *Bone* **2012**, *50*, 420–427.

(33) Ramesh, S.; Cohen, Y.; Aurbach, D.; Gedanken, A. *Chemical Physics Letters* **1998**, *287*, 461–467.

(34) Kikuchi, H.; Ouchida, W.; Nakamura, M.; Goto, C.; Yamada, M.; Hoshi, N. *Electrochemistry Communications* **2010**, *12*, 544–547.

(35) Ziganshina, S. A.; Bukharaev, A. A.; Shamsetdinova, L. I.; Chuklanov, A. P.; Bizyaev, D. A. *Journal of Surface Investigation-X-Ray Synchrotron and Neutron Techniques* **2009**, *3*, 725–729.

(36) Martin, M.; Roschier, L.; Hakonen, P.; Parts, U.; Paalanen, M.; Schleicher, B.; Kauppinen, E. I. *Appl. Phys. Lett.* **1998**, *73*, 1505–1507.

(37) Couteau, O.; Roebben, G. *Meas. Sci. Technol.* **2011**, *22*, 8.

(38) McCarty, G. S.; Weiss, P. S. *Chem. Rev. (Washington, DC, U. S.)* **1999**, *99*, 1983–1990.

(39) Grobelny, J.; DelRio, F. W.; Pradeep, N.; Kim, D.-I.; Hackley, V. A.; Cook, R. F. In *Characterization of Nanoparticles Intended for Drug Delivery*; McNeil, S. E., Ed. 2011; Vol. 697, pp. 71–82.

(40) Billinge, S. J. L.; Levin, I. *Science* **2007**, *316*, 561–565.

(41) Foster, A. S.; Barth, C.; Shluger, A. L.; Reichling, M. *Phys. Rev. Lett.* **2001**, *86*, 2373–2376.

(42) Giessibl, F. J. *Rev. Mod. Phys.* **2003**, *75*, 949–983.

(43) Lantz, M. A.; Oshea, S. J.; Welland, M. E. *Phys. Rev. B* **1997**, *56*, 15345–15352.

(44) Kelley, T. W.; Granstrom, E.; Frisbie, C. D. *Adv. Mater.* **1999**, *11*, 261–264.

(45) Byers, J. C.; Tamiasso-Martinhon, P.; Deslouis, C.; Pailleret, A.; Semenikhin, O. A. *J. Phys. Chem. C* **2010**, *114*, 18474–18480.

(46) Hasegawa, S. *Current Opinion in Solid State & Materials Science* **1999**, *4*, 429–434.

(47) Oshea, S. J.; Atta, R. M.; Murrell, M. P.; Welland, M. E. *J. Vac. Sci. Technol. B* **1995**, *13*, 1945–1952.

(48) Foerster, M.; Gutierrez, D. F.; Rebled, J. M.; Arbelo, E.; Rigato, F.; Jourdan, M.; Peiro, F.; Fontcuberta, J. *J. Appl. Phys.* **2012**, *111*.

(49) Dey, S.; Jejurikar, S.; Bhattacharya, S. K.; Banerji, A.; Adhi, K. P.; Dharmadhikari, C. V. *J. Appl. Phys.* **2010**, *108*.

(50) Cho, S. H.; Park, S.-M. *JOURNAL OF PHYSICAL CHEMISTRY B* **2006**, *110*, 25656–25664.

(51) Kim, Y.; Zhao, J. W.; Uosaki, K. *J. Appl. Phys.* **2003**, *94*, 7733–7738.

(52) Son, J. Y.; Kim, D. Y.; Kim, H.; Maeng, W. J.; Shin, Y. S.; Shin, Y. H. *Electrochem. Solid-State Lett.* **2011**, *14*, H311–H313.

(53) Jiang, F. Z.; Zhang, D. S.; Lin, Y.; Song, Y. L.; Xiao, X. R.; Jiang, L.; Zhu, D. B. *Surf. Interface Anal.* **2001**, *32*, 125–129.

(54) Ok, Y.-W.; Park, W.-K.; Kim, H.-M.; Kim, K.-B.; Kim, D. *Metals and Materials International* **2008**, *14*, 481–485.

(55) Lee, S.; White, H. S. *J. Electrochem. Soc.* **2004**, *151*, B479–B483.

(56) Olbrich, A.; Ebersberger, B.; Boit, C.; Vancea, J.; Hoffmann, H.; Altmann, H.; Gieres, G.; Wecker, J. *Appl. Phys. Lett.* **2001**, *78*, 2934–2936.

(57) Boxley, C. J.; White, H. S.; Gardner, C. E.; Macpherson, J. V. *JOURNAL OF PHYSICAL CHEMISTRY B* **2003**, *107*, 9677–9680.

(58) Kumar, M. K.; Tan, L. K.; Gosvami, N. N.; Gao, H. *J. Appl. Phys.* **2009**, *106*.

(59) Borup, R.; Meyers, J.; Pivovar, B.; Kim, Y. S.; Mukundan, R.; Garland, N.; Myers, D.; Wilson, M.; Garzon, F.; Wood, D.; Zelenay, P.; More, K.; Stroh, K.; Zawodzinski, T.; Boncella, J.; McGrath, J. E.; Inaba, M.; Miyatake, K.; Hori, M.; Ota, K.; Ogumi, Z.; Miyata, S.; Nishikata, A.; Siroma, Z.; Uchimoto, Y.; Yasuda, K.; Kimijima, K.-I.; Iwashita, N. *Chem. Rev. (Washington, DC, U. S.)* **2007**, *107*, 3904–3951.

(60) Wagner, F. T.; Yan, S. G.; Yu, P. T. In *Handbook of Fuel Cells: Fundamentals, Technology and Applications*; Vielstich, W.; Yokokawa, H.; Gasteiger, H. A., Eds. John Wiley &Sons, Ltd.,: Chichester, UK,, 2009; Vol. 5, pp. 250–263.

(61) Huang, S.-Y.; Ganesan, P.; Park, S.; Popov, B. N. *J. Am. Chem. Soc.* **2009**, *131*, 13898–13899.

(62) Subban, C. V.; Zhou, Q.; Hu, A.; Moylan, T. E.; Wagner, F. T.; DiSalvo, F. J. *J. Am. Chem. Soc.* **2010**, *132*, 17531–17536.

(63) Wang, D.; Subban, C. V.; Wang, H.; Rus, E.; DiSalvo, F. J.; Abruña, H. D. *J. Am. Chem. Soc.* **2010**, *132*, 10218–10220.

(64) Halalay, I. C.; Merzougui, B.; Carpenter, M. K.; Swathirajan, S.; Garabedian, G. C.; Mance, A. M.; Cai, M. **2009**.

(65) Avasarala, B.; Murray, T.; Li, W.; Haldar, P. *J. Mater. Chem.* **2009**, *19*, 1803.

(66) Ganesan, R.; Lee, J. S. *Angewandte Chemie-International Edition* **2005**, *{44}*, {6557–6560}.

(67) Yang, X. G.; Wang, C. Y. *Appl. Phys. Lett.* **2005**, *{86}*.

(68) Nie, M.; Shen, P. K.; Wu, M.; Wei, Z.; Meng, H. *Journal of Power Sources* **2006**, *{162}*, {173–176}.

(69) Zhong, H. X.; Zhang, H. M.; Liu, G.; Liang, Y. M.; Hu, J. W.; Yi, B. L. *Electrochemistry Communications* **2006**, *{8}*, {707–712}.

(70) Liu, Y.; Ishihara, A.; Mitsushima, S.; Ota, K.-I. *Electrochimica Acta* **2010**, *{55}*, {1239–1244}.

(71) Lee, K.; Ishihara, A.; Mitsushima, S.; Kamiya, N.; Ota, K.-I. *Electrochimica Acta* **2004**, *49*, 3479–3485.

(72) Ernst, W. D.; Stone, C.; Wheeler, D. *Fuel Cell System Cost for Transporationa-2008 Cost Estimate*; National Renewable Energy Laboratory, 2009; pp. 1–62.

(73) Shao, Y.; Liu, J.; Wang, Y.; Lin, Y. *J. Mater. Chem.* **2009**, *{19}*, {46–59}.

(74) Chen, Z.; Higgins, D.; Yu, A.; Zhang, L.; Zhang, J. *Energy Environ. Sci.* **2011**, *{4}*, {3167–3192}.

(75) Lide, D. R.; Bruno, T. J. *CRC Handbook of Chemistry and Physics*; 87 ed. CRC Press, 2012.

(76) Ishihara, A.; Lee, K.; Doi, S.; Mitsushima, S.; Kamiya, N.; Hara, M.; Domen, K.; Fukuda, K.; Ota, K. *Electrochem. Solid-State Lett.* **2005**, *{8}*, {A201–A203}.

(77) Shibata, Y.; Ishihara, A.; Mitsushima, S.; Kamiya, N.; Ota, K.-I. *Electrochem. Solid-State Lett.* **2007**, *{10}*, {B43–B46}.

(78) Berger, L. I. *Semiconductor Materials*; CRC Press: Boca Raton, FL, 1997.

(79) Bellosi, A.; Landi, E.; Tampieri, A. *Journal of Materials Research* **1993**, *8*, 565–572.

(80) Highfield, J. G.; Bowen, P. *Anal. Chem.* **1989**, *61*, 2399–2402.

(81) AROMAA, J.; RONKAINEN, H.; MAHIOUT, A.; HANNULA, S. P. *Surface and Coatings Technology* **1991**, *49*, 353–358.

(82) MUNZ, W. D. *Journal of Vacuum Science & Technology A: vacuum, Surfaces and Films* **1986**, *{4}*, {2717–2725}.

(83) Carvalho, S.; Rebouta, L.; Cavaleiro, A.; Rocha, L. A.; Gomes, J.; Alves, E. *THIN SOLID FILMS* **2001**, *398*, 391–396.

(84) Stüber, M.; Schier, V.; Holleck, H. *Surface and Coatings Technology* **1995**, *74*, 833–837.

(85) Mitterer, C.; Mayrhofer, P. H.; Beschliesser, M.; Losbichler, P.; Warbichler, P.; Hofer, F.; Gibson, P. N.; Gissler, W.; Hruby, H.; Musil, J.; Vlček, J. *Surface and Coatings Technology* **1999**, *120-121*, 405–411.

(86) Zhang, S.; Sun, D.; Fu, Y.; Du, H. *Surface and Coatings Technology* **2003**, *167*, 113–119.

(87) Herbert, F. W.; Yildiz, B.; Van Vliet, K. J. *MRS Proc.* **2011**, *1297*, mrsf10–1297–p10–63.

(88) Yildiz, B.; Chang, K.-C.; You, H.; Miller, D.; Bearat, H.; McKelvy, M. Washington, D.C., 2007.

(89) Disalvo, F. J.; Yildiz, B. Communication between Frank DiSalvo and Bilge Yildiz.

(90) Gregoire, J. M.; Tague, M. E.; Cahen, S.; Khan, S.; Abruña, H. D.; DiSalvo, F. J.; van Dover, R. B. *Chem. Mater.* **2010**, *{22}*, {1080–1087}.

(91) *Measuring the Resistivity and Determining the Conductivity Type of Semiconductor Materials Using Four-Point Collinear Probe and the Model 6221 DC and AC Current Source*; 2615; Keithley Instruments, Inc.: Cleveland, Ohio, 2005; pp. 1–4.

(92) Clark, J. Questions and Answers Regarding Sample Size and Correction Factors http://www.four-point-probes.com/correct.html (accessed May 2013).

(93) Gregoire, J.; Lobovsky, M.; Heinz, M.; DiSalvo, F.; van Dover, R. *Phys. Rev. B* **2007**, *76*, 195437.

(94) Gregoire, J. M.; van Dover, R. B. *Journal of Vacuum Science & Technology A: vacuum, Surfaces and Films* **2008**, *26*, 1030–1036.

(95) Gallagher, P. K.; Sinclair, W. R.; Bacon, D. D.; Kammlott, G. W. *J. Electrochem. Soc.* **1983**, *130*, 2054–2056.

(96) Frankenthal, R. P.; Siconolfi, D. J.; Sinclair, W. R.; Bacon, D. D. *J. Electrochem. Soc.* **1983**, *130*, 2056–2060.

(97) Mehta, S. M.; Patel, S. R. *J. Am. Chem. Soc.* **1951**, *73*, 224–226.

(98) Pourbaix, M. *Atlas of Electrochemical Equilibria in Aqueous Solutions*; National Association of Corrosion Engineers, 1974.

CHAPTER 5

RARE-EARTH/TRANSITION METAL PEROVSKITES AS OXYGEN REDUCTION CATALYSTS IN ALKALINE SOLUTIONS

Work in this chapter was performed in collaboration with an undergraduate researcher: Michael De Sienna

In Chapter 1, several of the challenges inhibiting the full-scale deployment of fuel cell technologies were discussed. Among these challenges are the deficiencies of carbon-based catalyst supports. My efforts to develop new, non-carbon supports have been discussed in the preceding chapters, while this chapter will focus on the challenge of developing new, less-expensive catalyst materials for fuel cell reactions.

I was introduced to this project in the summer of 2011 after a report[1] appeared in Nature Chemistry discussing the use of perovskite lanthanum-transition metalates as oxygen reduction catalysts in alkaline electrolytes. Although I had not worked on catalytic materials before, my experience with oxides and the apparent activity of these catalysts inspired me to synthesize some of these materials to see if we could learn more about them, and perhaps build on the reported results. Michael De Sienna, a new undergraduate researcher in the group, joined me in this effort (executing a large portion experiments himself), and the results presented here represent our work with these materials obtained over the last year and half.

5.1 Oxygen Reduction in Alkaline Solutions

As discussed in Chapter 1, the oxygen reduction reaction (ORR) occurs at the cathode in polymer electrolyte membrane fuel cells (for both acidic and alkaline fuel cells), and has been called by some "God's collective punishment to electrochemists," due to notoriously slow kinetics and significant overpotential losses generated from driving the reaction at moderate

current densities. Platinum, or perhaps Pt_3Co, is currently the best ORR catalyst available for acidic systems[2-6], although Pt-free catalysts such as Pd and Pd-M alloys[7-13], Fe or Co containing prophyrins[14], transition metal carbides[15], and oxides/oxynitrides[15] have also been reported to possess limited ORR activity.[16]

In contrast to acidic electrolytes, ORR in alkaline solutions has reportedly faster kinetics leading to smaller overpotential losses. [17-19] Additionally, non-noble metal catalysts (such as Ni or Co) may *potentially* be used due to the insolubility and higher stability of such metals and their oxides in alkaline solutions at potentials present in a fuel cell[20] (as reported in Pourbaix diagrams[21]). Among the materials studied as potential ORR catalysts in alkaline electrolytes are: Pd-based catalysts[22], Ru-based catalysts[23], Fe-containing porphyrins[24], nickel-cobalt spinels[25-30], manganese oxide based catalysts[19,28-33], as well as elemental Au, Ag, Co and Ni[20] have proven to be the most promising alternatives to Pt-based electrocatalysts for alkaline fuel cell applications. Each of these catalysts presents individual challenges ranging from long-term stability, to producing H_2O_2 (via a 2-electron reduction of oxygen) rather than water (via a 4-electron pathway). Several review articles focusing on alkaline fuel cell technology and ORR in base are available[34-38] which provide detailed discussions of the state of the field and the challenges which remain unresolved.

The latter challenge (i.e. the production of peroxide) has been a persistent problem for researchers developing non-noble ORR catalysts for alkaline systems. Generally, the production of peroxide should be minimized due the corrosive (oxidizing) nature of the peroxide anion (especially to polymeric membrane materials), and because more energy is generated per O_2 molecule by the 4-electron reduction to water. Furthermore, strongly adsorbed HO_2^- has been reported to lower the overpotential for peroxide production, further promoting the 2-electron

pathway over the 4-electron reduction to water.[39] Despite numerous studies[6,37,40-54], the precise mechanism of peroxide formation (or oxygen reduction) is not well understood. Observing and detecting intermediates formed on a catalytic surface has proven difficult in both acidic and basic electrolytes[39], and different catalysts appear to promote different reaction mechanisms (i.e. adsorbate formation energies, surface orientation, and electron transfer steps are not necessarily the same for different catalysts). It is clear that ORR electrocatalysis continues to be the primary challenge inhibiting the widespread deployment of fuel cell technologies.

5.2 Perovskites for ORR

In addition to the catalyst materials mentioned previously, perovskite oxides with the general formula ABO_3 (A is generally a main group element or rare earth, and B a transition metal) have been reported as attractive alternatives to noble metals because of their ORR activity in alkaline solutions and low cost.[14,55] The ideal perovskite structure consists of a primitive cubic unit cell with A-atoms at the corners, and oxygen atoms on each face. The B-atom resides at the center of the cubic unit cell, and forms a BO_6 octahedral unit with the face-centered oxygen atoms. This octahedral unit can distort in shape lending structural complexity and flexibility to perovskite compounds.[56]

The perovskite crystal lattice can serve as a versatile host for a variety of mixed metal oxides due to its ability to accommodate distortions, as well as both iso- and aleo-valent doping on the A- and B-sites.[56] Furthermore, the crystal structure and properties (e.g. ionic transport, electronic conductivity, and ORR activity) vary significantly depending on the nature and relative stoichiometry of different A-site (typically La, Pr, Gd or alkaline earths: e.g. Ca, Sr, Ba) and B-site (typically Ti, V, Cr, Mn, Fe, Co, and Ni) cations.[57,58]

Perovskite oxides (such as $LaNiO_3$) have been studied as ORR catalysts since the 1970s. Matsumoto *et al*[59-61] reported moderate ORR activity for substituted $LaNiO_3$ (i.e. $LaNi_{1-x}M'_xO_3$; M'=Fe, Co, V), and concluded that the degree of overlap of the B-site atoms' *d*-orbitals (particularly those with e_g symmetry) plays a significant role in tuning the ORR activity. Furthermore, mechanistic studies suggest that the B-site stoichiometry of La-based perovskites significantly contributes to the chemisorption of O_2 to the catalytically active surface, and that adsorbate formation is the rate-limiting step for perovskite catalysts.[62,63] A conflicting report by Bockris and Otagawa[64] concludes that the desorption of OH^- from the perovskite surface is the rate-limiting step, and that lattice O atoms from the perovskite may be released and replaced with O from reduced-chemisorbed O_2 molecules (determined using ^{18}O labeled perovskites). Furthermore, this study also concluded that the mechanism of ORR changed for perovskites with different B-site transition metals.

There are two main mechanisms proposed for oxygen reduction on perovskite catalysts in base.[64,65] The first involves the reduction of oxygen in two 2-electron transfer steps (which produces the HO_2^- anion as an intermediate), while the second involves the direct 4-electron reduction of O_2 to H_2O. There is still significant debate as to which mechanism predominates, as both mechanisms are observed for various La-based perovskite catalysts. For example, Tulloch *et al*[66] reported that $LaMnO_3$ strongly favors the peroxide mechanism (81% H_2O_2 formation by Rotating Ring-Disk Electrode; RRDE), while substituting 60% Sr on the La-site (i.e. $La_{0.4}Sr_{0.6}MnO_3$) reduced peroxide formation significantly (15% H_2O_2 formation by RRDE). Sunarso *et al*[67], on the other hand, reported that $LaMO_3$ and $LaM_{1-x}M'_xO_3$ (M/M'=Cr, Mn, Fe, Ni, Co) catalysts perform ORR entirely by the 4-electron pathway, and that $LaCoO_3$ and $LaNi_{0.5}Mn_{0.5}O_3$ showed the highest ORR current densities at the most positive onset potential

(from RRDE experiments). Additional reports that support both mechanisms are also available,[57,68-70] each suggesting a different optimum stoichiometry for achieving the highest catalytic performance.

Many of the early investigations of the ORR mechanism on La-based perovskite catalysts utilized bulk, porous electrodes. Often, these electrodes made quantitative determinations difficult as the electrode porosity made determining catalyst surface area and oxygen diffusion rates difficult. Only in recent years have studies of thin-layer perovskite electrodes become available.[58,66,67,71,72] Such studies have increased the quantitative accuracy of ORR activity and electrochemical stability measurements.

Using the thin-layer electrode approach[73], Suntivich *et al*[1] measured the ORR activity of 15 substituted and un-substituted La-based perovskites, and concluded that ORR on these catalysts proceeds via the direct, 4-electron pathway (including compounds like $LaMnO_3$, previously reported to favor the 2-electron pathway). Combining these electrochemical measurements with theoretical calculations, the authors reported that the number of electrons in surface, transition-metal, e_g-type orbitals (as well as the covalency of the $B_{surface}$-O bond) in La-based perovskite catalysts can be used as a descriptor for ORR activity, and that perovskites with an e_g filling ≈ 1 show the highest ORR activity (i.e. $LaNiO_3$ or $LaMnO_{3+\partial}$ are the closest to $e_g = 1$). This finding is in opposition to previous reports[59-61] that suggest that the electronic effects of *bulk* atom orbitals play a more significant role in the ORR activity.

5.3 Preparation of La-Based Perovskite Catalysts

Perovskite oxides can be synthesized using a variety of techniques including traditional ceramic methodologies[59,61], sol-gel methods[74-77], co-precipitation[1,78], and various thin-film deposition techniques (MBE, PLD, etc.).[79-81] Typically each of these techniques requires subsequent thermal annealing in air or oxygen as amorphous or sub-stiochiometric oxides are generated. Hence, perovskite catalysts for fuel cell applications often have significantly larger particle sizes (20 nm to several μm) and lower surface areas (0.25-10 m^2/g) than noble metal nanoparticle catalysts, such as Pt, that are used in acidic electrolytes. However, because the relative cost of perovskite oxides compared to Pt or Au, larger particle size is less of an inhibiting factor, as long as suitable ORR activity can be achieved.[14] The perovskites studied in this chapter were prepared following the method presented by Suntivich *et al*[1], wherein metal nitrate precursors were dissolved with citric acid in water, dried, and fired at high temperatures in air.

5.3.1 Materials

Hydrated metal nitrates (metals= La (III), Ca (II), Sr(II), Cr(III), Mn(II), Fe (III), Co(II), Ni (II), Cu (II); ACS grade, > 97%) were obtained from Sigma Aldrich; Ammonium Vanadate (NH_4VO_3, ACS grade) was obtained from Fischer Scientific; Citric Acid (anhydrous, ACS grade, >98%) was obtained from J T Baker; Ammonium Hydroxide (NH_4OH, 18M, ACS grade) was obtained from J T Baker; Nafion solution(5 % in aliphatic alcohols) was obtained from Sigma Aldrich; Potassium Hydroxide (KOH, ACS grade) was obtained from Fischer Scientific; Argon (Ar, analytical grade < 50 ppm H_2O) was obtained from Airgas; Oxygen (O_2, medical grade) was obtained from Airgas; Carbon Black (Vulcan XC-72) was obtained from Cabot.

5.3.2 Synthesis and Characterization of $LaMO_3$ (M=V, Cr, Mn, Fe, Co, Ni)

In a typical synthesis, stoichiometric amounts of metal nitrate (or NH_4VO_3 for V-containing samples) precursors were added to a round bottom flask with anhydrous citric acid in a molar ratio of 1:5. The precursors were dissolved in DI water, and the total metal ion concentration was brought to 0.1 M. The pH of the precursor solution was then adjusted to 7 by titrating with concentrated NH_4OH. The neutralized solution was then transferred to a petri dish, and dried in a drying oven at 125 ºC overnight to form a gel. The gel was then calcined at 450 ºC for 6 hours in air. The as-calcined powder varied in color depending on the metals used in the perovskite, and required further heating to form the crystalline perovskite phase. The heating conditions for each sample are listed in Table 5.1. The final products were confirmed to be single phase by powder X-Ray diffraction (pXRD).

Table 5.1 Synthesis conditions of perovskite samples*

Perovskite Compound	*Temp (ºC)*	*Time (hr)*	*Space Group*[ß]	*PDF Number*
$LaVO_3$	800[†]	6	*P n m a*	04-009-3170
$LaCrO_3$	1000	6	*P n m a*	04-016-5697
$LaMnO_3$	1000[§]	6	*P n m a*	04-016-2205
$LaMnO_{3+\partial}$	1000	2	*R -3 c*	04-015-9961
$LaFeO_3$	600	2	*P n m a*	04-013-6814
$LaCoO_3$	800	6	*R -3 c*	04-015-9971
$LaNiO_3$	600	6	*R -3 c*	04-013-6811
$La_{0.5}Ca_{0.5}MnO_3$	1000[§]	2	*P n m a*	01-076-8548
$LaMn_{0.5}Ni_{0.5}O_3$	600	2	*P b n m*	01-075-2903
$LaMn_{0.5}Cu_{0.5}O_3$	500[§]	2	*P n m a*	--
$LaCo_{0.5}Mn_{0.5}O_3$	1000[§]	6	*P b n m*	04-012-5611
$LaCo_{0.5}Ni_{0.5}O_3$	800[§]	6	*R -3 c*	01-073-2813
$LaCo_{0.3}Ni_{0.7}O_3$	600	6	*R -3 c*	--

* Heated in air unless otherwise noted

§ Heated in Ar

† Heated in forming gas (N_2/H_2)

ß All have distorted perovskite structure types by pXRD

Figure 5.1 shows pXRD patterns and SEM images of several perovskite compounds. Each of the perovskite compounds was confirmed to be single phase by pXRD. Generally, the particle size and morphology of each of the perovskite compounds were similar. In Figure 5.1b one can see that a typical particle size is on the order of 200-300 nm, while the crystalline domain size (determined from pXRD line broadening) was about 20-50nm indicating that the individual particles are polycrystalline. Additionally, when comparing the $LaMnO_3$ image (left) to the $LaFeO_3$ image (right) one can see that the faceting and sintering behavior of different perovskite compounds varies. The $LaMnO_3$ sample appears more crystalline, and more well-defined faceting of the particles can be seen, while the $LaFeO_3$ sample appears smoother, less porous, and more well sintered. Such behavior is not unexpected as the annealing conditions varied for each of the compounds. It is interesting however, that the Fe-containing sample was annealed at a lower temperature but appears more highly sintered than the Mn-containing sample.

The two images shown in Figure 5.1b represent the extremes of particle morphology (i.e. all of the samples fall between these levels of sintering and particle shape). The BET surface area of each of the perovskites ranged between 10 and 16 $m^2\ g^{-1}$, which is relatively high compared to reports of other perovskite compounds prepared by similar methods[1,66,71], but substantially lower than typical Pt nanoparticle surface areas.

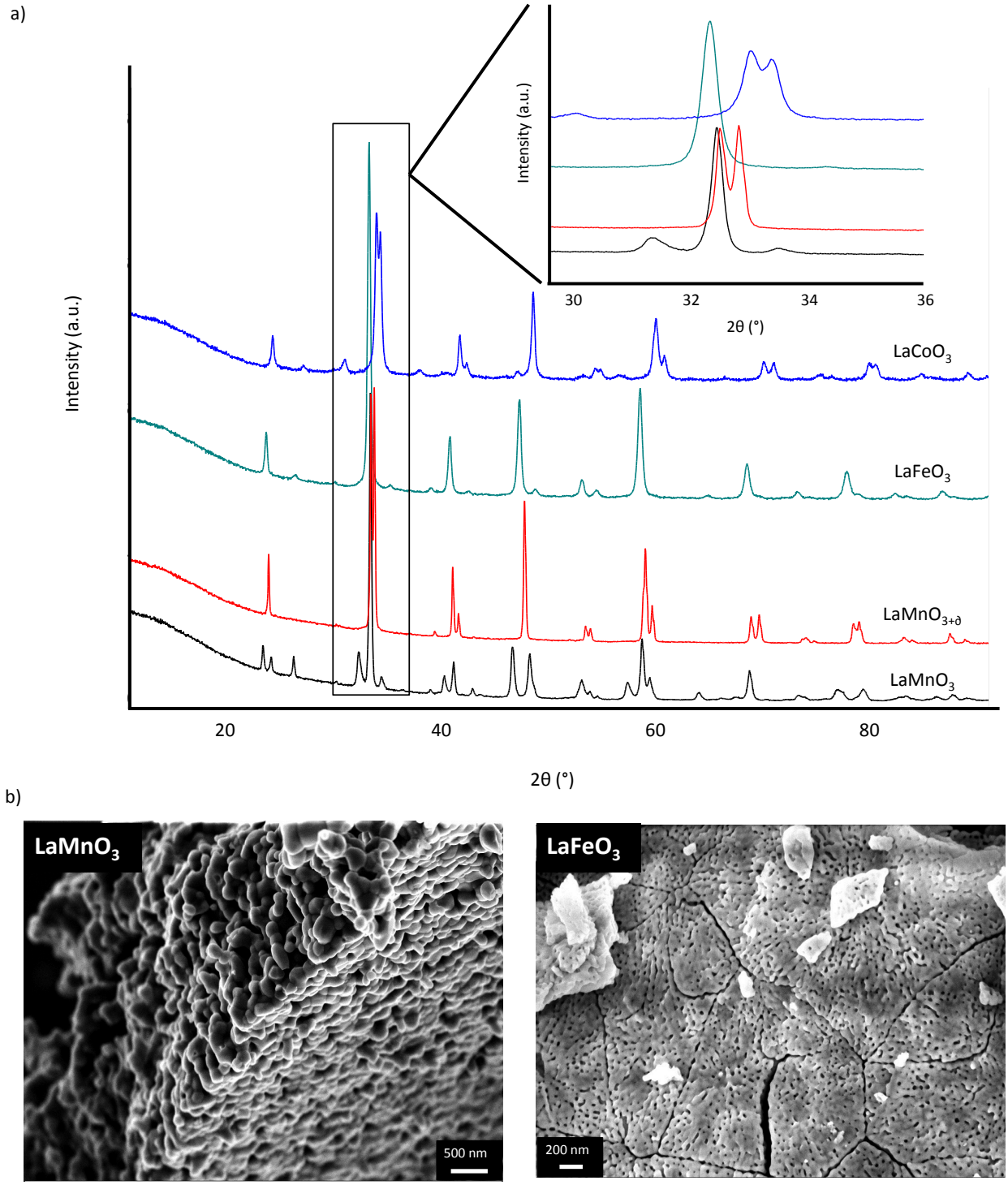

Figure 5.1 (a) pXRD patterns of several perovskite oxide catalysts. Each compound has a distorted perovskite structure type. Distortions in the BO_6 octahedral unit generate additional reflections for some compounds. Each of the synthesized compounds were found to be single phase. (b) SEM images of $LaMnO_3$ (left) and $LaFeO_3$ (right). Generally each of the compounds had similar particle size and morphology. The small particles sinter into larger units as a result of the high thermal annealing temperature. The $LaFeO_3$ sample showed the most "smooth" sintering, while the $LaMnO_3$ sample showed the most granular. The BET surface area of the as-prepared perovskites was between 10-16 $m^2\ g^{-1}$.

5.4 Chemical Stability of Perovskite Catalysts

The chemical stability of several perovskite oxide catalysts in alkaline solutions has been investigated by Hyodo *et al.*[57,82,83] The authors reported that upon immersing samples of the catalysts in 9 M NaOH for 12 hours at 80 ºC, only $LaCrO_3$ and $LaFeO_3$ appeared stable by pXRD (i.e. no other crystalline phases were observed in the pXRD pattern). Other perovskites that were tested included $LaNiO_3$, $LaCoO_3$, and $LaMnO_3$, however each of these samples showed significant changes in their pXRD patterns after stability testing, including the appearance of $La(OH)_3$. In addition to simple ABO_3 perovskites, the authors also studied several A-substituted and B-substituted samples. The authors found that the addition of 20-40% Sr on the A-site improved the apparent chemical stability (i.e. no secondary phases were detected by pXRD post stability testing).

Building on these results, we explored the chemical stability of the perovskite catalyst samples in alkaline solutions. Approximately 100 mg of each sample was placed in a vial and covered with either 3 M or 0.1 M KOH. The vials were capped tightly and placed into an oil bath at 80ºC and left for 3 weeks. After the stability test, the test solution was decanted off and the samples were rinsed thoroughly with DI water. The results of these stability tests are summarized in Table 5.2.

Table 5.2 Stability Testing in KOH Solutions for 3 weeks at 80 ºC

Perovskite Compound	*Stability in 3 M KOH*	*Stability in 0.1 M KOH*
$LaVO_3$	--	P,S
$LaCrO_3$	--	P,S
$LaMnO_3$	P,D	P,S
$LaMnO_{3+\partial}$	P,D	P,S
$LaFeO_3$	--	P,S
$LaCoO_3$	X,D	P,S
$LaNiO_3$	X,D	P,S
$LaMn_{0.5}Cu_{0.5}O_3$	--	P, S
$LaMn_{0.5}Cu_{0.5}O_3$ (MIT Prep)	--	P,S
$LaMnO_3$ (MIT Prep)	--	P,S

P - Single phase perovskite by pXRD
X - Multiple phases by pXRD
S - Same particle size, shape by SEM
D - Visible differences in SEM images before and after testing
-- Experiment not performed

Figure 5.2 shows pXRD patterns and SEM images of $LaCoO_3$ and $LaNiO_3$ before and after stability testing in 3 M KOH solution for 3 weeks at 80 º C. In both cases $La(OH)_3$ is visible in the pXRD pattern (starred peaks) indicating a lack of chemical stability in 3 M KOH. Additionally, needle (for $LaNiO_3$) and plate-like (for $LaCoO_3$) crystallites of second phases (corrosion products) are visible in the SEM images showing phase segregation at the surface of the particles. The secondary crystallite morphology is consistent with solution growth, indicating that La, Ni, and Co were likely leached from the perovskite material into solution, and then nucleated crystallites on the surface of the perovskite grains. It is unclear from how deep the metals were leached, as the parent perovskite compound is still visible by both pXRD and

SEM. It is likely, however, that at least several tens of nm of surface layers are depleted simply by observing the presence of $La(OH)_3$.

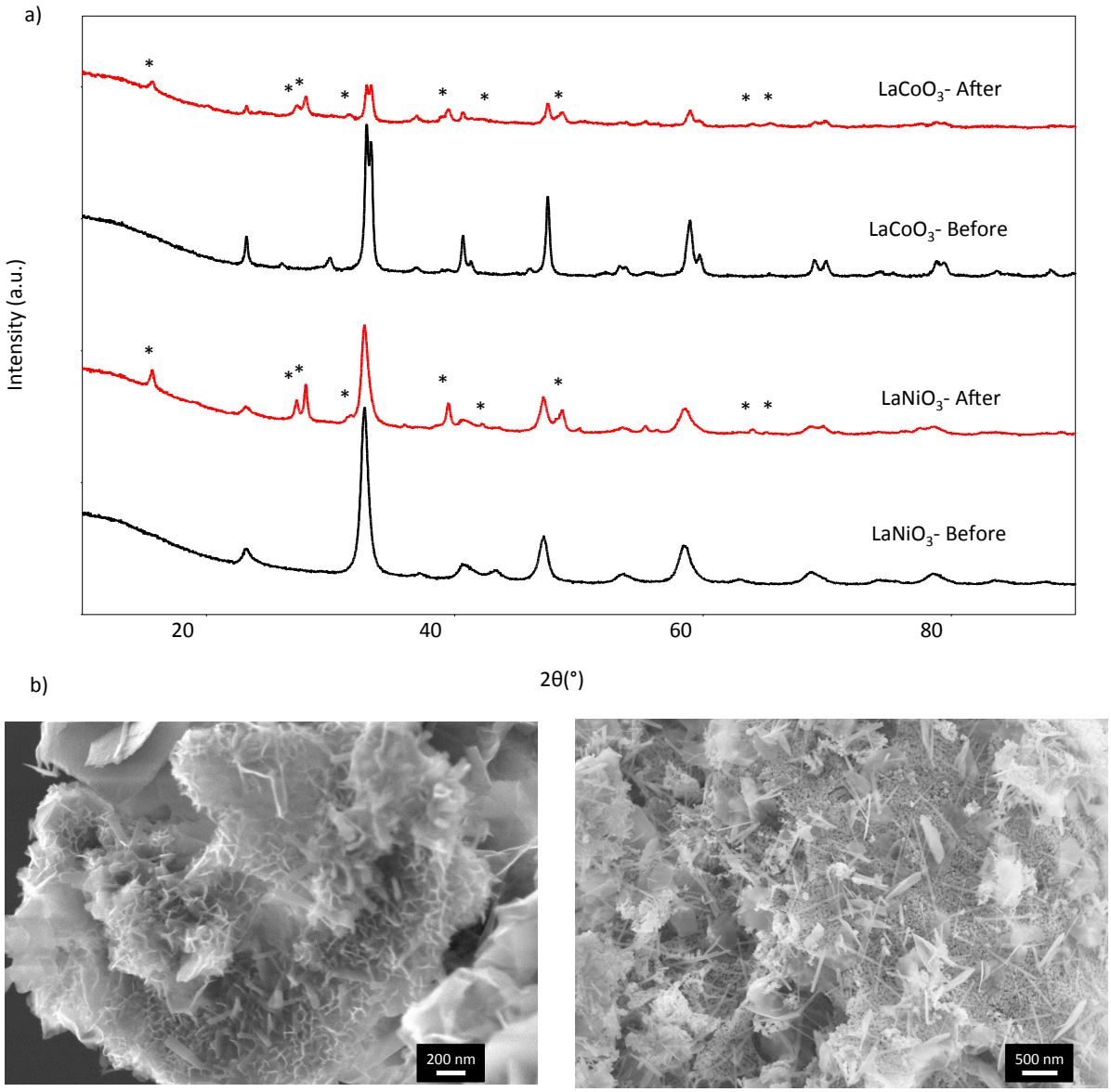

Figure 5.2 (a) pXRD of $LaCoO_3$ and $LaNiO_3$ before (black) and after (red) chemical stability testing in 3 M KOH for 3 week at 80 ºC. Note the presence of $La(OH)_3$ in the pXRD after the stability testing (starred peaks) indicating La leaches from the perovskites under these conditions. (b) SEM images of $LaCoO_3$ (left) and $LaNiO_3$ (right) after stability testing. Note the presence of plate-like (left) and needle-like (right) crystals in the seem images. Small amounts of CoO and NiO were also visible in the pXRD pattern, however their intensity does not show up on this scale.

In addition to $LaNiO_3$ and $LaCoO_3$, $LaMnO_3$ was also tested in 3 M KOH at 80 º C for three weeks. While no apparent changes in the pXRD pattern were observed for either of the Mn-containing samples tested, small growths on the parent perovskite material were observed in SEM images (shown in Figure 5.3). The fact that no changes were observed in the pXRD pattern of the $LaMnO_3$ sample indicates that the growths are either amorphous, or a small mole fraction (<3% or so) of the product.

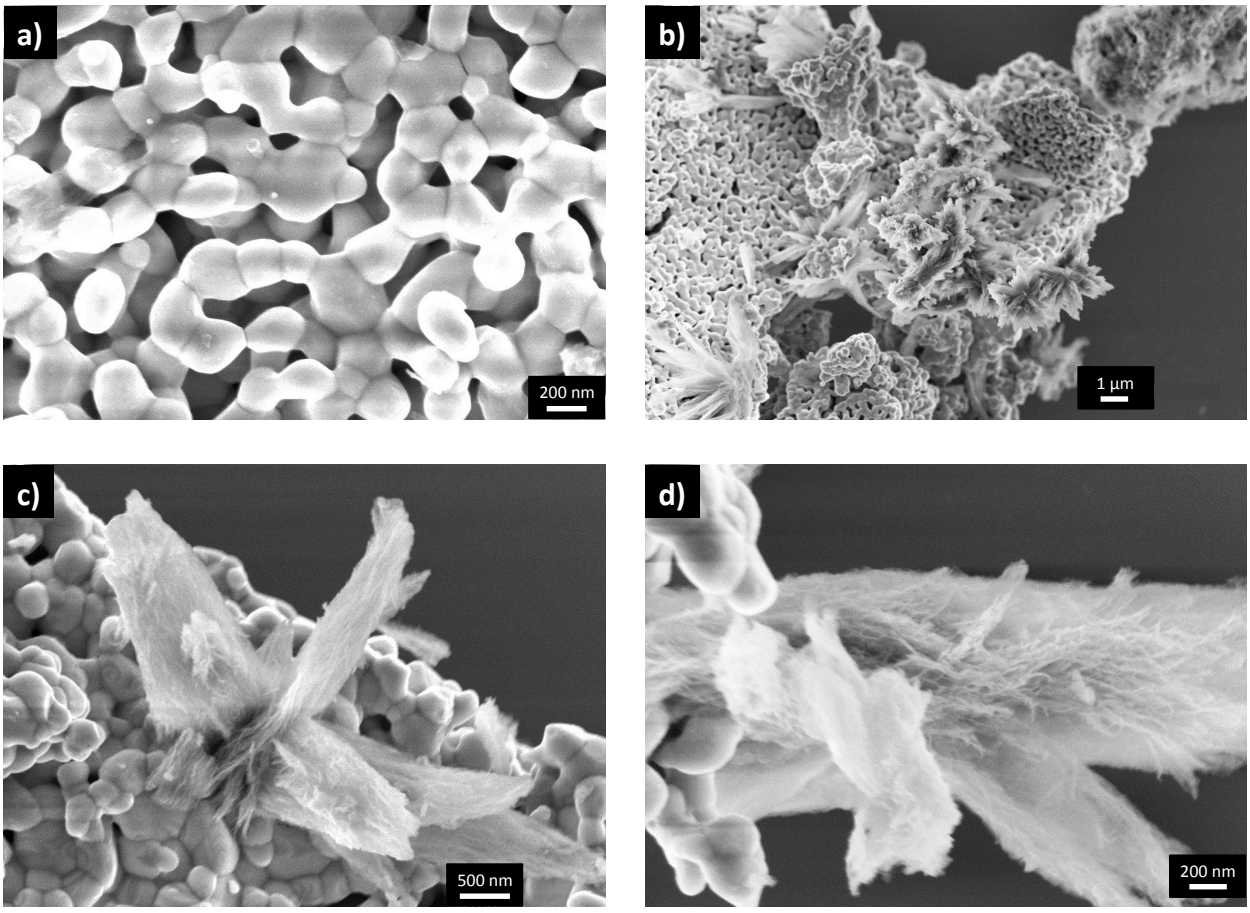

Figure 5.3 SEM images of $LaMnO_3$ before (a) and after (b-d) stability testing. Notice the growth of some secondary material on the surface of the perovskite grains. No secondary phase was detected by pXRD, hence this phase is likely amorphous. (b) shows that these growths are found in all areas of the sample, with varying density. (c) and (d) shows a close-up view of one of these growths. In (d) the rods or "strings" of material can be seen with a diameter of approximately 10-20 nm. EDX shows a 50:50 La:Mn ratio, and probes too large a volume to isolate a single growth.

Figure 5.3d shows a close up of a growth and its rod-like structure. The rods appear to have a diameter between 10-20 nm without significant variation in other growths inspected around the sample. The average total size is on the order of 1-3 μm in diameter. Energy Dispersive X-ray spectroscopy (EDS) shows that the average metals ratio (La:Mn) is 50:50; however, the probe volume of the EDS is too large to isolate the beam to only the corrosion product. Furthermore, attempts to separate and isolate the growths from the $LaMnO_3$ by ultra-sonicating were unsuccessful.

The morphology of these growths appear to be different from the morphology of the plate-like and rod-like crystals found in the Ni and Co samples; however, the shape is consistent with nucleation and growth from some species in solution. It was hypothesized that the growths could be some Si-based species that come from etching of the glass vial in which the experiment was conducted; however, this is not likely as such growths were only observed in the $LaMnO_3$ case. While the origin of the these growths remains unclear, only $LaMnO_3$ seems stable in 3 M KOH when considering only the pXRD patterns.

In addition to testing the perovskite stability in 3 M KOH, tests were also conducted in 0.1 M KOH. As summarized previously in Table 5.2, almost all of the perovskites tested appear stable by both SEM and pXRD in 0.1 M KOH. The only exception was $LaCoO_3$, which showed some inhomogeneity in metals content when analyzed by EDS (some particles were 50:50, while others were 33:66).

Generally, one can use thermodynamic models (e.g. Pourbaix diagrams[21]) to predict the stability of a material (i.e. insolubility and redox behavior) as a function of pH and applied potential; however, such models typically only consider the equilibrium between the active material (i.e. a single metal) and water. Adding additional ions (from an electrolyte or from

other metals in a compound) can alter material stability significantly by adding to, or changing the pertinent equilibria. For example, Ti metal under low potential and low pH conditions, in the presence of SO_4^{2-} anions tends to form soluble $TiO(SO_4)^-$ species whereas Ti metal under the same pH and potential conditions in DI water (without any SO_4^{2-} present) tends to form insoluble TiO_2. Furthermore, in cases where a surface with limited stability is in contact with a liquid (such that the concentration of ions in solution is small, say arbitrarily $\sim 10^{-6}$ M), the surface can experience significant restructuring due to the constant exchange of surface and solvated ions. Considering such equilibria is important, especially for catalytic materials that rely on the surface stoichiometry and structure for optimum performance, for achieving accurate stability models.

In order to augment our experiments with thermodynamic understanding, a model (similar to a Pourbaix Diagram) for the dissolution behavior $LaMnO_3$ has been developed using Density-Functional calculations by Eva Smith[84] (through a collaboration fostered by EMC^2). The model suggests that $LaMnO_3$ is thermodynamically stable and insoluble in the pH and potential region of interest for alkaline fuel cells. It is important to remember however, that such a model only predicts the predominant species present at a given pH and potential condition, and does not necessarily suggest that there are zero ions in solution at a given potential/pH condition in a "region of stability" on a Pourbaix-type diagram. Indeed small concentrations of cationic and anionic species are likely present at all pH/potential conditions, with the concentration of a given species being determined by the thermodynamic equilibrium of the system under study.

While still under development, this model can be applied to other perovskite compounds, both substituted and un-substituted, in-order to develop a more complete understanding of the thermodynamic and kinetic factors at play in the dissolution dynamics of these materials. Figure 5.4 shows the Pourbaix-type diagram calculated by Eva Smith.

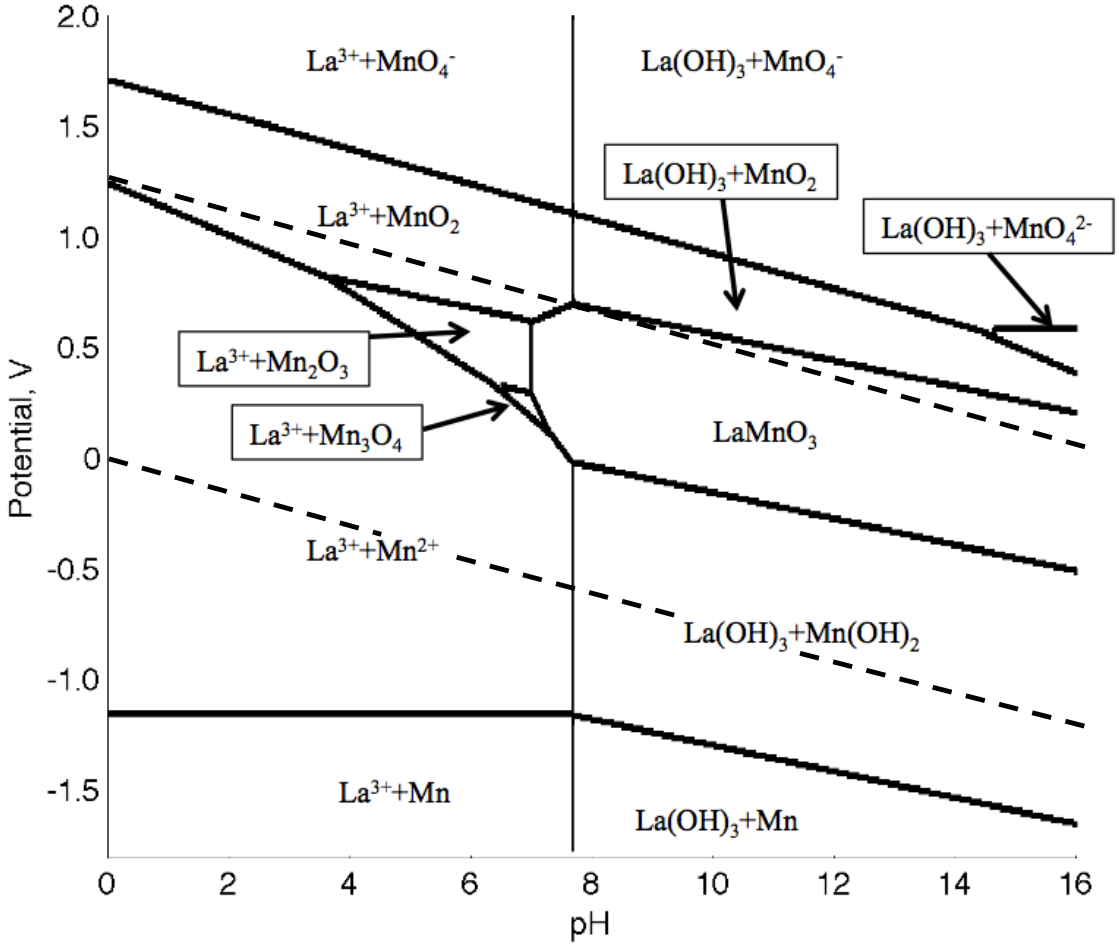

Figure 5.4 Potential vs. pH diagram calculated for $LaMnO_3$. The dashed lines show the stability window of H_2O and have a slope of -59 mV/pH unit. Note the calculated stability of $LaMnO_3$ at the equilibrium potential of ORR at pH 14 (top dashed line). *Image courtesy of Eva Smith*.

Overall, these results raise questions about the chemical stability of these materials, and their potential utility as catalysts in alkaline fuel cells. Previously reported[57,82,83] results suggest at least short-term (up to 12 hours) stability in 9 M base, while our results indicate that many of the perovskite materials are not stable over longer time scales. Furthermore, the stability of these materials in the presence of bound ionic species (such as those associated with polymeric membrane materials) is not well understood. It is clear that additional experiments regarding the dissolution behavior and chemical stability of these compounds is required before firm conclusions are drawn about their potential use as ORR catalysts in alkaline solutions.

5.5 Measuring Electrocatalytic Performance

5.5.1 Electrode Preparation

The electrochemical performance of the perovskite catalysts was evaluated using rotating disk electrode voltammetry (RDE) following the method reported by Suntivich *et al*[73]. Similar to the methods presented in Chapter 3, the perovskite materials were prepared as inks, and drop cast onto cleaned, polished, 5 mm glassy carbon (GC) disk electrodes (polished to mirror finish with 0.05 μm alumina slurry, and cleaned by sonicating in 0.2 M NaOH for 10 minutes). Generally, the catalyst ink was prepared by combining the active catalyst (10 mg) with 20 wt% carbon black (2 mg, Vulcan XC-72) in 2 mL of THF. Approximately 100 μL of 5% Na^+-exchanged Nafion® solution (a commercial 5% Nafion solution was titrated to pH 10 with aqueous 0.1M NaOH) was also added to aid in binding. The suspension was ultrasonicated for 10 minutes to achieve a homogenous ink with an overall composition of 5 mg ml^{-1} perovskite oxide, 1 mg ml^{-1} carbon black, and 1 mg ml^{-1} Na^+-exchanged Nafion. The catalyst ink was applied to the cleaned, polished GC disk electrode to achieve a total loading of 250 μg cm^{-2} (i.e. 10 μL of ink suspension was drop cast onto the GC disk). As reported by Suntivich, the drop cast ink was dried by placing the "wet" electrode into a jar with a few mL of THF. The jar was lightly sealed, and placed in a hood to allow the THF vapor to slowly escape the jar. The THF vapor-liquid equilibrium in the jar atmosphere thus enabled the slow drying of the THF ink to achieve a uniform dispersion on the GC disk electrode. Figure 5.5 shows SEM images of a GC disk with as deposited ink.

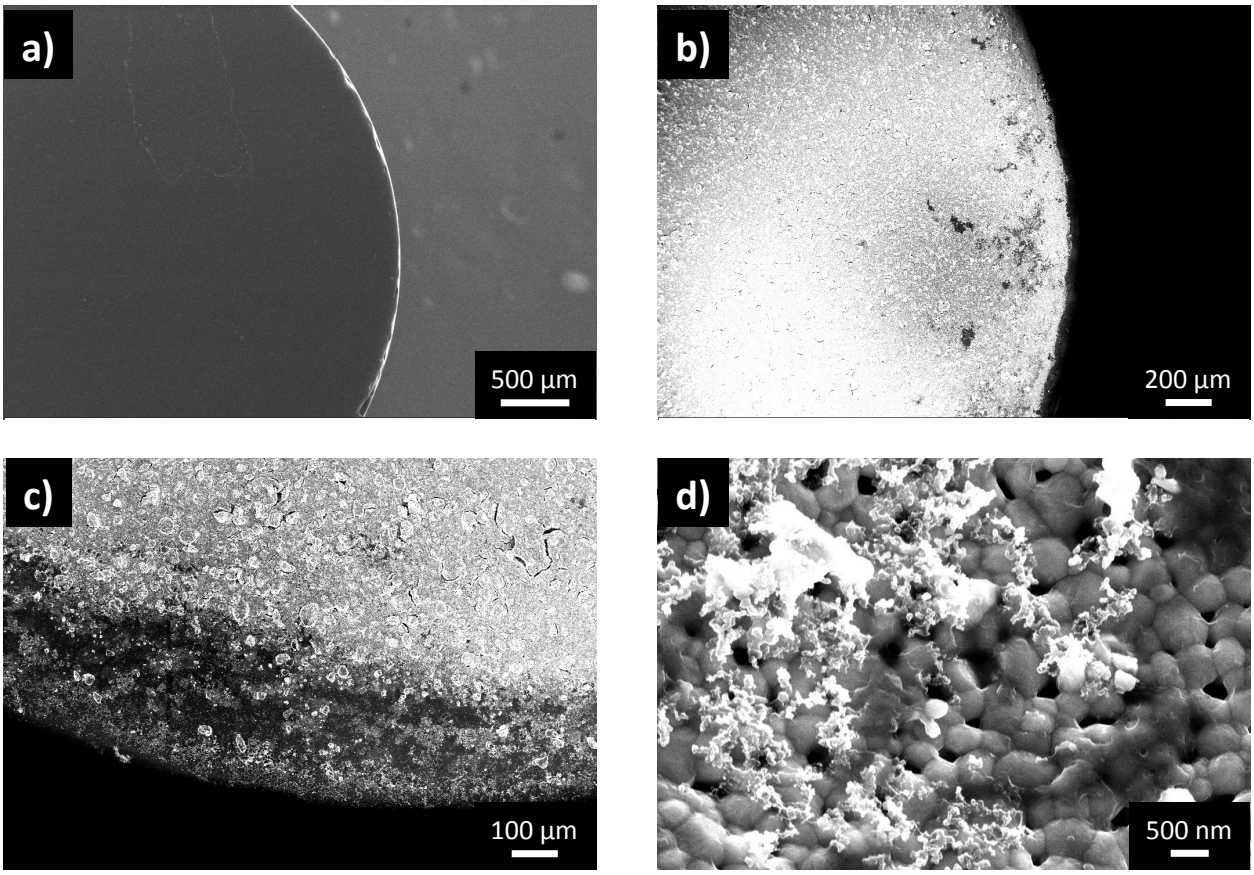

Figure 5.5 SEM images of the bare (a) and inked (b-d) GC electrode. Note in (b) the small "pin holes" that appear to have no catalyst. Also in (c) the edges of the GC electrode have a lower density of catalyst deposited. This is likely due to the wetting of the ink to the GC electrode. The ink bulges near the center, and is thin at the edges resulting in a lower concentration of ink at the edge as it dries. (d) The lighter small particles are the Vulcan XC-72 on top of the perovskite catalyst (round particles of 200-500 nm in diameter). The purpose of the carbon black is to aid with conductivity and with electrically connecting the oxide catalyst to the GC electrode.

Figure 5.5a shows the bare GC electrode after polishing and cleaning. A small amount of the polishing medium (alumina) was still visible on the surface; however, overall the GC electrode appeared clean and well polished by SEM. Figure 5.5b-d shows images of the inked GC electrode. In Figure 5.5b small "pin holes" can be seen which do not contain any of the catalyst ink. Overall only a few pinholes were seen on the films, which indicates a *fairly* well dispersed ink that covers >95% of the GC electrode. Figure 5.5c shows the edge detail of the inked, GC electrode. The apparent density of the oxide ink is lower at the edges. This is likely due to the drying of the ink onto the GC electrode. The THF suspension wets to the GC electrode and bulges near the center. Therefore there is a higher concentration of oxide ink at the center than at the edge. The edges dry faster due to there being less solvent, and hence a lower density of catalyst at the edge is expected. Finally Figure 5.5d shown a close up of the as-deposited oxide catalyst. The smaller lighter features are the Vulcan XC-72, which was added to aid with conductivity and to help make full electrical contact between the catalyst and the GC electrode.

5.5.2 Experiment Parameters

In a typical electrochemical experiment three electrodes are used; the working electrode, the counter electrode, and the reference electrode.[85] The working electrode consists of the active material (the inked GC electrode in this case), while the reference electrode is comprised of a stable, well-behaved redox system that provides a constant potential, against which the working electrode potential is measured (the Standard Hydrogen Electrode is the universal standard while the Ag/AgCl electrode is more commonly used in practice).[86] The counter (or auxiliary) electrode is the source or drain for current that flows thru the working electrode. Typically the

counter electrode potential is not measured, and an electrode material with a high surface area (relative to the working electrode) is used to ensure that any electrochemical process occurring at the counter electrode is fast relative to the process at the working electrode.[87]

Every report on the catalytic activity of perovskite oxides for ORR in alkaline media (at least those surveyed) utilized a Pt counter electrode when performing electrochemical measurements. This presents a challenge since any trace amount of Pt in the electrochemical cell may contaminate the performance of the non-noble metal material.[88] For example, in a typical experiment a 5 mm GC disk electrode has an area of approximately 0.2 cm^2. Assuming 10^{15} atoms cm^{-2} for a single monolayer (ML) coverage and 30 mL electrolyte volume, the concentration of Pt in solution necessary to form one ML need only be about 10 nM. Additionally, there are numerous reports of sub-ML Pt coverage drastically improving the performance of non-precious metal catalysts[8,89-92], hence even a fraction of the Pt needed to form one ML may alter the properties of a non-noble metal catalysts. Furthermore, it is standard practice when performing electroanalytical chemistry to scrupulously clean glassware using aggressive techniques (such as soaking in highly acidic and basic cleaning solutions) such that nM and pM amounts of contaminants adsorbed onto the glass do not attenuate the performance of materials under study.[87,93] It is unclear why so many reports of non-precious metal catalysts continue to utilize Pt as a counter electrode; however, in an effort to remove this *potential* influence from the measurement of the perovskite performance, a carbon foam counter electrode was used. Some experiments using a coil of Pt wire as the counter electrode were conducted for comparison (a separate cell was used for Pt-containing and non Pt-containing experiments).

A three-electrode cell was assembled using a new Pyrex crystallization dish as the electrochemical cell (having never been exposed to Pt or other contaminants). Typical

electrochemical cells use glass frits that separate the cell in to three chambers: one for each electrode. In our initial experiments such a cell was used, however artifacts in the current response from the clogging of the glass frits was observed. Using a single-chamber cell removed these artifacts and enables us to see current responses consistent with various rotating speeds of the electrode (i.e. current responses that changed proportionally with the speed of the rotor). The cell was filled with 0.1 M KOH as the electrolyte with the same electrode arrangement as in traditional three chamber cells (i.e. reference, working, and counter electrodes in a horizontal line approximately 1-2 cm apart. An RDE experiment was performed in Ar and O_2 saturated electrolyte at speeds of 100, 400, 900, and 1600 RPM. The test gas was allowed to bubble in solution for 15 minutes prior to each measurement, and was continuously bubbled during cycling (the bubble rate was adjusted to prevent bubble formation on the working electrode). A Ag/AgCl reference electrode was used for all measurements. The perovskite catalysts were tested for ORR by scanning from 0.300 to -0.600 V vs. Ag/AgCl at 10 mV s^{-1} at room temperature (25 ºC).

Additionally, a Au disk working-electrode was used in lieu of a GC disk for some experiments. This technique was originally reported by former group member Dr. Chin Subban[94], and was used for oxide materials to facilitate greater electrical contact between the active material and the disk electrode. A commercial Au disk electrode was used, and the ink drop cast method (with the same parameters as described before) was used to apply the oxide catalyst to the Au electrode. Au is also a well-known catalyst for ORR in alkaline solutions[20], so it is likely in these situations that some of the observed ORR activity arises from the Au disk. The extent of the activity, however, will be limited by the extent to which O_2 saturated electrolyte can reach the Au disk through the perovskite catalyst.

5.5.3 The Levich Equation

RDE experiments are governed by the Levich Equation (Equation 5.1), which describes the current response due to the mass-transport limited delivery of a redox active species to the working electrode surface. The theory from which the Levich Equation is derived is discussed elsewhere[85], while the equation is shown for the purposes of this discussion.

$$i_l = 0.62\, n\, F\, A\, {D_O}^{2/3} \nu^{-1/6} \omega^{1/2} C_O \tag{5.1}$$

$$i^{-1} = (0.62\, n\, F\, A\, {D_O}^{\frac{2}{3}} \nu^{-\frac{1}{6}} \omega^{\frac{1}{2}} C_O)^{-1} + \, i_k^{-1} \tag{5.2}$$

In a typical RDE experiment, the current response over a potential range at several rotation speeds is collected. For a reduction process, past some potential the current will become constant and is the mass-transport limited current (i_l), meaning that as soon as the analyte reaches the working electrode surface it is reduced (or the analyte is reduced as quickly as it can be delivered). Plotting the limiting current (at a given potential for all speeds) versus the square root of the rotation speed ($\omega^{1/2}$, in units of $s^{-1/2}$) typically results in a linear plot with a y-intercept of zero. Plots that deviate from linearity are said to be kinetically limited, and a plot of the inverse limiting current versus $\omega^{-1/2}$ (a so-called Koutecky-Levich plot, equation 5.2) typically results in a linear plot with the y-intercept being the inverse of the kinetic current associated with the process.

A Levich analysis of RDE data typically enables one to determine the diffusion constant (D_O, units of $cm^2\ s^{-1}$) of the analyte in solution, in the case that the number of electrons (n) transferred during the redox process is known. Conversely, if one knows the diffusion constant of the analyte ($1.90 \times 10^{-5}\ cm^2\ s^{-1}$ for O_2 in water[95,96]), a Levich analysis can be used in part to

determine the mechanistic steps associated with a complex redox reaction (e.g. the Oxygen Reduction Reaction). Additionally, the remaining terms in the Levich equation are constants or specific to the system under study. F is Faraday's Constant (96485 C mol^{-1}), A is the area of the working electrode (in units of cm^2, 0.1964 cm^2 for a 5 mm disk), v is the kinematic viscosity of the electrolyte (in units of $cm^2\ s^{-1}$, 0.01 $cm^2\ s^{-1}$ for aqueous electrolytes[95,96]), and C_O is the bulk concentration of the analyte under study (in units of mol cm^{-3}, 1.20 x 10^{-6} mol cm^{-3} for O_2 saturated solution at 25 ºC[95,96]).

5.6 Results and Discussion

Table 5.3 shows a summary of the RDE experiments conducted for the perovskite catalysts. Also included in the table are samples of $LaMnO_3$ and $LaMn_{0.5}Cu_{0.5}O_3$ prepared by the Shao-Horn group at MIT (i.e. the *same* materials studied by Suntivich and reported in Nature Chemistry[1]).

Each of the limiting current densities (normalized the geometric area of the working electrode, or 0.1964 cm^2 for a 5 mm disk diameter) shown in Table 5.3 were obtained at 0.400 V vs. RHE and 900 RPM in O_2 saturated 0.1 M KOH (except $LaCrO_3$ was taken at 1600 RPM). The most interesting feature of the data is in the electron count calculated from these limiting currents. None of them are integer values (as would be expected), and many of them are greater than 2. Non-integer values of electrons possibly indicates a large kinetic current associated with ORR on these catalysts, while electron counts greater than 2 may suggest some of the catalysts are performing ORR by the 4 electron pathway while others are performing via the 2 electron pathway. In the following discussion, a few examples from these experiments will be discussed in more detail.

Table 5.3 Summary of RDE experiments of perovskite catalysts.

Perovskite Compound	*Working Electrode*	*Counter Electrode*	j_l (mA cm_{disk}^{-2})†	$E_{1/2}$ (V)	n^f
$LaCrO_3$	GC disk	C foam	-1.89§	0.718	1.33
$LaMnO_3$	GC disk	C foam	-3.49	0.673	3.26
$LaMnO_3$	GC disk	Pt wire	-2.59	0.662	2.43
$LaMnO_3$	Au disk	C foam	-1.15	0.688	1.08
$LaMnO_{3+\partial}$	GC disk	C foam	-0.76¢	0.637	0.71
$LaMnO_3$ (MIT)	GC disk	C foam	-0.96	0.553	0.90
$LaMnO_3$ (MIT)	GC disk	Pt wire	-1.18	0.593	1.11
$LaMnO_3$ (MIT)	Au disk	C foam	-2.63	0.743	2.46
$LaFeO_3$	GC disk	C foam	-1.76	0.698	1.64
$LaCoO_3$	GC disk	C foam	-3.68	0.673	3.44
$LaNiO_3$	GC disk	C foam	-2.49	0.628	2.33
$LaNiO_3$	Au disk	C foam	-1.80¢	0.647	1.68
$LaMn_{0.5}Co_{0.5}O_3$	GC disk	C foam	-3.17	0.688	2.97
$LaNi_{0.5}Co_{0.5}O_3$	GC disk	C foam	-2.81	0.613	2.63
$LaMn_{0.5}Cu_{0.5}O_3$	GC disk	Pt wire	-3.15	0.693	2.95
$LaMn_{0.5}Cu_{0.5}O_3$ (MIT)	GC disk	C foam	-2.38	0.658	2.23
$LaMn_{0.5}Cu_{0.5}O_3$ (MIT)	GC disk	Pt wire	-2.26	0.658	2.12
$LaMn_{0.5}Cu_{0.5}O_3$ (MIT)	Au disk	C foam	-2.69	0.743	2.51
Pt/C (E-Tek)	**GC disk**	**C foam**	**-2.11**	**0.878**	**1.97**
Bulk Pt	**Pt disk**	**C foam**	**-2.69**	**0.824**	**2.51**

† Current at 0.4 V vs. SHE rotated at 900 RPM in O_2 saturated 0.1M KOH on 5 mm disk electrodes

§ Current at 1600 RPM

¢ Limiting current of 1st plataeu

ƒ Calculated from the Levich Equation $i_l = 0.62\ n\ F\ A\ D^{2/3}\ \nu^{-1/6}\ C_{O2}\ \omega^{1/2}$

Figure 5.6 shows RDE experiments of bare GC (right) and Au (left) disk electrodes in O_2 saturated 0.1 M KOH. Both disk materials show activity for ORR. The most notable feature is the plateau below 0.600 V vs. RHE for the GC electrode. This is classic behavior for ORR proceeding by the 2-electron, peroxide route. Furthermore, the $E_{1/2}$ of the ORR wave seems to be shifting to more negative potentials at higher rotation speeds, this is also indicative that there are significant kinetic limitations in performing ORR on the GC electrode. Additionally, the GC electrode is producing less current at the highest rotation speed than at the slowest. The expected Levich behavior would be a limiting current proportional to the square root of the rotation speed, and hence the scan at 1600 RPM should produce higher current than at 100 RPM assuming no additional kinetic challenges.

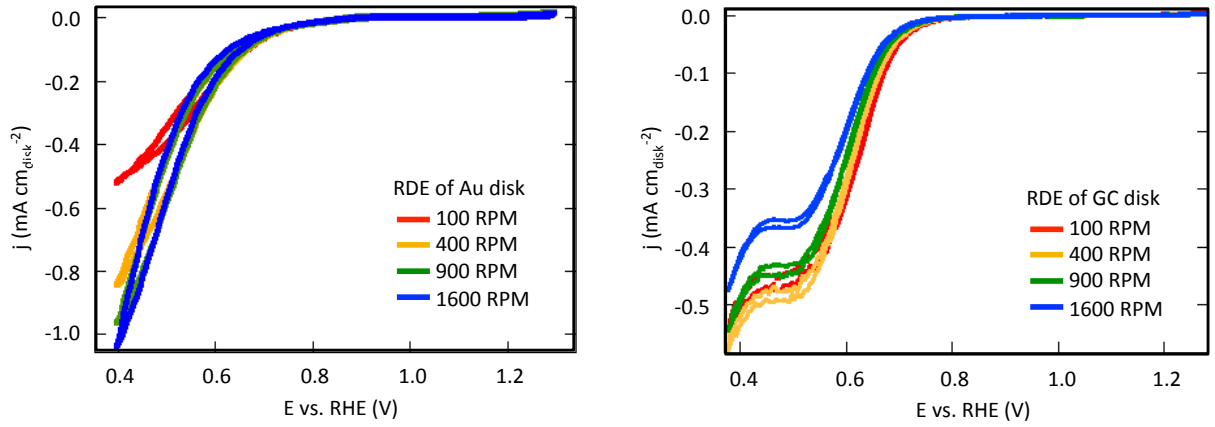

Figure 5.6 RDE study of cleaned, polished, and bare Au disk (left) and GC disk (right) electrodes in O_2 saturated 0.1 M KOH. Both electrodes show some activity from ORR, hence any observed activity of the perovskite catalysts will be some combination of the oxide and the disk material activities. Note for GC the plateau below 0.600 V vs. RHE. This is a classic sign of peroxide production, while similar behavior is not seen for the gold in this potential range. This suggests GC is a better catalyst for ORR than Au which is not true. Hence there is some problem with the experimental set up, and additional results will have to be carefully analyzed to remove this anomalous feature. Additionally, the $E_{1/2}$ of the GC electrode becomes more negative at higher rotation speeds, which is indicative of kinetic limitations of ORR on the electrode.

The Au disk electrode in Figure 5.6 (left) is also interesting. Au has been reported to be a good ORR catalyst in base[20] (although it is expected to produce less current than Pt[96]), and has been shown to reduce O_2 by the 2-electron, peroxide route in base.[97] Furthermore, Swider-Lyons *et al*[97] showed that at 0.4 V vs. RHE, Au should be in the first mass-transport limiting current regime for the 2-step mechanism, and that the onset for the 2nd 2-electron transfer occurs at approximately 0.3 V vs. RHE. While the 100 RPM scan appears to begin a plateau at about 0.4 V vs. RHE, the remaining scans are not, this too is indicative of significant kinetic limitations for the reduction of oxygen. Furthermore, the fact that GC appears to a better ORR catalyst than Au by these scans is disturbing and indicates some problem with our measurement of the catalytic performance of these electrodes. Sources within the experimental set up that might have contributed to this obscure behavior were evaluated, however none could be found. It was clear as we continued to study the perovskite catalysts, we would need to consider the quality of the data we were obtaining.

Figure 5.7 shows an RDE study of the non-stoichiometric $LaMnO_{3+\partial}$ in O_2 saturated 0.1 M KOH. The most prominent feature of the RDE scan is the appearance of plateau below 0.6 V followed by another redox wave near 0.4 V. This suggests that the catalyst is performing ORR via the two-step, 2-electron pathway, and is producing peroxide. Additionally, the plot on the left shows multiple scans at 900 RPM in which the current density is decreasing upon cycling suggesting that the catalyst is electrochemically unstable (or that catalyst is being lost from the GC electrode). The plot on the right shows the tenth cycle at several rotation speeds. Interestingly, the blue curve (corresponding to 1600 RPM) shows less current than the scan at 100 RPM. Typical Levich behavior would show that the current response is proportional to the square root of the rotation speed (hence the 1600 RPM scan should show 4x the current

response), however this is not seen. This is due to the instability of the catalyst, as the 1600 RPM experiment was performed last (i.e. after approximately 30 cycles at slower speeds) with each cycle decreasing somewhat in current (as is shown for the 900 RPM scan). It is clear from this data that $LaMnO_{3+\partial}$ is not electrochemically stable when cycling in the potential range of 0.4 V to 1.2 V vs. RHE. Furthermore this data also suggests that this catalyst favors the peroxide producing mechanism, while further studies are required to prove this conclusively.

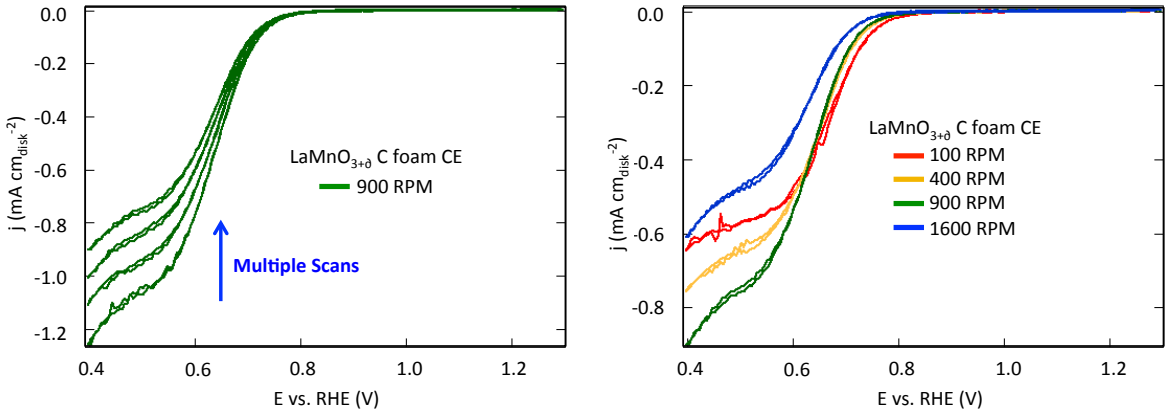

Figure 5.7 RDE data for $LaMnO_{3+\partial}$. The data on the left was obtained in O_2 saturated 0.1 M KOH at 900 RPM. Note that upon multiple cycles, the current is decreasing indicating that the catalyst is unstable. Note also the plateau below 0.6 V followed by more cathodic current below 0.4 V which is indicative of peroxide formation. The data on the right shows the full series of rotation speeds. Because of the instability of the catalyst, the scan at 1600 RPM shows lower current than the other scans when it should show more. Scans at each speed showed the same catalyst instability as the scan at 900 RPM.

Figure 5.8 shows an RDE study of the stoichiometric $LaMnO_3$ in O_2 saturated 0.1 M KOH using a C foam (a) and a Pt wire (b) counter electrode, as well as Levich (c) and Koutecky-Levich (d) analyses.

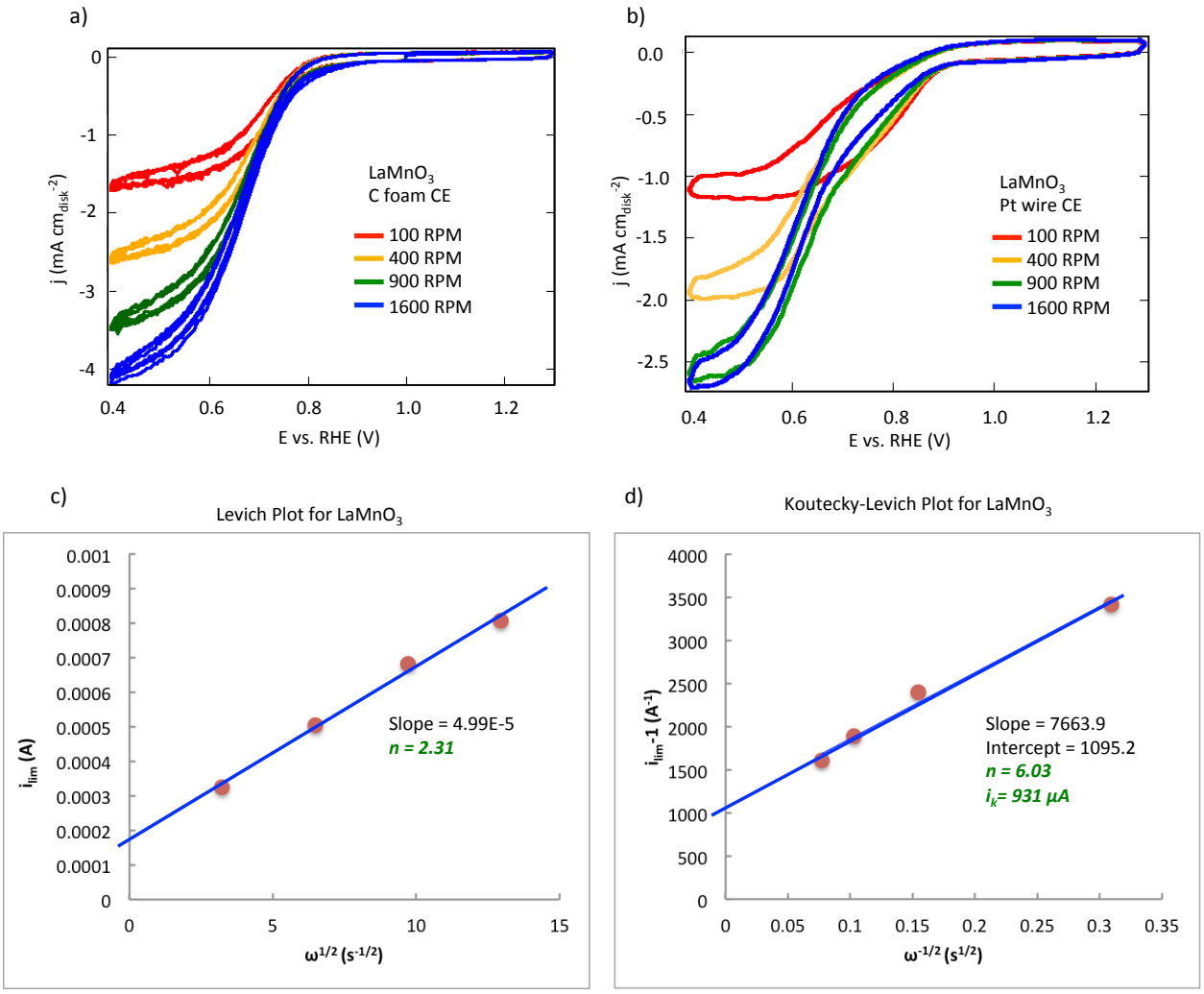

Figure 5.8 RDE study of $LaMnO_3$ with a C foam (a) and a Pt wire (b) counter electrode. Unlike the non-stoichiometric $LaMnO_{3+\partial}$, this catalyst does not appear to produce peroxide (i.e. there is not a plateau as observed in Figure 5.7), which may suggest that the mechanism of ORR is different on this catalyst, or that the same mechanism has different rate-limiting characteristics. The scans with the C CE appear to have higher current and less capacitance than the Pt CE scan. Additionally, the scan with the Pt CE does not seem to follow expected rotation-dependant current response in the 1600 RPM scan. (c-d) Levich and Koutecky-Levich plots for the C CE RDE data. The Levich plot yields an apparent electron transfer count of 2.31. The Koutecky-Levich (currents obtained at 0.6 V vs. RHE) plot shows a significant kinetic current of 931 µA (not current density), which is more current than was passed in the cell on any given scan. Additionally the apparent electron count is 6.03. As only 4 electrons can be transferred in the reduction of oxygen it is likely that there are non-faradaic processes that are inhibiting the kinetics of ORR on this catalyst.

Figure 5.8 a and b showed RDE experiments using two different counter electrodes. As discussed previously, using a noble metal counter electrode when studying non-noble metal catalysts can possibly lead to spurious results due to deposition of noble metal atoms onto the catalytic surface. The most interesting feature is that using the C foam CE electrode apparently produces more current density than using the Pt wire CE. Furthermore, using a Pt wire CE seems to cause higher capacitance (i.e. the hysteresis between the negative-going and positive-going scans is greater). It is important to note that simply changing the counter electrode would not necessarily cause these effects alone. However the catalyst material in both cases is from the same preparation, using the same ink-deposition technique. The GC electrode used for each experiment was different in an effort not to contaminate the equipment used for Pt-free studies.

An additional interesting feature is the lack of a plateau below 0.6 V as was observed in Figure 5.7 for the non-stoichiometric manganate. Using the data from the C foam CE experiment, Levich (c) and Koutecky-Levich (d) plots were constructed. The Levich analysis yields an apparent electron count of 2.31. If this catalyst were operating via the 2-electron peroxide mechanism an electron count of approximately 2 would be expected. Furthermore, a Levich analysis assumes 100% mass-transport control in the limiting current regime. One could argue that the voltammograms never truly reach a mass-transport limited current which is further bolstered by the deviation from linearity at low rotation speeds (i.e. the plotted data seems to approach a non-zero y-intercept) suggesting additional kinetic limitations involved in the ORR mechanism.

Using the Koutecky-Levich (KL) plot (Figure 5.8d) one can calculate the apparent kinetic current by plotting the inverse limiting current versus the inverse of the square root of the rotation speed. In this case the data should appear linear with a slope proportional to the inverse

electron count and the y-intercept being the inverse kinetic current. Using the current at 0.6 V vs. RHE (which is in the kinetic region), a KL analysis yields an apparent electron count of 6.03 and a kinetic current of 931 μA (note this is not a current density). 931 μA is more current that was produced for any of the individual scans before they were scaled to the disk electrode geometric area, and only 4 electrons can be transferred for ORR, hence this data suggest significant kinetic limitations in performing ORR on this catalyst, and suggests that there are non-faradaic processes involved in the mechanism. These non-faradic processes may be enhanced when using a Pt wire CE, which may explain the larger apparent capacitance. The exact origins of this anomalous electron count is unknown, yet it is clear that there are significant hurdles to performing ORR on this catalyst (at least from our preparation). As stated previously, $LaMnO_3$ reportedly favors the 2-electron mechanism[66], while Suntivich *et al* finds that it is among the highest performing 4-electron catalysts[1]. It is clear that many questions regarding the exact performance of this material remain unanswered, and that $LaMnO_3$ (especially the non-stoichiometric variant) does not appear to possess the necessary chemical and electrochemical stability required for long-term operation in a fuel cell.

Figure 5.9 shows a similar RDE study for $LaNiO_3$ using a GC (a) and Au (b) disk electrode. $LaNiO_3$ appears somewhat more electrochemically stable than $LaMnO_3$ although decreasing current upon cycling is observed in the 1600 RPM scan. A Levich analysis of this data results in an apparent electron transfer number of 2.33, which suggests $LaNiO_3$ reduces oxygen via the 2-electron, peroxide pathway.

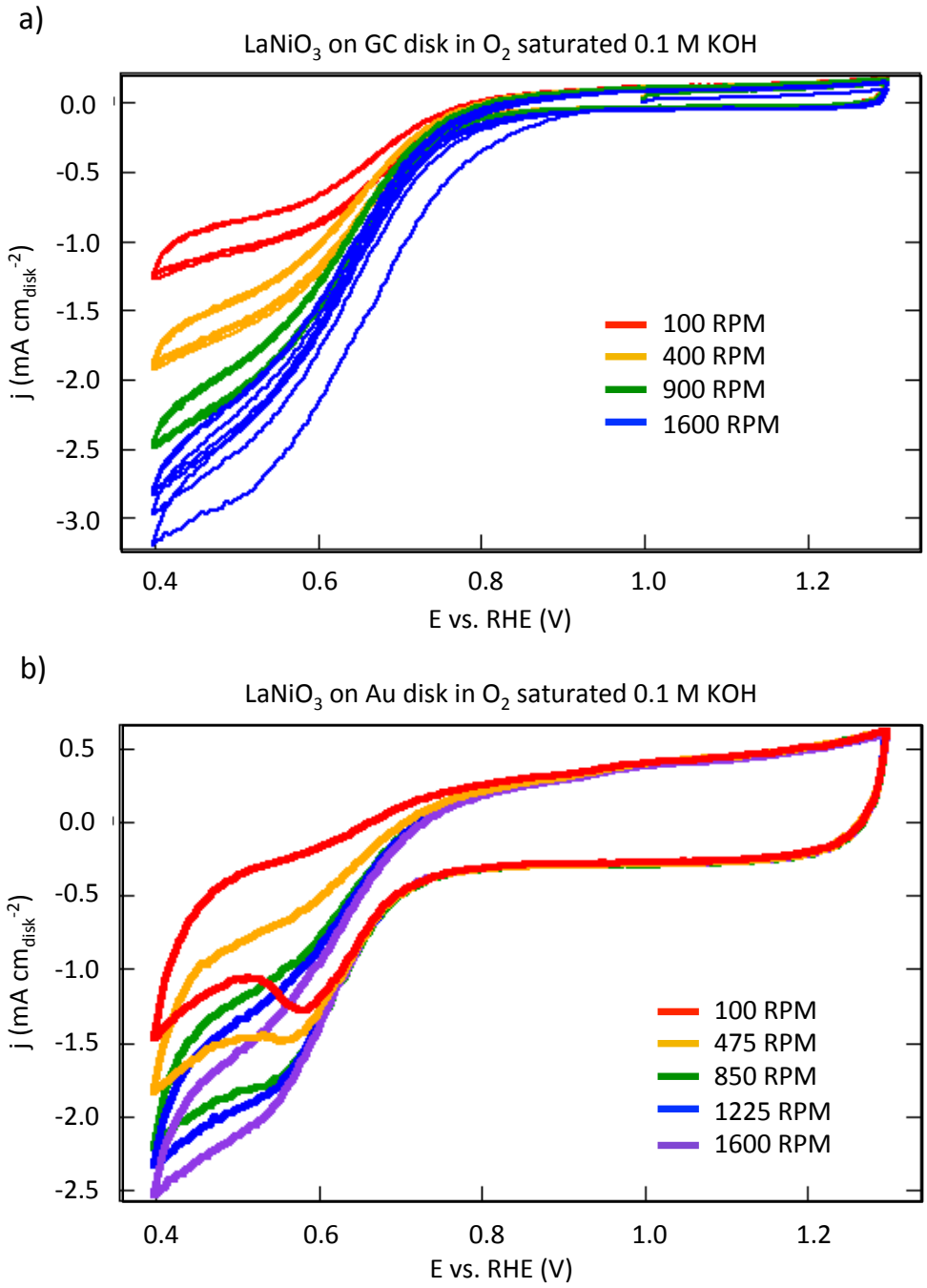

Figure 5.9 RDE study of $LaNiO_3$ on a GC (a) and Au (b) 5 mm disk electrodes. Note the decreasing current in the 1600 RPM scan of the GC disk experiment which may suggest that $LaNiO_3$ is electrochemically unstable. (b) RDE study of $LaNiO_3$ on a Au disk electrode. Au is also an ORR catalyst in base, so the resultant current is a convolution of the activities of Au and the perovskite catalyst. Note the appearance of a wave near 0.6 V vs. RHE at low rotation speeds which disappears at higher rotation speeds. This is is a surface redox process from an an unknown source.

Figure 5.9b shows an RDE study of $LaNiO_3$ on a 5 mm Au electrode. While similar currents are seen for both the GC and Au supported samples, the appearance of a redox wave at approximately 0.6 V vs. RHE at low rotation speeds is interesting, and arises from some unknown surface process. It is unclear why the wave is visible at low rotation speeds but appears to disappear at higher rotation speeds. It is possible that some of the perovskite catalyst is lost from the working electrode, however the typical current loss upon cycling associated with that complication is not seen in the Au scans.

In comparing the RDE studies for $LaNiO_3$ and $LaMnO_3$ it is interesting to note that each catalyst appears to reduce oxygen in different ways (either by different mechanisms or at different rates). This speaks to the frustration and complexity we've experienced with perovskite catalysts, as well as conflicting reports regarding the characteristics and activity of perovskite catalysts. Each of the perovskites prepared were studied using RDE with results summarized in Table 5.3. Notably, $LaCrO_3$, $LaMnO_{3+\partial}$, $LaFeO_3$, and $LaCoO_3$ all appeared electrocatalytically unstable (i.e. they showed decreasing current upon cycling at a given rotation speed) while the B-substituted samples showed marginally better stability and activity. $LaCoO_3$ showed the highest apparent electron count (3.44) from the Levich analysis. It is unclear from the data we've collected if La-based perovskites will be suitable replacements for noble metal catalysts in alkaline solutions; however, our results do raise additional questions regarding the stability of these materials in fuel cell like conditions. Further experiments will be required in order to draw firm conclusions regarding utility of perovskite oxide catalysts for alkaline fuel cells.

In order to validate our electrochemical results and to rule-out any sources of error arising from the preparation of the perovskite oxides, samples of the materials reported by Suntivich[1]

were requested from Dr. Yang Shao-Horn and collaborators at MIT. We received samples of $LaMnO_3$ and $LaMn_{0.5}Cu_{0.5}O_3$ prepared by the Shao-Horn group that were approximately 2-years old and were the same samples whose catalytic performance was reported in Nature Chemistry. pXRD patterns were taken of the samples, which showed that the MIT samples were identical to our samples. SEM images showed that the particle morphology was similar, but that the overall particle sizes of the MIT samples were larger (approximately by a factor of 10) compared to our preparation. BET surface area measurements also showed that the MIT samples had lower surface as of approximately 6 $m^2\ g^{-1}$ (compared to our samples which were 12-16 $m^2\ g^{-1}$). The larger apparent particle size is not surprising as the MIT samples were reportedly annealed at higher temperatures than the corresponding Cornell samples, which likely resulted in a larger degree of sintering and particle growth. Additionally, the MIT samples were over 2-years old, and therefore slow reactions with H_2O vapor, O_2 or other impurities in air may have altered the surface composition or structure. Figure 5.10 shows a comparison of the pXRD (a) and SEM images (b) for $LaMnO_3$ prepared at Cornell (left) and MIT (right). Ultimately, we concluded that the samples were similar enough on which to base a fair comparison of electrocatalytic performance.

a)

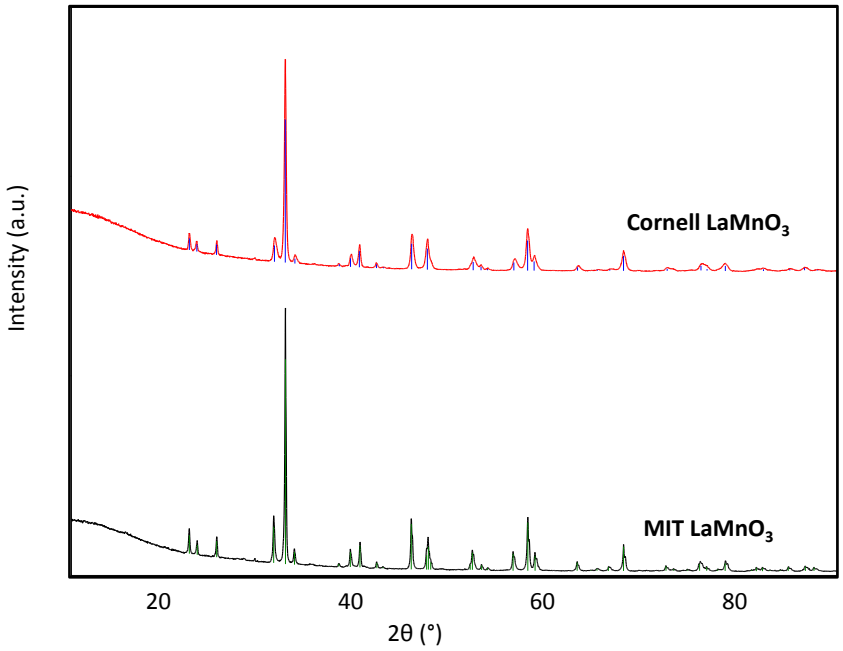

b)

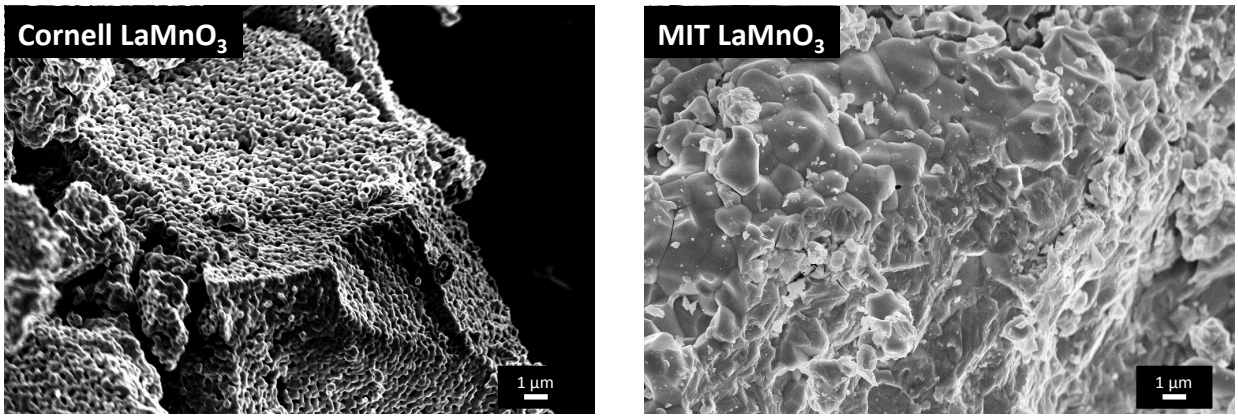

Figure 5.10 (a) pXRD patterns of Cornell (red) and MIT (black) prepared $LaMnO_3$. (b) SEM images of Cornell (left) and MIT (right) prepared $LaMnO_3$. The scale bar in each image is the same. The sample prepared at Cornell has a significantly smaller particle size than that of the MIT sample. The BET surface areas were approximately 14 $m^2\ g^{-1}$ (Cornell) and 6 $m^2\ g^{-1}$ (MIT).

To evaluate the electrocatalytic performance of the MIT prepared catalyst, the same electrode preparation methods and experimental parameters for the Cornell prepared samples were used. Figure 5.11 shows the results of the RDE studies of the MIT $LaMnO_3$ using a C foam (top) and a Pt wire (bottom) CE.

Comparing the RDE studies of the MIT (Figure 5.11) and Cornell (Figure 5.8) $LaMnO_3$ samples, one can see that the Cornell prepared sample shows significantly higher current density than the MIT sample (approximately -0.8 mA cm^{-2} for MIT and approximately -3.5 mA cm^{-2} for Cornell). Additionally, as shown in Table 5.3 the half-wave potential (perhaps a better measure of overpotential than an arbitrary "on-set" potential) is 120 mV more positive for the Cornell sample than for the MIT sample (0.673 vs. 0.553 mV respectively). Although these two materials are the same identical phase and stoichiometry, the particle sizes are different which may account for the significantly higher currents observed for the Cornell prepared sample. In order to determine if differences in particle size and surface area were responsible for the difference in observed current density, the current was renormalized to the surface area of the perovskite as measured by N_2-physisorption (i.e. BET) The resultant current densities were 0.029 mA cm^{-2} for the MIT prepared sample and 0.056 mA cm^{-2} for the Cornell sample (using the 100 RPM scan as an example). Generally, the Cornell prepared sample out-performed the MIT sample by a significant margin in each case. While normalizing the current to the catalyst surface area is a more quantitatively accurate measure of the catalyst's activity, normalizing to the geometric area of the disk is consistent with MIT's original report, and enables an "apples-to-apples" comparison of the two materials.

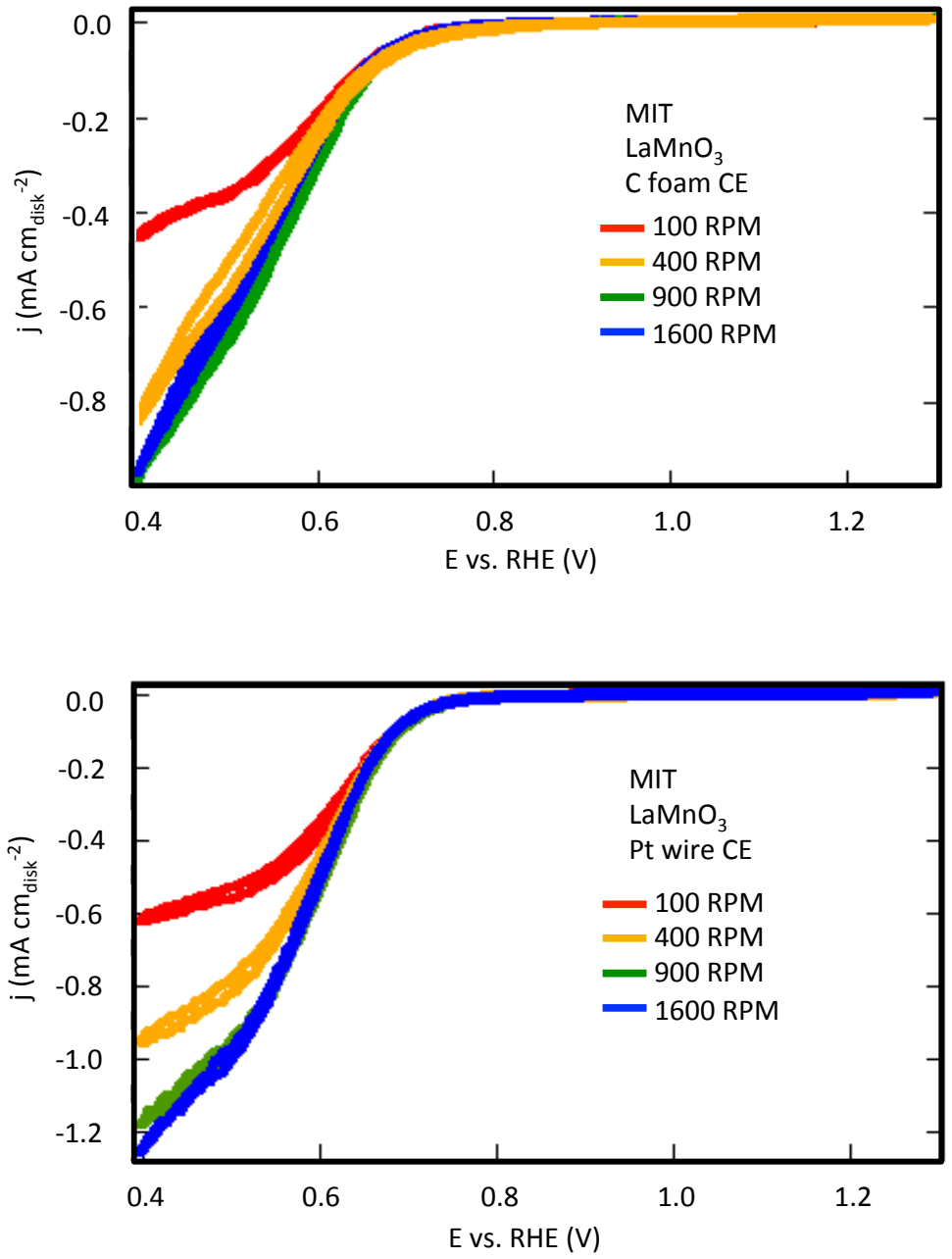

Figure 5.11 RDE study of MIT prepared $LaMnO_3$ with a C foam (above) and a Pt wire (below) counter electrode. Note the higher current density obtained when using a Pt wire counter electrode. There are no obvious differences in sample preparation nor apparent differences in the catalyst ink deposition. Note also the subtle appearance of two redox waves which are visible in the 900 and 1600 RPM scans using the Pt wire CE (and in the 100 RPM scan using the C foam CE), which may indicate peroxide formation.

Figure 5.12 shows an RDE study for the second sample MIT provided: $LaMn_{0.5}Cu_{0.5}O_3$. Scans using both a C foam (a) and Pt wire (b) CE are shown, and appear to have similar current densities (although the scans using the Pt wire CE have a slightly higher current density). Figure 5.12c shows a Levich analysis for the data obtained using a C foam CE which results in an apparent electron transfer count of 1.78 suggesting the formation of peroxide during ORR. Additionally, the fact that the current density does not approach zero at low rotation speeds suggests that there is likely some non-faradic, kinetic current resulting from some mechanistic step in ORR. Figure 5.12d shows a Koutecky-Levich analysis (using currents at 0.6 V vs. RHE, which is in the kinetic region) of the same data set, which yields an apparent electron count of 2.78 and a kinetic current of 782 μA.

The Koutecky-Levich (KL) analysis of this data resulted in a slope of 16657 A^{-1} $s^{1/2}$, or 3.27 mA^{-1} cm_{disk}^2 $s^{1/2}$. Originally, this same sample was reported by Suntivich *et al*[1] to show a KL slope of approximately 11 mA^{-1} cm_{disk}^2 $s^{1/2}$. From this data the authors calculated an apparent electron count of 4, and reported no apparent kinetic current. It is unclear why there is such a discrepancy between these two analyses of the same sample (using the exact same experimental parameters). We are currently working with the authors to resolve these issues, while it is clear that the reproducibility of the published data is questionable.

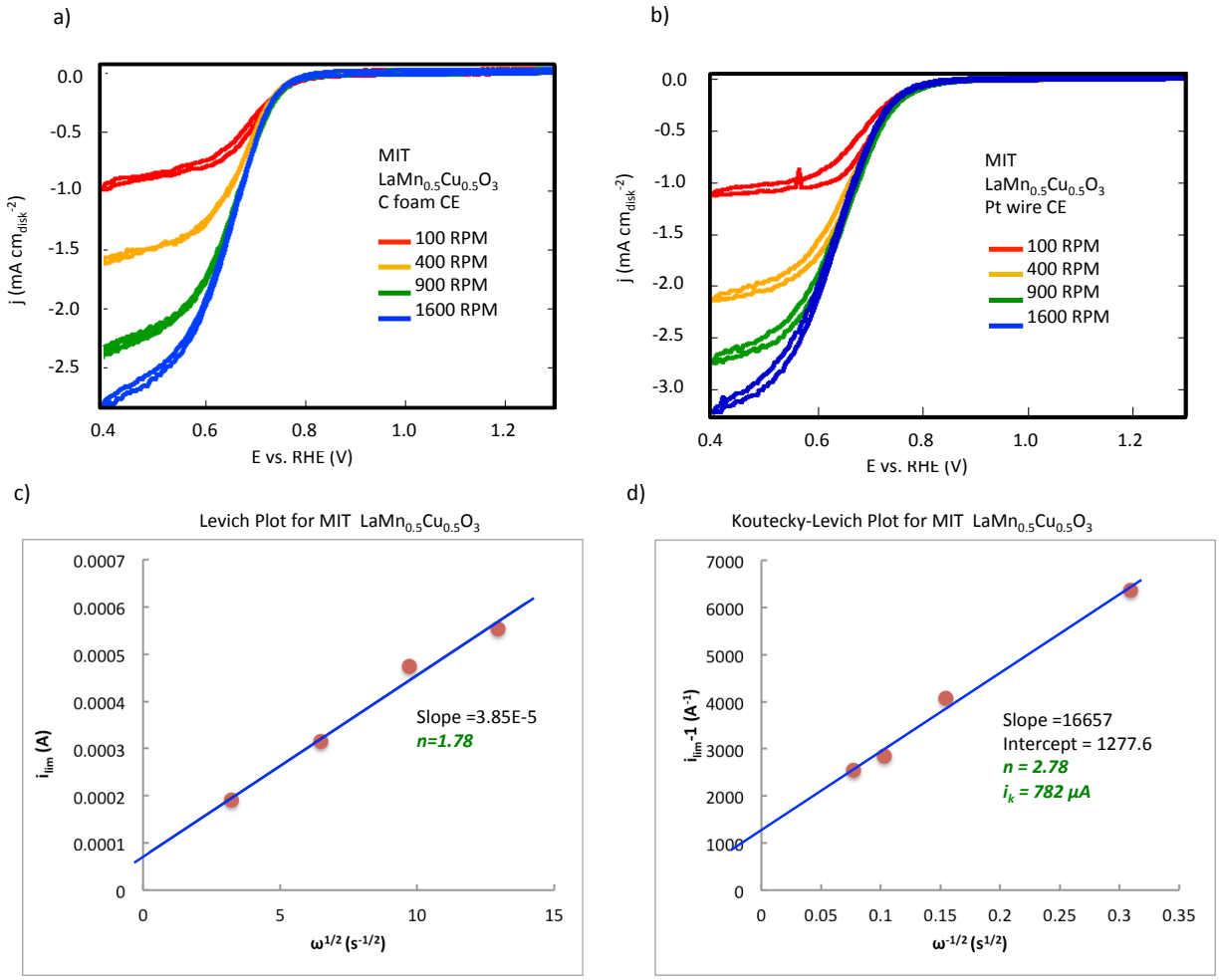

Figure 5.12 RDE studies of MIT prepared $LaMn_{0.5}Cu_{0.5}O_3$ using a C foam (a) and Pt wire (b) CE. Both scans show approximately the same current density, although the scans using the Pt wire CE are slightly higher. (c) A Levich analysis of the data obtained using the C foam CE. The apparent electron count was determined to be 1.78 which suggest that peroxide is being produced. Note that the data does not trend to zero current at low rotation speeds, which suggest that there is some kinetic background current. (d) Koutecky-Levich (currents taken at 0.6 V vs. RHE) analysis of the RDE study using a C foam CE. As described in Figure 5.8, the apparent kinetic current (not current density) was calculated to be 782 µA which is more current than was passed for any individual scan. However, unlike Figure 5.8, the apparent electron count was determined to be 2.78. Overall this data suggests significant kinetic limitations in performing ORR on these perovskite catalysts, and conflicts with the data that was published in Nature Chemistry by the Shao-Horn Group.

Ultimately, the perovskite samples prepared at Cornell appear to outperform the MIT samples by a significant margin. It is unclear whether this is due purely to differences in particle size and shape, or if other experimental parameters are influencing the results. Future work between MIT and Cornell should focus on assuring accurate electrochemical measurements so that a consensus can be reached. Despite the conflicting electrochemical performance data, one thing that we have agreed on is the relative instability of these perovskite catalysts in simulated fuel cell conditions. Unless a chemically stable stoichiometry can be found, it is unlikely that these non-noble metal catalysts will have significant impact in future fuel cell technologies.

As a final comparison, a 5 mm Pt disk electrode and commercially prepared Pt/C (50 wt %, E-Tek) were studied, and compared with the Cornell prepared perovskites. Figure 5.13 shows an RDE study of Pt/C (top) and a comparison of the performance of these catalysts (bottom).

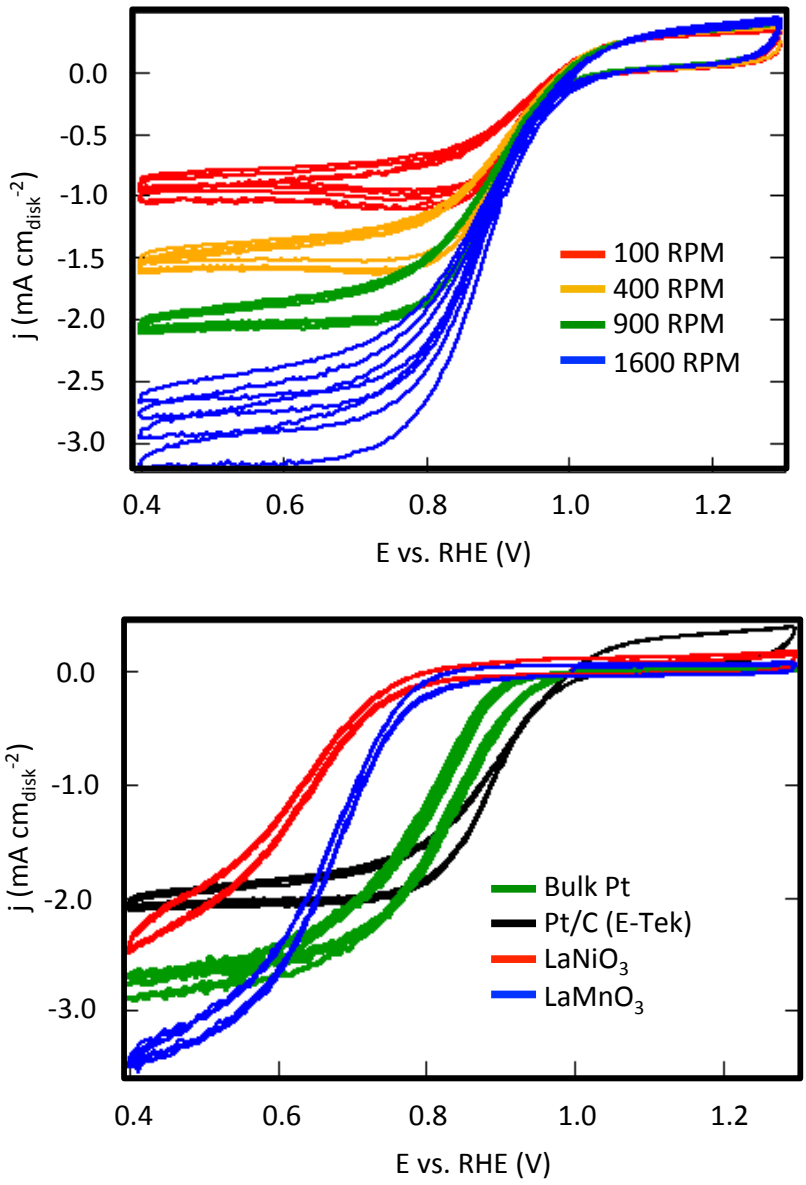

Figure 5.13 RDE study of commercial Pt/C (top) and a comparison of Pt with $LaNiO_3$ and $LaMnO_3$. (top) the 1600 RPM scan shows decreasing current upon cycling possibly indicating a lost of some of the catalyst from the GC disk electrode. (bottom) A comparison of a 5 mm Pt disk electrode (green), Pt/C (black), $LaNiO_3$ (red), and $LaMnO_3$ at 900 RPM in O_2 saturated 0.1 M KOH. Both Pt catalysts show the most positive onset potential, while the oxide catalyst show an approximate 0.6 V overpotential for ORR (considering the $E_{1/2}$).

The RDE study for Pt/C shown in Figure 5.13top was obtained by preparing a catalyst ink suspension and drop casting onto a GC electrode using the same preparation technique as for the perovskite catalyst. The most distinctive feature of the Pt/C scan is the wide potential range over which a mass-transport limiting current can be observed (approximately 0.8 V to 0.4 V vs. RHE). Additionally, there appears to be only one redox wave, which suggests a single step mechanism for ORR. The Pt disk electrode showed similar performance and current densities (as can be observed in Figure 5.13bottom). Another interesting feature is the decreasing current in the 1600-RPM scan as a function of cycling. It is unlikely that Pt is becoming poisoned and losing activity in this environment, therefore the decreasing current is likely due to a loss of active material from the working electrode.

Figure 5.13bottom shows a comparison of the Pt catalysts with $LaMnO_3$ and $LaNiO_3$ at 900 RPM in O_2 saturated 0.1 M KOH. The most interesting feature is the significantly higher overpotential observed for the perovskite catalysts (from the $E_{1/2}$). As discussed in Chapter 1, every bit of potential sacrificed as overpotential translates to less power produced by the fuel cell. While there is a balance to be struck between acceptable overpotentials and cost of materials, sacrificing 0.6 V for using an oxide catalyst may be considered too high a cost in performance loss. Additionally, the slopes of the kinetic regions of each scan appear to change suggesting that the kinetics of ORR on perovskites and Pt catalyst are different. It is very likely that the mechanism of ORR is different for Pt and oxide catalysts based solely on differences in the nature of the surface. Certainly adsorbate formation thermodynamics and kinetics are different, and has already been discussed as it pertains to perovskite catalysts.

As shown in Table 5.3, the apparent electron transfer count from the Pt/C data was 1.97 while the apparent count for the Pt disk electrode was 2.51. This is somewhat unexpected since

Pt is known to be (essentially) the best catalyst for ORR in acidic and basic solutions Only seeing an electron count near 2 suggests that there may be some problems associated with our experimental set-up. This calls into question many of the results presented in this Chapter. Future work in this system should focus on the quantitative accuracy of the electrocatalytic performance of these materials. It is unfortunate that these issues were not resolved before the writing of this dissertation; however, much was learned about these catalysts and their behavior, which will aid in the answering of the remaining questions regarding the performance of perovskite oxide catalysts.

5.7 Conclusions

In this chapter, La-based transition metal perovskites were studied as potential non-noble metal catalysts for ORR in alkaline electrolytes. We find that in each of the materials studied, it appears that these catalysts favor the two, 2-electron step mechanism, forming peroxide rather than the direct 4-electron reduction to water as has been previously reported. Furthermore, we find that the un-substituted perovskites we studied are chemically unstable over 3 weeks at 80 ºC in 3 M KOH.

Additionally, we discussed a comparison of perovskite catalysts prepared at Cornell and MIT, and concluded that there is some disagreement between our findings. While we are continuing to work with our collaborators at MIT to reach a common understanding of the properties of these materials, it is clear that several questions remain regarding the potential suitability of perovskite catalysts for ORR in alkaline solutions.

Future work in this area should focus on achieving an accurate, quantitative understanding of the mechanism of ORR on these types of catalysts. Furthermore, the stability

and dissolution dynamics should be studied in more detail so as to fully understand the thermodynamic and kinetic factors that affect long-term durability and performance.

REFERENCES

(1) Suntivich, J.; Gasteiger, H. A.; Yabuuchi, N.; Nakanishi, H.; Goodenough, J. B.; Shao-Horn, Y. *Nature Chem* **2011**, *3*, 546–550.

(2) Chen, S.; Ferreira, P. J.; Sheng, W.; Yabuuchi, N.; Allard, L. F.; Shao-Horn, Y. *J. Am. Chem. Soc.* **2008**, *130*, 13818–13819.

(3) Chen, S.; Sheng, W.; Yabuuchi, N.; Ferreira, P. J.; Allard, L. F.; Shao-Horn, Y. *J. Phys. Chem. C* **2009**, *113*, 1109–1125.

(4) Ruban, A. V.; Skriver, H. L.; Nørskov, J. K. *Phys. Rev. B* **1999**, *59*, 15990.

(5) Markovic, N. M.; Schmidt, T. J.; Stamenkovic, V.; Ross, P. N. *Fuel Cells* **2001**, *1*, 105–116.

(6) Stamenkovic, V.; Schmidt, T. J.; Ross, P. N.; Markovic, N. M. *J. Phys. Chem. B* **2002**, *106*, 11970–11979.

(7) Shao, M. H.; Sasaki, K.; Adzic, R. R. *J. Am. Chem. Soc.* **2006**, *{128}*, {3526–3527}.

(8) Zhang, J.; Mo, Y.; Vukmirovic, M. B.; Klie, R.; Sasaki, K.; Adzic, R. R. *JOURNAL OF PHYSICAL CHEMISTRY B* **2004**, *{108}*, {10955–10964}.

(9) Xiao, L.; Zhuang, L.; Liu, Y.; Lu, J.; Abruña, H. D. *J. Am. Chem. Soc.* **2009**, *{131}*, {602–608}.

(10) Yeh, Y.-C.; Chen, H. M.; Liu, R.-S.; Asakura, K.; Lo, M.-Y.; Peng, Y.-M.; Chan, T.-S.; Lee, J.-F. *Chem. Mater.* **2009**, *{21}*, {4030–4036}.

(11) Wang, W.; Huang, Q.; Liu, J.; Zou, Z.; Zhao, M.; Vogel, W.; Yang, H. *Journal of Catalysis* **2009**, *{266}*, {156–163}.

(12) Yang, J.; Lee, J. Y.; Zhang, Q.; Zhou, W.; Liu, Z. *J. Electrochem. Soc.* **2008**, *{155}*, {B776–B781}.

(13) Salvador-Pascual, J. J.; Citalan-Cigarroa, S.; Solorza-Feria, O. *Journal of Power Sources* **2007**, *{172}*, {229–234}.

(14) Gasteiger, H. A.; Kocha, S. S.; Sompalli, B.; Wagner, F. T. *Applied Catalysis B: Environmental* **2005**, *56*, 9–35.

(15) Borup, R.; Meyers, J.; Pivovar, B.; Kim, Y. S.; Mukundan, R.; Garland, N.; Myers, D.; Wilson, M.; Garzon, F.; Wood, D.; Zelenay, P.; More, K.; Stroh, K.; Zawodzinski, T.; Boncella, J.; McGrath, J. E.; Inaba, M.; Miyatake, K.; Hori, M.; Ota, K.; Ogumi, Z.; Miyata, S.; Nishikata, A.; Siroma, Z.; Uchimoto, Y.; Yasuda, K.; Kimijima, K.-I.; Iwashita, N. *Chem. Rev. (Washington, DC, U. S.)* **2007**, *107*, 3904–3951.

(16) Wang, B. *Journal of Power Sources* **2005**, *152*, 1–15.

(17) Markovic, N. *J. Electrochem. Soc.* **1997**, *144*, 1591.

(18) Wang, Y.; Li, L.; Hu, L.; Zhuang, L.; Lu, J.; Xu, B. *Electrochemistry Communications* **2003**, *5*, 662–666.

(19) Yang, C. *International Journal of Hydrogen Energy* **2004**, *29*, 135–143.

(20) Demarconnay, L.; Coutanceau, C.; Léger, J. M. *Electrochimica Acta* **2004**, *49*, 4513–4521.

(21) Pourbaix, M. *Atlas of Electrochemical Equilibria in Aqueous Solutions*; National Association of Corrosion Engineers, 1974.

(22) Yang, Y. F.; Zhou, Y. H.; Cha, C. S. *Electrochimica Acta* **1995**, *40*, 2579–2586.

(23) Prakash, J.; Joachin, H. *Electrochimica Acta* **2000**, *45*, 2289–2296.

(24) Gojković, S. L.; Gupta, S.; Savinell, R. F. *JOURNAL OF ELECTROANALYTICAL CHEMISTRY* **1999**, *462*, 63–72.

(25) Heller-Ling, N.; Prestat, M.; Gautier, J. L.; Koenig, J. F.; Poillerat, G.; Chartier, P. *Electrochimica Acta* **1997**, *42*, 197–202.

(26) Hu, Y.; Tolmachev, Y. V.; Scherson, D. A. *JOURNAL OF ELECTROANALYTICAL CHEMISTRY* **1999**, *468*, 64–69.

(27) Rashkova, V.; Kitova, S.; Konstantinov, I.; Vitanov, T. *Electrochimica Acta* **2002**, *47*, 1555–1560.

(28) Ponce, J.; Rehspringer, J. L.; Poillerat, G.; Gautier, J. L. *Electrochimica Acta* **2001**, *46*, 3373–3380.

(29) Mao, L.; Sotomura, T.; Nakatsu, K.; Koshiba, N.; Zhang, D.; Ohsaka, T. *J. Electrochem. Soc.* **2002**, *149*, A504.

(30) Matsuki, K.; Kamada, H. *Electrochimica Acta* **1986**, *31*, 13–18.

(31) Klápště, B.; Vondrák, J.; Velická, J. *Electrochimica Acta* **2002**, *47*, 2365–2369.

(32) Yang, J.; Xu, J. J. *Electrochemistry Communications* **2003**, *5*, 306–311.

(33) Mao, L. *Electrochimica Acta* **2003**, *48*, 1015–1021.

(34) Varcoe, J. R.; Slade, R. C. T. *Fuel Cells* **2005**, *5*, 187–200.

(35) McLean, G. F.; Niet, T.; Prince-Richard, S.; Djilali, N. *International Journal of Hydrogen Energy* **2002**, *27*, 507–526.

(36) Antolini, E.; Gonzalez, E. R. *Journal of Power Sources* **2010**, *195*, 3431–3450.

(37) Ramaswamy, N.; Mukerjee, S. *Advances in Physical Chemistry* **2012**, *2012*, 1–17.

(38) Zhong, C.-J.; Luo, J.; Fang, B.; Wanjala, B. N.; Njoki, P. N.; Loukrakpam, R.; Yin, J. *Nanotechnology* **2010**, *21*, 062001.

(39) Zhang, T.; Anderson, A. B. *Electrochimica Acta* **2007**, *53*, 982–989.

(40) Anderson, A. B.; Cai, Y.; Sidik, R. A.; Kang, D. B. *JOURNAL OF ELECTROANALYTICAL CHEMISTRY* **2005**, *580*, 17–22.

(41) Roques, J.; Anderson, A. B. *J. Fuel Cell Sci. Technol.* **2005**, *2*, 86.

(42) Anderson, A. B.; Roques, J.; Mukerjee, S.; Murthi, V. S.; Markovic, N. M.; Stamenkovic, V. *J. Phys. Chem. B* **2005**, *109*, 1198–1203.

(43) Toda, T.; Igarashi, H.; Watanabe, M. *J. Electrochem. Soc.* **1998**, *145*, 4185–4188.

(44) Markovic, N. M.; Schmidt, T. J.; Grgur, B. N.; Gasteiger, H. A.; Behm, R. J.; Ross, P. N. *J. Phys. Chem. B* **1999**, *103*, 8568–8577.

(45) Mukerjee, S.; Srinivasan, S.; Soriaga, M. P.; McBreen, J. *J. Electrochem. Soc.* **1995**, *142*, 1409–1422.

(46) Iwasita, T.; Xia, X. *JOURNAL OF ELECTROANALYTICAL CHEMISTRY* **1996**, *411*, 95–102.

(47) Markovic, N. M.; Ross, P. N., Jr *Surface Science Reports* **2002**, *45*, 117–229.

(48) Uribe, F. A.; Zawodzinski, T. A., Jr *Electrochimica Acta* **2002**, *47*, 3799–3806.

(49) Roques, J.; Anderson, A. B. *Surface Science* **2005**, *581*, 105–117.

(50) Kostadinov, L. N.; Anderson, A. B. *Electrochem. Solid-State Lett.* **2003**, *6*, E30.

(51) Li, X.; Gewirth, A. A. *J. Am. Chem. Soc.* **2005**, *127*, 5252–5260.

(52) Wei, Y.; Wu, K.; Wu, Y.; Hu, S. *Electrochemistry Communications* **2003**, *5*, 819–824.

(53) Anderson, A. B.; Albu, T. V. *J. Am. Chem. Soc.* **1999**, *121*, 11855–11863.

(54) Shao, M.-H.; Liu, P.; Adzic, R. R. *J. Am. Chem. Soc.* **2006**, *128*, 7408–7409.

(55) Jörissen, L. *Journal of Power Sources* **2006**, *155*, 23–32.

(56) Mitchell, R. H. *Perovskites: Modern and Ancient*; Almaz Press Inc.: Thunder Bay, Ontario, 2002.

(57) Neburchilov, V.; Wang, H.; Martin, J. J.; Qu, W. *Journal of Power Sources* **2010**, *195*, 1271–1291.

(58) Niu, Y.; Sunarso, J.; Liang, F.; Zhou, W.; Zhu, Z.; Shao, Z. *J. Electrochem. Soc.* **2011**, *158*, B132.

(59) Matsumoto, Y.; Yoneyama, H.; Tamura, H. *Journal of Electroanalytical Chemistry and Intefacial Chemistry* **1977**, *80*, 115-121.

(60) Matsumoto, Y.; Tamura, H.; Yoneyama, H. *Chemistry Letters* **1975**, 661–662.

(61) Matsumoto, Y.; Yoneyama, H.; Tamura, H. *Journal of Electroanalytical Chemistry and Interfacial Electrochemistry* **1977**, *79*, 319–326.

(62) Tseung, A.; Bevan, H. L. *Journal of Electroanalytical Chemistry and Interfacial Electrochemistry* **1973**, *45*, 429–438.

(63) Behret, H.; Binder, H.; Sandstede, G. *Electrochimica Acta* **1975**, *20*, 111–117.

(64) Bockris, J. O.; Otagawa, T. *J. Phys. Chem.* **1983**, *87*, 2960–2971.

(65) Yeager, E. *Electrochimica Acta* **1984**, *29*, 1527–1537.

(66) Tulloch, J.; Donne, S. W. *Journal of Power Sources* **2009**, *188*, 359–366.

(67) Sunarso, J.; Torriero, A. A. J.; Zhou, W.; Howlett, P. C.; Forsyth, M. *J. Phys. Chem. C* **2012**, *116*, 5827–5834.

(68) Wang, X.; Sebastian, P. J.; Smit, M. A.; Yang, H.; Gamboa, S. A. *Journal of Power Sources* **2003**, *124*, 278–284.

(69) Voorhoeve, R. J. H.; Remeika, J. P.; Freeland, P. E.; Matthias, B. T. *Science* **1972**, *177*, 353–354.

(70) Voorhoeve, R. J. H.; Johnson, D. W.; Remeika, J. P.; Gallagher, P. K. *Science* **1977**, *195*, 827–833.

(71) Choi, B. H.; Park, S.-A.; Park, B. K.; Chun, H. H.; Kim, Y.-T. *Materials Research Bulletin* **2013**, 1–25.

(72) Yuasa, M.; Shimanoe, K.; Teraoka, Y.; Yamazoe, N. *Electrochem. Solid-State Lett.* **2011**, *14*, A67.

(73) Suntivich, J.; Gasteiger, H. A.; Yabuuchi, N.; Shao-Horn, Y. *J. Electrochem. Soc.* **2010**, *157*, B1263.

(74) Vassiliou, J. K.; Ziebarth, R. P.; Hornbostel, M.; DiSalvo, F. J. *Journal of Solid State Chemistry* **1989**, *81*, 208–216.

(75) Singh, R. N.; Tiwari, S. K.; Singh, S. P.; Singh, N. K.; Poillerat, G.; Chartier, P. *Faraday Trans.* **1996**, *92*, 2593.

(76) Baythoun, M. S. G.; Sale, F. R. *J Mater Sci* **1982**, *17*, 2757–2769.

(77) Chick, L. A.; Pederson, L. R.; Maupin, G. D.; Bates, J. L.; Thomas, L. E.; Exarhos, G. J. *Materials Letters* **1990**, *10*, 6–12.

(78) Colomer, M. T.; Fumo, D. A.; Jurado, J. R.; Segadaẽs, A. M. *J. Mater. Chem.* **1999**, *9*, 2505–2510.

(79) Nilsen, O.; Peussa, M.; Fjellvåg, H.; Niinistö, L.; Kjekshus, A. *J. Mater. Chem.* **1999**, *9*, 1781–1784.

(80) McCormack, M.; Jin, S.; Tiefel, T. H.; Fleming, R. M.; Phillips, J. M.; Ramesh, R. *Appl. Phys. Lett.* **1994**, *64*, 3045.

(81) Jin, S.; McCormack, M.; Tiefel, T. H.; Ramesh, R. *J. Appl. Phys.* **1994**, *76*, 6929.

(82) Hyodo, T.; Miura, N.; Yamazoe, N. 1995; Vol. 393, p. 79.

(83) Hyodo, T.; Shimizu, Y.; Miura, N.; Yamazoe, N. *Denki Kagaku* **1993**, *61*, 1458.

(84) Smith, E. H. *The Prediction of Solubility in Water of New Ionic Materials*; Unpublished: Ithaca, NY, 2013.

(85) Bard, A. J.; Faulkner, L. R. *Electrochemical Methods: Fundamentals and Applications*; 2nd ed. John Wiley & Sons: New York, 2000.

(86) *Educators Reference Guide for Electrochemistry*; 3rd ed. LMPROF1; Pine Instrument Company: Grove City, PA, 2000; pp. 1–70.

(87) Kissinger, P.; Heineman, W. R. *Laboratory Techniques in Electroanalytical Chemistry*; 2nd ed. CRC Press: New York, 1996.

(88) Abruña, H. D. Fundamentals of Electrochemistry. *CHEM629: Graduate Course at Cornell University* **2010**.

(89) Adzic, R. R.; Zhang, J.; Sasaki, K.; Vukmirovic, M. B.; Shao, M.; Wang, J. X.; Nilekar, A. U.; Mavrikakis, M.; Valerio, J. A.; Uribe, F. *Top Catal* **2007**, *46*, 249–262.

(90) Brankovic, S. R.; Wang, J. X.; Adzic, R. R. *Electrochem. Solid-State Lett.* **2001**, *4*, A217.

(91) Zhang, J.; Lima, F. H. B.; Shao, M. H.; Sasaki, K.; Wang, J. X.; Hanson, J.; Adzic, R. R. *J. Phys. Chem. B* **2005**, *109*, 22701–22704.

(92) Sasaki, K.; Wang, J. X.; Balasubramanian, M.; McBreen, J.; Uribe, F.; Adzic, R. R. *Electrochimica Acta* **2004**, *49*, 3873–3877.

(93) Kuwana, T. *Analytical Electrochemistry: A Laboratory Manual*; Analytical Science Digital Library, 2007; pp. 1–9.

(94) Subban, C. V. Synthesis and Characterization of Mixed-Metal Oxides for Catalyst Support Applications in Proton Exchange Membrane Fuel Cells, Cornell University, 2012.

(95) Luo, Z.; Lim, S.; Tian, Z.; Shang, J.; Lai, L.; MacDonald, B.; Fu, C.; Shen, Z.; Yu, T.; Lin, J. *J. Mater. Chem.* **2011**, *21*, 8038.

(96) Song, C.; Zhang, J. *PEM fuel cell electrocatalysts and catalyst layers: fundamentals and applications. Springer, London* **2008**.

(97) Swider-Lyons, K.; Baturina, O. A.; Garsany, Y. *Low-Platinum Catalysts for Oxygen Reduction at PEMFC Cathodes*; V.C.3; Naval Research Laboratory: Washington, D.C., 2006; pp. 1–4.

FINAL THOUGHTS

LOOKING TO THE FUTURE

This dissertation has discussed only a few of the challenges facing fuel cell technology. While much has been learned about new types of materials and novel approaches to solving these challenges have been developed, much still remains to be done before fuel cell technology can be fully realized.

The ongoing work at the Energy Materials Center at Cornell is a testament to the resolve with which today's researchers are working to address the energy challenge our world faces. While fuel cells are interesting in principle due to their seemingly simple and idealized promise of clean, abundant energy conversion, other more sustainable technologies such power generation from wind, photovoltaic, and biomass sources are also competing for valuable research dollars. Unless some revolutionary new materials are developed which improve PEM fuel cell durability and performance, it is difficult to think that fuel cells will be able to keep pace with the rapidly changing needs of the world energy economy (certainly at least for wide-spread automotive deployment).

It is my sincere hope that the work presented in this dissertation will aid future researchers as they continue to develop new materials and methodologies to address the barriers to widespread fuel cell deployment, specifically the work I've done with nitride support materials. It is clear from the results discussed in this dissertation that binary metal nitride materials may possess the required conductivity and long-term chemical stability that current carbon-based supports lack. Furthermore the work on sputtering nitride thin-films will hopefully contribute to the scientific community's understanding of the complex passivation behavior of

surface oxide layers on nitride materials. Drawing from the steel industry, it will be interesting to see the effects of including Cr, V, or Mo into nitride compounds on their corrosion resistance.

Perovskite catalysts, by our experiments alone, do not appear to possess the necessary activity or chemical stability required for long-term operation in PEM fuel cell conditions. There is, however, some questions regarding the accuracy of the electrochemical experiments we performed, as Pt catalysts did not behave as was typically expected. While no technical errors were found in the experimental set up, some currently unknown factors may have contributed to, or been the source, of the conflicting results obtained. Furthermore, while the chemical stability of La-based perovskites does not appear to be sufficient in basic solutions, the effect of bound-anionic species (such as ionomers) on the stability of these materials is unknown. Long-term testing in an actual fuel cell will be required to determine conclusively if oxide catalysts will be suitable replacements for noble-metal catalysts in alkaline fuel cells.